Density of states measurements on semiconductor and thin film materials using photocurrent methods

Nastiti Puspitosari

université PARIS-SACLAY

NNT : 2018SACLS018

Density of states measurements on semiconductor and thin film materials using photocurrent methods

Thèse de doctorat de l'Université Paris-Saclay
préparée à l'Université Paris Sud

École doctorale n°575
Electrical, Optical, Bio : Physics and Engineering (EOBE)

Spécialité de doctorat : Physique

Thèse présentée et soutenue à Gif-Sur-Yvette, 22 Janvier 2018, par

Nastiti Puspitosari

Composition du Jury :

Pere Roca i Cabarrocas Directeur de Recherche CNRS, LPICM (UMR 7647)	Président
Nicolas Barreau Enseignant chercheur, IMN-MIOPS (UMR 6502)	Rapporteur
Laurent Lombez Chargé de recherche CNRS, IRDEP (UMR 7174)	Rapporteur
Olivier Acher Ingénieur, Société Horiba	Examinateur
Christophe Longeaud Directeur de Recherche CNRS, GeepS (UMR 8507)	Directeur de thèse

Thèse de doctorat

Titre : Mesure de densité d'états des semi-conducteurs et couche minces en utilisant des méthodes de photo-courants

Mots clés : densité d'états, semi-conducteurs couches minces, spectroscopie photo-courant

Résumé : Les recherches sur les matériaux en couches minces dédiées à l'industrie solaire restent un sujet d'intérêt avec le nombre croissant de types de matériaux incorporés en tant qu'absorbeur dans un dispositif solaire. Le besoin de techniques de caractérisation est donc aigu pour l'optimisation des matériaux et leur incorporation dans des cellules photovoltaïques.
Dans cette thèse, une méthode de photo-courant basée sur la spectroscopie de photo-courant à transformée de Fourier (FTPS) est utilisée pour effectuer des mesures sur des matériaux en couches minces et des cellules solaires. Notre FTPS a été développée pour réaliser 3 types de mesures: 1) mesure de réflexion et de transmission (R/T), 2) spectroscopie du coefficient d'absorption (α), et 3) mesure de réponse spectrale, efficacité quantique externe et densité de photo-courant court-circuit. Cette dernière est spécifiquement utilisée pour les cellules solaires. Nous avons utilisé les résultats de R/T pour effectuer une simulation numérique donnant l'épaisseur, l'indice de réfraction, la rugosité du film et le α optique.
Une modélisation de la densité d'états (DOS) en utilisant le logiciel DeOSt automatisé avec l'algorithme TLBO (Teacher Learner Based Optimization) a été développée pour trouver les valeurs des paramètres de DOS les mieux adaptées afin de reproduire le α expérimental. Une analyse de sensibilité a été faite pour trouver les paramètres DOS les plus importants parmi 15-17 paramètres. Nous avons mesuré plusieurs échantillons de a-Si: H déposés sous différentes conditions de dépôt, et utilisé nos résultats pour étudier leur DOS. Une comparaison des mesures de α sur a-Si: H déposé sur un substrat de verre et incorporé dans une cellule solaire a également été réalisée. Cette étude a conclu qu'une correction du spectre α doit être effectuée pour les mesures sur les cellules solaires.

Title : Density of states measurements on semiconductor and thin film materials using photocurrent methods

Keywords : density of states, thin film semiconductors, photocurrent spectroscopy

Abstract : Investigations on thin film materials dedicated to the solar industry are still a matter of interest with the growing numbers of material types incorporated as absorbers in a solar cell. The need of characterization techniques is therefore acute for the optimization of materials and their incorporation in solar devices.
In this thesis, a photocurrent method based on Fourier Transform Photocurrent Spectroscopy (FTPS) is used to perform the measurements of thin film materials and solar cells. Our FTPS was further developed to perform 3 types of measurements: 1) reflection and transmission (R/T) measurement, 2) absorption coefficient (α) spectroscopy, and 3) spectral response, external quantum efficiency, and short circuit photocurrent density measurements. This latter is specifically used for solar cells. We used the R/T results to perform numerical simulations giving the thickness, refractive index, film roughness, and optical α.
A modeling of the density of states (DOS) using the software DeOSt automated with the Teacher Learner Based Optimization (TLBO) algorithm was achieved to find the best suited DOS parameter values to reproduce the experimental spectrum of α. A sensitivity analysis was performed to find the most important DOS parameters among 15-17 parameters. For the experimental studies, we have measured several a-Si:H thin film samples prepared under different deposition conditions, and used their α spectra to study their DOS. A comparison of α measurements on a-Si:H thin films deposited on a glass substrate and incorporated in a solar cell device stack was also conducted. This study concluded that a correction of the α spectrum measured on solar cells had to be done.

Université Paris-Saclay
Espace Technologique / Immeuble Discovery
Route de l'Orme aux Merisiers RD 128 / 91190 Saint-Aubin, France

Acknowledgement

First and foremost I wish to thank my PhD supervisor, Dr. Christophe Longeaud, for being supportive since the days I began working on the Constant Photocurrent Method (CPM) during my Master internship in the laboratory GeePs. I remember he used to tell me that CPM was not the greatest characterization technique and that we will be able to build a better and faster characterization technique than this one. After I was done with my Master internship, I was honored that he gave me the opportunity to be a part of his research team as a PhD student and began to work on this new technique, the Fourier Transform Photocurrent Spectroscopy (FTPS). Ever since, Christophe has supported me not only by providing research guidance, but also academically and emotionally through the rough road to finish this thesis. He helped me come up with brilliant ideas and perfections over the past three years and a half. During the most difficult times when writing this thesis, he gave me the moral support and the freedom I needed to move on. The research on FTPS in this thesis, truly, would not be successfully implemented and documented without his abundant support.

I would like to thank the researchers and engineers in GeePs who have helped me overcome my difficulties during my thesis by being available and open to answer my questions. Denis, for being very kind and insightful to me and for teaching me about life and personal quality to carry on my thesis project. Jean-Paul Kleider, has taught me to have a wider perspective and to build wisdom in solving research problems. Jose Alvarez, who countless times voluntarily helped me look for some equipment and explained every single thing I had no idea about without any prejudice. Marie, who came up to introduce me to Christophe for my Master internship and who has given moral support to push on the sensitivity analysis study in my thesis. Sylvain, for being very energetic and optimistic every day. I especially would like to thank Sylvain for giving his support and ideas during the critical moment, when I was preparing my PhD defense slides. Arouna, who kept my passion to save the planet as he has always been passionate to push forward the implementation of photovoltaics in Burkina Faso. Special thanks for Rudi, who helped me with the Diplot software, without him I would not be able to fully operate this software. Alexandre, who has given me many ideas for the optic improvements in my FTPS bench. Aurore, for flowing positivity and keeping me motivated during the days I needed the most. Laurent and Olivier, who helped me with any informatics and computer problems.

I cannot find words to express my gratitude to my fellow PhD students in GeePs. Alexandra, for being there to support me and to have discussions about almost any-

thing. Redouane and Lucif, for sharing funny jokes and ideas during the coffee breaks. Cyril, for sharing his passion to fight climate change and for giving me a clearer view in any aspect. Sincerely, I shared with all of you beautiful unforgettable moments during my thesis.

Lastly, I would like to express my regards and gratitude to all of those who supported me in any respect during the completion of my thesis project. My family, who has been patiently waiting for me to finish my thesis. Thank you for my mom, dad, and sister for understanding my situation which has prevented me from seeing them often. My friends, for being loyal and for cheering me up at any time. Marko, for his constant support and for being who you are.

Contents

Chapter 1

Introduction

The importance of the development of renewable energy in the 21^{st} century has become very significant as the supply of fossil fuels is depleting, and as the carbon emissions caused by their consumption highly contribute to global warming and their cost becomes comparable to conventional energy production. In the past 50 years, the development of renewable energies was mainly focused on the hydro power due to the abundance of water on Earth. Furthermore, the systems of energy conversion from water have been well mastered due to their simplicity, such as the dam system. In the mean time, other sources of renewable energy such as wind and solar energies were developed at a much slower rate despite of their abundance. This is a result of their complexity and disadvantages compared to fossil fuel and hydro energy. For example, the poor conversion efficiencies of the early designs resulted in high costs of energy production, making them non-competitive in the energy market. However, years of research and development lead to significant improvements in conversion efficiencies while the material capital costs have plummeted. Furthermore, these sources have an intermittent and poorly predictable character, posing a challenge for satisfying the energy demand. This resulted in a tremendous amount of research in the domains of energy storage and production forecasting, both being aimed at surpassing this limitation. Today, solar and wind energy sources are becoming economically competitive with fossil fuels in an increasing number of countries, and we observe a rapid rise in installed capacity on a global level. Nevertheless, these sources represent a small share of the global energy supply, and more development is needed to allow for a complete transition to renewable energy. The discussion topic related to the research in the wind energy sources is beyond the scope of this thesis. Meanwhile, the research in the field of solar energy represents the main focus of this work.

The concept of energy harvesting from solar radiation is done through the absorption of light in a semiconductor material incorporated in solar cells. The solar cells design promotes the separation of positive and negative carriers induced by a potential difference that leads to current generation. This means that the role of the semiconductor material used for the light absorption is of primary importance in the solar energy harvesting. From 1976 to 2017, the research and development of semiconductor materials used in solar cells has progressed as much as 46% in terms of solar cell's efficiency [1]. The research on solar cell materials is focused on the

search of best performing materials by improving current and inventing new solar cell technologies. A well-performing material is the one with good optical and electrical properties, the latter depending on the density of defects in the material. Material defects are responsible of decreasing the carrier collection in the solar cells, leading to a decreased current generation.

In order to assess the factors limiting the performance of these materials, characterization techniques were developed to study their optical and electrical properties of the semiconductor material for solar cells. Optical characterizations measure the optical properties of the material such as its transmittance, reflectance, and absorptance as function of the incident photon energy. Transmittance, T, and reflectance, R, are particularly important optical parameters related to the absorptance, A, of the material as $A = 1 - R - T$. Usually, materials for solar cells are designed to optically absorb the photon energy higher than that corresponds to the band gap energy of the material, as it is a semiconductor. The electrical characterizations are useful tools to measure the electrical properties and, some of them can be used to obtain information on the absorption coefficient of the material as a function of impinging photon energy. This absorption coefficient can be linked to the defects present in the semiconductor material [2–15].

1.1 Brief overview of defect density characterization of a semiconductor material using photocurrent methods

The electrical characterization techniques to measure the absorption coefficient of a material are often based on photoconductivity properties, which means that these techniques use the generation of photocurrent in the studied material. The absorption coefficient of the material as a function of photon energy is proportional to the ratio of the photocurrent generation in the material and the flux of the impinging photon energy [16]. Most of these photocurrent techniques analyze the generation of the photocurrent for each photon energy of the impinging light onto the material. Photocurrent generation, proportional to the absorption coefficient, is the product of all possible electronic transitions in the semiconductor materials. Semiconductor material is comprised of electronic states, where two carrier types are present : electrons and holes.

Except in the case of a very intrinsic semiconductor, where the contributions of each type of carrier to the photocurrent are equivalent provided $\mu\tau_e = \mu\tau_h$, one usually deals with semiconductors in which one type of carrier, called the majority carrier, dominates over the other type, called the minority carrier. In the following, we shall assume that we are dealing with a semiconductor in which electrons are the majority carriers. This assumption will not hamper the description of the phenomena.

Semiconductors are known for the presence of two bands of electronic states, in which electrons can be found, separated by a gap of energy in which, ideally, no electronic states are present. These two bands are the valence band completely filled

at 0 K and the conduction band completely empty at 0 K. At higher temperature thermal energy can be provided to some electrons of the valence band so they can reach the states of the conduction band. A transition of an electron from the valence band toward the conduction band leaves a completely filled band minus one electron and the complete behavior of the system (full band – one electron) is assimilated to the behavior of a fictive particle named hole. Hence, under dark and at a given temperature, the valence band contains holes generated by the thermally activated departure of electrons toward the conduction band. The bands occupancy is described via a Fermi-Dirac statistics in which the dark Fermi level plays a major role, the states below the Fermi level being mainly occupied and the states above being mainly empty. It is these two types of carriers populating the bands that contribute to the current if a field is applied to the semiconductor.

The band occupancy can be modified at a given temperature if one shines light onto the material with a photon energy higher than the band gap. In this case, photons interacting with the electrons of the valence band transfer their energy to these carriers and transitions of electrons toward the conduction band occur that modify the electronic states occupancy in both bands since an electron transition toward the conduction band creates a hole in the valence band. Under steady state illumination the generation of carriers, holes and electrons, is compensated by their recombination to eventually reach a balance between generation and recombination. If no states are present in the band gap the main recombination process is a band to band recombination between electrons and holes. The two types of carriers participate to the photo-generated current if a field is applied to the semiconductor but if the electrons are the majority carriers their contribution to the photocurrent will overpass that of holes. The picture gets more complicated when defect states are present in the band gap. The origins of these states are numerous and we can quote, without being exhaustive, the presence of impurities, vacancies, dislocations and twins for crystalline materials or the disorder in amorphous materials. As in the case of an ideal semiconductor, at a given temperature the states occupancy is driven usually by a Fermi-Dirac statistics and all the states below the Fermi level are mostly filled whereas those above the Fermi level are mostly empty including the defect states. These states are detrimental to the performances of the semiconductor since they add a recombination path to the previous band to band recombination. Indeed, these states can capture an electron of the conduction band followed by a hole of the valence band to perform recombination and the total number of available carriers in the bands decreases. The more the defects in the band gap, the lower the photocurrent will be and the semiconductor may not be adapted to solar energy conversion. That is why all the research on solar cell fabricator try to minimize the number of defects present in the semiconductor. For that purpose the defect density must be estimated for instance as function of fabrication conditions to optimize the semiconductor performances.

Since the defect density influences the photocurrent flowing into a semiconductor, some characterization techniques to estimate the defect density are based on the photoconductivity properties of the studied materials. We cannot quote all the techniques that have been elaborated for that purpose and we shall only present briefly the principle of the one we have used in this work.

As described above, photons interact with the electrons of the material and the absorption of the light spectrum as function of the photon energy indicates the amplitude of the interaction between photons and electrons. The photon will interact with the valence band electrons but will also interact with the filled defect states in the band gap, in both cases promoting electrons into the conduction band giving rise to a photocurrent. The amplitude of the interaction, and therefore the photocurrent intensity, depends on the number of electrons available for a given transition and thus on the number of states filled by electrons. Therefore, measurement of the absorption spectrum as function of the photon energy, for below gap photon energy, may provide information of the defect density present in the gap. It is that property that we have used to obtain a spectroscopy of the defect density for the states located below the Fermi level.

1.2 Problem description and research approach

To implement a proper defect characterization in the semiconductor material, a reliable photocurrent measurement to obtain a good absolute absorption coefficient spectrum is necessary. Some of the photocurrent techniques to obtain the absorption coefficient are Dual Beam Photoconductivity (DBP) [17–19], Photo-thermal Deflection Spectroscopy (PDS) [20], Constant Photocurrent Method (CPM) [2, 21–23], and Fourier Transform Photocurrent Spectroscopy (FTPS) [24–29]. Among these photocurrent methods, FTPS is until now not only the fastest but also gives high precision and high resolution results. FTPS uses the same principles as CPM, which is to keep the photocurrent generated on the semiconductor material constant for each given photon energy. In CPM, a monochromatic light source with a given photon energy is used, hence the measurement time is very long if a high resolution measurement is sought, e.g. a CPM measurement on a material with a spectral range of 600 – 1800 nm with a 10 nm resolution can go up to several hours. By replacing the monochromatic light source with a white light source, and process the measurement data using an FTIR spectrometer, the FTPS measurement goes very much faster, i.e. $\sim$ 1 minute, than if the same measurement with the same spectral range and resolution was done using CPM.

Nevertheless, the FTPS proposed by Poruba et al. [24], Holovsky et al. [25], and Melskens et al. [30] did not take into consideration the suppression of the interference fringes in the absorption coefficient curve, which has to be eliminated to obtain a more accurate absorption coefficient spectrum. Yet, older photocurrent measurement versions e.g. Transmission CPM [23] and Absolute CPM [21] have successfully removed the interference fringes in the absorption coefficient spectrum. To suppress these interferences, these previously proposed FTPS methods have to be post processed using a numerical simulation. In addition, to obtain an absorption coefficient spectrum in its absolute value, optical measurements, i.e. transmission and reflection measurements, are needed to calculate the optical absorption coefficient of the semiconductor material, which is used to calibrate the absorption coefficient spectrum measured by FTPS. The current proposed versions of FTPS do not support the

optical measurement of the material, therefore, a transmission and reflection measurement using a classical UV-Visible spectrometer has to be performed to obtain the optical properties, necessary for the absorption coefficient spectrum calibration.

As previously explained, the absorption coefficient spectrum is linked to the distribution of the defect density present in a semiconductor material. To yield the information of the distribution of the defect density, several methods are proposed such as using the derivative of the absorption coefficient or a fitting by a sum of error functions [31, 32]. The first method is done using a computational mathematics and needs a regularization method to obtain a noise free derivative which makes it a quite complex method to obtain a correct result [33, 34]. The second method is used by Melskens et al. [30] and is done without the calculation of the derivative, thus the calculation time is much faster. Nevertheless, error function as a primitive Gaussian function, does not have any direct physical quantities equivalence to the defect density distributions. Another approach is done using a curve fitting method, where the absorption coefficient spectrum is fitted using fitting functions composed of the convolution integrals of the possible electronic transitions between the states of the density of defects of the semiconductor. With this method, the fitting functions have to be correctly chosen according to the possible type of electronic transitions at each photon energy for the entire range of photon energy in the absorption coefficient spectrum. The solution of the fitting functions finally gets quite complex since the criteria of the fitting, the starting values of the parameters, and the solver has to be defined for individual fitting function. Hence, in the current state of the art, the accurate definition of a defect density distribution from the absorption coefficient still has to make a compromise between the amount of the calculation time and the complexity of the calculation. If the distribution of the density of states, especially the defect states of the material, can be extracted from any of the chosen methods, the direct relation of the density of states distribution parameters to the absorption coefficient has not yet been very well mastered.

According to the current problem in the state of the art of defect density determination of a semiconductor material from its absorption coefficient spectrum, the research approach in this thesis can be simplified into the following list of research questions:

1. What kind of simple, reliable and fast characterization technique has to be chosen to perform the optical and electrical measurements for obtaining a correct absolute absorption coefficient of a semiconductor material and a solar cell?

2. How to deduce a correct absorption coefficient spectrum from the measurement?

3. How to determine the defect density distribution of a semiconductor material from its absorption coefficient using a more efficient method?

4. If the defect density distributions are linked to the absorption coefficient spectrum, which of those defect density distribution parameters are the most influential on the absorption coefficient?

5. How does the absorption coefficient spectrum of a semiconductor material compare to that of a solar cell incorporating the same semiconductor material for its absorber layer?

1.3 Thesis outline

The optical measurements (transmission and reflection), and the absorption coefficient measurements using the photocurrent concept and realized with an FTIR spectrometer are proposed in this thesis to provide simple, reliable, and fast measurements. The bases of an FTIR spectrometer and the photocurrent measurement using an FTIR spectrometer are explained in detail in Chap. 2. In this chapter we also show that with a single and same bench we can perform transmission, reflection, absorption measurements and FTPS measurements on thin film materials as well as spectral response of solar cells. The experimental setup and procedures, as well as the data treatment of the raw measurement data are detailed for the case of measurement on a semiconductor thin film and on a solar cell.

The determination of the optical properties of the semiconductor material deduced from its transmission and reflection measurements, such as the refractive index, thickness, and surface roughness is explained in Chap. 3. In this chapter, several methods to determine the optical properties from the measurements are proposed and compared. By using some of the optical properties values, the optical absorption coefficient of the studied material can be calculated. The calculated optical absorption coefficient is subsequently used to calibrate the absorption coefficient spectrum from the photocurrent measurement using FTPS. Some a-Si:H thin films with different deposition conditions and given optical properties are used as samples to evaluate the measurement results using our bench.

The determination of the defect density distribution from the absorption coefficient spectrum measured with FTPS is approached using the modeling of the density of states of a semiconductor material to reproduce the absorption coefficient spectrum by a numerical computation. Two types of density of states models, i.e. standard and defect-pool models, reproducing the same absorption coefficient are used to compare different distributions of the defect density in a semiconductor material. Density of states model involves multiple parameters, therefore, the values of these parameters are quite complicated to extract if a good fit between the measured and computed absorption coefficient is desired. Instead of using manual adjustment, the values of density of states parameters are extracted with a Teacher Learner Based Optimization (TLBO) algorithm [90]. This algorithm was chosen as it was successfully used to extract solar cell parameters from their I-V measurement result. The optimization of the density of states parameter search from an absorption coefficient using TLBO is detailed in Chap. 4. In this chapter, the influence of each density of states parameter on the absorption coefficient is approached using a sensitivity analysis study [92]. This sensitivity analysis is particularly interesting to understand the most influential parameters on the absorption coefficient, among all of the density of states parameters.

Examples of the density of states parameters determination on a-Si:H samples, as the ones used for the determination of the optical properties are presented in Chap. 5. The results of the density of states of these samples are compared using two models: standard and defect-pool density of states models. In this chapter, the comparison of the measurement of the absorption coefficient on a semiconductor material deposited on a transparent non-conductive substrate and on a solar cell incorporating the same material for its absorber layer is also studied.

Finally, the main conclusions of this research project are given in Chap. 6.

Chapter 2

The Bases of Fourier Transform Infrared Spectrometer : Application to Photocurrent Measurements

The experiments in this project have been performed with a Fourier Transform Infrared (FTIR) spectrometer. This chapter is written to unveil how a spectrum is measured by an FTIR spectrometer and its application to photocurrent measurements. An FTIR spectrometer can be used to collect a spectrum of absorption or emission of a material (in form of solid, liquid, or gas) with a high spectral resolution over a wide spectral range [35]. This means for example, that the absorption spectroscopy performed by an FTIR spectrometer measures how much light is absorbed or transmitted by a material at each wavelength. A basic example of this kind of spectroscopy is the "dispersive spectroscopy" which is mostly used in a UV-Visible spectrometer, where a beam of monochromatic light is used to illuminate a sample and, how much light is absorbed by the sample is measured [36]. The same measurement is repeated, performed by choosing the wavelength of the light emitted by the monochromatic light source using an optical filter.

The spectroscopy performed by an FTIR spectrometer uses a more advanced technique, where the light source is no longer monochromatic. Broadband light source containing many wavelengths is used in an FTIR spectrometer. By using the Fourier transform, basically we *encode* the information of the measurement at each wavelength, compile it in one *package*, and *decode* the information at each wavelength. That means that the absorption measurement of a material using an FTIR results in the information on how much light is absorbed by the material for each specific wavelength in a single shot. Hence, the FTIR spectroscopy gives a bigger advantage over dispersive spectroscopy by yielding an absorption spectrum of a material for each wavelength at a faster rate and usually with a higher precision.

In order to yield a spectrum, an FTIR spectrometer uses the principle of a Michelson interferometer to generate the raw data (package) called as "interferogram" (see Fig. 2-1) and later processes (decodes) the interferogram using a mathematical pro-

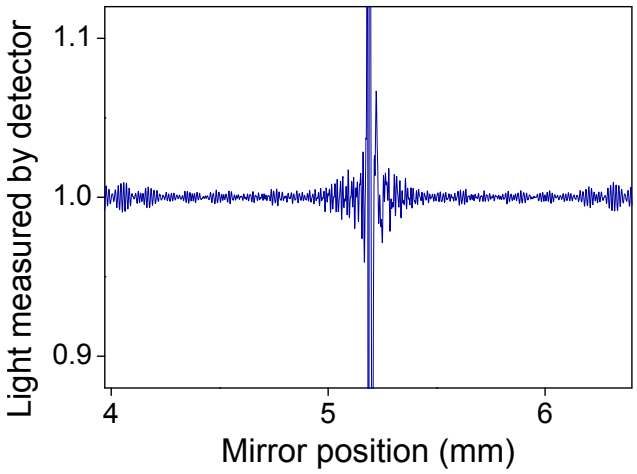

Figure 2-1: An example of interferogram given by an FTIR spectrometer

cess called Fourier Transform (FT). In this project, we have used an FTIR spectrometer to perform photocurrent measurements on samples, resulting in photocurrent spectra for given materials at each wavelength.

This chapter will present the principles of an FTIR spectrometer based on a Michelson interferometer and its interferogram generation using Fourier Transform in Sec. 2.1. The following Sec. 2.2 will explain the application of an FTIR spectrometer to photocurrent measurements on semiconductor materials. The detailed explanation related to the experimental setup and how to obtain the results of reflectance/transmittance, absorption coefficient, and spectral response-EQE can be found in Secs. 2.3, 2.4, and 2.5, respectively.

2.1 Generation of an interferogram by a Michelson Interferometer

Despite of how much faster is the measurement rate performed by an FTIR spectrometer compared to one performed using dispersive spectroscopy, the spectroscopy technique done by an FTIR spectrometer is much less intuitive than dispersive spectroscopy. Instead of using a monochromatic beam, a broadband light source containing many wavelengths is emitted at once in an FTIR spectrometer. Then, the proportion of the light being absorbed by the sample is measured. Afterwards, the same measurement is repeated many times, but with a modification of the combination of wavelengths being emitted by the light source due to the movement of one of the Michelson mirrors. This sampling of measurements give data points, and finally the computer gathers all the data points and process the data backwards in order to yield the absorption spectrum for each wavelength.

In order to modify the combination of the wavelengths of the light beam, a movable and a fixed mirror are used in an FTIR spectrometer. The position of the

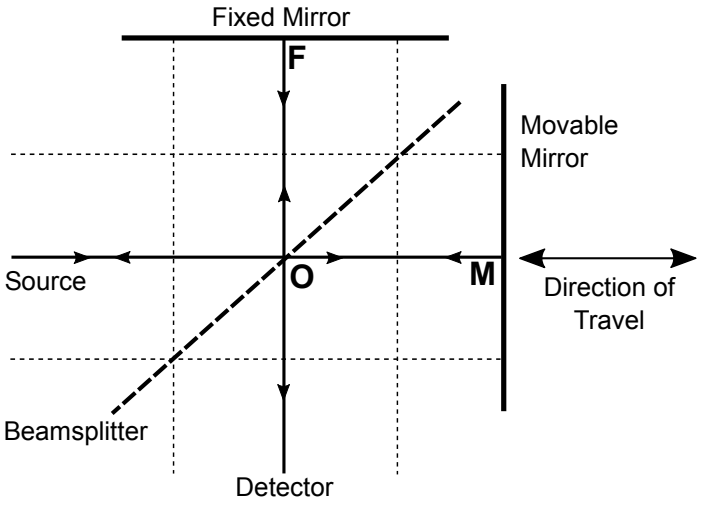

Figure 2-2: Scheme of a Michelson interferometer

movable mirror will enable the modification of the wavelength combination by blocking or transmitting light beam with different wavelength at each measurement. This technique is adopted from the principles of a Michelson interferometer. The following explanation will describe the principles of a Michelson interferometer and its generation of raw data called interferogram.

Generation of an interferogram

The most common FTIR spectrometers are based on an ideal Michelson interferometer, as depicted in Fig. 2-2. The interferometer uses a source with a light beam supposed to be perfectly collimated. The interferometer is designed so that it can divide the incoming light beam into two paths and then recombine the two beams after a path difference has been introduced. A detector measures the variation of beam intensity that is created taking account of the interferences occurring between the beams. The detector measures this variation of intensity as a function of path difference. Fig. 2-2 is a representation of a simple form of a Michelson interferometer, consisting of two perpendicular plane mirrors. One of the mirrors is movable along the axis that is perpendicular to its plane, and the other mirror has a fixed position. The collimated light beam from the source is partly transmitted and reflected by the beam splitter, which is located at the intersection of the perpendicular axes of each mirror. Each part of the beam continues towards a mirror. The partially transmitted beam continues to the movable mirror (point M), and the partially reflected beam continues to the fixed mirror (point F). The beam splitter and mirrors are supposed to be ideal. The beamsplitter has a transmission and a reflection coefficient of 0.5. The reflected beams gathering at the beam splitter are again partially transmitted and reflected, either to the detector or back to the source. The interferences between the beams affect the resulting beam intensity either measured by the detector or going back to the source. The beam intensity is expressed as a function of the travel path difference of the beam and yields a spectral information in an FTIR spectrometer

called interferogram. The beams going back to the source is of the least of interest for this kind of FTIR spectroscopy, and thus only the beam measured by the detector is used as the information for FT signal processing.

To understand the generation of interferogram in a Michelson interferometer, an ideal situation with a source of infinitely narrow wavelength width and collimated monochromatic light beam is considered. The wavelength of the source can be considered as λ_0 (in cm), so that the wavenumber ν_0 (in cm^{-1}) is :

$$\nu_0 = \frac{1}{\lambda_0} \tag{2.1}$$

The intensity at this wavenumber will be denoted as $I(\nu_0)$. The intensity is recorded by the detector when the movable mirror is held stationary at different positions. The path difference is defined as the difference between distances of the beams that travel to the fixed and movable mirrors and back to the beam splitter. The path difference, that will be noted as optical path difference (OPD), can be calculated as $2(OM - OF)$ where the points O, M, and F can be seen in Fig. 2-2:

$$\delta = 2(OM - OF) \tag{2.2}$$

Using the above equation, the phase difference between the two interfering beams can be calculated as follows:

$$\varphi = \frac{2\pi\delta}{\lambda_0} \tag{2.3}$$

When the OPD is zero (this can be called *zero path difference* (ZPD)), the movable mirror and the fixed mirror are equidistant of the beam splitter. In the case of ZPD, the two beams recombine perfectly at the beam splitter with the same phase. In this case, the beams interfere constructively and the intensity of the interferences is the sum of the intensity of each beam reaching the fixed and movable mirror. In this phenomenon all the beams reach the detector and no beam reaches back the source.

In order to explain why there is no radiation returning to the source in the case of ZPD, it is important to take into account the phenomenon of reflection. The beam being reflected by a mirror at normal incidence and beam splitter will undergo a phase change of 180° and 90°, respectively. In the case of a beam being transmitted by the beam splitter, there is no phase change. For the beam going back to the detector, the beams reflected by the fixed and movable mirrors undergo a total phase change of 270°. Hence, with the same phase change, the beams recombine constructively in the detector direction. While for the beams returning to the source, the total phase change difference is 180° (The total phase changes for the beam going to fixed and movable mirrors are 360° and 180°, respectively) resulting in destructive interferences. In this case the two beams have opposite phases and thus no beam returns to the source. This phenomenon is illustrated in Fig. 2-3A.

Illustrating the case when the mirror displacement is $\frac{1}{4}\lambda_0$, the retardation is now $\frac{1}{2}\lambda_0$, making the difference in the length of the beam travel path (going and returning to fixed and movable mirror) one-half wavelength. At the beam splitter, the beams

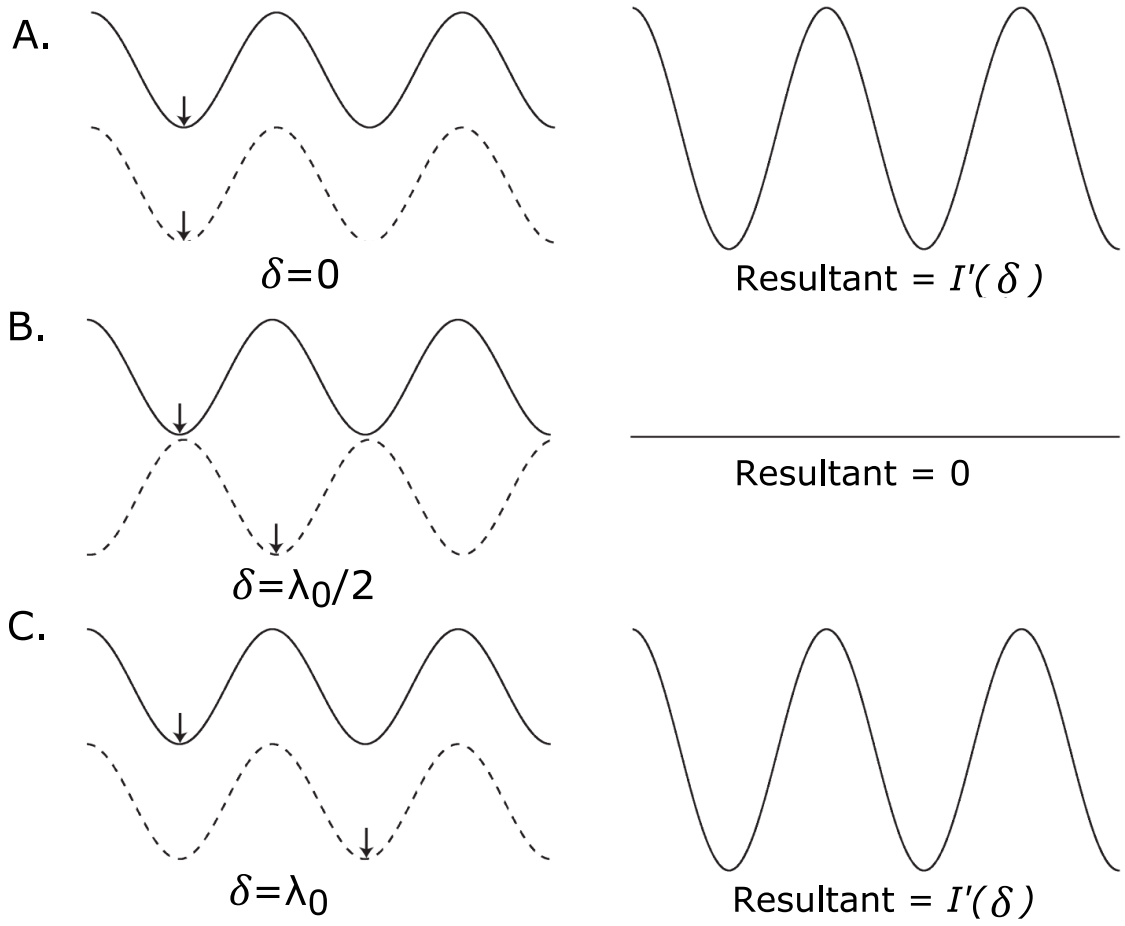

Figure 2-3: Phase of the electromagnetic waves from fixed (solid line) and movable (dashed line) mirrors at different values of the optical retardation: (A) zero path difference; (B) path difference of one-half wavelength; (C) path difference of one wavelength. Note that constructive interferences occur for both (A) and (C) and all other retardations of integer numbers multiple of wavelength, λ_0. [35]

have opposite phases and thus create a destructive interference toward the detector. Here, there is no beam going to the detector. But, photons are considered as a form of energy hence, in case of destructive interferences, photons travel to a different direction, which is back to the source of the interferometer. Illustration of this phenomenon is described in Fig. 2-3B. If the movable mirror is again displaced further with a distance of $\frac{1}{4}\lambda_0$, the retardation is now λ_0, and the beams recombine with the same phase change at the beam splitter (Fig. 2-3C). Hence it appears constructive interferences in the detector direction. When the movable mirror is displaced with a constant velocity, the signal at the detector varies sinusoidally. The maximum of the cosinus function occurs when the retardation is a multiple integer of λ_0. The intensity of the beam at the detector can be denoted as a function of retardation, $I^{'}(\delta)$. The maximum intensity of the beam in the detector is equal to the intensity of the source $I(\nu_0)$ when $\delta = n\lambda_0$ (n being an integer). When the value of intensity is not maximum, it can be calculated as follows :

$$I'(\delta) = 0.5I(\nu_0)\left(1 + \cos 2\pi\frac{\delta}{\lambda_0}\right) \tag{2.4}$$

or

$$I'(\delta) = 0.5I(\nu_0)(1 + \cos 2\pi\nu_0\delta) \tag{2.5}$$

The intensity function from Eqs. 2.4 and 2.5 are both composed of a constant or dc component of $0.5I(\nu_0)$ and a modulated or ac component of $0.5I(\nu_0)cos2\pi\nu_0\delta$. In spectrometric measurement, only the modulated part is important and is referred as an interferogram $I''(\delta)$. Thus, the interferogram of an ideal interferometer can be described as :

$$I''(\delta) = 0.5I(\nu_0)\cos 2\pi\nu_0\delta \tag{2.6}$$

In terms of practical implementation, there are several factors affecting the signal measured at the detector. For the beam splitter, it is very difficult to find an ideal beam splitter with a reflectivity and transmittance of 50%, since usually these values vary over the beam wavelength. This problem is resolved by multiplying the $I(\nu_0)$ by a wavenumber dependent factor. The response of the detector used to measure the intensity of the beam is also wavenumber-dependent, thus the same solution as in the case of the beam splitter is applied. The other thing to be taken into account is the response of the amplifier used to amplify the detector signal since it is strongly dependent on the modulation frequency. Amplifiers have usually a limited bandwidth and thus the amplification can be wavenumber dependent. Therefore, the value of the interferogram is not only proportional to the intensity of the source but also to the efficiency of the beam splitter, the response of the detector, and the characteristics of the amplifier. Therefore, if the wavenumber correction factor for the beam splitter is denoted as $H(\nu_0)$, the final modulated part of the interferogram being measured denoted by $S(\delta)$ (in volt) can be described as in the equation

$$S(\delta) = 0.5H(\nu_0)G(\nu_0)I(\nu_0)\cos 2\pi\nu_0\delta \tag{2.7}$$

where $G(\nu_0)$ is the response of the detector and amplifier in $V.W^{-1}$ for the wavenumber

ν_0. The term $0.5H(\nu_0)G(\nu_0)$ is usually known as the transfer function denoted as $2B(\nu_0)$. The transfer function modifies the intensity of the source with a correction factor that takes into account the characteristic of the instruments used in the system. Finally, the interferogram can be written as:

$$S(\delta) = 2B(\nu_0) I(\nu_0) \cos 2\pi\nu_0\delta \tag{2.8}$$

From the above expression, we can observe that $S(\delta)$ is the cosine Fourier transform of $B(\nu_0)I(\nu_0)$.

A Michelson interferometer that uses a source with more than one wavelength creates an interferogram as the sum of the interferograms that correspond to each wavelength. Examples of spectra and their interferograms are presented in Fig. 2-4. Figs. 2-4A and B, represent the case of two closely spaced lines (with a separation between the two lines of 0.014 nm) that occur in the Michelson's experiment using the red Balmer lines in the hydrogen spectrum. Figs. 2-4C and D represent Lorentzian profiles, which yield sinusoidal interferograms with an exponentially decaying envelope. As can be concluded from Fig. 2-4 C and D, a rapid decay is expected for broadband spectral sources. When the width of the spectral band is narrower, the width of the envelope of the interferogram is larger. In the case of a monochromatic source, the width of the interferogram envelope is infinitely large (e.g. pure cosine wave).

Now, we can introduce the concept of the Fourier Transform of the interferogram. The concept of FT is introduced in order to reconstruct the spectrum measured by the FTIR spectrometer at each wavelength. Since the interferogram can be represented as the cosine FT of $B(\nu_0)I(\nu_0)$, the final spectrum is obtained by calculating the inverse function of the cosine FT of the interferogram, $S(\delta)$. In the application of Michelson interferometer as in a commercial FTIR spectrometer, the movable mirror is moved at a constant velocity, $V^{'}$ in $cm.s^{-1}$. By using this velocity, we have the possibility to describe the interferogram as a function of time rather than retardation, δ. This problem can be resolved by understanding the retardation as a function of time as described in Eq. (2.9):

$$\delta = 2V't(in \;\; cm) \tag{2.9}$$

giving a new form of Eq. (2.8) as:

$$S(t) = 2B(\nu_0) I(\nu_0) \cos 2\pi\nu_0 2V't. \tag{2.10}$$

For any cosine wave of frequency f, the amplitude of the signal after time t is given by :

$$A(t) = A_0 \cos 2\pi ft \tag{2.11}$$

where A_0 is the maximum amplitude of the wave. Comparing the Equations 2.10 and 2.11 we remark that the frequency f_{ν_0} of the interferogram $S(t)$ corresponds to the radiation of the wavenumber, ν_0, which is often known as the Fourier frequency, and is given by:

$$f_{\nu_0} = 2V'\nu_0 \tag{2.12}$$

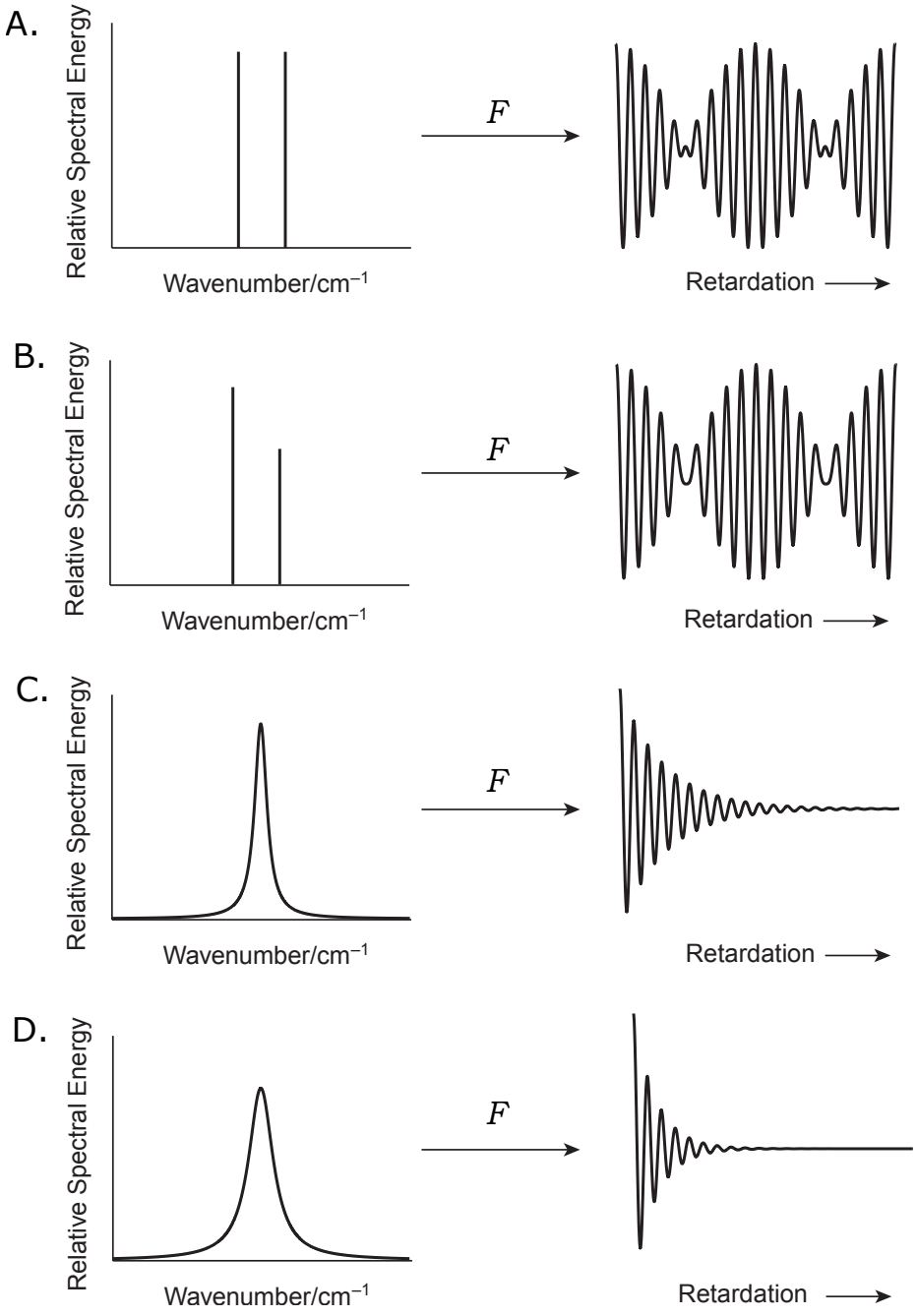

Figure 2-4: Simple spectra and interferograms: (A) Two infinitesimally narrow lines of equal intensity. (B) Two infinitesimally narrow lines of unequal intensity. Note that the amplitude of the beat signal in the interferogram never goes to zero. (C) Lorentzian band centered at the average of the lines in (A) and (B): the frequency of the interferogram is identical to that of (A) and (B) and the envelope decays exponentially. (D) Lorentzian band at the same wavenumber as (C) but of twice the width. The exponent of the decay for the interferogram has a value equal to the double of the exponent for (C). [35]

In a Michelson interferometer, the optical path difference which changes at a certain rate is called the OPD velocity, V. This velocity is two times that of the scanning mirror velocity V'.

$$V = 2V' \tag{2.13}$$

Thus, the Fourier frequency can be determined as:

$$f_{\nu_0} = V\nu_0 \tag{2.14}$$

The application of a Michelson interferometer in the FTIR spectrometer is modified when the source is no longer monochromatic but a continuum source. Hence, the interferogram can be represented by the integral over all the wavenumbers of the continuum source. It can be described as :

$$S(\delta) = 2\int_0^{+\infty} B(\nu) I(\nu) \cos 2\pi\nu\delta d\nu \tag{2.15}$$

Or,

$$S(\delta) = \int_{-\infty}^{+\infty} B(\nu) I(\nu) \cos 2\pi\nu\delta d\nu \tag{2.16}$$

The spectrum $B(\nu)I(\nu)$ can be calculated using the inverse Fourier Transform.

$$B(\nu) I(\nu) = \int_{-\infty}^{+\infty} S(\delta) \cos 2\pi\nu\delta d\delta \tag{2.17}$$

Or,

$$B(\nu) I(\nu) = 2\int_0^{+\infty} S(\delta) \cos 2\pi\nu\delta d\delta \tag{2.18}$$

Theoretically, from Eq. (2.18) the complete spectrum can be measured from 0 to $+\infty$ (in cm^{-1}) at infinitely high resolution. However, to achieve this, moving the mirror along an infinitely long distance is necessary (with δ varying between 0 and $+\infty$). To reconstruct the spectrum with a finite resolution, measuring the signal over a limited retardation has to be performed. In addition, Eq. (2.18) reconstructs the product of the spectrometer transfer function and the real spectrum $B(\nu)I(\nu)$.

Bases for measurement of photocurrent

In the case of FTIR usage for photocurrent measurement of a coplanar thin film semiconductor sample, bias voltage is applied to the sample while it is illuminated by the FTIR source with a constant flux. The photocurrent is thus generated in between the two electrodes on the sample. An FTIR spectrometer generally processes the raw data in form of voltage, hence an I/V converter is used to convert the photocurrent of the sample to voltage before sending it to the FTIR for further treatment. The role of the I/V converter is very important in the determination of the spectrometer transfer function, $B(\nu)$. The I/V converter usually has a modifiable amplification gain that comes with a certain bandwidth. Since the I/V converter post-process the photocurrent as function of the FTIR source, whose wavenumber is mainly driven

by the Fourier frequency of the scanning mirror, the bandwidth of the selected amplification gain of the I/V converter must be greater than the Fourier frequency of the highest wavenumber. The detail about the effect of the I/V converter to the spectrometer transfer function spectrum, $B(\nu)$, will be explained in Sec. 2.2. The voltage after the conversion can subsequently be processed by the FTIR resulting in the spectrum $B(\nu)I(\nu)$. To correct the noise of the system, one must conduct a basic noise baseline measurement. In this measurement, the FTIR source is blocked, hence no light source, and the I/V converter is set with the amplification gain needed for the photocurrent measurement of the illuminated sample, to ensure that the spectrometer transfer function $B(\nu)$remains the same. The suppression of the noise baseline can be denoted by:

$$B(\nu)(I(\nu) - I_{BLnoise}(\nu)) = B(\nu)I_{sample}(\nu) \tag{2.19}$$

and

$$B(\nu)(I(\nu) - I_{BLnoise}(\nu)) = B(\nu)I_{diode}(\nu) \tag{2.20}$$

when a photocurrent is measured by a photodiode.

The Eqs. (2.19) and (2.20) shows that with a single measurement we can suppress the noise baseline effect but the contribution of $B(\nu)$ still exists, hence the real spectrum generated by the sample or diode, $I_{sample}(\nu)$ or $I_{diode}(\nu)$, cannot be extracted directly from one measurement. In the photocurrent measurement using FTIR, which will be detailed in the following section, the effect of $B(\nu)$ is suppressed using a reference measurement. This reference measurement is generally a photocurrent measurement using a photodiode, measuring the flux of the incoming light source for instance, which is used to normalize the photocurrent measured with the sample. The normalization can be done using the following formula:

$$\frac{B(\nu)I_{sample}(\nu)}{B(\nu)I_{ref}(\nu)} = \frac{I_{sample}(\nu)}{I_{ref}(\nu)} \tag{2.21}$$

The last point to be addressed is the FTIR resolution. The mechanism to determine the FTIR resolution is illustrated in Fig. 2-5. This figure illustrates how the resolution of the spectrum measured interferometrically depends on the maximum retardation of the scan. Fig. 2-5 considers the case of a spectrum consisting of a doublet with identical intensity. Fig. 2-5A represents the spectrum, Fig. 2-5B represents the interferogram of each spectrum, and Fig. 2-5C represents the resultant of the interferograms.

If the doublet is separated by a distance of $\Delta\nu$ which is equal to ν_1–ν_2 , the cosine waves of the interferograms as presented in Fig. 2-5B are no longer in phase after a retardation of 0.5 $(\Delta\nu)^{-1}$. The interferograms are again in phase after a retardation of $(\Delta\nu)^{-1}$. Therefore, a retardation of $(\Delta\nu)^{-1}$ is required to go through one complete period of the beat frequency. Interferogram that is measured only to half of this retardation will not readily be distinguished from the interferogram of the source. If the spectrum is separated with a narrower distance, a greater value of retardation is expected for the cosine waves to be in the same phase. Therefore, spectral resolution

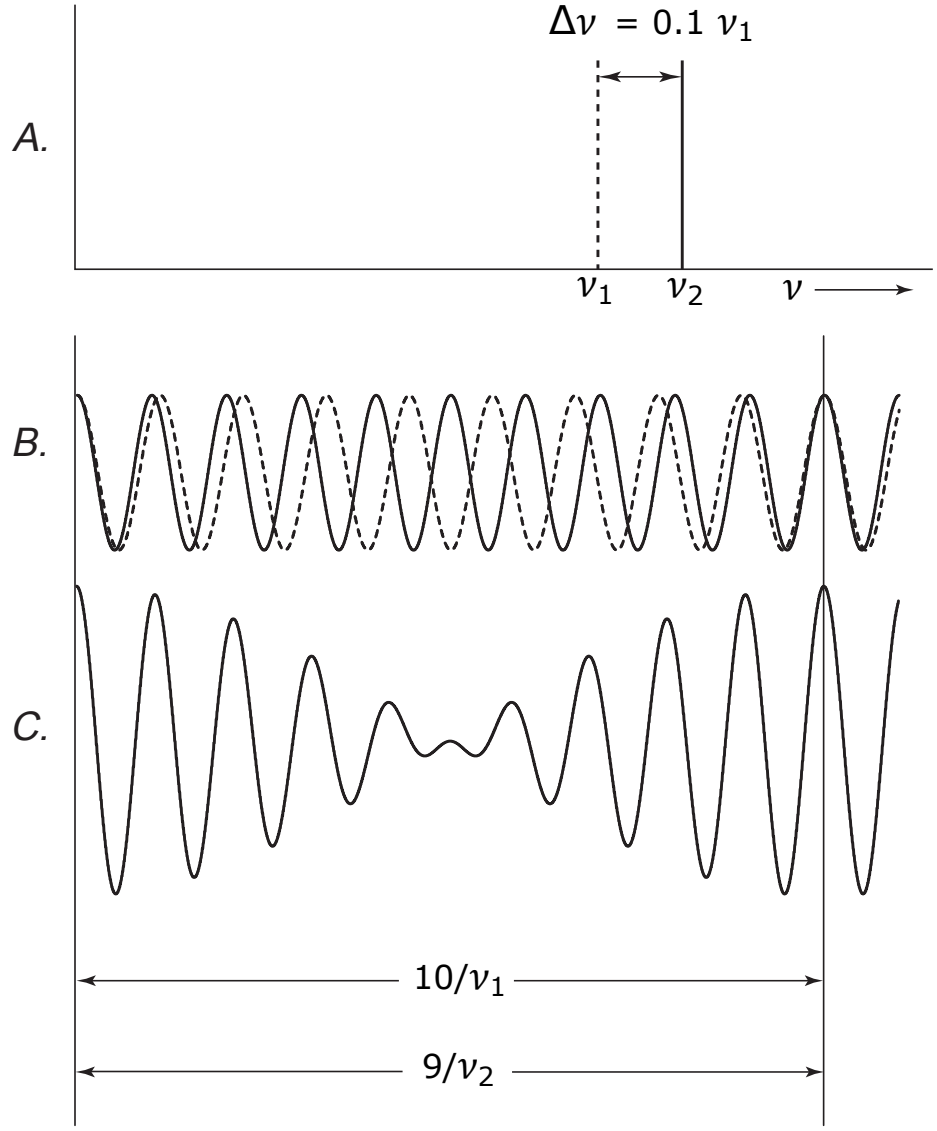

Figure 2-5: (A) Spectrum of two lines of equal intensity at wavenumbers ν_1 (dashed line) and ν_2 (solid line) separated by 0.1 ν_1, (B) interferogram for each spectral line shown individually as solid and dashed lines, respectively, (C) resulting interferogram with the first maximum of the beat signal at $10/\nu_1$, to resolve these two spectral lines it is necessary to generate an optical retardation of at least this value. [35]

depends on the maximum retardation of the interferometer. The above explanation shows that the two waves become in phase after the zero retardation point when $\delta = (\Delta\nu)^{-1}$. Hence if the maximum retardation of the interferometer is Δ_{max}, the best resolution, $\Delta\nu$, obtained from this interferometer is:

$$(\Delta\nu) = (\Delta_{\max})^{-1} \tag{2.22}$$

During the photocurrent measurement using an FTIR spectrometer, the resolution is generally set with a data spacing of 4 cm^{-1} for the given wavenumber range, 5000-25000 cm^{-1}. It means that for the lower range, 5000 - 5004 cm^{-1}, the wavelength resolution is 1.6 nm. For the upper range, 25000-25004 cm^{-1}, the resolution is 0.06 nm. It can be seen that with data spacing of 4 cm^{-1}, the wavelength resolution is largely sufficient for a high precision measurement result (especially when a smaller data spacing of wavenumber is set, for higher wavelength resolution). As it is compared to the measurement using a classical UV-Visible dispersive spectrometer, an FTIR yields an equal or even higher resolution measurement results with a faster rate of measurement.

2.2 Photocurrent measurement using an FTIR

We have seen in the previous section that the measurement with an FTIR spectrometer of a photocurrent spectrum, with the noise baseline and spectrometer transfer function correction, can be performed using Eq. (2.21). According to the type of measurement, the definition of the $I_{sample}(\nu)$ and $I_{ref}(\nu)$ can be different. This section covers the essential principle and the experimental setup of the photocurrent measurement using an FTIR spectrometer for a thin film semiconductor material deposited on glass, and a solar cell. For the thin film sample on glass, we can perform reflectance and transmittance (R/T), as well as Fourier Transform Photocurrent Spectroscopy (FTPS) measurement, while for the solar cell sample we can perform spectral response measurement.

For the R/T measurement, the $I_{sample}(\nu)$ is the photocurrent generated by a photodiode, due to the incoming photon flux either transmitted through the sample or reflected by the sample. The reference measurement, for the R/T, is the photocurrent measurement of the direct incoming photon flux using a photodiode. This reference measurement yields the $I_{ref}(\nu)$ in Eq. (2.21).

For the FTPS measurement, it is required that a pair of coplanar electrodes (with 1 mm distance between them) is deposited on top of the film. One electrode is used to apply a bias voltage while the other collect the generated photocurrent. In the case of FTPS measurement, the I_{sample} is the photocurrent generated by the sample under the illumination of the FTIR light source. I_{ref} is obtained by measuring the photocurrent generated by the photodiode which is placed behind the sample, measuring the transmitted photon flux.

In the case of the spectral response measurement of a solar cell, I_{sample} is obtained by measuring the generated short circuit current when the solar cell is under the

illumination of the FTIR light source. The reference measurement which yield the I_{ref} is done using a calibrated silicon diode which measures the direct incoming photon flux.

The characteristic of the I/V converter is very crucial to fix the spectrometer transfer function $B(\nu)$ spectrum as the selection of the amplification gain affects the bandwidth of the I/V converter during the measurements. In most of the existing I/V converters, the amplification gain increases while the bandwidth decreases. Table 2.1 shows the variation of the bandwidth and amplification gain of an I/V converter type FEMTO DLCPA-200.

Table 2.1: Variation of bandwidth and amplification gain of FEMTO DLCPA-200 I/V converter.

Amplification Gain	10^3	10^4	10^5	10^6	10^7	10^8	10^9
Cut-off Frequency (kHz)	500	500	400	200	50	7	1

The I/V converter bandwidth frequency corresponds to the cut-off frequency of a low pass filter (see Fig. 2-6). In order to obtain a correct signal, the bandwidth of the I/V converter has to be higher or at least equal to that of the maximum Fourier frequency, calculated from Eq. (2.14).

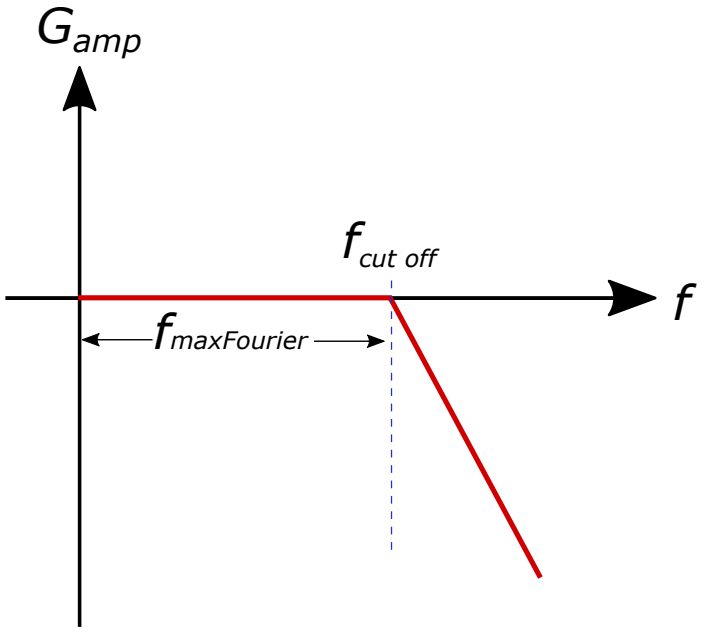

Figure 2-6: Low pass filter characteristic of the I/V converter. When the filter type is low pass, the amplification gain for frequencies above the cut-off frequency (f_{cutoff}) will no longer correspond to the selected amplification gain (G_{amp}). The highest Fourier frequency ($f_{maxFourier}$) must be below or equal to the f_{cutoff} to stay in the selected G_{amp}.

In the photocurrent measurement, the lowest scanning mirror velocity is chosen in order to minimize the effect of signal degradation due to the sample frequency

dependence and to obtain a higher measurement precision. Typically, scanning mirror velocity is set at 0.158 cm/s. So, for the highest wavenumber, for example 400 nm or 25000 cm^{-1}, the Fourier frequency is 7.9 kHz. Hence, if the amplification gain is chosen at 10^8, the highest Fourier frequency surpasses the cut-off frequency of the I/V converter. As a consequence, if a thin film semiconductor sample is measured using an amplification gain of 10^8, the reference measurement must use the same amplification gain, to ensure the same spectrometer baseline spectrum $B(\nu)$. A problem may occur when the photodiode used for the reference measurement generates a high photocurrent leading to current overload in the I/V converter. In this case, the FTIR light source should be attenuated, resulting into a lower incoming photon flux and thus no current overload. The other approach is to set the measurement of thin film with a lower amplification gain, for example 10^7. If the generated photocurrent is too small, the bias voltage applied to the sample can always be adjusted so that a higher signal is obtained. With this amplification gain, the I/V converter has a cut-off frequency of 50 kHz, which is largely sufficient to pass the highest Fourier frequency. Then, if the reference measurement is set at the amplification gain a little or far below 10^7, there will be no noticeable $B(\nu)$ spectrum difference, hence no attenuation of the flux for the reference measurement is needed. In general, the above problem does not occur in the R/T and spectral response measurement. Typically I/V converter amplification gain is sufficient at 10^4 to 10^6, for both measurement of thin film (or solar cell) sample and reference. These amplification gains have a cut-off frequency far above the highest Fourier frequency.

The following subsection will explain the general experimental setup of the photocurrent measurement using an FTIR spectrometer. For each type of photocurrent measurement, such as R/T, FTPS, and spectral response, a small modification of the general experimental setup is needed.

The detail about the characterizations of a thin-film semiconductor material deposited on a non-conductive substrate including transmittance and reflectance (R/T) and FTPS for absorption coefficient will be discussed in Sec.2.3 and 2.4, whereas the spectral response measurement of a solar cell will be presented in the last section of this Chapter.

2.2.1 Experimental setup for photocurrent measurement

The types of photocurrent measurement for thin film semiconductor sample, deposited on a non-conductive and transparent substrate such as glass, are R/T and FTPS measurement. The measurement of spectral response is exclusively possible for solar cells. In this setup, the FTIR spectrometer has a spectroscopy range of 400-25000 cm^{-1}, or 400 to 2500 nm, with a halogen lamp as a light source. We use a Thermo Scientific Nicolet iS50R as in Fig. 2-7. To conduct the photocurrent measurement, we have used the experimental setup as depicted in Fig. 2-8.

A halogen lamp is chosen to match the spectral range needed for the photocurrent measurement. Our FTIR spectrometer has the possibility to process an external input, which is an important aspect, because in the photocurrent measurement we are going to process the photocurrent generated by the samples or by the photodiodes.

Figure 2-7: FTIR spectrometer Thermo Scientific Nicolet iS50R.

For the choice of the beam splitter, quartz is preferable due to its reflectance and transmittance factor of 50% in the wavelength range of study, compatible with those needed for ideal Michelson interferometry. All the mirrors in the FTIR spectrometer have been covered with aluminum to reach the optimum reflectivity in the wavelength range of study.

In our experimental setup, the samples are measured externally, outside the sample compartment. To do so, the beam of light, 2.4 cm in diameter, exiting the Michelson interferometer and focused in the standard FTIR to the film position in the sample compartment is even more focused by a silica lens, 5 cm in diameter and approximately 5 cm of focal length (f/1), onto the entrance of one of the two branches of a bifurcated optical fiber bundle from Newport Corp. (entrance diameter 3.2 mm, numerical aperture NA = 0.22). This branch of the optical fiber bundle was fixed onto an XYZ mount to optimize the collection of the light coming out of the FTIR. A filter wheel is set in between the lens and the optical fiber entrance to select appropriate wavelength ranges. In this way the light of the FTIR can be easily shone onto a sample located at the output of the fiber bundle (output diameter 4.7 mm, NA = 0.22) with the only constraint that the sample must be set close and perpendicular to the output of the fiber. The system we have designed to collect the light of the FTIR is compact and can be easily inserted into the sample compartment of the FTIR as shown in Fig. 2-9.

In the FTIR sample compartment, we have placed several optical filters on a rotating wheel between the lens and the optical fiber. A filter is mainly used to eliminate the portion of the incoming photons which gives the greatest response of the sample or the highest photocurrent. By eliminating this part, the precision of the part where the signal is weak can be improved and thus the dynamic range of the measurement can be increased. Typically, this can be done by setting a higher amplification gain of the I/V converter. The procedure of which filter to use for each

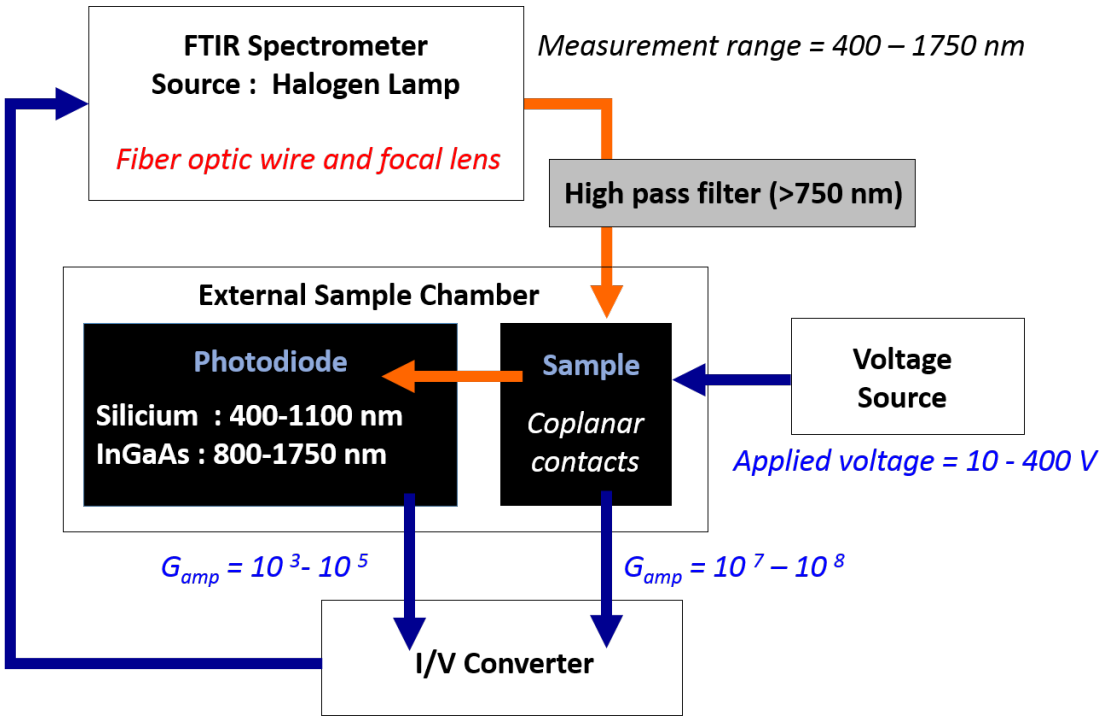

Figure 2-8: Setup configuration of our photocurrent measurement using an FTIR spectrometer in the FTPS technique. The FTIR spectrometer is operated between 400 and 1750 nm, where the source light is sent in front of the external sample holder through an optical fiber. Optical high pass filter can be used to improve the dynamic range of the measurement. Two types of photodiodes are used to measure the flux intensity of the source, the photodiodes sensitivity being chosen to match the measurement spectral range. Voltage source is used to apply bias voltage to the sample. Low noise I/V Converter is chosen with adjustable amplification gain to amplify the signal before treatment by the FTIR.

measurement will be detailed in the following paragraphs.

The I/V converter facilitates the raw signal conversion to voltage before sending it to the FTIR. A good choice of I/V converter is very important. For the photocurrent measurement, it is necessary to have a high quality I/V converter with high signal to noise ratio, because typically the generated signal from the thin film sample is quite low. Hence a small noise can disturb the sample's signal. The I/V converter bandwidth, associated to the choice of amplification gain, should also be larger than the highest frequency of the FTIR spectrometer associated to the scanning velocity, the reason of which was previously explained in this section. The device criteria and setup explained in the above paragraphs are the general rules for all the photocurrent measurements: R/T, FTPS and spectral response, using an FTIR spectrometer. Nevertheless, the following paragraphs will explain more specifically the setup for each measurement.

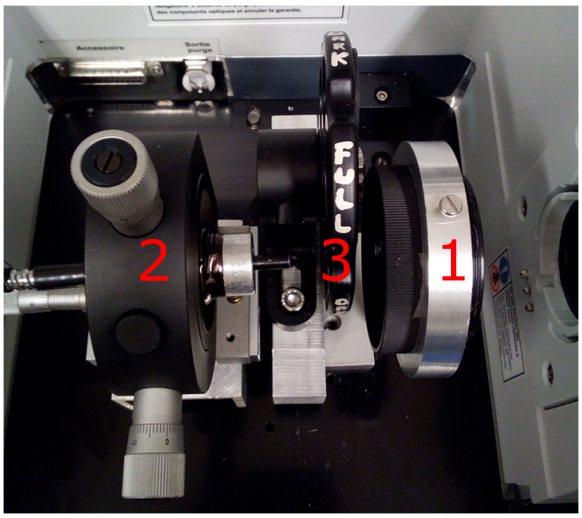

Figure 2-9: System designed to collect the light from the Michelson interferometer of the FTIR: (1) a silica lens concentrating the light on the entrance of one leg of a bifurcated optical fiber bundle (2), and a filter wheel in between to select different ranges of wavelengths (3).

R/T measurements

For the R/T measurement, the deposition of electrodes on the film side is not necessary because there is neither applied bias voltage nor photocurrent generation in the sample. In this measurement, the photocurrent is generated by the photodiodes which measure the transmitted and reflected portion of light by the sample. To measure the photocurrents, the sample is placed in an external sample chamber on a sample holder. The incoming light is delivered by the optical fiber which is placed in front of the sample. The sample should be placed on a sample holder in a sample frame with a possibility to hold the sample still and perpendicular to the incoming light. The sample frame has two slots, in which a sample holder with a sample and a photodiode holder can be inserted. This is particularly important for the transmittance measurement, where the photodiode is placed behind the sample (see Fig. 2-10A). Two sample frames are provided in order to simplify the measurement process, particularly for the reflectance measurement, where the photodiode which measures the reflected light, is placed away from the sample which is positioned in the sample frame of the transmission measurement side. Usually the use of an optical filter is not necessary since the R/T experiment does not need a large dynamic for the spectra measurements.

The choice of photodiodes depends on the spectral range chosen for the measurement. In this measurement, the spectral range used is 5700-25000 cm^{-1} (400-1750 nm). Crystalline silicon and InGaAs photodiodes were chosen to accomplish the measurement within this given spectral range. A silicon photodiode covers the spectral range of 9000-25000 cm^{-1} (400-1111 nm) while the InGaAs is covering 5555-12500 cm^{-1} (800-1800 nm). The common spectral range of these two diodes is 9000-12500

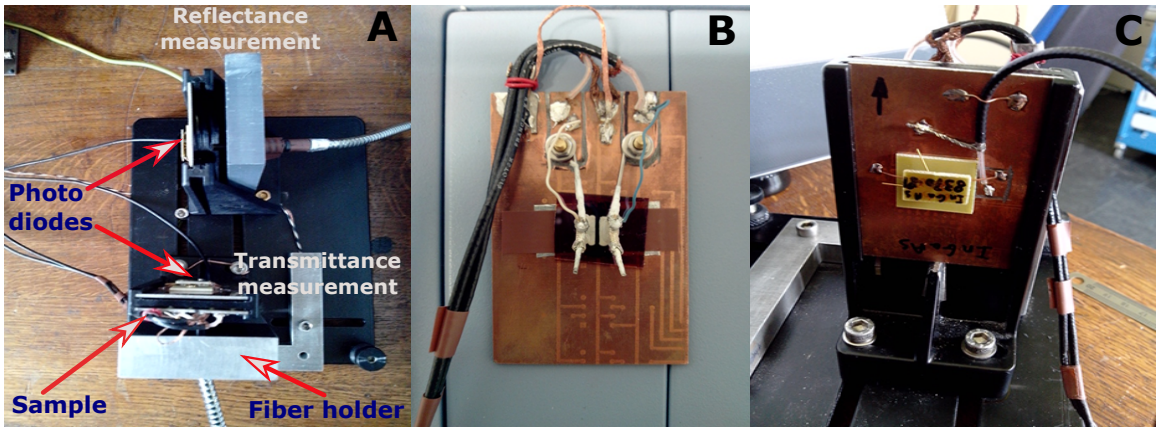

Figure 2-10: (A) Sample holders are inserted in the sample frame. Sample frame has two slots to facilitate the transmittance measurement, one for the sample holder holding the sample facing the optical fiber, and one for the photodiode holder placed behind the sample. For reflectance measurement, the photodiode holder is placed away from the sample, measuring the reflected light from the sample which is placed in the sample frame on the transmittance measurement side. (B) The sample holder, holding the sample with coplanar contacts for FTPS measurements. One electrode is used to transmit the photocurrent generated by the sample and the other to apply the bias voltage. (C) The InGaAs photodiode placed in the frame behind the slot with the sample holder in it, for the transmittance measurement, in R/T and FTPS.

cm^{-1} (800-1111 nm). In this common spectral range, it is expected that the measured flux intensity of the incoming light is the same. Fig. 2-11 displays the spectral sensitivity of these two photodiodes.

The I/V converter gain for the R/T measurements is typically in the range of 10^4 to 10^6. The lower range is typically used for the reference measurement using only the photodiodes without sample and the higher range is when the transmittance of the sample is measured, mainly due to a lower signal generated in the photodiodes. The spectrum is scanned at the scanning mirror velocity of 0.158 cm/s with 20-40 scans. More scans mean smoother final spectrum due to the averaging process. The setup details for the R/T measurement such as the sample or photodiode positioning and the choice of photodiodes, will also be adapted to the FTPS measurements. The details of which are explained in the following paragraphs.

FTPS measurements

FTPS on a thin-film semiconductor sample measures the absorption coefficient using the ratio of the generated photocurrent of the sample when it is illuminated by the FTIR source, and the transmitted part of light measured by the photodiodes placed behind the sample. In this measurement, coplanar electrodes have to be deposited to apply a bias voltage and collect the photocurrent of the sample. Coplanar electrodes are 1 cm in height with a thin gap of 1 mm in between them. Voltage is applied to one electrode and the other electrode transmit the photocurrent to the I/V converter, as

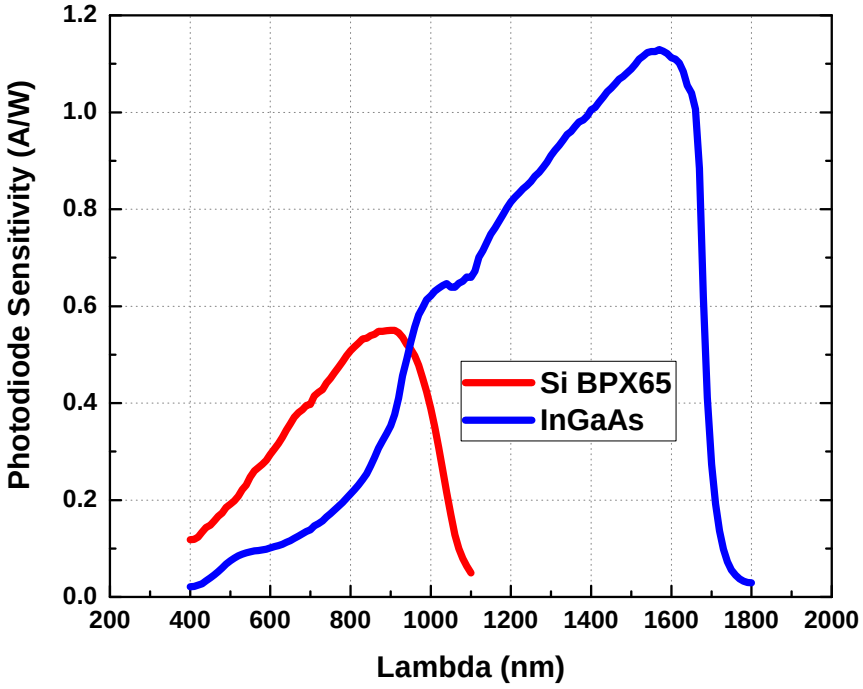

Figure 2-11: Spectral sensitivity of the two photodiodes. Blue line represents the spectral sensitivity of the InGaAs photodiode and the red line represents the spectral sensitivity of the silicon photodiode.

represented in Fig. 2-10B. The applied voltage range is generally between 10-400 V, depending on the sample type and the sample photoconductivity. The best applied voltage can be chosen by considering the signal-to-noise ratio at the output of the I/V converter using an oscilloscope.

The role of the optical filter in FTPS measurement is quite essential, because in the region of low photon energy, samples are usually less absorbing and the signal is very weak. Without the optical filter, the weak signal cannot be amplified. Indeed, when a higher gain is set to amplify the whole spectrum, the part where the signal is the greatest will lead to current overload of the I/V converter. Hence, high pass optical filters are chosen to cut off the high wavenumbers, the region of high energy photons which gives the greatest signal. For the FTPS measurement, we place a high band pass filter which cuts-off all the wavenumber above 13400 cm^{-1} (below 746 nm). Below this wavenumber, typical sample's signal is weak and the dynamic range of the measurement is very low. The use of a filter allow to over amplify this part of the spectrum without saturation of the I/V converter.

The sample positioning on the sample holder and the choice of the photodiodes are the same as for the transmittance measurements. While placing the sample, it is important to ensure that the incoming light beam illuminates the area between the two electrodes of the sample, hence the transmitted light can be measured by the photodiode placed behind the sample. If we look at the spectral sensitivity of the photodiodes in Fig. 2-11, we can conclude that the use of the optical filter can

be only coupled with the use of the InGaAs photodiode due to its sensitivity range. When the silicon photodiode is used, an optical filter is then not useful.

The I/V converter amplification gain should be chosen wisely, since we have seen that the use of a high amplification gain such as 10^8 will deteriorate the signal for the lowest wavelength, 400 nm, due to the Fourier frequency. The reference measurements using the photodiode should then use the same amplification gain to minimize the spectrometer baseline disagreement. Thus, it is advised that the FTPS measurement of the sample uses a lower amplification gain with a higher cut-off frequency and that the sample signal is increased using a higher bias voltage.

In the FTIR, the scanning velocity is set at its lowest, 0.158 cm/s, with 40 or above number of scans, depending on the sample. Some samples may result in a noisy signal because of the weak sample signal interfering with surrounding noise, thus a high scanning number is necessary to have more averaging points and finally to obtain a smooth signal.

Spectral response measurements

As we have seen, the R/T and FTPS measurements have similar setup. On the other hand, the spectral response measurement for solar cell will have a slight modification compared to those of R/T and FTPS. One of the reason of which is the measurement range of interest, which affect the photodiode and FTIR source choice. In the following paragraphs, these special modifications for solar cell measurements will be explained.

The spectral response is calculated as the ratio of the short circuit current generated by the solar cell, and the photocurrent of a calibrated photodiode measuring the direct incoming photon flux. The wavelength range of interest of this measurement is between 400-1100 nm, typical sensitivity range of most solar cells. By considering the wavelengths of interest, only a silicon photodiode is used for the reference measurement. To amplify the signal in the weak region, an optical filter passing the wavelengths in the range of 400 to 650 nm or 15384-25000 cm^{-1} can be mounted. This is due to the usual solar cell's low response in the same spectral region (above 15384 cm^{-1} or below 650 nm) and also to the low emission of the halogen source in the blue region. In the case where the solar cell measurement uses an optical filter for the signal amplification, the reference measurement using a calibrated silicon photodiode can be directly coupled with the optical filter. As the halogen source emits very low blue light, a weak generation of signal from the solar cells can be expected, resulting to a very low dynamic range of the measured spectrum. The use of the optical filter helps to amplify the weak signal but the result of the amplified signal can be still noisy, due to the weak source emission in this range. Hence, we modified the FTIR light source. The halogen lamp chosen as the FTIR source is coupled with blue LEDs (see Fig. 2-12A). As a result, the spectrum of the source in the blue region is reinforced, and thus the generated signal from the solar cell is higher. When the blue LEDs are incorporated in the source, the use of an optical filter as mentioned above is no longer necessary.

For the spectral response measurement using an FTIR spectrometer, we place

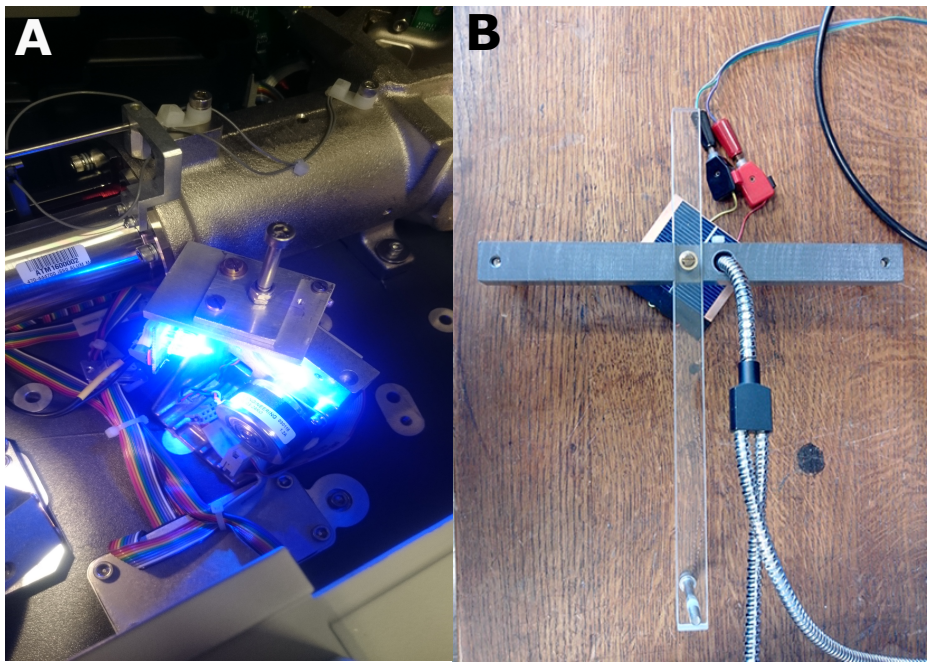

Figure 2-12: (A) System for applying an optical bias through the mounting of blue LEDs inside the FTIR spectrometer. (B) System for positioning the common fiber facing a crystalline silicon solar cell of 5X5 cm^2.

the part of the fiber where the two branches meet (main branch) in the support we have designed for the spectral response measurement (see Fig. 2-12B). This support tightens and keeps the fiber facing vertically the solar cell sample placed flat on the table. It is necessary to position the optical fiber outlet facing the solar cell sample so that all the light coming out of the optical fiber illuminates the solar cell. Various adjustments such as screwing of the feet,or positioning of the fiber in its housing can be added as extra setups to achieve a better adjustment. For small solar cell samples, we can reduce the diameter of the beam (ranging from 1 to 4 mm) at the end of the optical fiber.

For the reference measurement, a fiber holder facing the calibrated diode is set. The only calibrated photodiode we use for the spectral response measurement is a silicon diode, UDT221, which covers a range of wavelengths from 350 to 1100 nm. The spectral sensitivity of the calibrated silicon photodiode is presented in Fig. 2-13.

The generated photocurrent from the solar cell or the calibrated photodiode is connected to the I/V converter, for which the choice of the I/V converter amplification gain stays in the range of 10^4 to 10^5, for both solar cell and reference measurements. For the FTIR setting, scanning mirror velocity was set at 0.158 cm/s with 20 scans.

The experimental setup explained in this section is a general setup for the photocurrent measurement using an FTIR spectrometer. Details with regard to the measurements procedures and to obtain the final spectra of R/T, FTPS, and spectral response, will be explained in more detail in Sections 2.3 to 2.5.

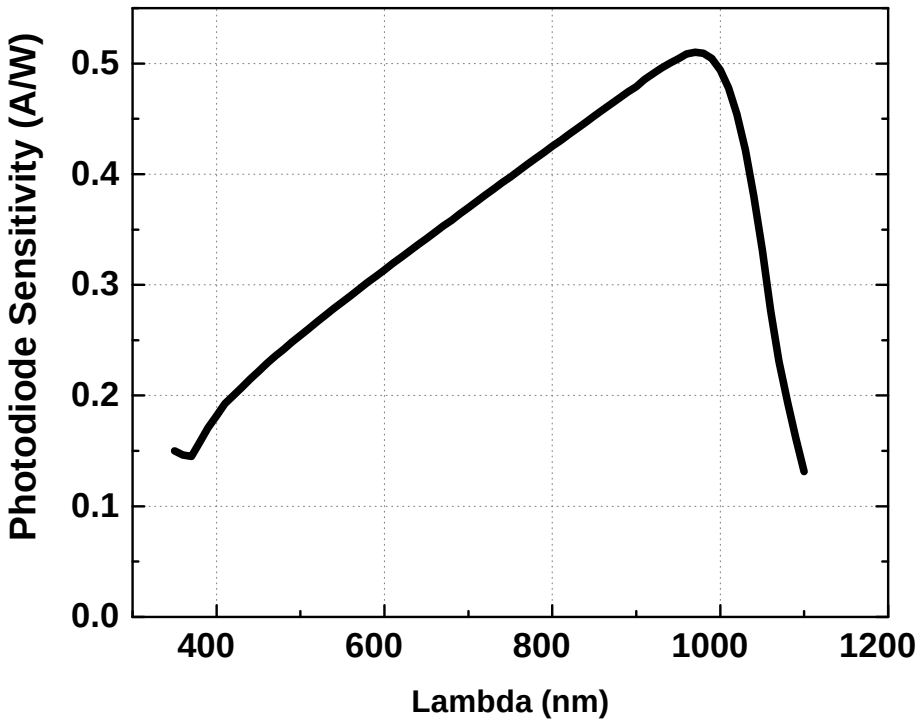

Figure 2-13: Spectral sensitivity of the calibrated silicon photodiode UDT 221.

2.3 Transmittance and reflectance measurement of semiconductor material using an FTIR spectrometer

In this section we explain how to measure the transmittance and reflectance of a semiconductor material using an FTIR spectrometer instead of the usual UV-Visible spectrometer which operates using the principles of dispersive spectroscopy. As stated, the measurement using the FTIR has a bigger advantage due to the short measurement time and the high resolution result. To measure the transmittance and reflectance using an FTIR spectrometer, the sample is exposed to the light coming out of the Michelson interferometer. Transmittance is obtained by having the information of the amount of light being transmitted by the sample, and reflectance is obtained by knowing the amount of reflected light by the sample.

In order to get the information of the amount of light being transmitted and reflected by the sample, we have used photodiodes. In the case of transmittance measurements, the photodiode is placed behind the sample to capture the transmitted light. In the case of reflectance measurement the photodiode is placed away from the sample, and is exposed to the light being reflected by the sample. The detail how we obtain the reflected light from the sample is found in the experimental setup part of this subsection. The photocurrent generated by the photodiodes is then amplified and injected in the external input of the FTIR spectrometer and is ready to be processed to obtain the photocurrent spectrum at each wavelength.

2.3.1 Obtaining the transmittance and reflectance spectra

In the transmittance measurement, we use the ratio of the photocurrent density (generated by the photodiodes) when the sample is placed in front of the photodiode, $J_{transmitted}$, and the photocurrent density when no sample is placed, thus measuring the incident flux, $J_{incident}$. The measurement of the incident flux serves as the reference measurement.

$$\frac{B(\nu)J_{sample}(\nu)}{B(\nu)J_{reference}(\nu)} = \frac{B(\nu)J_{transmitted}(\nu)}{B(\nu)J_{incident}(\nu)} \tag{2.23}$$

From the above equation, the effect of the transfer function, $B(\nu)$, is suppressed. In order to get the true transmittance value, we need to obtain the ratio of the flux intensity transmitted by the sample, $F_{transmitted}(\nu)$ and the incident flux intensity impinging the sample, $F_{incident}(\nu)$:

$$T(\nu) = \frac{F_{transmitted}(\nu)}{F_{incident}(\nu)} \tag{2.24}$$

In our experiment, the flux intensity at each wavelength $F(\nu)$ is measured by the photocurrent density generated by the photodiode. The following formula describes the relation between the flux and the photodiode current:

$$F(\nu) = \frac{J_{photodiode}(\nu)}{SR_{photodiode}(\nu)}.\frac{A_{photodiode}}{hc\nu} \tag{2.25}$$

where $J_{photodiode}$ is the current density generated by the photodiode at each wavenumber (in $A.cm^{-2}$), $SR_{photodiode}$ is the sensitivity of the photodiode at each wavenumber (A/W), h is the Planck constant, c is the speed of light, and $A_{photodiode}$ is the surface of the photodiode (in cm^2). Using Eqs. (2.23) to (2.25) it can be seen that:

$$T(\nu) = \frac{J_{transmitted}(\nu)}{J_{incident}(\nu)} \tag{2.26}$$

The transmitted spectrum simply is the ratio of the two photocurrent spectra taking account of the reflectance of the aluminum mirror.

For the case of reflectance measurement, we use the ratio of the photocurrent density of the reflected beam by the sample, $J_{reflected}$, and the photocurrent density of the reflected beam by the reference, $J_{reference}$. In our experiment, we have chosen an aluminum mirror as the reference.

$$\frac{B(\nu)J_{sample}(\nu)}{B(\nu)J_{reference}(\nu)} = \frac{B(\nu)J_{reflected}(\nu)}{B(\nu)J_{aluminum}(\nu)} \tag{2.27}$$

As in the case of the transmittance measurement, it can be demonstrated that

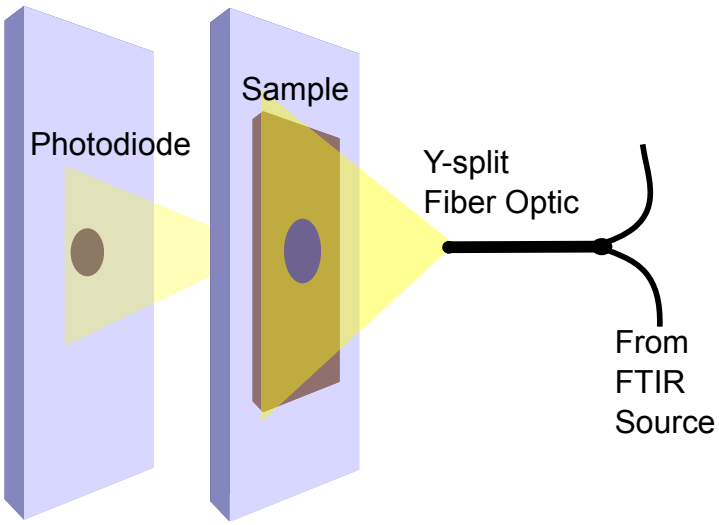

Figure 2-14: Configuration of the sample, photodiode, and optical fiber in the sample compartment for transmittance measurement. The photodiode is placed behind the sample, measuring the part of light being transmitted by the sample.

the reflectance spectrum is simply the ratio of the two photocurrent spectra.

$$R(\nu) = \frac{J_{reflected}(\nu)}{J_{reference}(\nu)} \tag{2.28}$$

2.3.2 Experimental setup and procedures of transmittance and reflectance measurement

The schematic diagram of the system is as shown in Fig. 2-8. In the transmittance measurement, it is important to ensure that the incoming light beam from the optical fiber is directly facing the sample. The photodiode is placed behind the sample and its position is aligned with the incoming light. It means that the photodiode has to be well positioned behind the sample. Fig. 2-14 visualizes the configuration of the sample, photodiode, and optical fiber in the external sample chamber. In the Fig. 2-14, we can see that the incoming light beam is transmitted through the sample, and reaches the photodiode behind the sample. Transmitted flux intensity of the incoming light is measured through the generated photocurrent density of the photodiode placed behind the sample.

The incident flux intensity in the transmittance measurement can be measured by removing the sample from the sample holder, while keeping the photodiode in the sample holder. In this configuration the photodiode will measure the flux intensity of the incoming light beam, coming out of the Michelson interferometer.

For the reflectance measurement, the configuration of the sample and optical fiber is the same as in the transmittance measurement. The difference lies in where we position the photodiode. Since we need to measure the reflected flux intensity of the incoming light, we position the photodiode not behind the sample but away from the

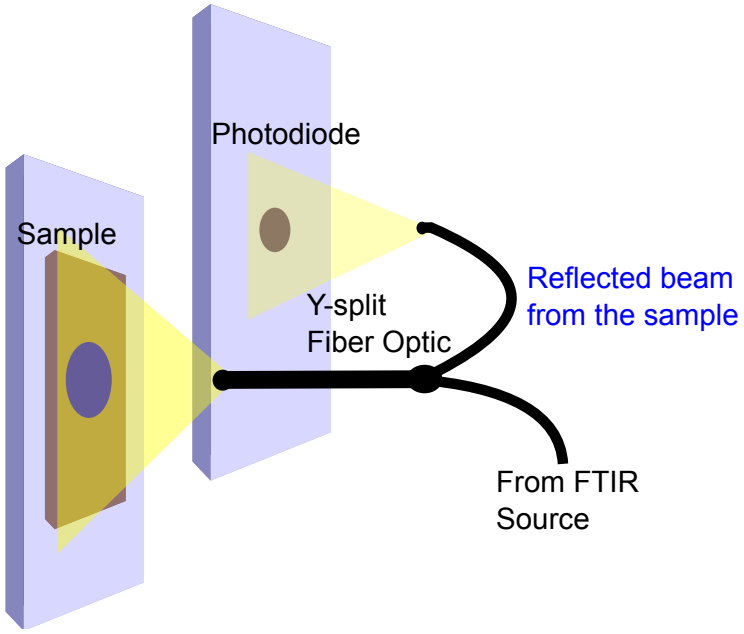

Figure 2-15: Configuration of the sample, photodiode, and optical fiber in the sample compartment for reflectance measurement. One of the branch of the optical fiber is going towards the photodiode, which is placed away from the sample, measuring the part of light being reflected by the sample.

sample. Fig. 2-15 shows the configuration of the sample, photodiode, and optical fiber for the reflectance measurement.

From Fig. 2-15, we can see that the incoming light reaches the sample, and a fraction of the reflected light reaches the photodiode through one branch of the optical fiber. Thus, the photocurrent generated by the photodiode represents the intensity of the reflected light by the sample.

In this reflectance measurement, the flux intensity of the incident light is measured by placing an aluminum mirror instead of the sample in the sample holder sending a fraction of the reflected light to the photodiode. The aluminum mirror serves as a reference for the reflectance measurement taking into account its characteristic as depicted in Fig. 2-16.

As explained in Section 2.2, two kinds of detectors are used for different spectral ranges. Hence, during the transmittance and reflectance measurement we performed separate measurements using these two photodiodes. To finally obtain the transmittance and the reflectance of the sample at each wavenumber, we have conducted the transmittance and reflectance measurements with the configuration as in Figs. 2-17 and 2-18 and using the following procedure:

1. Measurement of the transmitted light by the sample using the silicon photodiode.

2. Measurement of the reflected light by the sample using the InGaAs photodiode.

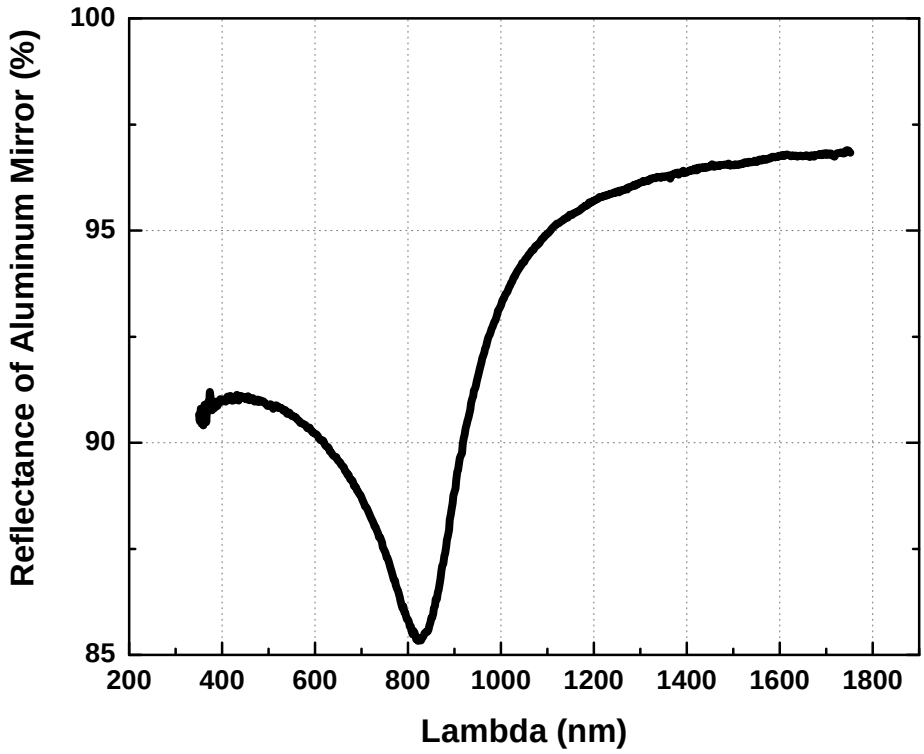

Figure 2-16: Reflectance of the aluminum mirror for the reflectance measurements.

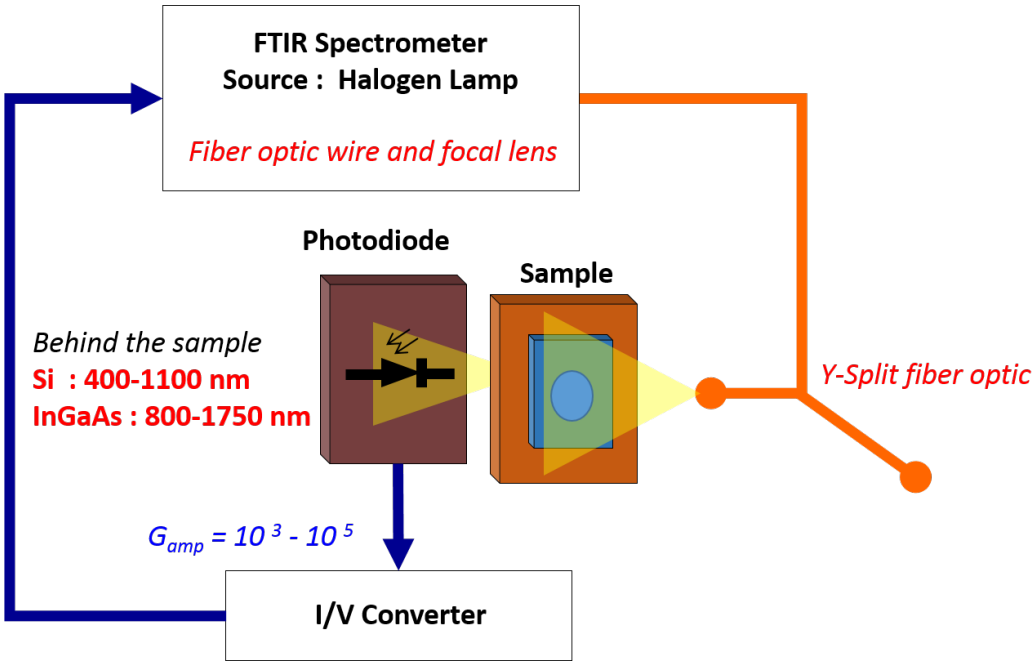

Figure 2-17: System configuration for the transmittance measurement.

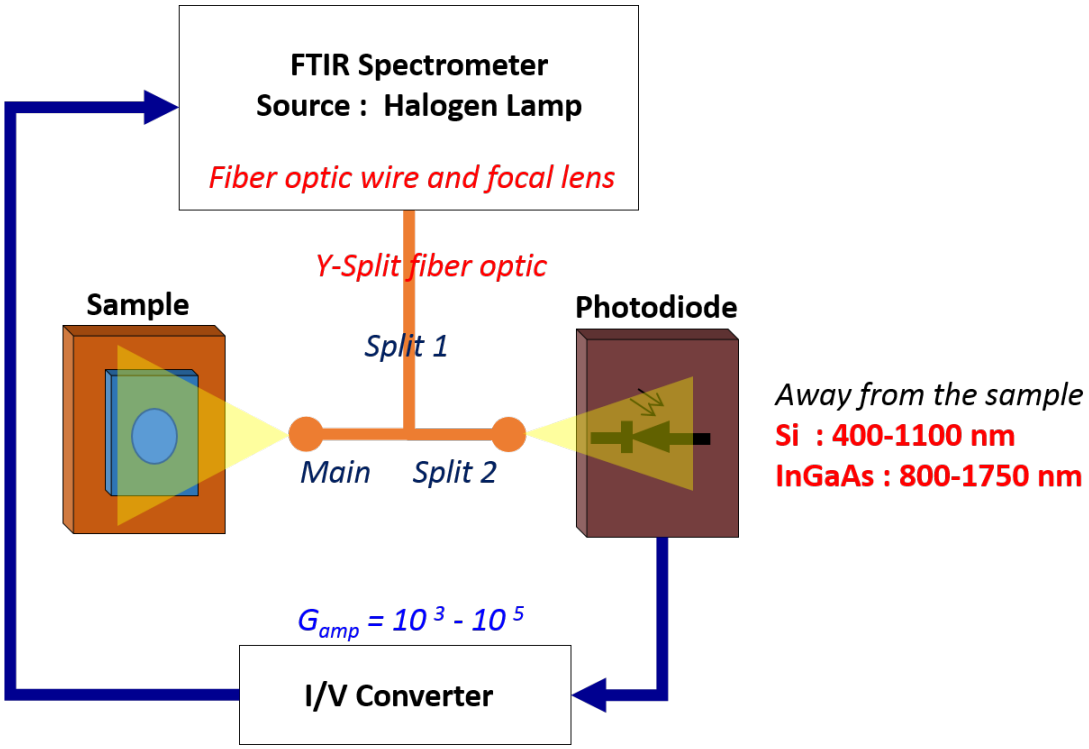

Figure 2-18: System configuration for the reflectance measurement.

3. Measurement of the transmitted light by the sample using the InGaAs photodiode.

4. Measurement of the reflected light by the sample using the silicon photodiode.

5. Measurement of the incident light (by removing the sample from the sample holder) using the InGaAs photodiode.

6. Measurement of the incident light using the silicon photodiode.

7. Measurement of the reflected light by the aluminum mirror using the InGaAs photodiode.

8. Measurement of the reflected light by the aluminum mirror using the silicon photodiode.

With this procedure we can calculate the transmittance and reflectance of a thin film using Eqs. (2.26) and (2.28) The amplification gain has to be taken into account in the calculation of the photocurrents, since it may not be the same for the signal from the sample or from the reference. To obtain the transmittance and reflectance from both film and substrate (glass) sides, we can use the procedure above for one side and repeat it for the other side. An example of the measured transmittance and reflectance of a hydrogenated amorphous silicon (a-Si:H) sample can be found in Fig. 2-19.

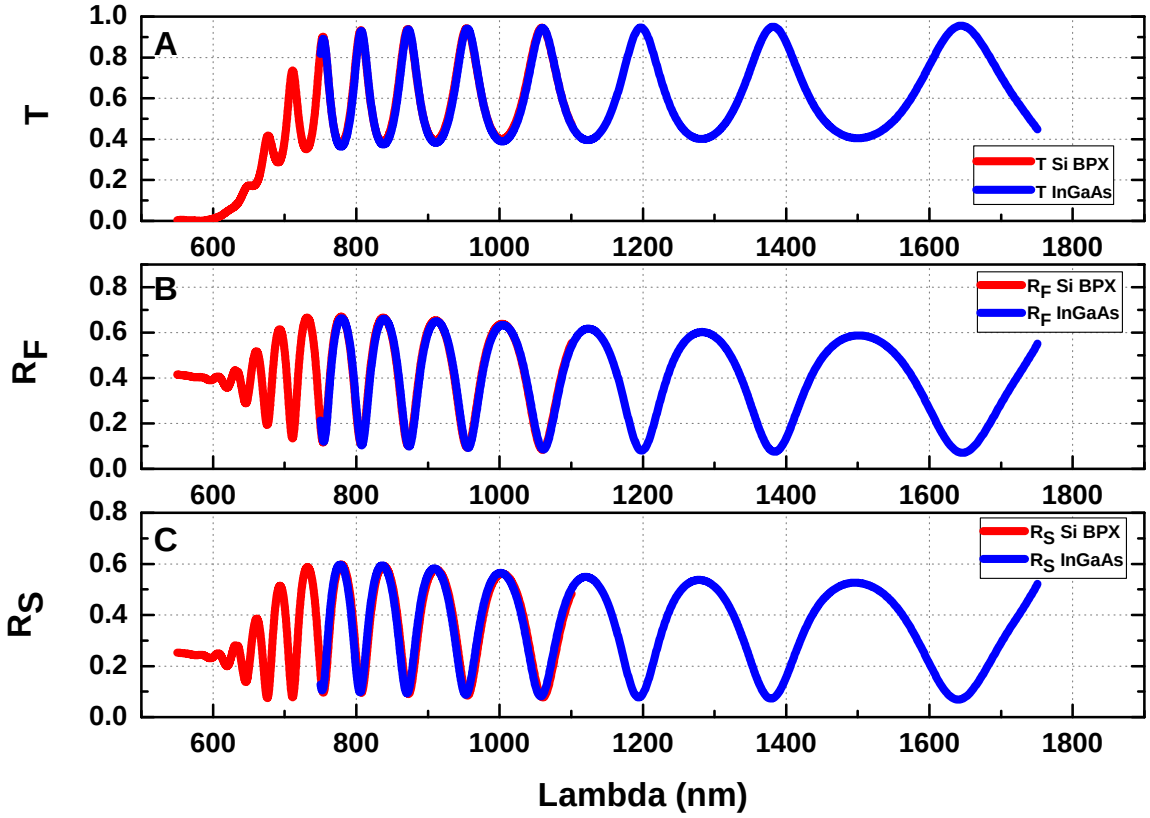

Figure 2-19: (A) Example of transmittance, T, measured on an a-Si:H sample. (B) Example of reflectance of an a-Si:H sample from the film side, R_F. (C) Example of reflectance of an a-Si:H sample from the substrate side, R_S. The transmittance and reflectance measurements are done using two photodiodes, c-Si and InGaAs.

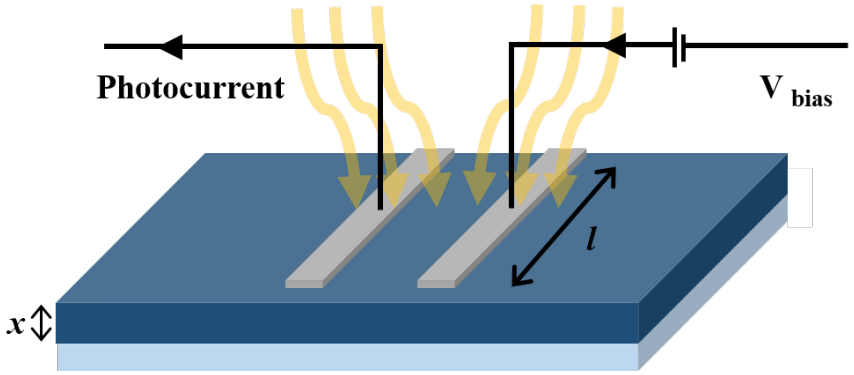

Figure 2-20: Semiconductor sample deposited on a non conductive substrate with bias voltage under monochromatic light illumination.

2.4 Absorption coefficient measurement of a semiconductor material using an FTIR spectrometer

When a semiconductor with two coplanar electrodes is polarized by a continuous bias voltage and is exposed to monochromatic light with a continuous flux intensity as depicted in Fig. 2-20, for a given depth x, the generation of the photocurrent can be described as:

$$dI_{ph}(x) = lE\sigma_{ph}(x)dx \ , \tag{2.29}$$

where E is the electric field applied between the electrodes, l is the length of the electrodes, and σ_{ph} is the photoconductivity, which can be described as :

$$\sigma_{ph}(x) = q\left(\mu_n \Delta n(x) + \mu_p \Delta p(x)\right) \ , \tag{2.30}$$

where q is the absolute value of the electron charge, μ_n and μ_p are the mobilities of electrons and holes, respectively. The excess electrons and holes generated in the presence of light are described as Δn and Δp:

$$\begin{aligned} \Delta n &= n(x) - n_0 \\ \Delta p &= p(x) - p_0 \ , \end{aligned} \tag{2.31}$$

where n_0 and p_0 are the concentrations of electrons and holes under dark. If we consider that the mobility of the electrons is much higher than that of holes, and that the concentration of electron under illumination is much higher than in the dark, the photoconductivity can be described as :

$$\sigma_{ph}(x) = q\mu_n n(x) \tag{2.32}$$

The electron concentration in a semiconductor material under illumination is the product of the generation rate of electrons and the electron lifetime. So, the photoconductivity is:

$$\sigma_{ph}(x) = q\mu_n \tau_n G(x) \ , \tag{2.33}$$

the generation rate of the electron can be expressed as:

$$G(x) = \eta(1-R)F_{dc}\alpha exp(-\alpha x) \ , \tag{2.34}$$

where η is the quantum efficiency of the electron generation, R is the reflection coefficient of the film deposited on glass, and α is the absorption coefficient of the semiconductor film for a given photon energy.

We can correlate how we obtain the absorption coefficient from the generated photocurrent in the semiconductor starting from the equation below:

$$dI_{ph}(x) = lEq\mu_n\tau_n\eta(1-R)F_{dc}\alpha exp(-\alpha x)dx \tag{2.35}$$

Hence the photocurrent generated across the thickness, d_f, of the film deposited on glass can be expressed as:

$$I_{ph}(x) = lEq\mu_n\tau_n\eta(1-R)F_{dc}\int_0^{df}\alpha exp(-\alpha x)dx \tag{2.36}$$

When the absorption coefficient, α, is low, and the film thickness is thin we have $\alpha df << 1$ and hence $\exp(-\alpha df) \simeq 1 - \alpha d_f$. Finally the generated photocurrent in the thin film is:

$$I_{ph}(x) = lEq\mu_n\tau_n\eta(1-R)F_{dc}\alpha d_f \tag{2.37}$$

In the case of a constant photocurrent, the quasi Fermi levels in the band gap of a semiconductor are kept constant. In consequence, the number of recombination centers also stays constant which assures a constant product of mobility and lifetime [37]. From the equation above, we have the proportionality of the generated photocurrent and the absorption coefficient as follows:

$$I_{ph} \sim F_{dc}\alpha \tag{2.38}$$

The photocurrent measurement which was performed to obtain the absorption coefficient of the semiconductor material is known as the constant photocurrent method (CPM) which was first known as the constant photoconductivity technique introduced by Grimmeiss and Monemar [16], involving an experimental setup as shown in Fig. 2-21A. This technique is known as the standard mode constant photocurrent method (SCPM). This experiment uses a monochromator to select the wavelength of the light impinging the sample. In between the monochromator and the sample, a beam splitter is installed. The beam splitter is used with transmittance and reflectance values of 50%. The beam reaching the beam splitter is half transmitted to the polarized sample and half reflected to the detector that measures a number of photons with energy $h\nu$. The measured reflected beam intensity thus corresponds to the incident flux of light impinging the sample. The relative variations of the absorption coefficient in SCPM are calculated through the ratio between the photocurrent generated in the sample and the flux intensity of the incident beam measured by the detector. In the SCPM result as seen in Fig. 2-21B, there exist interference fringes representing the multiple reflections in the film.

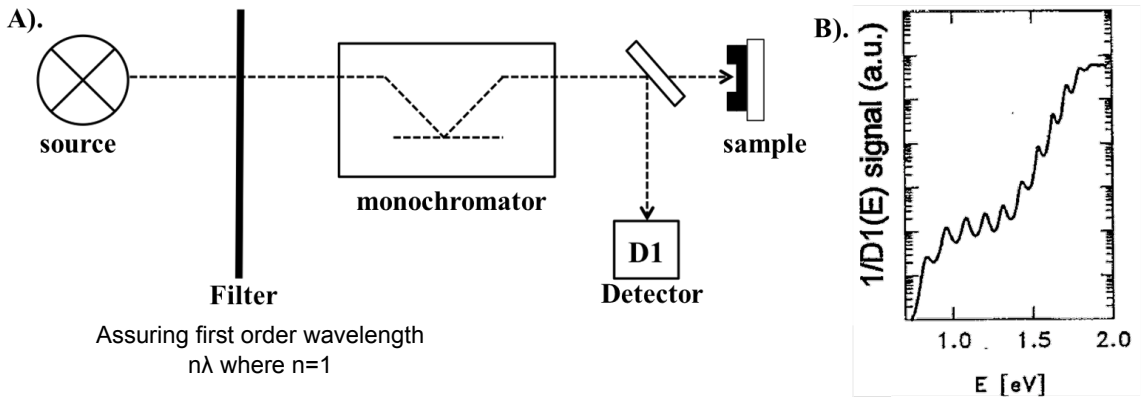

Figure 2-21: (A) Device configuration for the SCPM measurement, using one detector to measure the flux intensity of the source. (B) SCPM result where the interference fringes in the absorption coefficient spectrum are present [21].

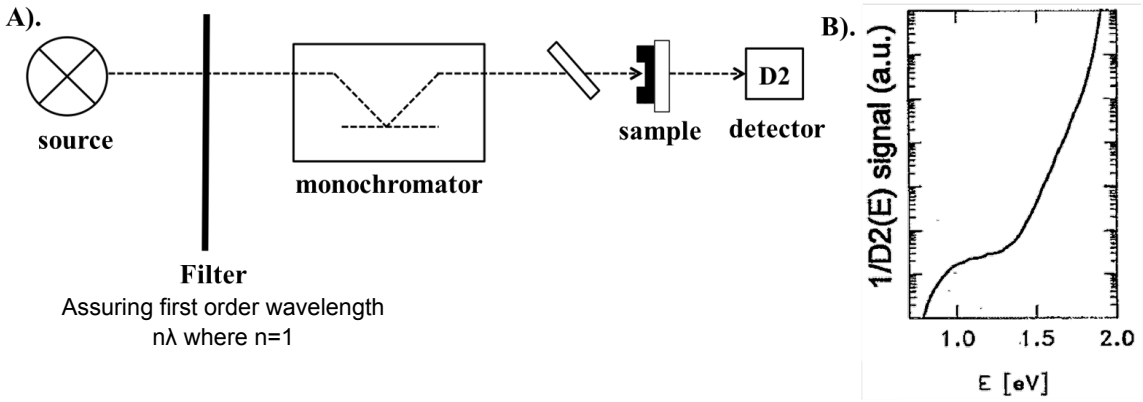

Figure 2-22: A). Device configuration for the TCPM measurement, using one detector placed behind the sample to measure the transmitted flux intensity of the source through the sample. B).TCPM result where the interference fringes in the absorption coefficient spectrum are no longer present [21].

A novel approach to CPM was proposed by using a photon detector placed behind the thin film sample. The experimental setup is described in Fig. 2-22A. This new method has been developed to suppress the interference fringes in the optical absorption spectra. The suppression of the interference fringes is done by using the transmitted instead of the incident light as a reference for the flux of light. The existence of the interferences in the transmitted light suppresses the interferences in the final ratio between the sample photocurrent and the detector photocurrent. This approach was applied by Sasaki in his paper [23] and further introduced as "transmission mode CPM" (TCPM).

The latest research in CPM was reported by [21], where the method coupled the SCPM and TCPM experimental setups. This technique is called Absolute CPM (ACPM) due to its capability to bring the absorption coefficient spectrum to its

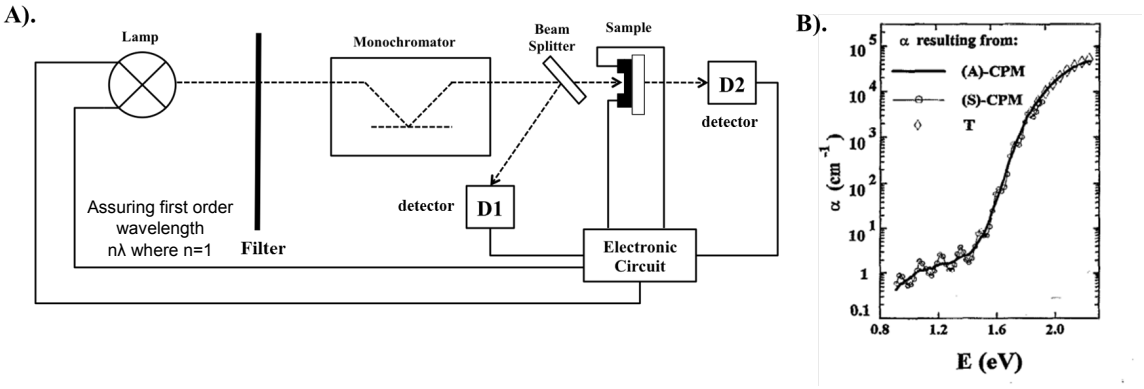

Figure 2-23: (A) Device configuration for the ACPM measurement, using two detectors, one placed behind the sample to measure the transmitted flux intensity of the source through the sample and one to measure the flux intensity of the source. The ratio of the measured transmitted and incident flux can be used to obtain the transmittance of the sample (B) ACPM result compared to SCPM where the interference fringes in the ACPM absorption coefficient spectrum are no longer present and the spectrum is calibrated to its absolute value using Ritter-Weiser formula [21].

absolute value by calibrating the CPM spectrum using the Ritter-Weiser formula [38]. The configuration of the ACPM and an example of its measurement result can be seen in Fig. 2-23.

The absorption coefficient measurement using ACPM has yield a great result despite of its long measurement time. The measurement time can go up to 24 or more hours for one sample. This is due to the measurement procedure of CPM which is very long caused by the use of a monochromatic light source. In order to get the absorption coefficient at each photon energy, the monochromator needs to change the photon energy at each step. For each photon energy, the photocurrent needs to be kept constant by adjusting the incoming flux of photon reaching the sample. The flux adjustment is done by adjusting the iris diameter of the monochromator outlet. All of these measurement procedures result in a long measurement time, and the time is even longer if we want to have a higher resolution measurement.

Recent method of absorption coefficient measurement of semiconductor material has been proposed using an FTIR spectrometer with a broadband light source instead of monochromatic. This technique is called FTPS (Fourier Transform Photocurrent Spectroscopy). This technique has been firstly introduced by Tomm *et al.* in 1997 [26], and later by Poruba and Vanecek in 2002 [28], [24]. These works have been carried out mainly for the purposes of R&D of thin film silicon photovoltaics where the quality of semiconducting layers is monitored. FTPS technique has been applied to measure different types of semiconductor materials such as in a broad study of microcrystalline silicon by FTPS which was made at Université de Neuchatel: Bailat in 2004 [39], Sculati-Meillaud in 2006 [40], and Python in 2009 [41]. It was used to study thin silicon films by Poruba *et al.* [42], thin silicon films deposited on various substrates by Vanecek *et al.* in [27], amorphous silicon thin films and solar cells by

Melskens *et al.* in 2008 [30], in CVD diamonds as reported by Kravets *et al.* [29] and by Vanecek *et al.* in [43], and in disordered semiconductors as reported by Poruba *et al.* in [44].

In the FTPS, the photocurrent is automatically kept constant during the measurement, as reported in [25]. The constant photocurrent is due to the constant flux intensity of the FTIR light illuminating the semiconductor sample, hence the formula of the photocurrent generation in the semiconductor sample in Eq. (2.36) is still valid.

As we have developed a photocurrent measurement technique using an FTIR spectrometer for the transmittance and reflectance measurements as described in Section 2.3, in FTPS measurement we replace the photodiodes with a semiconductor sample. This means that instead of measuring the photocurrent of the photodiodes, we measure the sample photocurrent when it is exposed to the incident light beam. Our FTPS measurement uses the principles of the absolute CPM in order to suppress the interference fringes in the absorption coefficient spectra, and to obtain its absolute value in cm^{-1}.

The details on how the absolute absorption coefficient spectrum is obtained are discussed in Sec. 2.4.1, and the details about the experimental setup and procedures of FTPS for absorption coefficient spectrum measurement are discussed in Section 2.4.2.

2.4.1 Obtaining the absorption coefficient spectrum

The absorption coefficient as described in Eq. (2.38) is measured by the FTIR spectrometer using Eq. (2.39). It can be described as the ratio of the photocurrent density generated by the sample under illumination, J_{sample} and the flux intensity of the part of light being transmitted by the sample, $F_{transmitted}$. The flux intensity of the transmitted light is obtained by measuring the photocurrent density of a photodiode placed behind the sample, $J_{transmitted}$. The measurement using the photodiode is used as the reference measurement.

$$\frac{B(\nu)J_{sample}(\nu)}{B(\nu)J_{reference}(\nu)} = \frac{B(\nu)J_{sample}(\nu)}{B(\nu)J_{transmitted}(\nu)} \tag{2.39}$$

In practice, the absorption coefficient, α in cm^{-1} can be calculated using Eq. (2.38).

$$\alpha(\nu) \sim \frac{J_{sample}(\nu)}{F_{transmitted}(\nu)} \tag{2.40}$$

where J_{sample} is the photocurrent density generated by the sample (in $A.cm^{-2}$), $F_{transmitted}$ is the flux intensity of the fraction of light transmitted through the sample measured by the photodiode (its value can be obtained using formula in Eq. (2.25)). The interest of using the transmitted light instead of the incident light in the calculation of absorption coefficient is to remove the interference fringes in the final absorption coefficient spectrum as reported by Sasaki [23].

The spectrum we obtain using the above equation gives us the trend and the dynamic range of the absorption coefficient spectrum, but not its absolute value. In

order to get the absolute value of the absorption coefficient spectrum, we need to calibrate the absorption coefficient value using the result of the transmittance and reflectance measurement, or only the transmittance measurement if the reflectance value of the sample is approached as in the calculation of absorption coefficient with the absolute constant photocurrent method in Vanecek *et al.* paper [21] using the Ritter-Weiser formula. The absorption coefficient value is calibrated in the wavelength region where the transmittance and reflectance spectra have no interference fringes.

If we take a look at the transmittance and reflectance spectra of a typical hydrogenated amorphous silicon thin film semiconductor material as depicted in Fig. 2-19, the interference fringes disappear in the low wavelength (high energy) region. Hence, the low wavelength region is the region where the absorption coefficient can be calibrated.

As explained above, the calculation of the absorption spectra can be obtained using the procedure as described in [21] when no reflectance measurement is performed and the film thickness of the sample is known. In this case, the absorption coefficient spectrum will be calibrated using only the transmittance spectrum. The procedure of the calibration is as follows:

1. Setting the transmittance T to the absolute scale. The maximum value of the transmittance, T_{max}, of a homogeneous thin film with thickness d_f, on a non absorbing thick substrate, is given by the optical refraction index n_s, of the substrate only [45]. In case of the Corning glass no. 7059 substrate with n=1.5 [46], T_{max} below approximately 1.2 eV equals 0.92 using Eq. (2.41). We use this value to set the transmittance spectrum to the absolute scale.

$$T_{max} = \frac{2n_s}{n_s^2 - 1} \tag{2.41}$$

2. Setting the A/T, A being the absorptance value and T the transmittance value, to the absolute scale by analyzing the R, T, and A at one chosen reference energy at which the absorptance is high enough to suppress the effect of the interferences. We set a relative spectrum of A/T into the absolute scale at one reference energy, E_0, in the high-energy region of the spectra in which the absorptance is high enough to suppress the multiple reflections in the film (e.g. $T = 0.05$) and, therefore, the values of T and R are almost free from the interference fringes here (see Fig.2-19).

   For a-Si:H, the reflectance R converges toward $R = 0.41$ for the case of light incident on the film side or R=0.26 for the light incident on the substrate side. We use this value together with the $T = 0.05$ to calculate the absorptance value at the reference point E_0, $A = 1 - T - R$, which gives $A = 0.54$ in the case of light incident on the film and 0.69 on the substrate side. Hence, the A/T at the reference point E_0 equals 10.8 for the light incident on the film side and 13.8 for the substrate side.

3. Calculate the spectral dependence of the optical absorption coefficient $\alpha(E)$ from the absolute A/T dependence using the Ritter-Weiser formula given in

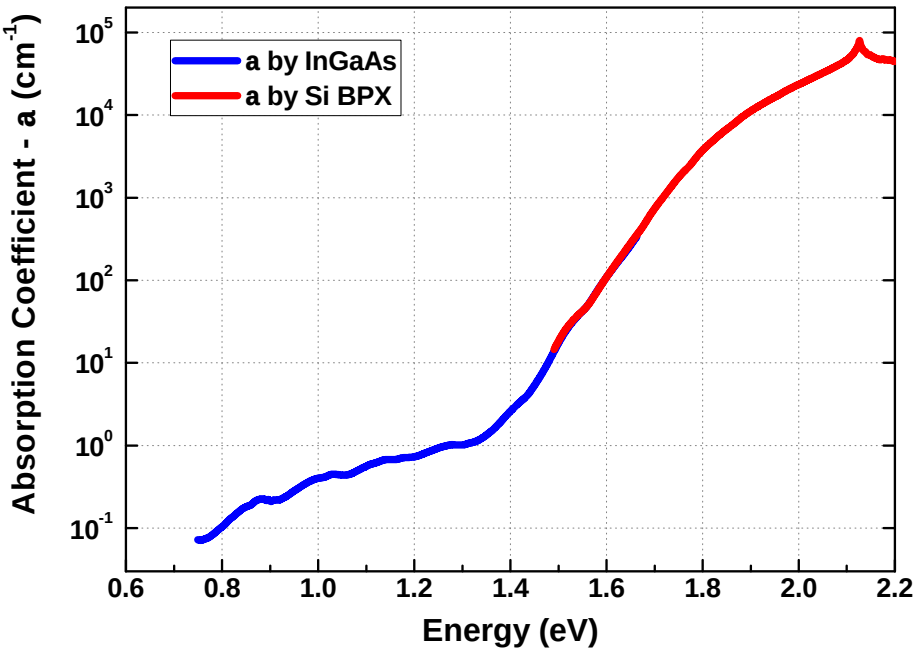

Figure 2-24: Example of an absorption coefficient spectrum of an a-Si:H sample calibrated to its absolute value using Ritter-Weiser formula. The measurements were done with the FTIR spectrometer using two detectors and one optical filter, high pass above 746 nm.

Eq. (2.42).

$$\alpha d = ln\left(0.5\left\{\left(1 - R_1\left(1 + \frac{A}{T}\right) + \left[(1 - R_1)^2 \times \left(1 + \frac{A}{T}\right)^2 + 4R_1\right]^{0.5}\right)\right\}\right) \tag{2.42}$$

where R_1, is the reflectivity of the back interface of a-Si:H film, i.e., either the interface a-Si:H/substrate for the case of light incident on the a-Si:H layer or interface a-Si:H/ambient for light incident through the substrate. The value of R_1, is in fact spectrally dependent but its variation influences only weakly the values of $\alpha(E)$ calculated from Eq. (2.42) and so we use an approximate constant value of R_1=0.21 for the front illumination of an a-Si:H film and R_1=0.36 for the illumination through the substrate. By this way we can obtain the spectral dependence of the optical-absorption coefficient $\alpha(E)$ in absolute units (cm^{-1}). Fig. 2-24 shows an absorption coefficient spectrum calibrated using the above procedure. It can be seen that the interference fringes are almost completely suppressed and that the spectrum is given in absolute values (cm^{-1}).

While in the above procedure we have assumed an estimated value for the reflectance of an a-Si:H sample for the calibration of the absorption coefficient spectrum, if possible it is recommended to perform the actual reflectance measurement. Indeed, the above value of R_1 was applied in the case of a-Si:H sample, and maybe different for another material. In any case, a measurement of R and T can be performed

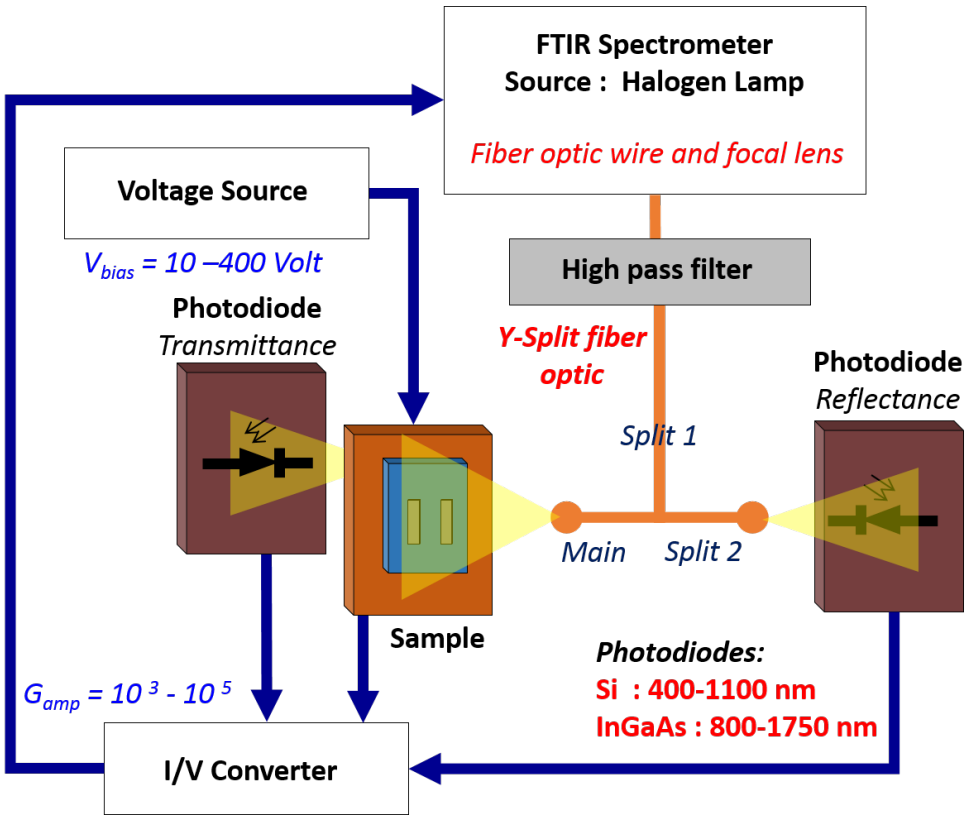

Figure 2-25: System configuration for the FTPS measurement to obtain an absorption coefficient spectrum, using two detectors, one placed behind the sample to measure the transmitted flux intensity of the source through the sample and one to measure the reflected flux intensity of the source by the sample. With this setup, we obtain the absorption coefficient spectrum, the transmittance, and the reflectance measurements.

following the procedure described in Sec. 2.3.

2.4.2 Experimental setup and procedures of absorption coefficient measurement

The measurement of the sample photocurrent is obtained by placing one pair of coplanar electrodes on the film side of the sample and by applying a voltage to the sample while it is exposed to the incident light from the Michelson interferometer of the FTIR spectrometer. The flux intensity of the transmitted light is measured using the same technique as for transmittance measurement, by measuring the current of a photodiode placed behind the sample. The system configuration for the absorption coefficient measurement is depicted in Fig. 2-25.

In order to verify whether the sample generates any photocurrent, we can check whether there is any difference when the sample is exposed to the light and when it is not with a voltmeter or an oscilloscope. To amplify the current input in the FTIR spectrometer, we can either increase the applied voltage or the amplification gain of

the I/V converter.

In amplifying the signal, we should always prioritize a high signal-to-noise ratio over the overall amplitude in order to obtain a correct measurement. In many cases, in the result of the sample photocurrent measurement we can see that we loose sensitivity in the high wavelength (low energy) region. This problem is due to a higher noise to signal ratio, which can be resolved by using an optical filter that cuts off the wavenumber region at which the signal is high. Then, we can increase the signal-to-noise ratio by increasing the amplification gain of the I/V converter.

The measurement of the flux intensity of the transmitted light is done by placing a photodiode behind the sample, as in the transmittance measurement. Two photodiodes, InGaAs and crystalline silicon, are used and the measurement using the InGaAs photodiodes is done with the optical filter to increase the signal-to-noise ratio and increase the dynamic range of the measurement. An example of the measured absorption spectrum of an a-Si:H sample using the FTIR spectrometer can be seen in Fig. 2-24. We perform the absorption coefficient measurement using the following procedure:

1. Measurement of the sample photocurrent with and without the optical filter.

2. Measurement of the flux intensity of the transmitted light using the silicon photodiode.

3. Measurement of the flux intensity of the transmitted light using the InGaAs photodiode with optical filter.

4. Measurement of the flux intensity of the incident light using the silicon photodiode.

5. Measurement of the flux intensity of the incident light using the InGaAs photodiode with optical filter.

6. Measurement of the flux intensity of the reflected light by the sample using the silicon photodiode.

The measurement of the flux intensity of incident light is useful to obtain the transmittance spectrum of the measured sample, which is the ratio of the flux intensities of transmitted to incident light. The transmittance value is calculated using the Eq. (2.26). To obtain the absorption coefficient spectrum in arbitrary value, that is obtaining only the trend of the absorption coefficient spectrum, the measurement of the photocurrent of the sample as explained above is sufficient. But, to obtain an absorption coefficient spectrum in absolute value, we need to calibrate the absorption coefficient result using both the transmittance and reflectance values of the sample or by only using the transmittance value if the criteria as stated in the above section 2.4.1 are met.

2.5 Spectral response measurement of solar cells using an FTIR spectrometer

The spectral response or quantum efficiency (QE) is essential for understanding current generation, recombination, and diffusion mechanisms in photovoltaics devices. The quantum efficiency in units of electron-hole pairs collected per incident photon is computed from the measured spectral response in units of amperes per watt as a function of wavelength [47].

As explained in the three different kind of photocurrent measurements above: transmittance, reflectance, and absorption coefficient measurements, we have used a semiconductor thin film deposited on a non-conductive substrate as a sample. In this section, this kind of sample will no longer be used. Instead, we will use a solar cell as a sample. The photocurrent measurement using an FTIR spectrometer can be applied to measure the spectral response of a solar cell with advantages compared to the typical solar cell spectral response measurement using a monochromator light source. The advantages of using the FTIR spectrometer are a shorter measurement time than the typical measurement using a monochromatic source, and a higher measurement resolution.

Solar cell spectral response measurement using FTIR spectrometer has been first reported by Poruba *et al.* in 2001 [28] on $\mu c - Si$ p-i-n solar cells, and later by Poruba *et al.* in 2003 on solar modules and layers on ZnO coated glass [42]. Method of evaluation of $\mu c - Si$ solar cells avoiding the effect of ZnO was well-developed by Python in 2009 [41]. Python *et al.* further observed the microcracks in solar cells as another type of defects in solar cells [48]. Measurements on a-Si:H solar cells were first published by Melskens *et al.* from University of Delft in 2008 [30]. In the mean time, the application to multi-junction solar cells was conducted by Poruba in 2001 [28], and finally the measurements to analyze the quality of tandem cells were conducted by Holovsky in 2007 [49].

2.5.1 Obtaining the solar cell spectral response spectrum

In the case of spectral response, SR, measurement, the SR value is obtained by measuring the ratio of the photocurrent generated by the solar cell under illumination, and the power of the incident light impinging the solar cell (see Eq. (2.43)).

$$SR(\nu) = \frac{I_{solarcell}(\nu)}{P_{incident}(\nu)} \ , \tag{2.43}$$

where $SR(\nu)$ is the spectral response in A/W, $I_{solarcell}$ is the generated photocurrent from the solar cell under incident light in A, and $P_{incident}$ is the incident power of the light source measured by a photodiode in Watt. Based on the above equation, the measurement of spectral response of a solar cell using FTIR spectrometer can be denoted as :

$$\frac{B(\nu)I_{sample}(\nu)}{B(\nu)I_{reference}(\nu)} = \frac{B(\nu)I_{solarcell}(\nu)}{B(\nu)I_{incident}(\nu)} \tag{2.44}$$

where the $I_{incident}$ can be used to calculate the $P_{incident}$ using the spectral response of the calibrated photodiode.

By knowing the spectral response, we are able to provide the external quantum efficiency (EQE) of the solar cell using Eq. (2.45).

$$EQE(\lambda) = SR(\lambda) \ \ \frac{1240}{\lambda \ (nm)} \tag{2.45}$$

Further, to obtain the density of short circuit current at each wavelength, we know the flux density of a light source at AM 1.5G, hence we can reconstruct the measurement condition as if the solar cell was under the illumination of AM 1.5G. The density of the short circuit current at each wavelength is the product of the spectral response and the power of AM 1.5G, as denoted in Eq. (2.46).

$$J_{SC}(\lambda) = SR(\lambda).P_{AM1.5G}(\lambda) \tag{2.46}$$

Where J_{sc} is the short circuit current density at each wavelength in $A/m^2/nm$, and $P_{AM1.5G}$ is the flux power of AM 1.5G in $W/m^2/nm$. To obtain the total short circuit current density of the solar cell in A/m^2 under AM 1.5G, we can integrate the density of short circuit current for all the wavelength range using the equation below,

$$J_{SC} = \int_{\lambda_0}^{\lambda} J_{SC}(\lambda) \ \ d\lambda \tag{2.47}$$

The measured power density of AM 1.5G we used to obtain the short circuit current is presented in Fig. 2-26.

2.5.2 Experimental setup and procedures of solar cell spectral response measurement

In spectral response measurements, we use a solar cell instead of a semiconductor thin film deposited on glass. The measurement of spectral response does not differ much from the FTPS measurement for absorption coefficient. In the spectral response measurement we have added blue LEDs at different wavelengths in order to increase the flux intensity in the blue region, where the spectral response is low. The added blue LEDs are placed inside the FTIR spectrometer. These LEDs can be mounted and dismounted by sliding the axes attached inside the FTIR spectrometer. The scheme of the configuration of this measurement is depicted in Fig. 2-27.

Due to the added blue LEDs, we have modified the properties of the incident light source. The modified flux intensity of the light source is presented in Fig. 2-28, measured with a silicon photodiode. The advantages of using LEDs is that spectra can be recorded in a single shot from 390 to 1100 nm. Two measurements must be done to calculate the spectral response of a cell.

The measurement procedure of the spectral response using the FTIR spectrometer is as follows:

1. Measurement of the solar cell photocurrent.

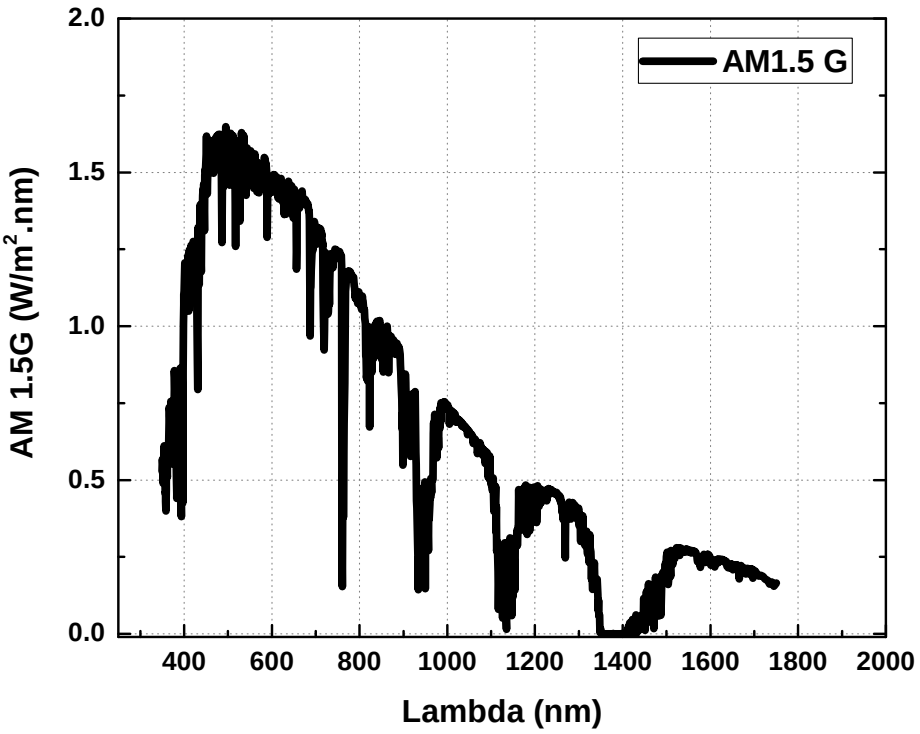

Figure 2-26: Flux density at AM15G.

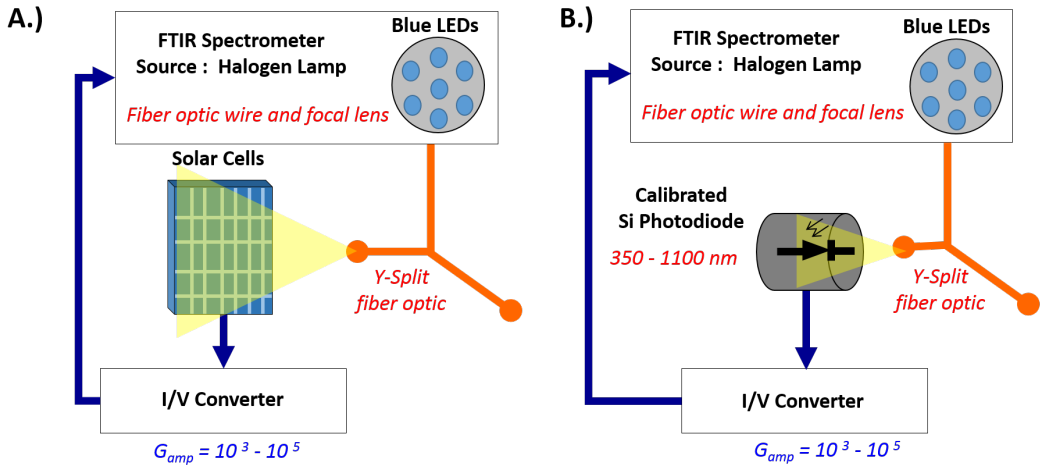

Figure 2-27: Scheme of the configuration of spectral response measurement of solar cell using the FTIR spectrometer. Blue LEDs are mounted inside the FTIR spectrometer with sliding axes in order to amplify the flux intensity in the blue region. A.) Device configuration of the spectral response measurement of solar cells. B.) Device configuration of the incident power intensity measurement of the FTIR light source.

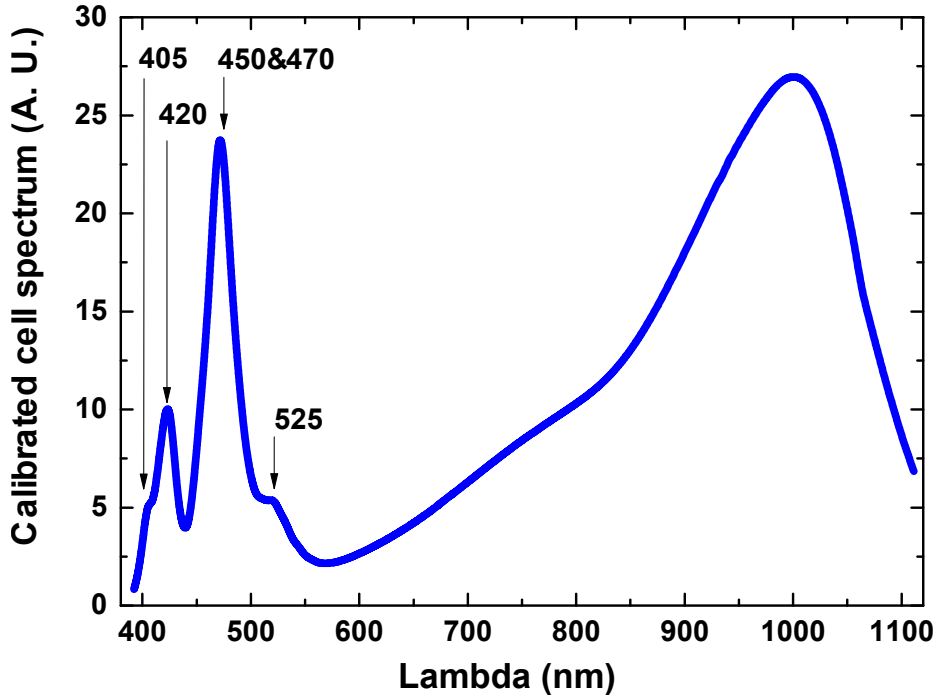

Figure 2-28: The modified incident flux intensity of the FTIR source due to the mounting of blue LEDs. The installed LEDs emit at the wavelengths of 405, 420, 450, 470, and 525 nm.

2. Measurement of the incident flux intensity using the calibrated photodiode UDT221.

The total measurement time is 20 seconds with a resolution between 0.5 to 1 nm, which is much faster than using typical monochromatic light source.

We have verified the precision of the same measurement performed using the FTIR and the typical measurement using monochromatic light source as presented in Fig. 2-29.

Using the given spectral response, we can obtain the EQE and the density of short circuit current using Eqs. (2.45) and (2.46). The EQE spectrum and the density of short circuit current of the same solar cell are found in Figs. 2-30 and 2-31, respectively.

The total short circuit current is 29.8 mA/cm^2, calculated using Eq. 2.47. Now, we can verify that the total short circuit current we obtain corresponds to the total short circuit current given by the fabricator of the solar cell, which is 30.8 mA/cm^2 [50], in rather good agreement.

Conclusions

In this chapter we have explained how to perform photocurrent measurements for thin film semiconductor samples deposited on a transparent non conductive substrate and solar cells, using the bases of FTIR spectrometry. Among the photocurrent measure-

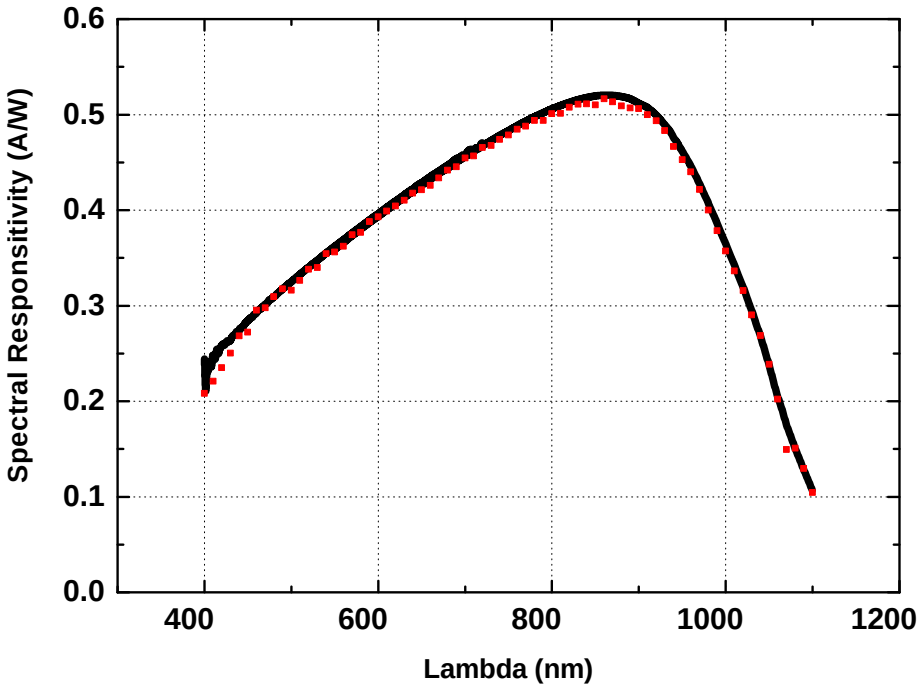

Figure 2-29: The comparison of spectral response of a crystalline silicon (c-Si) solar cell measurement using the FTIR spectrometer in black line and a monochromatic light source in red points.

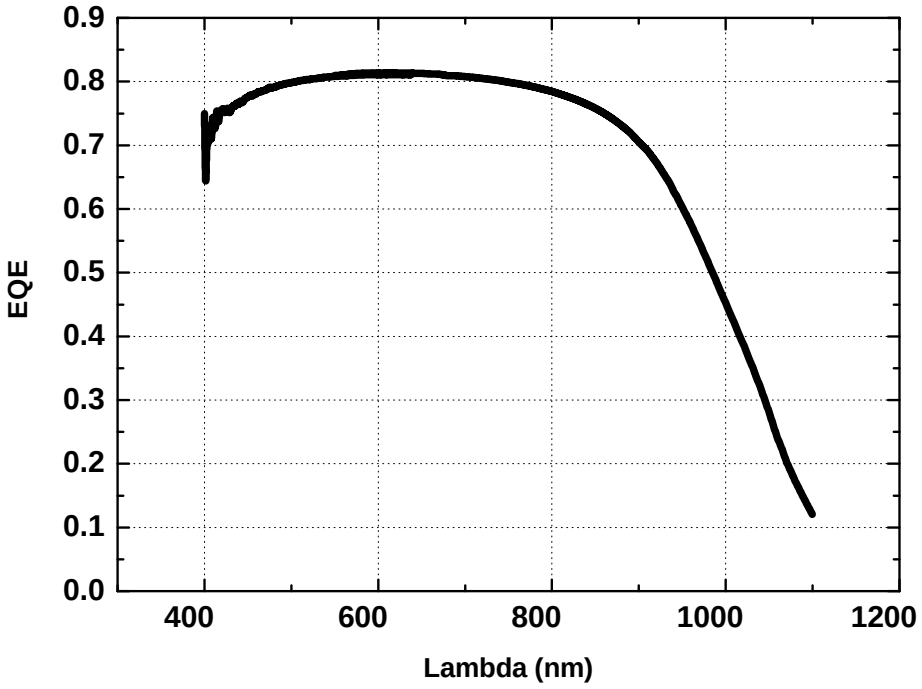

Figure 2-30: EQE of the c-Si solar cell.

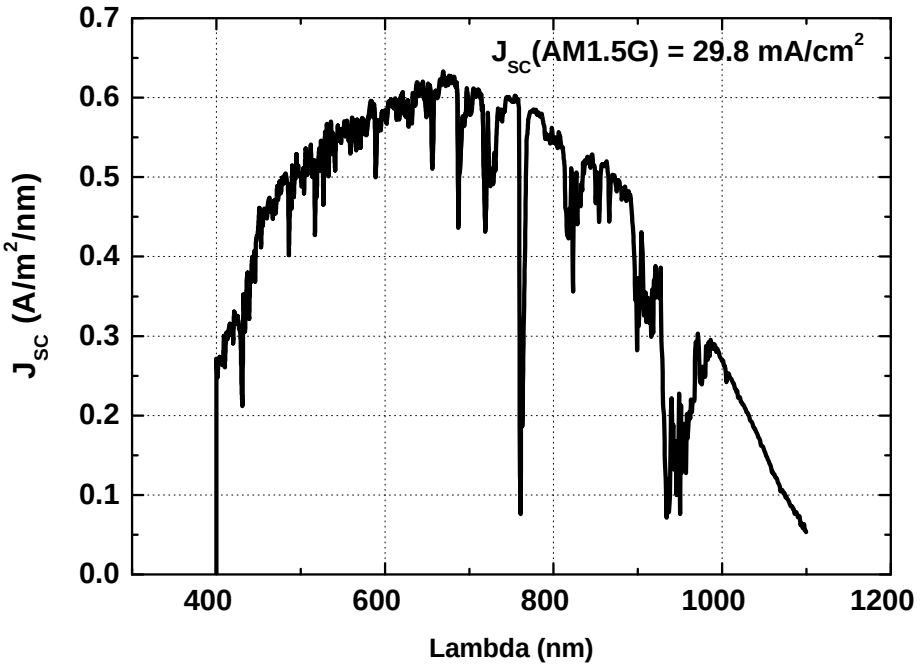

Figure 2-31: Density of short circuit current at each wavelength of the c-Si solar cell.

ments, R/T and FTPS can only be used to measure thin film samples on transparent non conductive substrate. The other one, spectral response measurement, can be performed only for solar cells. To obtain correct measurement results, experimental setup and procedures of each measurement using an FTIR spectrometer were also presented.

To our knowledge, the R/T measurement in this Chapter was the first conducted with an FTIR. It is quite simple but yield a fast and high precision results when compared to the use of a classic dispersive spectrometer. R/T measures a transmittance and reflectance spectrum of the thin film, both being useful to deduce the optical properties of the film such as its thickness, variation of refractive index and surface roughness, and also its absorption coefficient for each wavelength. Further, detailed explanations related to this topic will be discussed in Chapter 3.

FTPS measurement results in an interference-free absorption coefficient spectrum of the film. The measurement results in a large dynamic range of absorption coefficient spectrum thanks to an optical filter used to amplify the part when the signal is weak. The interferences in the absorption coefficient spectrum were successfully suppressed using the principle of ACPM, which is the ratio of the photocurrent generated by the film and the transmitted flux of light through the film measured by the photodiodes, when sample is under the illumination of the FTIR light source. An absorption coefficient spectrum at its absolute value can be obtained directly using the Ritter-Weiser formula shown in Eq. (2.42) when the film properties such as R/T and thickness are known previously. In the case when their values are not known, R/T measurement can be performed to determine its optical properties using the calculations in the next Chapter.

The measurement of solar cells properties such as its spectral response, EQE, and short circuit current density, J_{SC} was successfully demonstrated in this Chapter. The broadband light source of the FTIR spectrometer has replaced a monochromator in the existing spectral response, EQE, and J_{SC} measurement benches, bringing the advantage of simpler system configuration, faster measurement rate and higher measurement precision. The results of spectral response and EQE measurements on a solar cell using FTIR was compared to the ones measured using a monochromator, and the measured J_{SC} from the FTIR was compared to the given value from the solar cell's constructor. A good agreement is achieved when both measurement results are compared, hence it demonstrates the reliability of the solar cells measurements using an FTIR spectrometer.

Chapter 3

Determination of Thin Films Optical Properties and Absorption Coefficient

The determination of the optical coefficients of thin film semiconductor materials deposited on a transparent substrate through the transmission and reflection measurements is based on the method proposed in [51]. Nevertheless, we used the method described in [51] with several calculation revisions and modifications. In the transmission and reflection measurements on a thin film semiconductor material of thickness d deposited on a transparent non absorbing substrate, there are three media to be considered, which are the air, the film, and the non absorbing substrate. Their corresponding refractive indices are denoted by n_a, n_f, and n_s, respectively. The complex refractive indices are represented by $N_m = n_m + ik_m$, where the index m represents the medium. The imaginary term in the complex refractive index which is denoted by k_m, is related to the optical absorption coefficient α as follows :

$$k = \frac{\lambda}{4\pi}\alpha \ , \tag{3.1}$$

where λ is the wavelength. The refractive index of the thin film semiconductor material, n_f, varies with λ as in Eq. (3.2) using the modification of the Sellmeier formula by Herzberger [52].

$$n_f = n_{fa} + \frac{n_{fb}}{\lambda^2 - 0.028} \ , \tag{3.2}$$

where n_{fa} and n_{fb} are constants which depend on the material and are obtained using the fitting routine of the transmission and reflection measurements results which will be discussed later on in Sec. 3.1. The constant 0.028 is chosen independently of the type of the observed material. In Eq. (3.2)the wavelength λ is expressed in μm.

3.1 Scalar Scattering Theory of Reflectance and Transmittance of Thin Film on a Thick Substrate

One of the attenuation phenomena that may arise in the transmitted and reflected beam is induced by the scattered light due to the volume and/or surface inhomogeneities of the thin film semiconductor material. Surface inhomogeneities, also known as surface roughness, denoted by σ, can be observed through atomic force microscopy (AFM) experiment. The term surface roughness has to be considered as the surface roughness of the film with respect to its surrounding medium interface. Hence, there are two types of film surface roughness, which are the film surface roughness with respect to the air-film interface and the film surface roughness with respect to the film-substrate interface. These two film surface roughness types are denoted by σ_a and σ_s, respectively. The film surface roughness contributes to the loss of the amplitude of the transmitted and reflected light beam by means of light scattering. The loss due to the scattered light can be described by a scattering factor s [53]. In the case of the reflection between media 1 and 2, the loss of the reflected light beam from the rough surface back to the medium 1 due to the light scattering is described by :

$$s_{12}^{r} = \exp\left[-\frac{1}{2}\left(\frac{4\pi n_1 \sigma}{\lambda}\right)^2\right] \tag{3.3}$$

In the case of the loss of transmitted light beam through the rough interface to medium 2, the scattering factor can be described as:

$$s_{12}^{t} = \exp\left[-\frac{1}{2}\left(\frac{2\pi(n_1 - n_2)\sigma}{\lambda}\right)^2\right] , \tag{3.4}$$

where n_1 and n_2 correspond to the refractive indices of media 1 and 2, respectively.

To explain the scattering theory of the transmittance and reflectance of thin film semiconductor material with a rough interface deposited on a non absorbing substrate, it is necessary to take into consideration the multiple reflections that happen within the thin film. The reflectance spectra from the film side, $R_f(\lambda)$, and the substrate side, $R_s(\lambda)$, and the transmittance, $T(\lambda)$, can be described as functions of thin film parameters such as the film refractive indices n_f, optical absorption coefficient α_f, thickness d, surface roughness σ, and refractive index of ambient and substrate, n_a and n_s, respectively.

When a perpendicular incidental light wave is exposed to a smooth interface between media 1 and 2, the amplitude of Fresnel coefficients for both reflection and transmission can be described as :

$$r_{12} = \frac{N_1 - N_2}{N_1 + N_2} \tag{3.5}$$

$$t_{12} = \frac{2N_1}{N_1 + N_2} \tag{3.6}$$

When the contribution of medium interface roughness to the light scattering is introduced, the amplitude Fresnel coefficients are reduced by the scattering factors introduced in (3.3) and (3.4).

$$r_{12} = r_{12} s_{12}^r = \frac{N_1 - N_2}{N_1 + N_2} \cdot \exp\left[-\frac{1}{2}\left(\frac{4\pi n_1 \sigma_{12}}{\lambda}\right)^2\right] \tag{3.7}$$

$$t_{12} = t_{12} s_{12}^t = \frac{2N_1}{N_1 + N_2} \cdot \exp\left[-\frac{1}{2}\left(\frac{2\pi (n_1 - n_2)\sigma_{12}}{\lambda}\right)^2\right] \tag{3.8}$$

Converting the amplitude quantities into intensities of the transmitted and reflected beams between the two media is done as follows:

$$R_{12} = r_{12} r_{12}^* \tag{3.9}$$

$$T_{12} = \frac{n_2}{n_1} t_{12} t_{12}^* \ , \tag{3.10}$$

where r_{12}^* and t_{12}^* are the conjugates of r_{12} and t_{12}, respectively.

In the following, the above formulas are applied to the case of a thin film semiconductor material deposited on a non absorbing substrate of corning glass with a refractive index of 1.54. If the ambient is air, the complex refractive indices of the media are: $N_a = n_a = 1$, $N_f = n_f + ik_f$, and $N_s = n_s = 1.54$. Since the interaction between the media interfaces is taken into consideration, the calculation evaluates the cases for different media interfaces. The subscript index represents the media interface, for example af for air-film interface and vice versa for fa, sf represents the substrate-film interface and vice versa for fs, as represents the ambient-substrate interface and vice versa for sa.

The amplitude of Fresnel coefficients for reflection are calculated using the formulas as introduced in (3.7).

$$r_{af} = \frac{n_a - (n_f + ik_f)}{n_a + n_f + ik_f} \exp\left[-\frac{1}{2}\left(\frac{4\pi n_a \sigma_a}{\lambda}\right)^2\right] \tag{3.11}$$

$$r_{fa} = \frac{(n_f + ik_f) - n_a}{n_f + ik_f + n_a} \exp\left[-\frac{1}{2}\left(\frac{4\pi n_f \sigma_a}{\lambda}\right)^2\right] \tag{3.12}$$

$$r_{sf} = \frac{n_s - (n_f + ik_f)}{n_s + n_f + ik_f} \exp\left[-\frac{1}{2}\left(\frac{4\pi n_s \sigma_s}{\lambda}\right)^2\right] \tag{3.13}$$

$$r_{fs} = \frac{(n_f + ik_f) - n_s}{n_f + ik_f + n_s} \exp\left[-\frac{1}{2}\left(\frac{4\pi n_f \sigma_s}{\lambda}\right)^2\right] \tag{3.14}$$

The calculation for ambient-substrate and substrate-ambient does not involve any of the surface roughness coefficient, σ.

$$r_{as} = \frac{n_a - n_s}{n_a + n_s} \tag{3.15}$$

$$r_{sa} = \frac{n_s - n_a}{n_s + n_a} \tag{3.16}$$

From (3.15) and (3.16), it is obtained that $r_{as} = -r_{sa}$.

The amplitudes of the Fresnel coefficients for the transmission can be obtained using the formula in (3.8). Using the same evaluation procedure for each medium interface as in the calculation for reflection yields :

$$t_{af} = \frac{2n_a}{n_a + n_f + ik_f} \exp\left[-\frac{1}{2}\left(\frac{2\pi(n_a - n_f)\sigma_a}{\lambda}\right)^2\right] \tag{3.17}$$

$$t_{fa} = \frac{2(n_f + ik_f)}{n_f + ik_f + n_a} \exp\left[-\frac{1}{2}\left(\frac{2\pi(n_f - n_a)\sigma_a}{\lambda}\right)^2\right] \tag{3.18}$$

$$t_{sf} = \frac{2n_s}{n_s + n_f + ik_f} \exp\left[-\frac{1}{2}\left(\frac{2\pi(n_s - n_f)\sigma_s}{\lambda}\right)^2\right] \tag{3.19}$$

$$t_{fs} = \frac{2(n_f + ik_f)}{n_f + ik_f + n_s} \exp\left[-\frac{1}{2}\left(\frac{2\pi((n_f - n_s))\sigma_s}{\lambda}\right)^2\right] \tag{3.20}$$

$$t_{sa} = \frac{2n_s}{n_s + n_a} \tag{3.21}$$

$$t_{as} = \frac{2n_a}{n_a + n_s} \tag{3.22}$$

Once the amplitudes of Fresnel coefficients are calculated, they can be converted into the intensities of Fresnel coefficients using (3.9) and (3.10).

$$R_{af} = \frac{(n_a - n_f)^2 + k_f^2}{(n_a + n_f)^2 + k_f^2} \exp - \left[\left(\frac{4\pi n_a \sigma_a}{\lambda}\right)^2\right] \tag{3.23}$$

$$R_{fa} = \frac{(n_f - n_a)^2 + k_f^2}{(n_f + na)^2 + k_f^2} \exp - \left[\left(\frac{4\pi n_f \sigma_a}{\lambda}\right)^2\right] \tag{3.24}$$

$$R_{sf} = \frac{(n_s - n_f)^2 + k_f^2}{(n_s + n_f)^2 + k_f^2} \exp - \left[\left(\frac{4\pi n_s \sigma_s}{\lambda}\right)^2\right] \tag{3.25}$$

$$R_{fa} = \frac{(n_f - n_s)^2 + k_f^2}{(n_f + ns)^2 + k_f^2} \exp - \left[\left(\frac{4\pi n_f \sigma_s}{\lambda}\right)^2\right] \tag{3.26}$$

$$R_{sa} = \left(\frac{n_s - n_a}{n_s + n_a}\right)^2 \tag{3.27}$$

$$R_{as} = \left(\frac{n_a - n_s}{n_a + n_s}\right)^2 \tag{3.28}$$

The last two equations yield $R_{sa} = R_{as}$. Using the value of $n_a = 1$ and $n_s = 1.54$ yields $R_{sa} = R_{as} = 0.045$.

The intensities of Fresnel coefficients for transmission are:

$$T_{af} = \frac{4n_a^2}{(n_a + n_f)^2 + k_f^2} \exp\left[-\left(\frac{2\pi(n_a - n_f)\sigma_a}{\lambda}\right)^2\right] \frac{n_f}{n_a} \tag{3.29}$$

$$T_{fa} = \frac{4(n_f^2 + k_f^2)}{(n_f + n_a)^2 + k_f^2} \exp\left[-\left(\frac{2\pi(n_f - n_a)\sigma_a}{\lambda}\right)^2\right] \frac{n_a}{n_f} \tag{3.30}$$

$$T_{sf} = \frac{4n_s^2}{(n_s + n_f)^2 + k_f^2} \exp\left[-\left(\frac{2\pi(n_s - n_f)\sigma_s}{\lambda}\right)^2\right] \frac{n_f}{n_s} \tag{3.31}$$

$$T_{fs} = \frac{4(n_f^2 + k_f^2)}{(n_f + n_s)^2 + k_f^2} \exp\left[-\left(\frac{2\pi(n_f - n_s)\sigma_s}{\lambda}\right)^2\right] \frac{n_s}{n_f} \tag{3.32}$$

For the case of transmission of ambient-substrate and vice versa, we have:

$$T_{sa} = \left(\frac{2n_s}{n_s + n_a}\right)^2 \frac{n_a}{n_s} \tag{3.33}$$

$$T_{as} = \left(\frac{2n_a}{n_a + n_s}\right)^2 \frac{n_s}{n_a} \tag{3.34}$$

From (3.33) and (3.34), by using the value of $n_a = 1$ and $n_s = 1.54$, the value of T_{sa} and T_{as} is the same, which is 0.955. The same value is also found in the calculation of the intensity of Fresnel coefficients for transmission from the film side and substrate side, meaning that $T_{af}T_{fs} = T_{sf}T_{fa}$.

If the substrate is considered semi-infinite, the intensity of the Fresnel coefficients of reflectance and transmittance for both incidences (from the film side and substrate side) can be deduced as described by Poruba *et al.* [51]. In these following equations, the index notation of the reflectance and transmittance represents the incidence of the incoming light. Incidence from the film side is denoted by afs, meaning ambient/film/substrate, while incidence from the substrate side is denoted by sfa, meaning substrate/film/ambient.

$$R_{afs} = \frac{R_{af} + R_{fs}e^{-2\alpha d} + 2\sqrt{R_{af}R_{fs}}e^{-\alpha d}\cos(\varphi)}{1 + R_{af}R_{fs}e^{-2\alpha d} + 2\sqrt{R_{af}R_{fs}}e^{-\alpha d}\cos(\varphi)} \tag{3.35}$$

$$R_{sfa} = \frac{R_{sf} + R_{fa}e^{-2\alpha d} + 2\sqrt{R_{sf}R_{fa}}e^{-\alpha d}\cos(\varphi)}{1 + R_{sf}R_{fa}e^{-2\alpha d} + 2\sqrt{R_{sf}R_{fa}}e^{-\alpha d}\cos(\varphi)} \tag{3.36}$$

The intensity of Fresnel coefficient of transmittance for both incidences from the film and substrate gives the same value.

$$T_{afs} = T_{sfa} = \frac{T_{af}T_{fs}e^{-\alpha d}}{1 + R_{af}R_{fs}e^{-2\alpha d} + 2\sqrt{R_{af}R_{fs}}e^{-\alpha d}\cos(\varphi)} \tag{3.37}$$

For the above (3.35), (3.36), and (3.37), the variable φ is introduced as the consequence of the calculations of reflection and transmission coefficients of thin film on a non-absorbing semi-infinite substrate. The calculations involve the sum of the amplitudes of multiple beams that originates from the incident beams, and can be found in the Appendix A of [51]. From the mentioned calculations, φ describes the interferences and can be calculated as :

$$\varphi = \frac{4\pi n_f d}{\lambda} \tag{3.38}$$

The back surface influence still needs to be considered in the final result. When a thick substrate is used, meaning that the thickness is larger than the coherence length of the monochromatic light, it results in the suppression of the interference effect. Thus, to calculate the total reflection and transmission from both film and substrate side, we only need to take into consideration the sum of the intensities of multiple split beams. The total reflections from the film and substrate side are given in the following (3.39) and (3.40)

$$R_f = R_{afs} + T_{afs}R_{sa}T_{sfa} + T_{afs}R_{sa}R_{sfa}R_{sa}T_{sfa} + ... = R_{afs} + \frac{T_{afs}T_{sfa}R_{sa}}{1 - R_{sfa}R_{sa}} \tag{3.39}$$

$$R_s = R_{as} + T_{as}R_{sfa}T_{sa} + T_{as}R_{sfa}R_{sa}R_{sfa}T_{sa} + ... = R_{as} + \frac{T_{as}T_{sa}R_{sfa}}{1 - R_{sfa}R_{sa}} \tag{3.40}$$

While we need to make a distinction of reflection coefficients due to the direction of incident light, such dependency does not apply for the calculation of total transmittance. The total transmittance is the same for incoming light from film and substrate side.

$$T = T_f = T_s = T_{afs}T_{sa} + T_{afs}R_{sa}R_{sfa}T_{sa} + ... = T_s = \frac{T_{afs}T_{sa}}{1 - R_{sfa}R_{sa}} \tag{3.41}$$

The total reflection and transmittance coefficients as depicted in (3.39), (3.40), and (3.41) are basically the results we obtain by performing reflectance and transmittance measurements using a spectrometer. Hence, the reflectance and transmittance measurements results can be used to obtain the Fresnel coefficients of reflection and

transmission of the thin film material under study.

These equations below, (3.42), (3.43), and (3.44) can be used to determine the reflection and transmission Fresnel coefficients with the knowledge of the total reflectance and transmittance of the thin film material. The values of R_{afs}, R_{sfa}, and $T_{sfa} = T_{afs}$ can be calculated from the measurement of R_f,R_s, and T, the values of R_{sa}, T_{as}, and T_{sa} being calculated from the known value of the ambient and substrate refractive indices via (3.27) and (3.34).

$$R_{afs} = R_f - \frac{T^2 R_{sa}}{T_{sa}^2 + R_{sa}(R_s - R_{sa})} \tag{3.42}$$

$$R_{sfa} = \frac{R_s - R_{as}}{T_{as}^2 + R_{sa}(R_s - R_{sa})} \tag{3.43}$$

$$T_{afs} = T_{sfa} = \frac{T T_{as}}{T_{as}^2 + R_{sa}(R_s - R_{sa})} \tag{3.44}$$

To show how the optical parameters of a thin film can be deduced from the measurements, we can take the example of sample parameters as proposed in [51] and try to model the sample reflectance and transmittance spectra. In this case, we suppose a sample thickness of 0.5 μm and that this sample has an ambient-film interface surface roughness, σ_a, of 30 nm and has an energy dependent absorption coefficient $\alpha = 15000 * (E - 1.1)^4$, where E is the photon energy, and has the variation of refractive index as $n_f = 3.3 + \frac{0.2}{(\lambda^2 - 0.028)}$. From the given sample parameters, we can model its total reflectance and transmittance spectra using the proposed equations in (3.39), (3.40), and (3.41). The resulting spectra are depicted in Fig. 3-1. In the case when we perform reflectance and transmittance measurements using a spectrometer and would like to obtain the sample parameters such as n_f, α_f, d_f, and σ from the measurements results, we need to first determine the spectral range in which these parameters can be determined. This is important mainly because the information related to sample parameters can be obtained once we select the right spectral region to work with. In order to obtain those sample parameters, we first divide the spectral range into three regions :

1. Weak absorption region where the absorptance value is almost zero, $\alpha_f \sim 0$. This region will give us the information related to the thickness, d_f, and refractive index, n_f, of the film.

2. High absorption region where the transmittance value is almost zero, $T_f = T_s \sim 0$. In this region, we can obtain the information related to the sample surface roughness, σ, and its refractive index, n_f

3. Medium to high absorption region where the final product of the absorption and thickness of the film lies in the range of 0.05 to 5, or where the transmittance value is a bit higher than zero, $T_s = T_f > 0$. This region is mainly necessary to determine the absorption coefficient of the thin film materials, α_f.

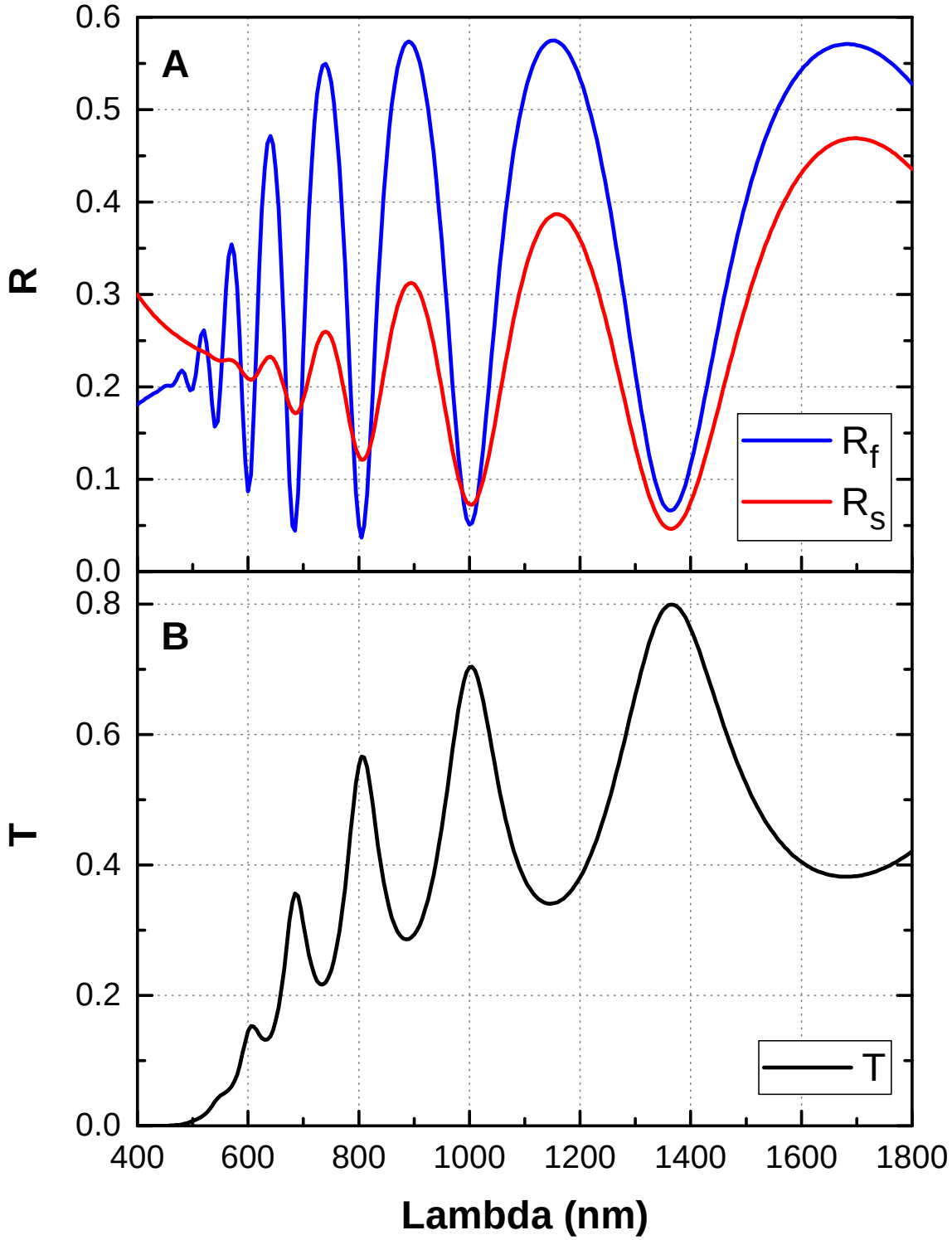

Figure 3-1: (A) Simulated reflectance of the sample from the film, R_f and substrate side, R_s, and (B) Simulated transmittance of the sample, the transmittance being the same in the case where the sample is illuminated either from the film or from the substrate side.

The calculations needed to obtain the sample parameters such as sample thickness, refractive index, and surface roughness using the above explanation about the spectral range are detailed in Sections 3.2 and 3.3, while the calculation of the absorption coefficient is detailed in Section 3.4.

3.2 Sample thickness and refractive index determination in the low absorption region

The information related to the sample thickness, d_f and its wavelength dependent refractive index, n_f, can be extracted from the reflectance and transmittance spectra where the interference fringes exist. It means that we observe the spectral range with a low absorption. The wavelength dependent refractive index follows the previously proposed Herzberger formula [52], $n_f = n_{fa} + \frac{n_{fb}}{\lambda^2 - 0.028}$. In order to obtain the material parameters n_{fa} and n_{fb}, we are going to observe the variation of $\cos(\varphi)$, where $\varphi = \frac{4\pi n_f d_f}{\lambda}$. The variation of $\cos(\varphi)$ can be obtained through fitting procedure of the presence of interference fringes in R. According to [51], we can fit through the following expression :

$$\frac{1}{1-R} = a(\lambda) + b(\lambda)\cos(\varphi) \tag{3.45}$$

Or, we can assume that $1 - R = T$ which from the above expression can be denoted as :

$$\frac{1}{T} = a(\lambda) + b(\lambda)\cos(\varphi) \tag{3.46}$$

$\cos(\varphi)$ variations can be obtained by fitting the envelope around the maxima and minima peaks of the Eqs. (3.45) or (3.46) using several fitting methods as described in this section.

In the following sections, we will discuss several fitting procedures. Due to the difficulties of finding $\cos(\varphi)$ we propose several fitting procedures using T and R. The detailed fitting procedures for the envelopes using T are detailed in sections 3.2.1 and the fitting through R is detailed in 3.2.2. Once we obtain the variation of $\cos(\varphi)$ through the fitting procedures, we can express $\cos(\varphi)$ using the Herzberger dispersion formula as denoted in [52].

$$\cos(\varphi) = \cos\left[\frac{4\pi d}{\lambda}\left(n_{fa} + \frac{n_{fb}}{\lambda^2 - 0.028}\right)\right] \tag{3.47}$$

where λ is expressed in μm. The parameters $n_{fa}d$ and $n_{fb}d$ can be obtained through simple fitting of Eq. (3.47).

3.2.1 $\cos(\varphi)$ through T

In this subsection, we will discuss the fitting of $\cos(\varphi)$ using Eq. (3.46). We can calculate the variations of the transmission through air/film/substrate or T_{afs}, and

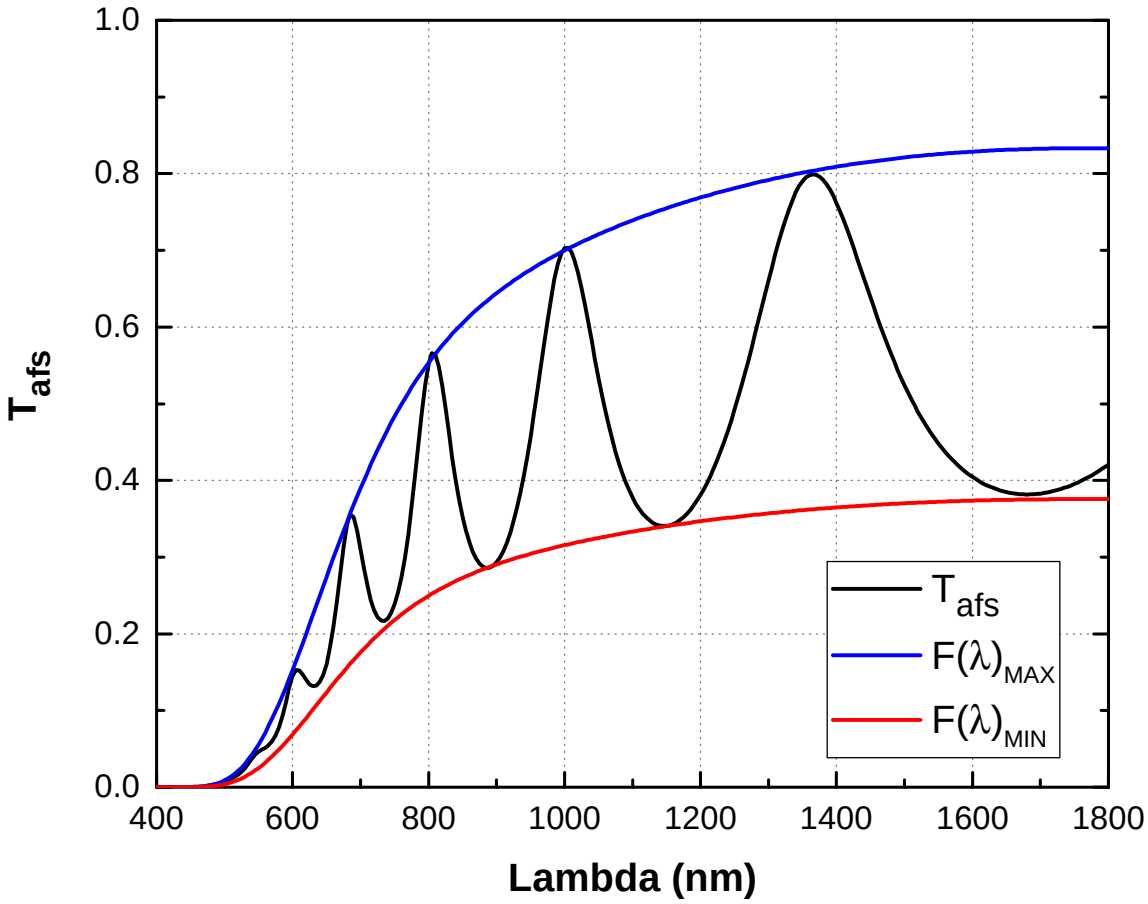

Figure 3-2: The result of T_{afs} envelopes fitting using the function described in (3.49). The constant factors, A_{min} and A_{max}, for the upper and lower envelopes are set to 0.927 and 0.418, respectively

rewrite Eq. (3.46) as:

$$\frac{1}{T_{afs}} = \frac{1 + R_{af}R_{fs}e^{-2\alpha d} + 2\sqrt{R_{af}R_{fs}}e^{-\alpha d}\cos(\varphi)}{T_{af}T_{fs}e^{-\alpha d}} = a(\lambda) + b(\lambda)\cos(\varphi) \quad , \qquad (3.48)$$

$\cos(\varphi)$ **fitting through variation of** T_{afs} **and** R_{afs}

A first fitting we tested came from the fact that if we consider the function:

$$F(\lambda) = \frac{T_{afs}}{1 - R_{afs}} = \frac{T_{af}T_s e^{-\alpha d}}{1 - R_{af}R_{fs}e^{-2\alpha d} - (R_{af} + R_{fs}e^{-2\alpha d})} \qquad (3.49)$$

we can see that this function does not depend on $cos(\varphi)$ and that it follows rather accurately the mean variations of T_{afs}. From this function we define two envelopes by multiplying it by two coefficients A_{max} and A_{min} in order to define two curves passing through the maxima and minima of the interferences observed on the T_{afs}

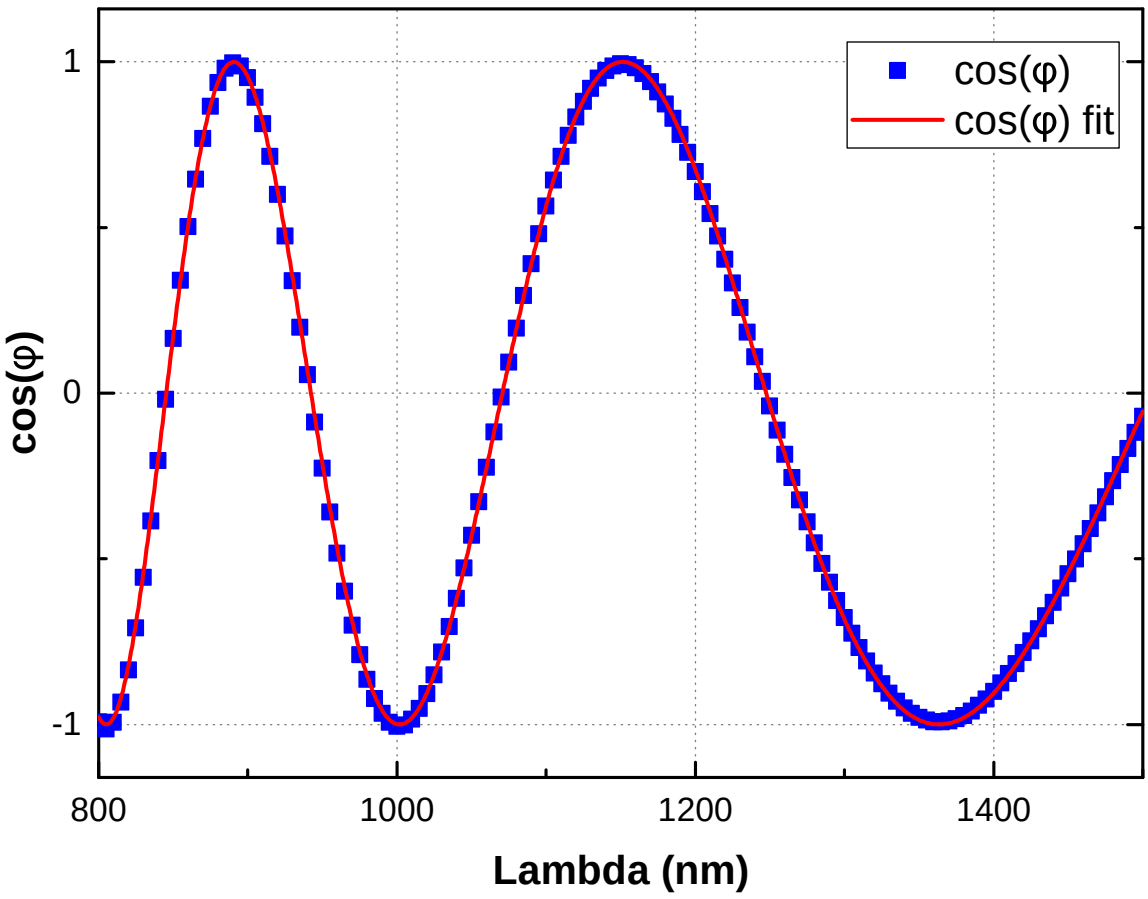

Figure 3-3: The result of cos(φ) fitting, using Herzberger function (3.47). The fitting parameters value found are $n_{fa}d = 1.6746$ and $n_{fb}d = 0.10683$.

curve. The result is presented in Fig.3-2.

From these envelopes, the variations of $cos(\varphi)$ are obtained using Eq. (3.48), resulting in $cos(\varphi) = \frac{1/T_{afs} - a(\lambda)}{b(\lambda)}$, where $a(\lambda)$ is $\frac{\frac{1}{F(\lambda)_{max}} + \frac{1}{F(\lambda)_{min}}}{2}$, and $b(\lambda)$ is $\frac{\frac{1}{F(\lambda)_{min}} - \frac{1}{F(\lambda)_{max}}}{2}$. The result of this fitting procedure is presented in Fig. 3-3. The resulting fit of cos(φ) in Fig. 3-3 is excellent since it follows quite well the variation of cos(φ) obtained from the envelope fitting of the T_{afs} curve.

cos(φ) fitting through Boltzmann functions

The fitting procedure of $cos(\varphi)$ using the maximum and minimum values of $F(\lambda)$ defined by Eq. (3.49) revealed experimentally very tricky. Indeed, $F(\lambda)$ was never found completely free from oscillations originating from the interferences. It was particularly true with the curves recorded with the UV-Visible spectrometer we used at the beginning of our study. It was essentially due to the fact that the transmittance measurements were done with the light perpendicular to the film whereas for the reflectance measurements the sample was tilted by an angle of 8°. In this case, the function $F(\lambda)$ presents always a small modulation and it becomes impossible to

determine the coefficients A_{max} and A_{min} to obtain a reliable fit of the maxima and minima of T_{afs}.

That is why we have tried to fit the maxima and minima of T_{afs} using a Boltzmann function. The Boltzmann function can be expressed as in (3.50):

$$F(\lambda) = \frac{A}{1 - \exp\left(B\left(\lambda_0 - \lambda\right)\right)} \tag{3.50}$$

where λ is expressed in μm, A is used to adjust the height in the high λ region and B is used to adjust the slope of the curve. The parameter λ_0 defines the inflection point of the curve. The envelopes resulting from the fitting procedure using the Boltzmann function denoted in (3.50) are represented in Fig. 3-4A. The resulting envelopes are not perfect as we can see because several minima and maxima of the interferences are not reached by the envelopes. The result of a non perfect fit can also be seen from the calculated $\cos(\varphi)$ result, whose value is surpassing the extrema of a cos function, $-1 \leq \cos(\varphi) \leq 1$. Nevertheless, the fit of $\cos(\varphi)$ can still be obtained with the values that are not very far from the previously obtained values while using the $T_{afs}/(1 - R_{afs})$ fitting procedure in Fig. 3-4B.

Since the shape of the T_{afs} curve has a dependency on the absorption coefficient, which varies with the photon energy, we can modify the Boltzmann function with a dependency to photon energy on $1/\lambda$ since the photon energy varies as $1/\lambda$. Thus, we can now propose a second Boltzmann function as in (3.51).

$$F(\lambda) = \frac{A}{1 + \exp\left(B.\left(\frac{1}{\lambda_0^n} - \frac{1}{\lambda^n}\right)\right)} \tag{3.51}$$

where λ is expressed in μm. The difference with the first Boltzmann function of Eq. (3.50) is that in Eq. (3.51) we can choose the power of $1/\lambda$ to improve the fit of the maxima and minima. We have found that with $n \geq 2$ it was possible to define envelopes following the maxima and minima of T_{afs} down to rather short wavelengths ($\sim$ 600 nm). Examples of multiple terms of the Boltzmann function as denoted in (3.51) for T_{afs} fitting procedure are given in Fig. 3-5 and Fig. 3-6, respectively with $n = 2$ and $n = 4$.

In Fig. 3-5, we can see an improvement of the resulting envelopes fit compared to the one obtained using the basic conventional Boltzmann function defined by Eq. (3.50), although we can still remark that the second last maximum and the last minimum are not perfectly passed and covered by the envelopes. Now, if we look at the resulting fit of $\cos(\varphi)$ in Fig. 3-5B, the variations of $\cos(\varphi)$ are in a good agreement with the cos function, and hence the $\cos(\varphi)$ fit follows almost all the points of $\cos(\varphi)$.

Although we had a quite good fit for the T_{afs} curve as represented in Fig. 3-5, we can see that in the region where the transmission is almost zero, i.e. in the low wavelength region, the envelopes did not fit perfectly the T_{afs} curve. Hence, we performed the fitting procedure using a Boltzmann function with higher power, in this case $n = 4$. The result of a higher power Boltzmann function can be seen in Fig. 3-6, where it can be qualitatively said that the fit of the envelopes are quite good.

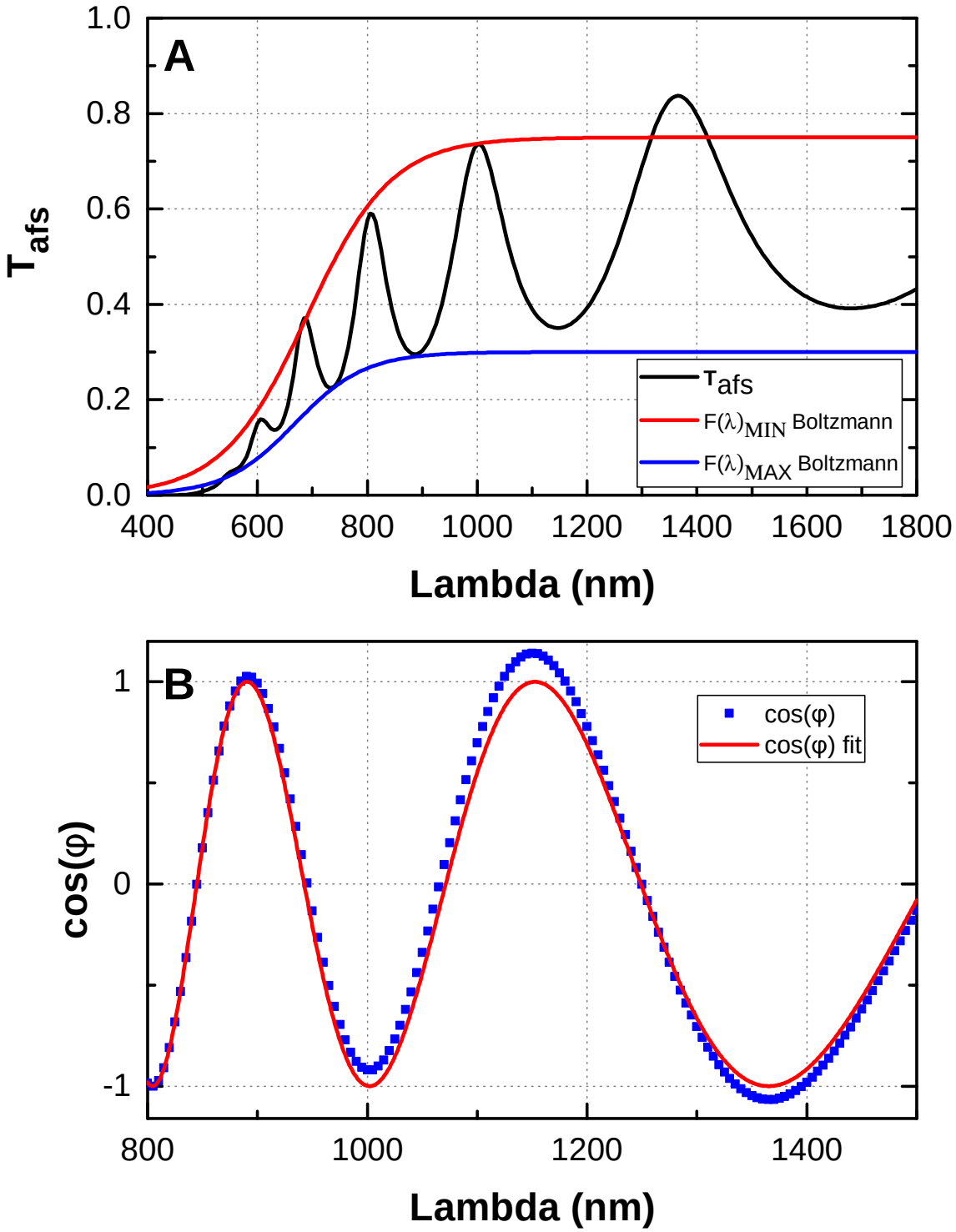

Figure 3-4: (A) The result of T_{afs} envelopes fitting using Boltzmann function (3.50). The upper envelope has the Boltzmann parameters as follows $A = 0.75$, $B = 13$, and $\lambda_0 = 690$ nm. While $A = 0.3$, $B = 15.6$, and $\lambda_0 = 668$ nm are set for the lower envelope. (B) Fitting result of $\cos(\varphi)$ with $n_{fa}d = 1.679$ and $n_{fb}d = 0.103$.

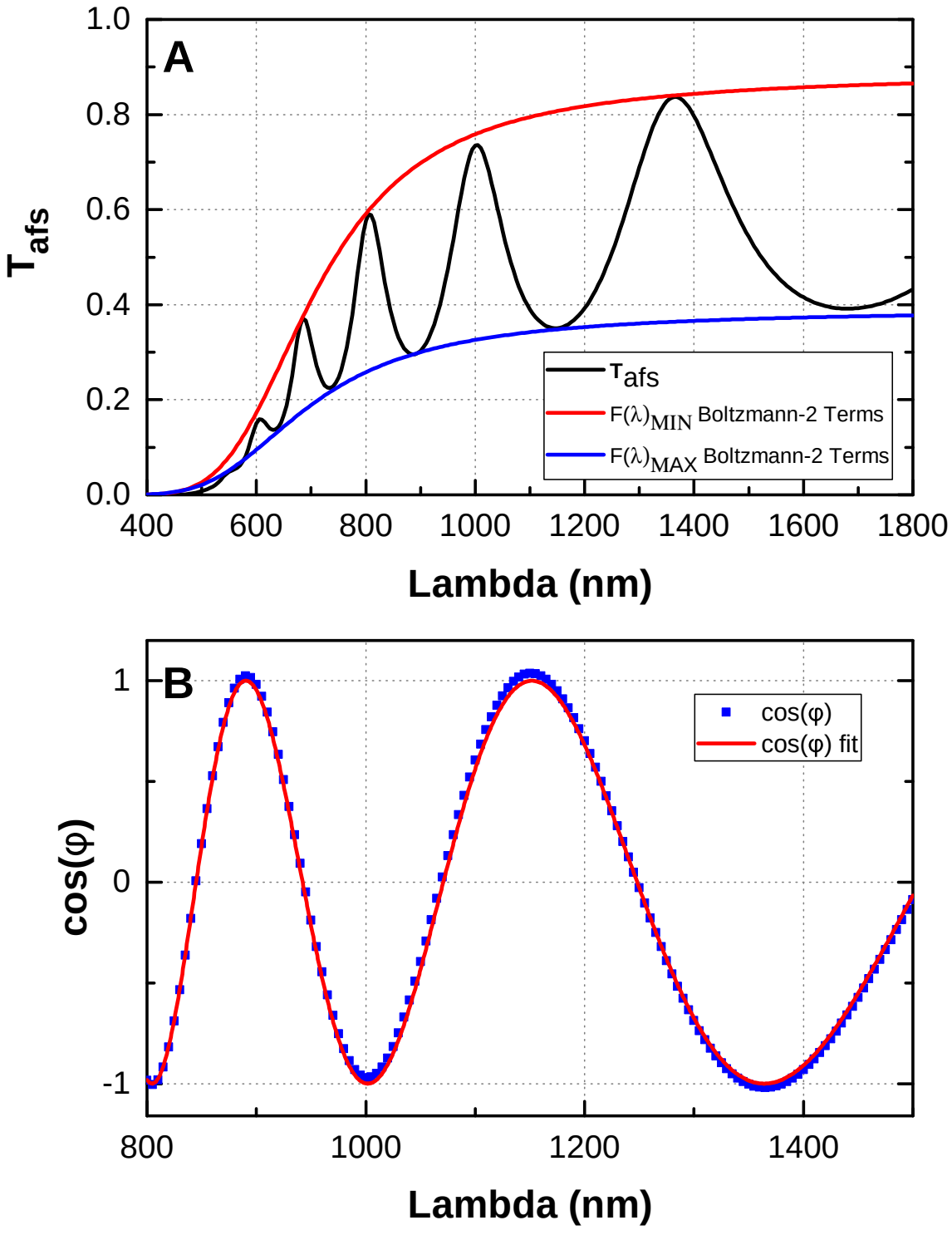

Figure 3-5: (A) The result of T_{afs} envelopes fitting using Boltzmann-2 Terms function (3.51), where $n = 2$. The upper envelope has the Boltzmann parameters as follows: $A = 0.925$, $B = 1.68$, and $\lambda_0 = 725$ nm. While $A = 0.4183$, $B = 1.4$, and $\lambda_0 = 725$ nm are set for the lower envelope. (B) Fitting result of $\cos(\varphi)$ with $n_{fa}d = 1.677$ and $n_{fb}d = 0.104$.

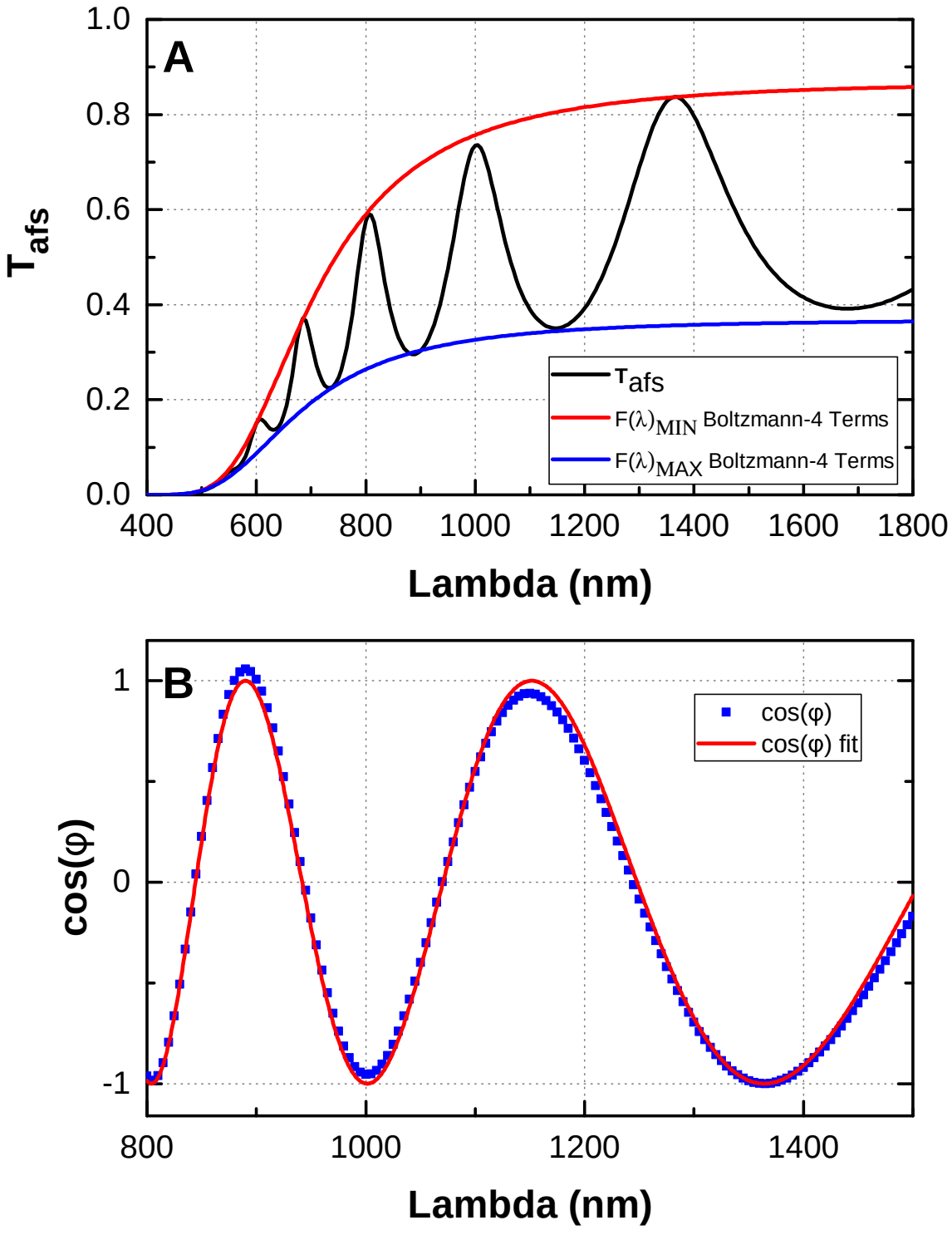

Figure 3-6: (A) The result of T_{afs} envelopes fitting using Boltzmann-4 Terms function (3.51), where $n = 4$. The upper envelope has the Boltzmann parameters as follows: $A = 1.35$, $B = 0.345$, and $\lambda_0 = 875$ nm. While $A = 0.598$, $B = 0.29$, and $\lambda_0 = 885$ nm are set for the lower envelope. (B) Fitting result of $\cos(\varphi)$ with $n_{fa}d = 1.678$ and $n_{fb}d = 0.103$.

But, when we plotted the calculated $\cos(\varphi)$ variations of this fitting procedure, we can remark that the fit was not perfect since the variation of $\cos(\varphi)$ is slightly over passing the maximum value of cos function.

Though the envelopes calculated with a higher power are better following the interference maxima and minima at short wavelengths it can be seen that the deduced $n_{fa}d$ and $n_{fb}d$ values are not very different from one value of the power of $1/\lambda$ ($n = 2$) to the other ($n = 4$). Besides, the adjustment of the power value may be sample dependent. In any case $n = 2$ gives rather satisfactory results and it seems useless to try to get a better fit of the envelopes at short wavelengths.

$\cos(\varphi)$ **fitting through** cosh **function**

Another fitting procedure to fit the upper and lower envelopes of T_{afs} can be proposed based on the Eq. (3.37). This equation can be expressed as follows:

$$T_{afs} = \frac{Ae^{\alpha d}}{1 + B^2 e^{-2\alpha d} + Be^{-\alpha d}\cos(\varphi)} \tag{3.52}$$

where $A = T_{af}T_{fs}$ and $B = \sqrt{R_{af}R_{fs}}$. Now, if we express $B = \exp(-\beta)$, Eq. (3.52) becomes:

$$T_{afs} = \frac{A}{2B}\frac{1}{\frac{e^{\beta+\alpha d}+e^{-\beta-\alpha d}}{2} + \cos(\varphi)} \tag{3.53}$$

Then, we can simplify the above equation to :

$$T_{afs} = \frac{A}{2B}\frac{1}{\cosh(\beta + \alpha d) + \cos(\varphi)} \tag{3.54}$$

Now, we can use an equation close to Eq. (3.54) to fit the upper and lower envelopes of T_{afs} curve. This fitting procedures can be called as $1/\cosh$ function, whose form can be written as in Eq. (3.55).

$$F(\lambda) = \frac{a}{\cosh\left(b \cdot \frac{1}{\lambda^c} - d\right)} \tag{3.55}$$

The result of this fitting procedures using the previously given example is represented in Fig. 3-7. The resulting upper and lower envelopes are quite good, where they reach the maxima and minima of the interferences in the T_{afs} curve. Now, looking at the result of the calculated $\cos(\varphi)$, we can see that the variation in the low wavelength region is over passing the maximum value of cos function. Hence, the envelope fits are not perfect.

To obtain a precise determination of the surface roughness and refractive index, we need to obtain the best fit possible for the T curve. Nevertheless, based on the fitting procedures above, we can see that there is no one best fitting procedure for the transmittance data. Hence, to obtain the best fit result, we have to perform a qualitative assessment for each fitting procedure of T.

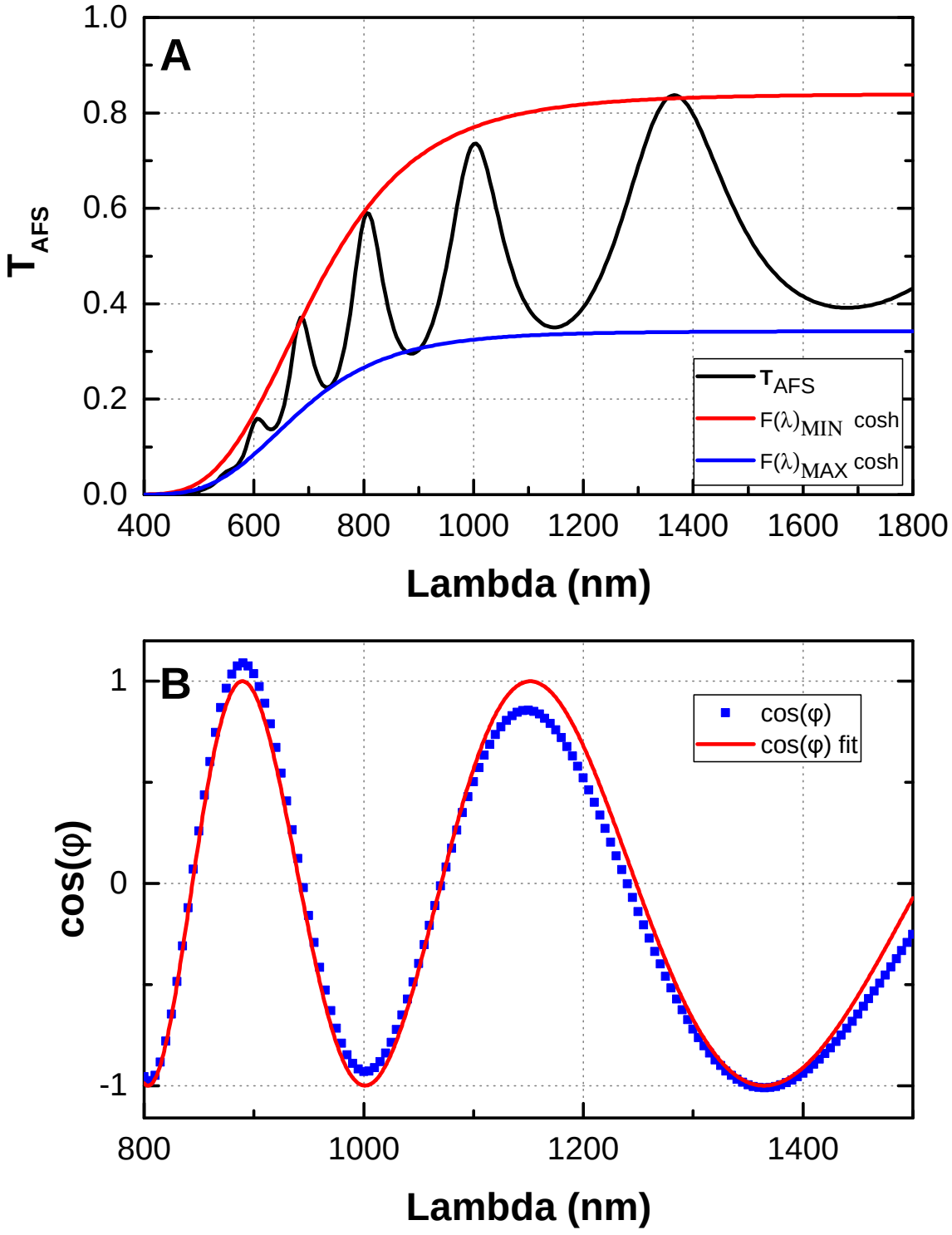

Figure 3-7: (A) The result of T_{afs} envelopes fitting using cosh function. The upper envelope has the cosh function parameters as follows: $a = 0.3425$, $b = 0.339$, $c = 3.56$ and $d = 0.01$. While $a = 0.84$, $b = 0.425$, $c = 3.3$ and $d = 0.001$ are set for the lower envelope. (B) Fitting result of $\cos(\varphi)$ with $n_{fa}d = 1.679$ and $n_{fb}d = 0.101$.

3.2.2 $\cos(\varphi)$ through R

The developments above show that there are several possible manners to extract information on the optical properties of thin films from the treatment of the transmittance data. However, we have seen that this treatment seems to lack of accuracy. That is why in this section we show that the same type of information can be extracted from the reflectance data.

If we consider that $R_{as} + T_{as} = 1$ we can calculate $1/(1 - Rs)$ from Eq. (3.40) to obtain:

$$\frac{1}{1 - R_s} = \frac{1 - R_{sfa}R_{sa}}{T_{sa}(1 - R_{sfa})} \tag{3.56}$$

It can be shown that:

$$\frac{1}{1 - R_s} = a(\lambda) + b(\lambda)\cos(\varphi) \tag{3.57}$$

The variations of $1/(1 - Rs)$ are presented in Fig. 3-8A. Defining envelopes for the maxima and minima does not seem possible using classical functions as for the transmittance. That is why we have used cubic spline curves for this purpose to deduce $a(\lambda)$, $b(\lambda)$ and the $cos(\varphi)$ variations.

$\cos(\varphi)$ fitting through *spline* function

The fitting procedure of $1/(1 - R_s)$ is done using cubic spline as proposed in [54]. These methods differ with the fitting functions that were introduced when fitting through T. In cubic spline fitting, we do not introduce any function to obtain the maxima and minima envelopes of the $1/(1 - R_s)$. Fitting by cubic spline is done by first searching for the minima and maxima points in the $1/(1-R_s)$. Then, from these points we interpolate using cubic spline (according to the given wavelength range) so that we produce the maxima and minima envelopes. This method is very simple as we do not have to search for any coefficients. Only the data points of both envelopes matter. Figure 3-8 represents the result of the $1/(1 - R_s)$ fitting using cubic spline and the corresponding $\cos(\varphi)$ result. From Fig. 3-8, we can see that the cubic spline yields good fits for $1/(1 - R_s)$ curve. As a consequence, we obtained a perfect fit for $\cos(\varphi)$ curve.

A precise fitting of $cos(\varphi)$ is important to determine an accurate surface roughness and refractive index of the thin film sample. Based on the fitting procedures above, the $cos(\varphi)$ fitting through T by variation of T_{afs} and R_{afs}, Boltzmann, and *cosh* function has shown lack of precision due to the difficulty in finding the fitting parameters of each function. On the other hand, the fitting procedures through R by cubic spline yields a more accurate fit toward $cos(\varphi)$ with the advantage that no fitting parameter has to be set. Hence, a choice of the fitting function procedure of transmittance and reflectance data plays an important role in the simplification of the $cos(\varphi)$ fitting.

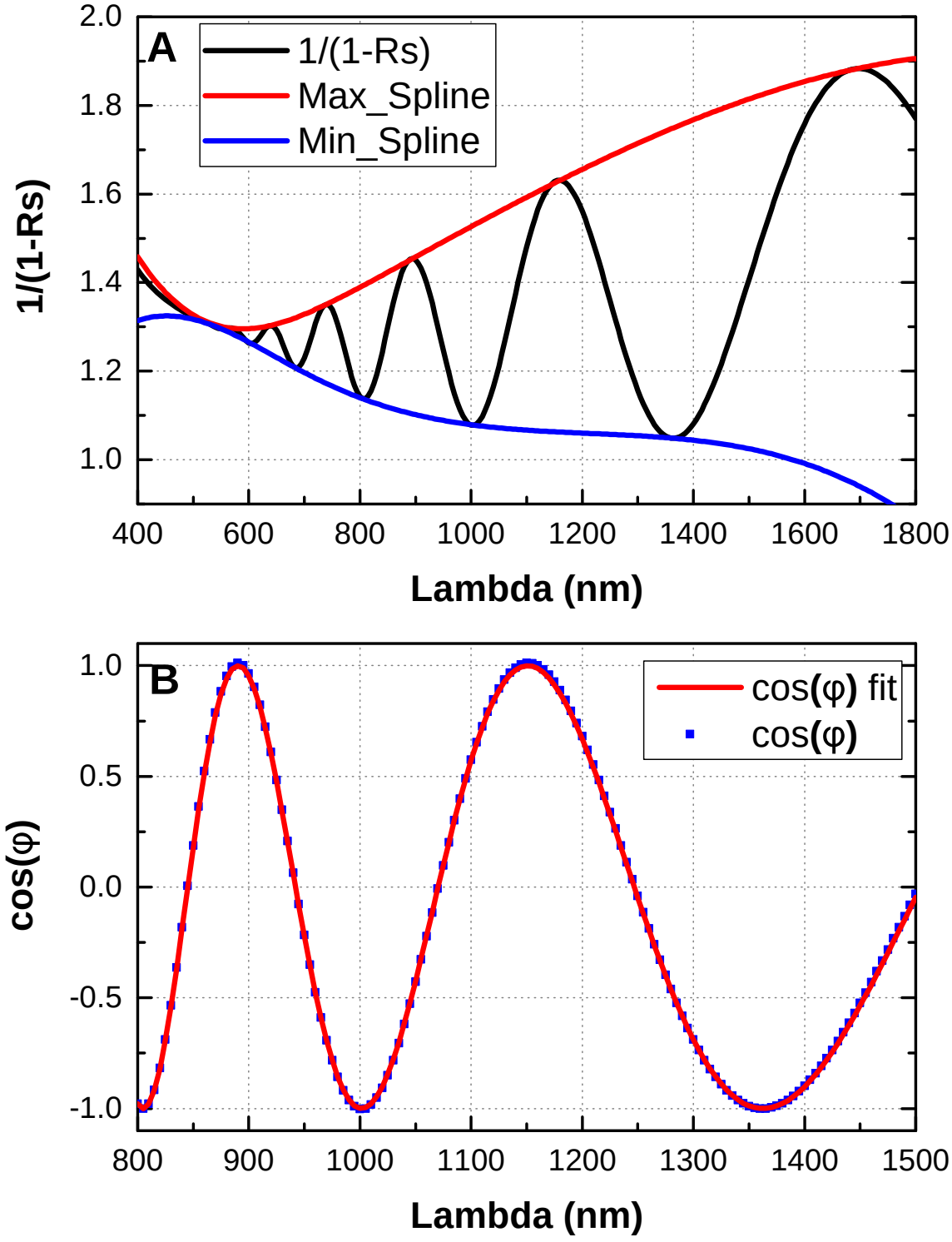

Figure 3-8: (A) The result of $1/(1-R_s)$ envelopes fitting using cubic spline. (B) Fitting result of $\cos(\varphi)$ with $n_{fa}d = 1.673$ and $n_{fb}d = 0.1075$.

3.3 Film thickness, surface roughness, and refractive index determination in high absorption region

In the case of thin film thickness determination, we can first calculate the real part of the thin film refractive index n_f, the information containing this n_f being found in the region of complete absorption where the interference fringes are no longer existing. Note that the Eq. (7) in [51] is wrong and cannot be used to calculate n_f. In the region where the absorption is high we can assume that $R_{sfa} \simeq R_{sf}$ according to (3.36). In addition, k_f as denoted in (3.25) will be small. If we assume that the value of the substrate roughness $\sigma_s \simeq 0$, which is often the case for the thin film material deposited on glass, n_f can be calculated according to Eq. (3.58).

$$n_f = n_s \frac{1 + \sqrt{R_{sfa}}}{1 - \sqrt{R_{sfa}}} \tag{3.58}$$

The resulting n_f calculated using (3.58) can be used to calculate the thin film thickness. This calculation can be performed using the knowledge of $\cos(\varphi)$ obtained through fitting. We can then compare the part of the $\cos(\varphi)$ that contains the information of Herzberger n_f approximation, as in (3.2). The n_f in Eq. (3.58) can be compared to that of Eq. (3.59) for a given λ in the appropriate region, which finally gives us the thin film thickness, d.

$$n_f d = d\left(n_{fa} + \frac{n_{fb}}{\lambda^2 - 0.028}\right) \tag{3.59}$$

the values of n_{fa} and n_{fb} being obtained from the fit of $\cos(\varphi)$.

Next, The determination of the thin film surface roughness, σ_a can be obtained through Eq. (3.60),assuming that $R_f \sim R_{fa}$ in the region of interest:

$$\sigma_a = \frac{\lambda}{4\pi n_a} \sqrt{\ln\left[\left(\frac{n_f - n_a}{n_f + n_a}\right)^2 \frac{1}{R_f}\right]} \tag{3.60}$$

where the parameter n_f is a constant value in the high absorption region (~ 400 nm) that can be chosen from n_f calculation using Eq. (3.58).

The variations of the surface roughness and refractive index for different fitting procedures using T and R data are presented in Tab. 3.1. The fitting procedures using T and R have a good agreement for the surface roughness and refractive index values, whereas a $\sim 3\%$ variation is found for the thickness value.

We can see that despite the lack of precision during the $\cos(\varphi)$ fitting through T using variation of $T_{afs}/(1 - R_{afs})$, Boltzmann, and *cosh* function, we still obtain a good agreement of σ_a and n_f. On the other hand, the value of the thickness has a slight variation of 3%. Hence, we can conclude that the determination of σ_a, n_f, and

Table 3.1: Result of the σ_a, n_f, and thickness of thin film material calculated from $cos(\varphi)$ fitting through T and R using several fitting functions.

	Fitting Function	σ_a	n_f	Thickness
	$T_{afs}/(1-R_{afs})$	30.023	4.949	0.488
	Boltzmann	30.023	4.949	0.496
T	Boltzmann-2 Terms	30.023	4.949	0.494
	Boltzmann-4 Terms	30.023	4.949	0.497
	1/cosh	30.023	4.949	0.494
R	cubic spline	30.023	4.949	0.503

thickness of thin film material on a non absorbing substrate can be obtain through the cos(φ) fitting using either the transmittance or reflectance data. In addition, in the following section, we observe that we need the transmittance and reflectance data in order to obtain the absorption coefficient of the thin film material. This means that the determination of σ_a, n_f, and thickness parameter either from transmittance or reflectance data has an equal advantage.

3.4 Determination of the Absorption Coefficient of a Thin Film on a Thick Substrate

The absorption coefficient can be deduced starting from Eq. (3.49). We can rewrite (3.49) into a second degree equation as denoted in (3.61).

$$-e^{2\alpha d} + \frac{(1 - R_{afs}T_{af}T_{fs})}{1 - R_{af}T_{afs}}e^{\alpha d} + R_{fs} = 0 \tag{3.61}$$

where R_{af}, R_{fs}, T_{af}, and T_{fs} are calculated using $k_f = 0$. The value of k_f is assumed to be 0 because at the low wavelength i.e: 400 nm (where $k_f = \frac{\lambda\alpha}{4\pi}$ and $\alpha(400\ nm) \simeq 3 \times 10^5$), k_f is $\simeq 0.003$. The value of k_f^2 when used in Eqs. (3.24) to (3.30) is then very negligible to the values of other parameters such as $(n_s - n_f)^2$. The Eq. (3.61) can be expressed in the form of $c + bx + ax^2 = 0$ with $x = e^{\alpha d}$. By calculating the discriminant, δ, we can find the unique positive solution of this second degree equation by:

$$X = \frac{-b - \sqrt{\delta}}{2a} \tag{3.62}$$

Hence, the absorption coefficient, $\alpha(\lambda)$ can be obtained as follows:

$$\alpha(\lambda) = \frac{1}{d}\ln\left(\frac{-b - \sqrt{\delta}}{2a}\right) \tag{3.63}$$

We can now calculate the absorption coefficient of the example of the thin film

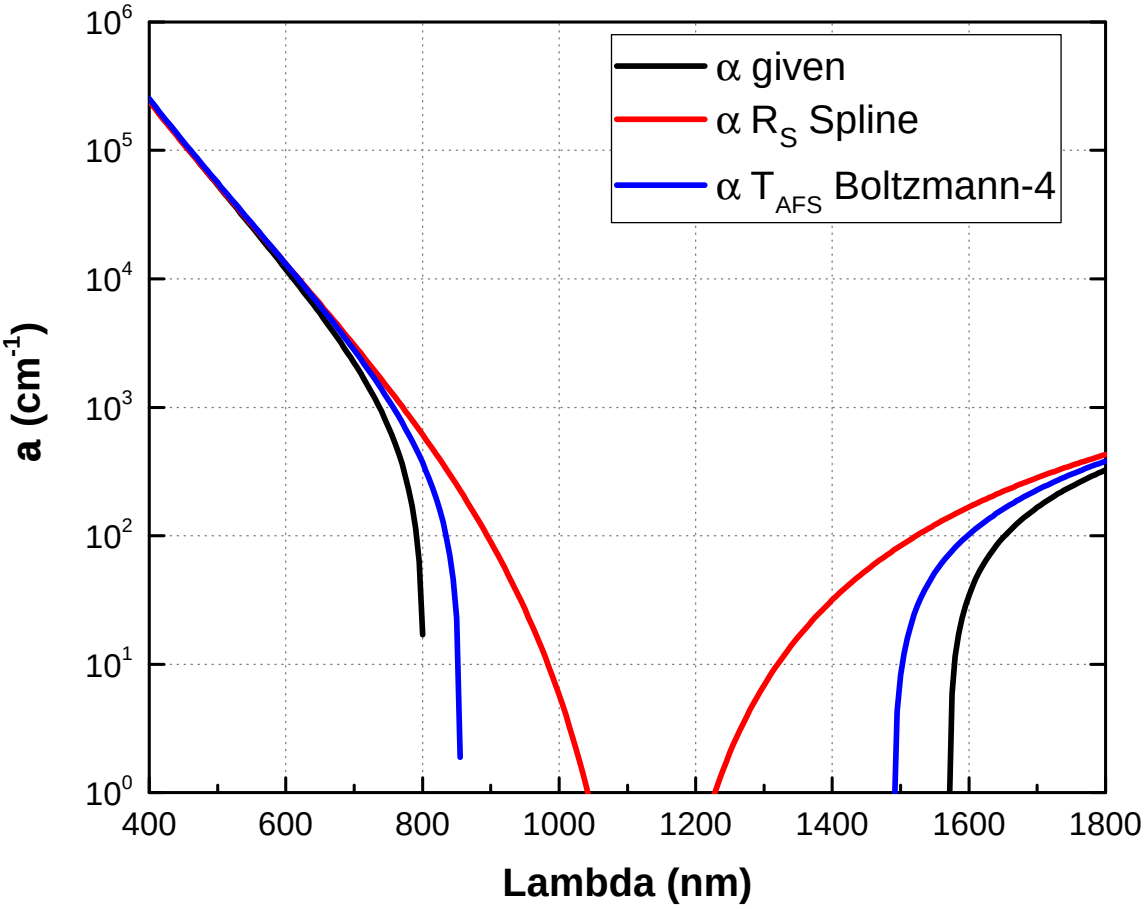

Figure 3-9: The result of absorption coefficient, $\alpha(\lambda)$. The black curve represents the given absorption coefficient.

semiconductor material with the equation above. The result of this absorption coefficient calculation is then compared to the given values of the absorption coefficient of $\alpha(E) = 15000 * (E - 1.1)^4$. Since there is only a slight variation of n_a and n_b values for each fitting procedure, we obtained the same rounded values for the sample thickness. Since these parameters are the only parameters that will distinguish the resulting procedure of the absorption coefficient for each fitting procedure, we obtain the same variation of wavelength dependent absorption coefficient for all the proposed fitting procedures. In Fig. 3-9, we can see that there is a good agreement between the given and the calculated value of absorption coefficient in the low wavelength region.

In order to validate the calculation of the absorption coefficient using Eq. (3.61), we will further compare this result with the result of the absorption coefficient calculated by Ritter-Weiser [38]. If we look back at the Eq. (3.61) and its simplified form i.e. $c + bx + ax^2 = 0$, we have $a = -1$, $b = \frac{(1-R_{afs})T_{af}T_{fs}}{(1-R_{af})T_{afs}}$, and $c = R_{fs}$. In the case when the thin film material surface roughness is zero, we obtain :

$$T_{af}T_{fs} = (1 - R_{af})(1 - R_{fs})\left(1 + \frac{k_f^2}{n_f^2}\right) \tag{3.64}$$

Now, if we reconsider the unique solution for the absorption coefficient as denoted in (3.63), and considering the absorptance, A as:

$$A = 1 - R_{afs} - T_{afs} \tag{3.65}$$

we finally obtain :

$$\alpha(\lambda)d = \ln\left(0.5\left[\left(1 - R_{fs})(1 + \frac{A}{T_{afs}}\right) + \left[(1 - R_{fs})^2\left(1 + \frac{A}{T_{afs}}\right)^2 + 4R_{fs}\right]^{0.5}\right]\right) \tag{3.66}$$

which corresponds to the absorption coefficient determination as proposed by Ritter Weiser [38] in the high absorption region.

3.5 Example of optical parameters determination on a-Si:H thin films

In this section R/T measurements were performed on three a-Si:H thin films using the FTIR spectrometer. The thin films were deposited on glass using radio frequency plasma-enhanced chemical vapor deposition (RF-PECVD). The deposition temperature was set at $175°C$, with a silane flow of 20 sccm and a deposition pressure of 120 mTorr. The distance between the electrodes was set at 17 mm with the RF power of 17 mW/cm^2. With these deposition parameters, the deposition rate was of the order of 0.7Å/s. The deposition times of sample 1604211, 1604212, and 1604213 were 1h30, 1h, and 30 minutes, respectively.

The results of the R/T measurements are presented in Fig. 3-10. These measurements show the classical a-Si:H thin film R/T results. As can be seen from the R/T results, sample 1604211 produces more interference fringes than the other two samples, whereas the least number of interferences fringes is found for sample 1604213. In the most common mode of usage, the interferences fringes pattern in the R/T measurement results combined with the refractive index of the sample can be used to identify the thickness of the sample [55]. Interference fringes in the R/T measurement can be seen as the results of constructive interferences between the light reflected from front and back surfaces of a thin film. A thick film will therefore exhibits more interference fringes than a thin one. Hence, comparing the number of interference fringes of each sample, we can deduce that the sample 1604211 is the thickest one whereas the sample 1604213 is the thinnest.

The values of the transmittance and reflectance of these films at 450 nm are presented in Tab. 3.2. From the table, the sample 1604213 yields the highest transmittance and the lowest reflectance (film side) at 450 nm, compare to the other samples. Meanwhile, all of these samples yield similar absorptance at 450 nm.

In order to determine the optical parameters of the thin films, an optical modeling, as explained in the previous sections, was applied to these samples. The results of the reflectance from the film side are used to fit the $\cos(\varphi)$ to determine the samples

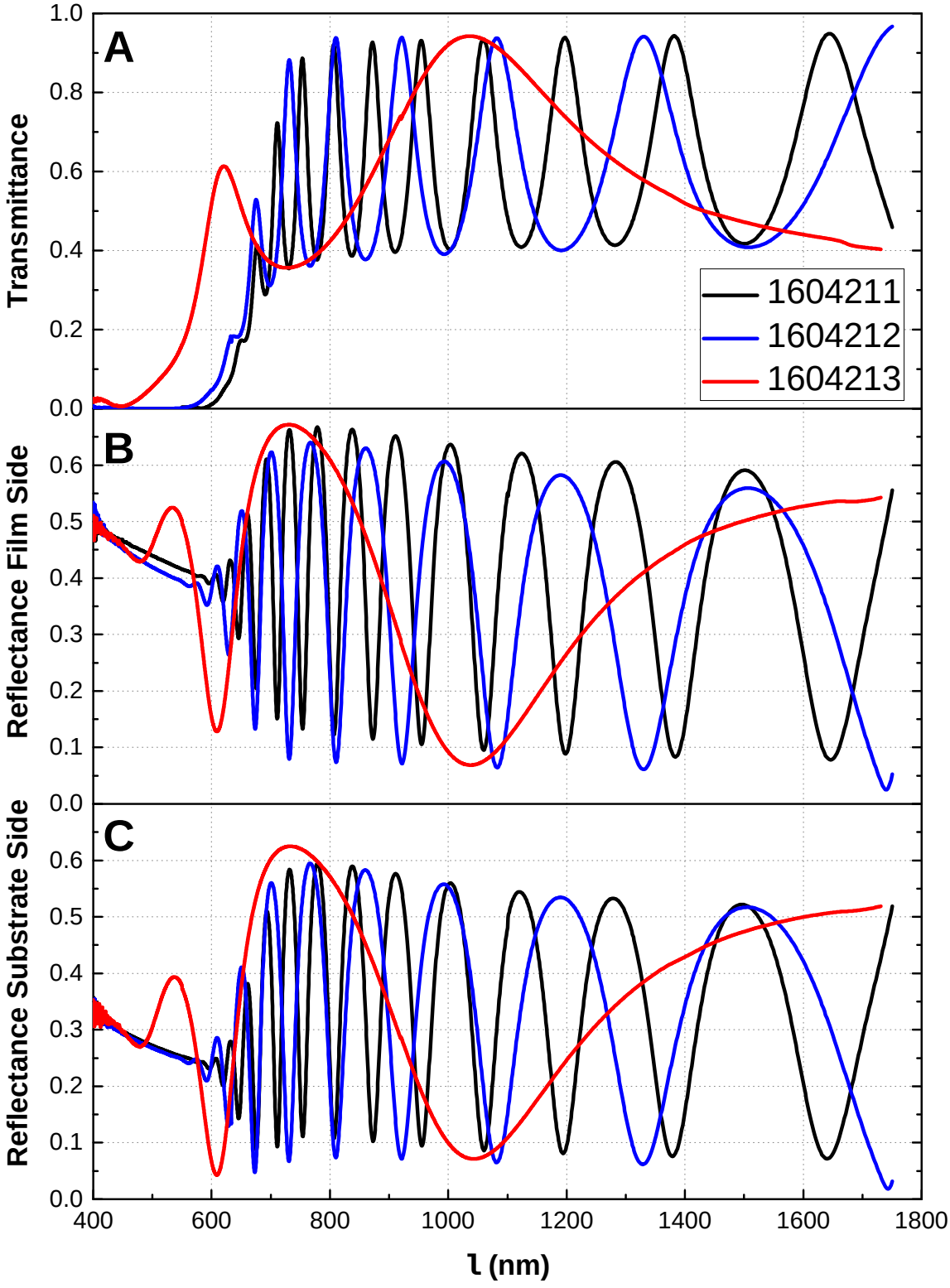

Figure 3-10: The measurement results of (A) transmittance, (B) reflectance from film side, and (C) reflectance from substrate side of three of a-Si:H samples

Table 3.2: The values of transmittance and reflectance from the film side, R_F and the substrate side, R_S of the a-Si:H films at 450 nm. Four decimal numbers are used to distinguish the values of R, T, and A of the samples.

Sample names	T	R_F	R_S	A
1604211	6.540×10^{-4}	0.4663	0.2966	0.5330
1604212	9.463×10^{-4}	0.4536	0.2925	0.5454
1604213	0.006	0.4562	0.2972	0.5376

refractive indices. The fitting of $\cos(\varphi)$ is done using the cubic spline method, as previously explained to be the simplest yet reliable fitting method. The wavelength range of $\cos(\varphi)$ is chosen between 600-1500 nm, where the interference fringes exist. The results of the $\cos(\varphi)$ fitting of the films are presented in Fig. 3-11. The $\cos(\varphi)$ fitting of sample 1604211 as shown in Fig. 3-11A shows that the fit curve does not correspond well to the actual $\cos(\varphi)$ curve below 650 nm as the amplitude of the interference fringes in this region is not stable yet. Nevertheless, above 650 nm, the fit curve provides a quite good agreement with the $\cos(\varphi)$ curve despite that the fit curve phase is slightly leading at 1000-1300 nm and has lower peaks at 800-1000 nm. For sample 1604212, the cubic spline fit curve provided a quite good $\cos(\varphi)$ fitting over the given wavelength range, as represented in Fig. 3-11B. The last sample, 1604213, has the least interference fringes number thus the $\cos(\varphi)$ fit at 600-1800 nm does not fit very well. On the other hand, when we analyze the fitting over all the wavelength range 400-1700 nm, the cubic spline curve provides a good fit in the region where the interference fringes occur, 500-1000 nm. Therefore, the $\cos(\varphi)$ fitting as shown in Fig. 3-11C may be still valid.

Table 3.3: Result of the n_f, thickness, and σ_a of a-Si:H thin films calculated from $cos(\varphi)$ fitting through T and R using cubic spline fitting functions.

Sample names	n_f @ 450 nm	thickness (μm) @ 450 nm	σ_a (nm) @ 450 nm
1604211	4.904	0.747	N/A
1604212	4.847	0.458	N/A
1604213	4.911	0.151	N/A

From the $\cos(\varphi)$ fitting, the optical parameters such as n_f, thickness, and surface roughness, σ_a of these samples can be determined. The values of these optical parameters at 450 nm are summarized in Tab. 3.3, where the values as a function of wavelength are presented in Fig. 3-12A and B, respectively for n_f and thickness values. From the results in Tab. 3.3, the n_f of all the three samples are similar at 450 nm. The sample 1604211 is found to be the thickest one and 1604213 is the thinnest one as expected from the number of interference fringes, as previously discussed. The σ_a of all the sample are impossible to calculate, the sample being too smooth, as

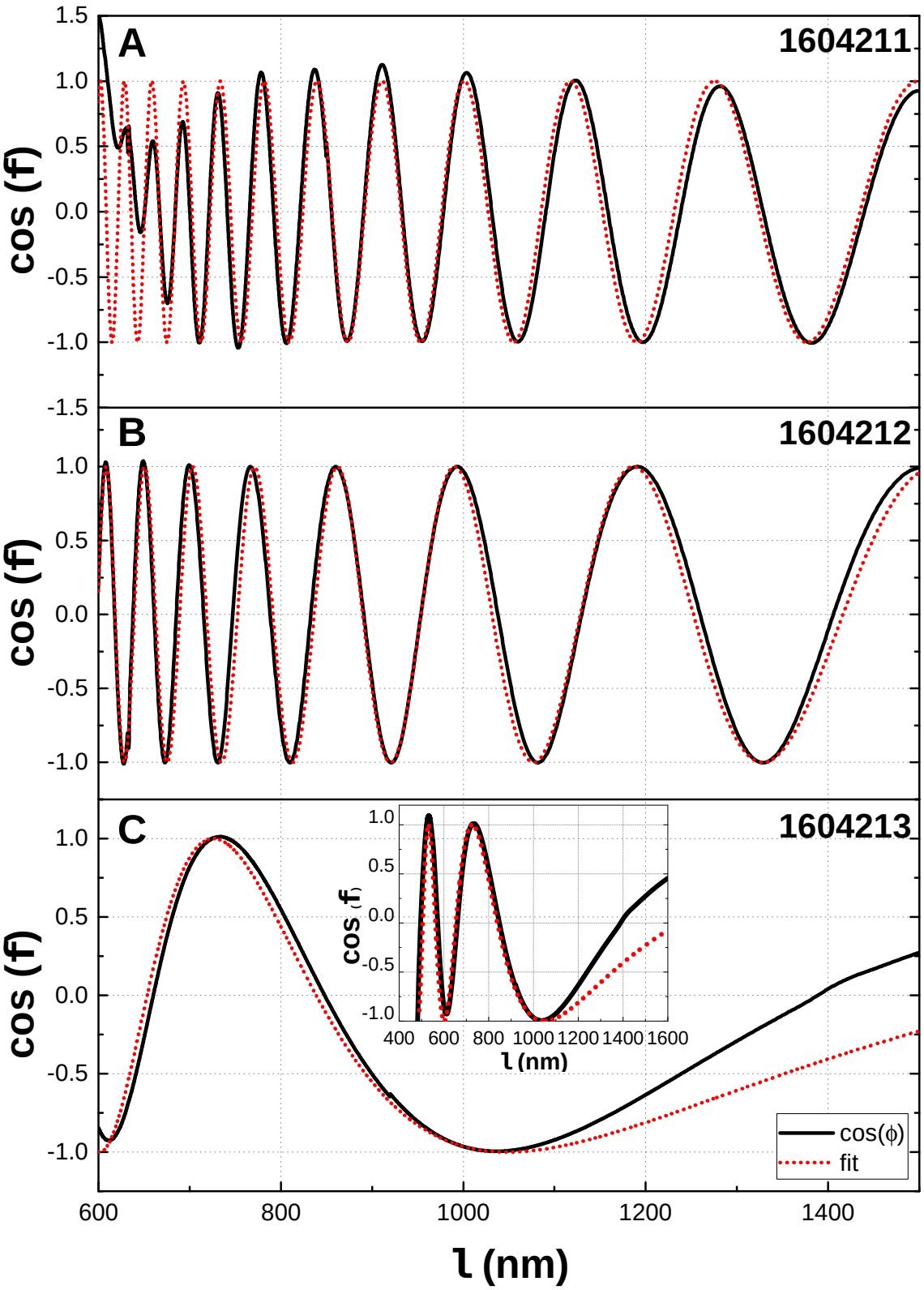

Figure 3-11: The results of cos(φ) fitting using cubic spline, calculated from R/T measurements of a-Si:H samples: (A) 1604211, (B) 1604212, and (C) 1604213.

expected for a-Si:H.

The R/T measurement results can be finally used to determine the optical absorption coefficient α_{optics} using Eq. 3.66. The calculated α_{optics} as function of wavelength are presented in Fig. 3-12C. From these plots, we obtain a typical α_{optics} of "standard" a-Si:H samples, where the absorption at 400 nm is of the order of 10^5. At 400 nm, α_{optics} of these samples are found at 7.798×10^4, 11.755×10^4, and 19.359×10^4 cm^{-1}, respectively for 1604211, 1604212, and 1604213. The highest α_{optics} is found for the thinnest sample, whereas the lowest absorption is obtained for the thickest one. It can be seen that the α_{optics} determination is accurate only in the range 400-650 nm. For higher wavelengths the dynamic of the measurement is too low to provide reliable results. These α_{optics} values will be used to calibrate the α_{FTPS} deduced from FTPS measurements.

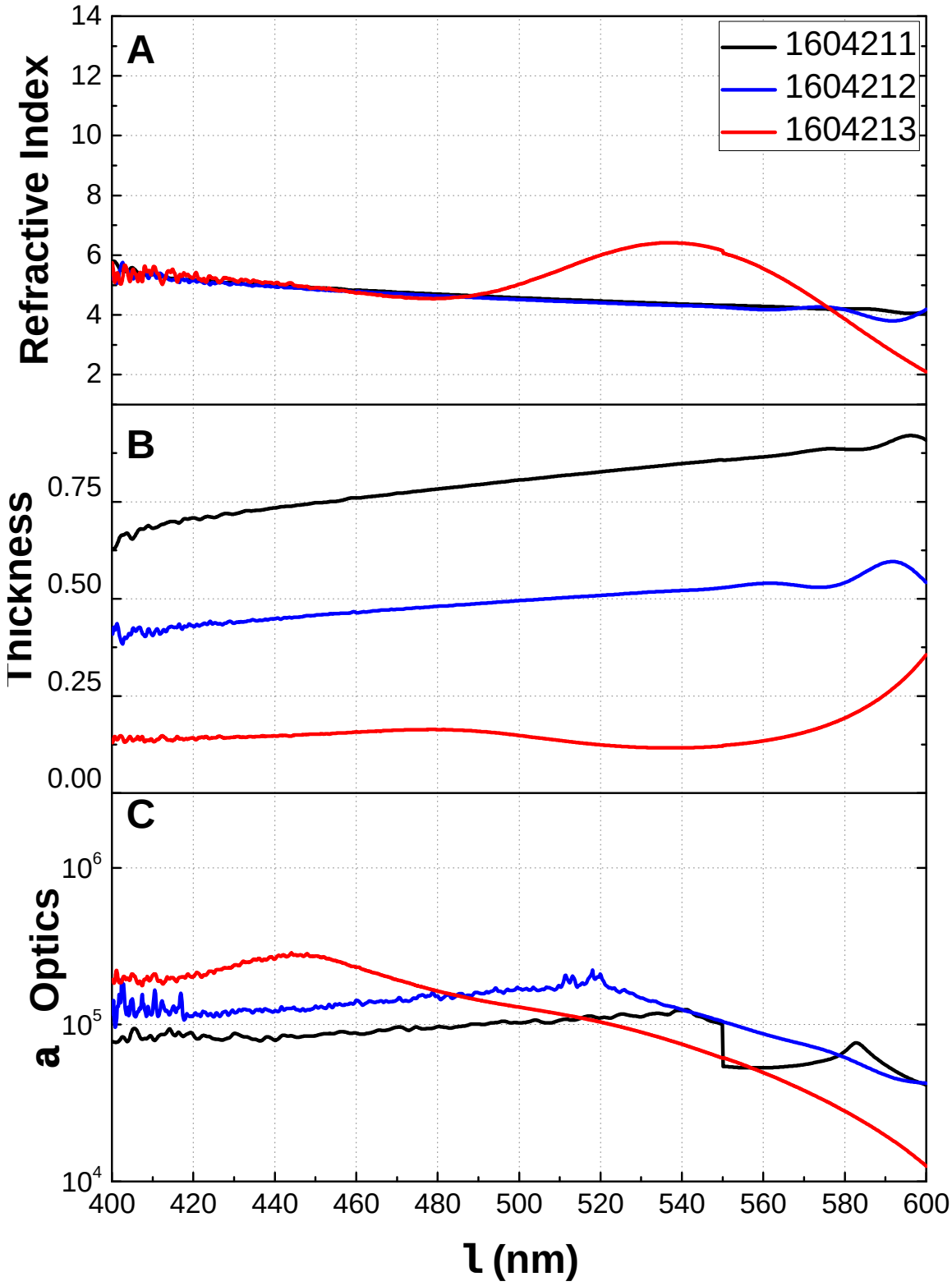

Figure 3-12: The calculated values of : (A) refractive index, (B) thickness, and (C) surface roughness, of a-Si:H samples from R/T measurements.

Chapter 4

Extraction and Sensitivity Analysis of Density of States Parameters from Absorption Coefficient

The determination of the density of states (DOS) parameters of thin film semiconductor materials from absorption coefficient is of great interest especially to estimate the defect density in the sub band gap region. The determination of the density of states parameters is calculated using a standard defect model or an improved defect pool model as proposed by Powell and Deane in 1993 [56]. We used these models to reconstruct the absorption coefficient spectrum that was obtained through the FTPS measurement. This particular topic is discussed in Sec. 4.1.

Due to the difficulties and the large number of the density of states parameters, we propose an extraction of these parameters using teaching learning based optimization (TLBO) algorithm as proposed by Patel *et al.* for the extraction of solar cell parameters from a single current–voltage characteristic [57]. The TLBO is implemented by developing a numerical simulation using MATLAB as a programming tool. The effectiveness of the algorithm has been validated by applying it to a theoretically calculated absorption coefficient spectrum as it could be obtained by FTPS measurements on a hydrogenated amorphous silicon (a-Si:H) thin film. It is observed that the TLBO algorithm has repeatedly converged to give consistent values of DOS parameters of the material with minimal control variables of the algorithm. The description of the TLBO algorithm for the extraction of the DOS parameters from the absorption coefficient spectrum is further discussed in Sec. 4.2.

As the number of parameters for DOS reconstruction is quite large, we analyzed the sensitivity of the absorption coefficient spectrum on the DOS parameters. The sensitivity analysis of these parameters will be beneficial to see to which DOS parameters the absorption coefficient spectrum is the most sensitive and how a small deviation of their values would bring a significant error towards the fitting of the absorption coefficient. This study is discussed in detailed manner in Sec. 4.3.

4.1 Determination of the DOS parameters from the absorption coefficient

The spectral dependence of a semiconductor material that is represented in the form of a light absorption spectrum or photocurrent can actually project the band structure of the electron configuration of the material. The defects and disorder are represented as electronic states in the material and are characterized by their density. The correlation between the absorption coefficient spectrum and the density of states in a semiconductor material can be denoted as in Equation (4.1):

$$\alpha(h\nu) = \frac{1}{h\nu} \int_{-\infty}^{+\infty} \sum_{i=1}^{m} Copt_i \; N_i(E) f_i(E) \sum_{j=1}^{m} Copt_j \; N_j(E+h\nu)[1-f_j(E+h\nu)]dE \quad (4.1)$$

assuming that there are m different type of states. $Copt_i$ is the optical matrix element. $f_i(E)$ is the occupation function of states i at the energy E. Index i is associated to the functions of the initial states, and j to the final states.

An example of the electronic transitions in the density of states of a thin film semiconductor is presented in Fig. 4-1B. The electronic transitions which contribute to the photocurrent measured through the FTPS technique are the electron transitions reaching the extended states of the conduction band and the transitions leaving holes in the extended states of the valence band. These possible transitions are presented as A, B_1, B_3, C_1 and C_2, whereas the remaining transitions (e.g. B_2) cannot be measured using the FTPS method. Another possible measurement which include the spectroscopy of these transitions is the Photothermal Deflection Spectroscopy (PDS) [20]. Note that FTPS measures the current due to the majority carriers. In the case of a-Si:H, the majority carriers will be electrons. However, in the following we shall present all the possible transitions, including those creating holes, to give a general expression for the absorption coefficient, α.

From Fig. 4-1A, the band to band electron transition, A, represents the absorption spectrum in the high energy region. When the photon energy is lower than the mobility band gap of the thin film semiconductor and a photocurrent is measured, it means that there are possible electron transitions from or towards the localized defect states creating electron in the extended states of conduction band, or leaving holes in the extended states of the valence band. Electron transitions from the valence band tail states toward the extended states of conduction, B_1, create electrons in the conduction band side. The electron transitions leaving the extended states of the valence band to generate electrons in the conduction band tail, B_3, create holes in the valence band side. Both of these transitions project the Urbach slope of the band tail states.

The low energy photons that enable electron transitions from the extended states of valence band toward the localized deep defect states, C_1, will leave holes in the extended states of the valence band, generating a photocurrent. Whereas the low energy photon leading to electron transitions from the localized states toward the extended states of the conduction band, generating photocurrent due to the creation

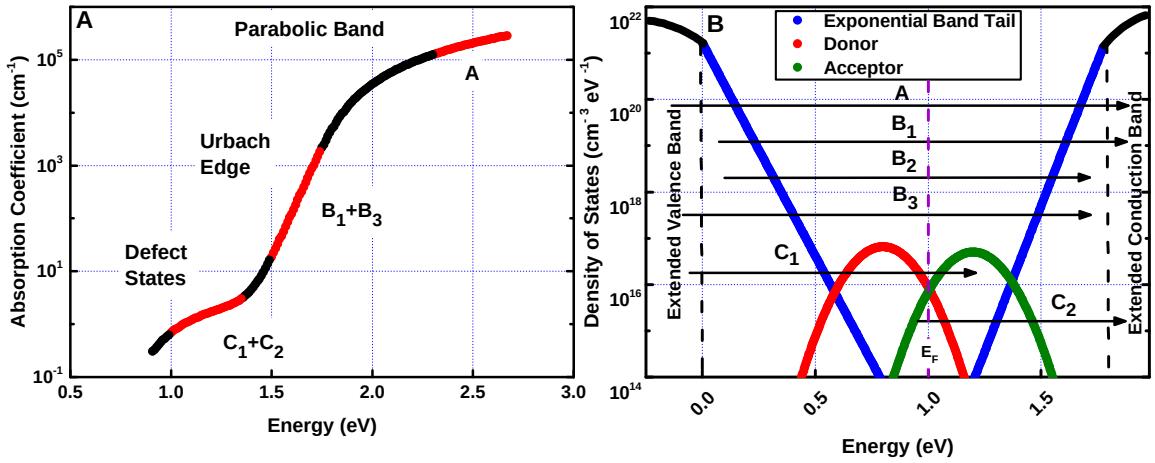

Figure 4-1: (A) Optical absorption coefficient (ex. Hydrogenated amorphous silicon (a-Si:H) sample) with indicated regions attributed to different electron transitions. (B) Band structure of the density of electronic states of a-Si:H.

of electrons in the conduction band is represented by transition C_2. These particular transitions, C_1 and C_2, result in the absorption spectrum in the low energy region.

In our numerical simulation, we use two types of density of states models. The first model corresponds to a standard density of states and the second model uses improved defect-pool as described in [56]. Based on these two models, the absorption coefficient is calculated using Eq. (4.1). The description of the model and the absorption calculation using the standard density of states and the defect-pool model are discussed in Subsections 4.1.1 and 4.1.2, respectively.

The numerical simulation to perform the calculation of the absorption coefficient from the density of states model of the thin film material is done using DeOSt [58]. DeOSt calculates the absorption coefficient of the sample at 300 K for all the possible optical transitions between full and empty states. The photon energy is varied between 0.6 eV to a value slightly higher than the band gap energy. In this simulation, samples are supposed to be under dark condition, and, thus, the occupation functions are those under dark equilibrium. In DeOSt, the densities of states can be represented using a standard model or a defect-pool model.

4.1.1 Standard density of states model and the calculation of the absorption coefficient

The standard density of states is modeled using parabolic distribution functions for the extended states bands and exponential distribution functions for the band tails. The deep defect states are represented in the form of Gaussian distribution functions. In this model we use one Gaussian distribution function acting as a donor and one Gaussian distribution acting as an acceptor. The representation of this standard model is depicted in Fig. 4-2.

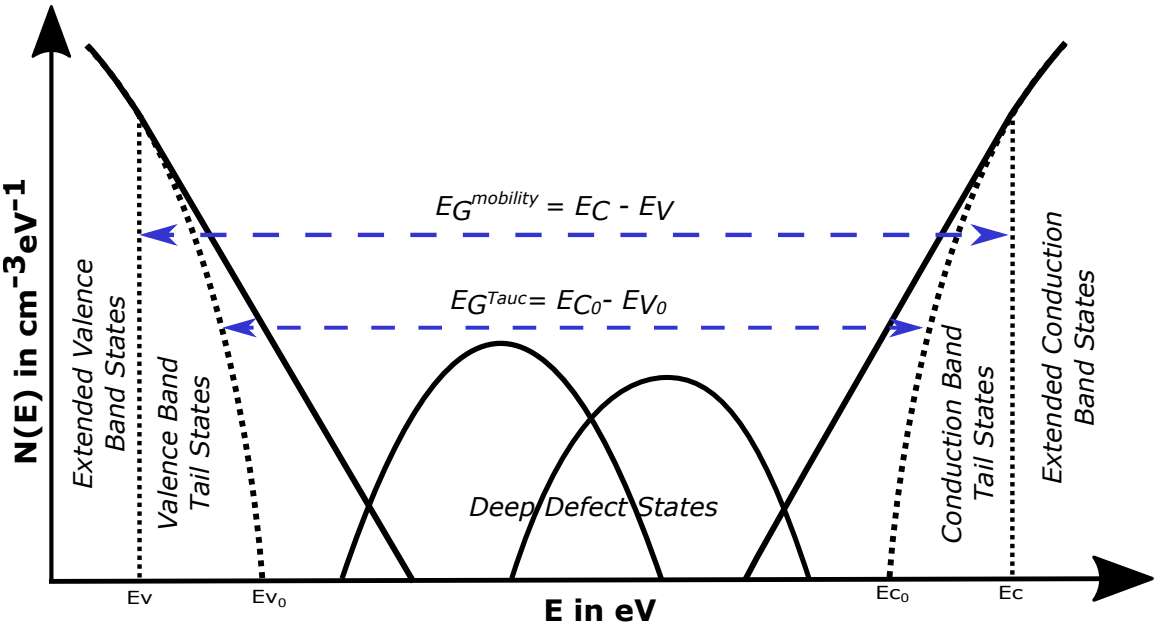

Figure 4-2: Standard density of states model. Valence and conduction band tails are represented by exponential distributions, and the extension of these bands continues with parabolic functions. Deep defect distributions are represented in form of Gaussian functions, where donor and acceptor distributions are placed toward the valence and conduction band, respectively. E_V and E_C represents the mobility threshold as defined by Davis and Mott [59]. The energy difference between these two values is referred as the mobility bandgap, $E_G = E_C - E_V$. E_{V0} and E_{C0} are the extrema of the parabolic function of the extended states of the valence and conduction band distributions, respectively. The difference between E_{C0} and E_{V0} corresponds to the optical band gap as defined by Tauc [60].

Extended band states - Standard DOS

The extended states of valence and conduction band states, below E_V and above E_C, are represented in form of parabolic distribution functions, as proposed by Tauc [60]. These distributions are denoted in Eq. (4.2).

$$N_V^{par}(E) = N_{EV}\sqrt{E_{V0} - E}, \qquad \text{where } E \leq E_{V0} \tag{4.2a}$$

$$N_C^{par}(E) = N_{EC}\sqrt{E - E_{C0}}, \qquad \text{where } E \geq E_{C0}\ , \tag{4.2b}$$

where for a-Si:H we have taken:

$$N_{EV} = N_{EC} = 6.7 \times 10^{21} cm^{-3} eV^{-3/2} \tag{4.3}$$

Band tail states - Standard DOS

The valence and conduction band tail state distributions are represented with exponential functions using Eq. (4.4). See Fig. 4-3 for the illustration of the band tail

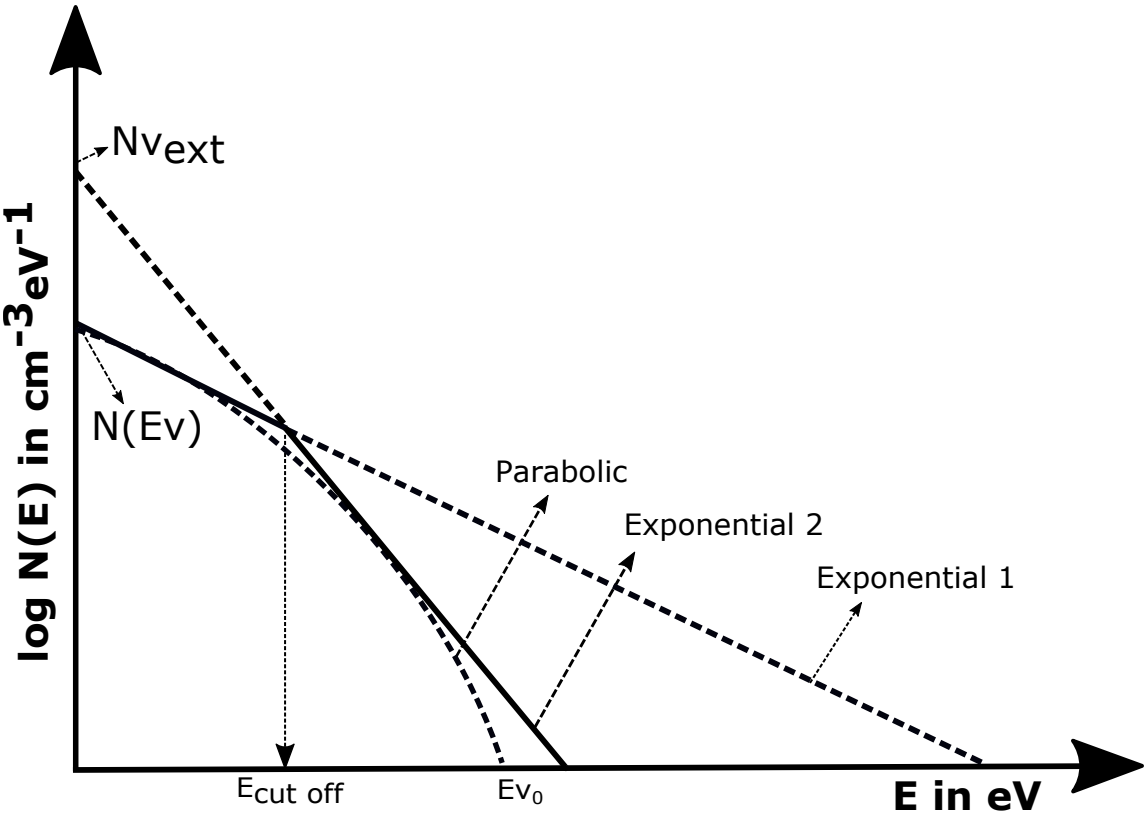

Figure 4-3: Definition of the extended states and tail states at the valence band side. Two exponential functions are used to describe the valence band tail whereas a parabolic distribution of states describes the extended states. The point where an exponential band tail joins the parabolic extended states is noted as $N(E_V)$. E_{cutoff} is the energy where the two exponential distributions join. The same type of state distributions can be defined for the conduction band side.

state distributions.

$$N_V^{exp}(E) = N_V^{exp} \exp\left(-\frac{E - E_V}{kT_V}\right), \qquad \text{for } E \geq E_V \tag{4.4a}$$

$$N_C^{exp}(E) = N_C^{exp} \exp\left(-\frac{E_C - E}{kT_C}\right), \qquad \text{for } E \leq E_C \tag{4.4b}$$

At the energies (E_V and E_C) where the parabolic extended states distributions join the exponential distributions of the tail states we assume that:

$$N_V^{exp}(E_V) = N_V^{par}(E_V) \tag{4.5a}$$

$$N_C^{exp}(E_C) = N_C^{par}(E_C) \tag{4.5b}$$

and

$$\frac{\partial N_V^{exp}(E)}{\partial E}\Big|_{E=E_V} = \frac{\partial N_V^{par}(E)}{\partial E}\Big|_{E=E_V} \tag{4.6a}$$

$$\frac{\partial N_C^{exp}(E)}{\partial E}\Big|_{E=E_C} = \frac{\partial N_C^{par}(E)}{\partial E}\Big|_{E=E_C} \tag{4.6b}$$

for continuity reasons. Just above or below these energies, we can write Eq. (4.4) as:

$$N_V^{exp}(E) = N(E_V)\exp\left(-\frac{E-E_V}{kT_V}\right), \qquad \text{for } E \geq E_V \tag{4.7a}$$

$$N_C^{exp}(E) = N(E_C)\exp\left(-\frac{E_C-E}{kT_C}\right), \qquad \text{for } E \leq E_C \tag{4.7b}$$

From Eq. (4.5) we shall have:

$$N(E_V) = N_{EV}\sqrt{E_{V0}-E_V} \tag{4.8a}$$

$$N(E_C) = N_{EC}\sqrt{E_C-E_C0} \tag{4.8b}$$

From Eq. (4.6) we obtain:

$$\frac{\partial N_{EV}^{par}(E)}{\partial E}\Big|_{E=E_V} = \frac{\partial\left(N_{EV}\sqrt{E_{V0}-E}\right)}{\partial E}\Big|_{E=E_V} = -\frac{1}{2}\frac{N_{EV}}{\sqrt{E_{V0}-E_V}} \tag{4.9a}$$

$$\frac{\partial N_{EC}^{par}(E)}{\partial E}\Big|_{E=E_C} = \frac{\partial\left(N_{EC}\sqrt{E-E_{C0}}\right)}{\partial E}\Big|_{E=E_C} = \frac{1}{2}\frac{N_{EC}}{\sqrt{E_C-E_{C0}}}\,, \tag{4.9b}$$

for the parabolic bands, and :

$$\frac{\partial N_{EV}^{exp}(E)}{\partial E}\Big|_{E=E_V} = \frac{\partial\left(N(E_V)\exp\left(-\frac{E-E_V}{kT_V}\right)\right)}{\partial E}\Big|_{E=E_V} = -\frac{N(E_V)}{kT_V} \tag{4.10a}$$

$$\frac{\partial N_{EC}^{exp}(E)}{\partial E}\Big|_{E=E_C} = \frac{\partial\left(N(E_C)\exp\left(-\frac{E_C-E}{kT_C}\right)\right)}{\partial E}\Big|_{E=E_C} = \frac{N(E_C)}{kT_C}\,, \tag{4.10b}$$

for the exponential band tails. From Eqs. (4.9) and (4.10) we have:

$$\frac{1}{2}\frac{N_{EV}}{\sqrt{E_{V0}-E_V}} = \frac{N(E_V)}{kT_V} \tag{4.11a}$$

$$\frac{1}{2}\frac{N_{EC}}{\sqrt{E_C-E_{C0}}} = \frac{N(E_C)}{kT_C} \tag{4.11b}$$

Using Eqs. (4.8) and (4.11) we finally obtain:

$$\frac{kT_V}{2} = E_{V0} - E_V \tag{4.12a}$$

$$\frac{kT_C}{2} = E_C - E_{C0}\ , \tag{4.12b}$$

and

$$N(E_V) = N_{EV}\sqrt{\frac{kT_V}{2}} \tag{4.13a}$$

$$N(E_C) = N_{EC}\sqrt{\frac{kT_C}{2}} \tag{4.13b}$$

The exponential band tails close to E_V and E_C can be then written as:

$$N_V^{exp}(E) = N_{EV}\sqrt{\frac{kT_V}{2}}\exp\left(-\frac{E-E_V}{kT_V}\right), \qquad \text{for } E \geq E_V \tag{4.14a}$$

$$N_C^{exp}(E) = N_{EC}\sqrt{\frac{kT_C}{2}}\exp\left(-\frac{E_C-E}{kT_C}\right), \qquad \text{for } E \leq E_C \tag{4.14b}$$

In the software DeOSt, the band tails can be defined with two exponential distributions, one exponential distribution as defined above and a second distribution located deeper in the gap. For one band tail these two distributions join at an energy defined as E_{cutoff}, the deepest distribution being defined by:

$$N_V^{exp}(E) = N_V^{EXT}\exp\left(-\frac{E-E_V}{kT_{V2}}\right), \qquad \text{for } E \geq E_V^{cutoff} \tag{4.15a}$$

$$N_C^{exp}(E) = N_C^{EXT}\exp\left(-\frac{E_C-E}{kT_{C2}}\right), \qquad \text{for } E \leq E_C^{cutoff} \tag{4.15b}$$

Figure 4-3 displays the distribution of states at the vicinity of E_V in the case where two exponential distributions of states are considered for the valence band tail.

Defect states - Standard DOS

The localized states in the sub band gap region are represented using Gaussian distributions of both donors and acceptors, see Fig. 4-4. The expression of these distributions is given in Eq. (4.16).

$$N_{defect}(E) = N_{max}\exp\left(-\frac{(E_{max}-E)^2}{2\sigma^2}\right) \tag{4.16}$$

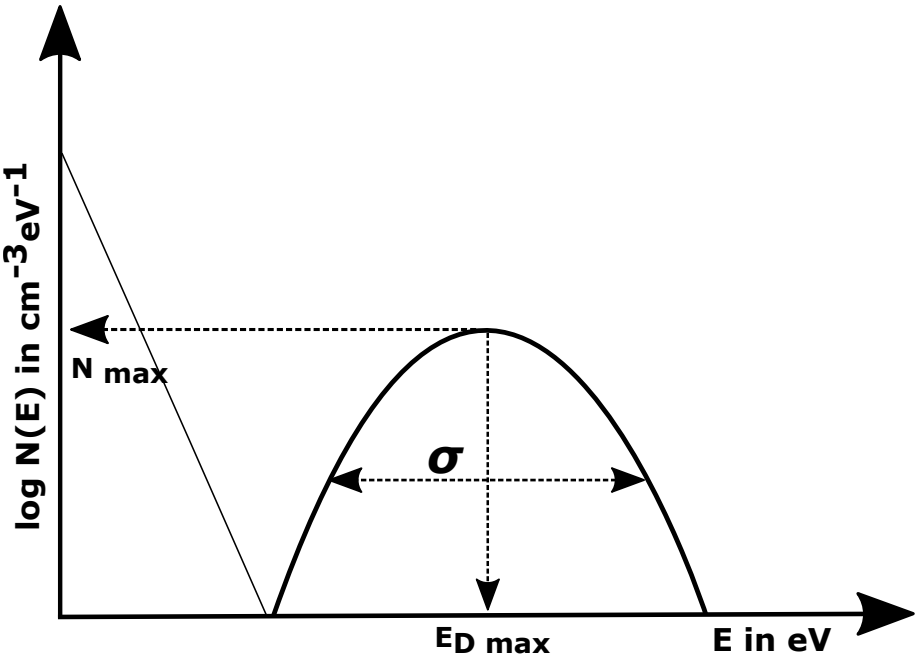

Figure 4-4: Deep defect states in the sub bandgap represented by a Gaussian distribution function. The characteristics of this function are the standard deviation, denoted as σ, the energy where the maximum of the Gaussian exists, E_{max}, and the maximum density of defect, N_{max}. A Gaussian donor distribution is placed near the valence band tail and a Gaussian acceptor distribution is placed near the conduction band tail.

Calculation of the absorption coefficient from the standard DOS model

Now that we have modeled the DOS of a thin film semiconductor material, we can use the corresponding DOS to calculate the absorption coefficient. In this calculation, we will use Eq. (4.1) as the basis of the absorption coefficient calculation. As explained, the absorption coefficient measured using photocurrent measurements reflects the electronic transitions A, B_1, B_3, C_1, and C_2 as in Fig. 4-1. The following calculation of the absorption coefficient will be based on each type of transition. It is particularly necessary to define the initial and the final states.

Transition A defines the band-to-band transition, which is possible when the photon energy impinging a semiconductor material is higher than the material's band gap energy. The transition A will contribute to the generation of the photocurrent due to the creation of an electron in the extended states of the conduction band and a hole in the extended states of the valence band. In this transition, the initial state is the extended states of the valence band, whose distribution of states is denoted in Eq. (4.2)a. The final state is in the extended states of the conduction band whose distribution is denoted in Eq. (4.2)b. Hence, we can calculate the absorption coefficient of

this kind of transition as in Eq. (4.17).

$$\alpha(h\nu) = \frac{1}{h\nu} \int_{E_C - h\nu}^{E_V} C_{VB}^{opt}\, N_{EV} \sqrt{E_{V0} - E}\;\; C_{CB}^{opt}\, N_{EC} \sqrt{E + h\nu - E_{C0}}\, dE \qquad (4.17)$$

We shall assume that the extended states on the valence band side are always full ($f(E) \simeq 1$) whereas the extended states on the conduction band side are always empty ($(1 - f(E + h\nu)) \simeq 1$).

In the following equations, we will use as in Eq. (4.17), abbreviations such as VB for valence band, CB for conduction band, VBT for valence band tail, CBT for conduction band tail, *don* for donor, and *acc* for acceptor.

Transition B_1 represents an electron transition from the valence band tail toward the extended states of the conduction band. Hence, an electron is created in the extended states of the conduction band, contributing to the photocurrent. The initial states are those of the valence band tail as denoted in Eq. (4.14) when a unique exponential band tail is used. In the case of two exponential distributions, we shall use Eq. (4.15) for $E \geq E_V^{cutoff}$. The final states are the extended states of the conduction band, as referred in Eq. (4.2)b. The calculation of the absorption coefficient due to the transition B_1 considering a unique exponential valence band tail can be denoted as :

$$\alpha(h\nu) = \frac{1}{h\nu} \int_{E_V}^{E_C} C_{VBT}^{opt}\; N(E_V) \exp\left(-\frac{E - E_V}{kT_V}\right)\; f_{VBT}(E) \; C_{CB}^{opt}\; N_{EC} \sqrt{E + h\nu - E_{C0}}\; dE \qquad (4.18)$$

In the case of two exponential distributions for the valence band tails, Eq. (4.18) is valid for the transition of photon energy from initial energy below E_V^{cutoff}. Hence, E_C as to be replaced by E_V^{cutoff} in the integral boundaries. In the other hand, when the initial photon energy is above E_V^{cutoff}, we shall apply the following expression:

$$\alpha(h\nu) = \frac{1}{h\nu} \int_{E_V^{cutoff}}^{E_C} C_{VBT}^{opt}\; N_V^{ext} \exp\left(-\frac{E - E_V}{kT_{V2}}\right) f_{VBT}(E) \; C_{CB}^{opt}\; N_{EC} \sqrt{E + h\nu - E_{C0}}\; dE \qquad (4.19)$$

Transition B_3 differs from transition A and B_1 because instead of an electron creation in the extended states of the conduction band, it is a hole creation in the extended states of the valence band which contributes to the photocurrent. The initial states are the extended states of the valence band as in Eq. (4.2)a, while the final states are the conduction band tail states. The calculation of the absorption coefficient using a unique or two exponential distribution functions can be done using the same principle as for transition B_1. For a unique exponential conduction band tail states,

the absorption coefficient is:

$$\alpha(h\nu) = \frac{1}{h\nu}\int_{E_V-h\nu}^{E_V} C_{VB}^{opt}\ N_{EV}\sqrt{E_{V0}-E}$$
$$C_{CBT}^{opt}\ N(E_C)\exp\left(-\frac{E_C-(E+h\nu)}{kT_C}\right)(1-f_{CBT}(E+h\nu))\ dE \tag{4.20}$$

and in the case of two exponential conduction band tail states, Eq. (4.20) is valid for $E \geq E_C^{cutoff}$. Hence, in the case of two exponential distribution functions for the tail states, the lower integral boundary of Eq. (4.20) should be $E_C^{cutoff} - h\nu$. For $E \leq E_C^{cutoff}$ we shall use:

$$\alpha(h\nu) = \frac{1}{h\nu}\int_{E_V-h\nu}^{E_C^{cutoff}-h\nu} C_{VB}^{opt}\ N_{EV}\sqrt{E_{V0}-E}$$
$$C_{CBT}^{opt}\ N_C^{ext}\exp\left(-\frac{E_C-(E+h\nu)}{kT_{C2}}\right)(1-f_{CBT}(E+h\nu))\ dE \tag{4.21}$$

The transitions C are of particular interest for the absorption coefficient measurement using FTPS. The generation of the photocurrent due to this transition reflects the existence of the deep defects present in the semiconductor material. In this type of transition, the photon energy is usually very low, below 1-1.2 eV.

The transition C_1 represents an electron leaving the extended states of the valence band toward localized or defect states in the sub bandgap region. Hence, the initial state of this type of transition can be denoted as in Eq. (4.2)a, whereas the final state can be defined using Eq. (4.16). The absorption coefficient due to this type of transition can be expressed as in Eq. (4.22):

$$\alpha(h\nu) = \frac{1}{h\nu}\int_{E_V-h\nu}^{E_V} C_{VB}^{opt}\ N_{EV}\sqrt{E_{V0}-E}$$
$$C_{acc}^{opt}N_{acc}^{max}(E)\ \exp\left(-\frac{(E_{acc}^{max}-(E+h\nu))^2}{2\sigma_{acc}^2}\right)(1-f_{acc}(E+h\nu))\ dE \tag{4.22}$$

Transition C_2 represents the transition of electrons present in the deep defect states toward the extended states of the conduction band. The initial states can be defined as those of a defect distribution as in Eq. (4.16) and the final states are the extended states of the conduction band, denoted in Eq. (4.2)b. The absorption coefficient can thus be written as:

$$\alpha(h\nu) = \frac{1}{h\nu}\int_{E_C-h\nu}^{E_C} C_{don}^{opt}\ N_{don}^{max}(E)\ \exp\left(-\frac{(E_{don}^{max}-E)^2}{2\sigma_{don}^2}\right) f_{don}(E)$$
$$C_{CB}^{opt}\ N_{EC}\sqrt{E+h\nu-E_{C0}}\ dE \tag{4.23}$$

The occupation probability, $f(E)$ which appears in the absorption coefficient calcu-

lation is calculated using the Fermi function [61] denoted as:

$$f(E) = \frac{1}{1 + \exp\left(\frac{E - E_F}{kT}\right)} \tag{4.24}$$

where E_F is the Fermi level energy under dark condition that can be calculated using the electrical neutrality of the charges present in the material.

By applying the occupation probability function in Eq. (4.24), we can calculate the absorption coefficient using Eqs. (4.17) to (4.23). In the numerical simulation using DeOSt, the set of parameters that were chosen to be manipulated to construct the DOS is shown in Table 4.1.

Table 4.1: List of standard model DOS parameters chosen to be manipulated using DeOSt.

Extended band states	N_{EV}, N_{EC}, E_G
Band tail states	$N_V^{EXT}, N_C^{EXT}, T_{V2}, T_{C2}, E_V^{cutoff}, E_C^{cutoff}, C_{CBT}^{opt}, C_{VBT}^{opt}$
Defect states	$N_{don}^{max}, N_{acc}^{max}, E_{don}^{max}, E_{acc}^{max}, \sigma_{don}, \sigma_{acc}, C_{don}^{opt}, C_{acc}^{opt}$

4.1.2 Defect-pool density of states model and the calculation of the absorption coefficient

There has been a number of experimental evidences, [62], [63], and [64], showing that the deep defect density of states in a semiconductor material, as amorphous silicon is dominated by the amphoteric silicon dangling bond (DB) states, and is determined by a chemical equilibrium process. The DBs formation involves the breaking of the Si-Si bonds [65] which are generally stabilized through hydrogen diffusion [64], [66]. DBs states which are formed due to the inherent disorder of the amorphous network can spread over a certain range of energy and can be considered as defect states in a semiconductor material like amorphous silicon. The energy range of these defect states leads to an energy shift of the peak of the formed defects. In the defect-pool model [67], [68], and [69], the energy shift is different for defects formed in the different charge states. In this model, defects charge states are comprised of +, 0, and - charge.

In the earlier defect-pool model proposed by Bar-Yam and Joannopoulos [70], the formation energy of a defect depends on its charge state and the difference in the formation energies depends on the Fermi energy and the energy of the defect itself. In their model, the defect formation energy for the neutral defect (charge state 0) was an arbitrary parameter and the defect formation energy of the charged defects (- and +) is relative to those neutral charge states. Branz and Silver [71] applied the defect-pool model proposed by Bar-Yam and Joannopoulos specifically to a-Si:H materials. This model has lead to a deeper understanding toward the deep defect states distribution but unfortunately there was neither an explanation related to the defect formation process nor on the hydrogen entropy contribution to the defect chemical potential.

The first incorporation of the hydrogen entropy and the explanation of the defect formation was introduced by Winer [72]. In this model, the defect density is calculated by assuming one type of defect charge state for a given material. That being said neutral defect charge D^0 is for intrinsic material, D^+ for p-type material, and D^- for n-type material. Hydrogen entropy contribution was calculated by assuming that each defect gained the entropy from all Si-H sites and not only from those at the same energy, which was incorrect. However, the result of the density of states calculation using this model was then underestimated.

Schumm and Bauer [73] improved the extended defect-pool model proposed by Winer by introducing a simultaneous formation of three defect charge states (in this model they are called D_e, D_z, and D_h). This model considers three independent chemical reactions forming the DBs in each charge state. But later in another paper [74] they corrected that the chemical reactions were not independent but depending on the defects formed in all three charges. Schumm and Bauer included the hydrogen entropy in their calculation but concluded that the energy spectrum of the density of states did not change upon the hydrogen entropy contribution. Hence, the hydrogen entropy was included only as a scaling constant.

Powell and Deane proposed an even more improved defect-pool model [56] showing that the energy spectrum of the density of states does depend on the number of Si-H bonds which are mediating the DB formations. In their model, they calculated the density of deep states and derived a simple expression for the energy separation of positively and negatively charged defect states. They concluded that the density of deep states depends on the main parameters of a defect-pool model.

In this work, we have chosen the defect-pool density of states model based on the improved defect-pool model proposed by Powell and Deane [56]. The following subsections will explain how the density of states is calculated using the improved defect pool model and how the absorption coefficient is calculated from this density of states model.

Improved defect-pool density of states model

The principles of this model are that the dangling bonds (DBs) are formed by the breaking of weak Si-Si bonds and that the density of the defects is determined by a chemical equilibrium between the weak bonds and the DBs. In this model, DBs are considered to be formed by three different microscopic chemical reactions.

$$\begin{aligned} WB &\rightleftharpoons 2DB, && \text{for i=0} \\ Si-H+WB &\rightleftharpoons (DB+Si-H)+DB, && \text{for i=1} \\ 2Si-H+WB &\rightleftharpoons (Si-H-H-Si)+2DB, && \text{for i=2} \end{aligned} \tag{4.25}$$

where i is the number of Si-H bonds mediating the weak-bond breaking chemical reaction. In each case two dangling bond are created. In the case of i=2, a second Si-H bond is broken, resulting in a doubly hydrogenated weak-bond site and two isolated defects.

To calculate the defect density, we will first determine a general expression for

the defect chemical potential, which is defined as the free energy change upon adding one extra defect to the system. The defect chemical potential for the amphoteric DB defects contains three terms: 1) the energy of the electrons of the defect, 2) the entropy associated with the electron occupancy of the defect, and 3) the additional entropy associated with the defect on alternative hydrogen densities.

The mean energy of electrons in the DB state is defined by the probability of a DB being in each of the three charge states. If the defect is positively charged, the defect's electron has been removed toward the Fermi level energy, E_F. If the defect charge is neutral, the defect's electron stays at the defect energy, E. In the case where the defect is negatively charged, an extra electron has to be moved from the Fermi level energy toward the defect, giving a total energy of $2E - E_F + E_U$, where E_U is the correlation energy needed to place two electrons on the same defect.

The mean energy of the electron is defined by:

$$< e >= E_F f^+(E) + E f^0(E) + (2E - E_F + E_U) f^-(E) \tag{4.26}$$

where f^+, f^0, and f^- are the occupancy functions of the amphoteric DB in each charge state. The occupancy functions, f for each charge states are denoted in Eqs. (4.27):

$$f^+(E) = \frac{1}{1 + 2\exp\left(\frac{E_F - E}{kT}\right) + \exp\left(\frac{2E_F - 2E - E_U}{kT}\right)} \tag{4.27a}$$

$$f^0(E) = \frac{2\exp\left(\frac{E_F - E}{kT}\right)}{1 + 2\exp\left(\frac{E_F - E}{kT}\right) + \exp\left(\frac{2E_F - 2E - E_U}{kT}\right)} \tag{4.27b}$$

$$f^-(E) = \frac{\exp\left(\frac{2E_F - 2E - E_U}{kT}\right)}{1 + 2\exp\left(\frac{E_F - E}{kT}\right) + \exp\left(\frac{2E_F - 2E - E_U}{kT}\right)} \tag{4.27c}$$

We shall remember that E is the energy of the amphoteric DB state, with the +/0 transition being at an energy E and the 0/- transition being at $E + E_U$.

The electron entropy is given by the Boltzmann definition [75] by $s = -\sum p_i \ln p_i$. p_i is defined as the probability of the system to be in any one state and the summation is over all possible states. In the case of DB, the electron entropy can be written as:

$$s_e = -\left\{ f^+(E) \ln f^+(E) + 2[f^0(E)/2] \ln(f^0(E)/2) + f^-(E) \ln f^-(E) \right\} \tag{4.28}$$

where the factor of 2 linked to the neutral charge state is due to the spin degeneracy of this state. The total entropy is zero when the defect is positively of negatively charged, i.e., $f^+ = 1$ or $f^- = 1$. When the defect is neutral, $s = \ln \frac{1}{2}$. In this case, the neutral defect is twice likely to form.

Using the Eqs. (4.26) and (4.28) we can obtain the defect energy potential, μ_d

without hydrogen entropy.

$$\begin{aligned} \mu_d &=< e > -kTs_e \\ \mu_d(E) = f^+[E_F + kT\ln f^+(E)] &+ f^0[E + kT\ln(f^0(E))/2] \\ &+ f^-[2E - E_F + E_U + kT\ln f^-(E)] \end{aligned} \tag{4.29}$$

By substituting the occupancy functions in Eq. (4.27) into the above equation, we found that the three terms in the square brackets in Eq. (4.29) are identical. If we consider that the sum of the occupation function of each charge states equals one, $f^+ + f^0 + f^- = 1$, μ_d can be expressed as:

$$\mu_d(E) = E_F + kT\ln f^+(E) \tag{4.30a}$$
$$= E + kT\ln(f^0(E)/2) \tag{4.30b}$$
$$= 2E - E_F + E_U + kTf^-(E) \tag{4.30c}$$

If we consider the effect of hydrogen involvement in the chemical reaction as in Eq. (4.25), we shall consider that a DB defect will be formed at energy E when the hydrogen atom is removed. The number of hydrogen sites is $HP(E)$, where H is the concentration of hydrogen and $P(E)$ is the energy distribution of sites which would form the DB defects at energy E (we shall consider that for state charge 0/- the energy is $E + E_U$). The probability that a defect exists at any hydrogen site is given by p_d which is:

$$p_d = \frac{iD(E)}{2HP(E)} \tag{4.31}$$

where $D(E)$ is the density of defects at energy E. The term $i/2$ found in the above equation is due to the fact that for every two defects formed, only i of these defects can swap hydrogen from distant sites. The total entropy can be calculated as:

$$s_H = -\sum p_d \ln(p_d) \tag{4.32}$$

which is the sum over $HP(E)$ hydrogen sites with identical p_d . Then dividing by the density of defects $D(E)$, we shall have the hydrogen entropy per defect at energy E as denoted by:

$$s_H = -\frac{i}{2}\ln\left(\frac{iD(E)}{2HP(E)}\right) \tag{4.33}$$

If we add this entropy to Eq. (4.30)b, we obtain a general expression of the defect chemical potential as:

$$\mu_d(E) = E + kT\ln\left[\frac{f^0(E)}{2}\right] + \frac{ikT}{2}\ln\left[\frac{iD(E)}{2HP(E)}\right] \tag{4.34}$$

The defect density at energy E calculation should take into account the probability of converting a weak-bond state at energy E_t. It considers that a weak bond forms two dangling bonds and it has to take into account the depletion of the weak-bond

states by the formed defects. Hence, the defect density $D(E)$ can be denoted as:

$$D(E) = [P(E)g_t(E_t) - D(E)] \exp -2[\mu_d(E) - E_t]/kT \tag{4.35}$$

where $P(E)g_t(E_t)$ is the density of weak bonds at energy E_t that will lead to potential defect sites at energy E. Now, if there is a distribution of weak-bond energies, we need to rewrite the Eq. (4.35) by integrating over the weak-bond energies:

$$D(E) = \int \frac{P(E)g_t(E_t)}{1 + \exp -2[\mu_d(E) - E_t]/kT} \, dE_t \tag{4.36}$$

The weak-bond sites are identified with the valence band tail states which are exponentially distributed in energy [76], denoted as:

$$N_V^{exp}(E) = N_{V0} \exp\left(-\frac{E - E_V}{kT_V}\right), \text{ for } E \geq E_V \tag{4.37}$$

where N_{V0} is the extrapolated density of tail states to the valence band mobility edge E_V, $N_{V0} = N(EV)$. In the software DeOSt, as explained in the standard density of states model in Section 4.1.1, we consider that if a unique exponential is used, we can apply Eq. (4.14) for the band tail states. In the case of two exponential band tail states, the first exponential distribution in Eq. (4.14) is valid when $E < E_V^{cutoff}$, and the second exponential distribution function for the band tail states can be calculated using Eq. (4.15)a.

Using Eq. (4.36) with the approximations that for $\mu_d < E_t$ all weak-bonds convert whereas for $\mu_d > E_t$ only a fraction of states using Boltzmann distribution converts, we can now modify $D(E)$ to:

$$D(E) = P(E)N_{V0} \, \frac{2(kT_V)^2}{k(2T_V - T)} \exp\left(\frac{-\mu_d(E)}{kT_V}\right) \tag{4.38}$$

where the defect-pool function $P(E)$ is assumed to have a Gaussian distribution as:

$$P(E) = \frac{1}{\sigma_{Pool}\sqrt{2\pi}} \exp\left(\frac{-[E - E_P]^2}{2\sigma_{Pool}^2}\right) \tag{4.39}$$

where σ_{Pool} is the pool width and E_p is the most probable energy in the distribution of available sites for defect formation. If we substitute μ_d in Eq. (4.36) with Eq. (4.34), we shall obtain:

$$D(E) = \gamma \left[\frac{2}{f^0(E)}\right]^{\rho T/T_V} P\left[E + \frac{\rho\sigma_{Pool}^2}{kT_V}\right] \tag{4.40}$$

where

$$\gamma = \left[\frac{N_{V0} \, 2(kT_V)^2}{k(2T_V - T)}\right]^{\rho} \left[\frac{i}{2H}\right]^{\rho - 1} \times \exp\left[\frac{-\rho}{kT_V}\left(E_P - E_V - \frac{\rho\sigma_{Pool}^2}{2kT_V}\right)\right] \tag{4.41}$$

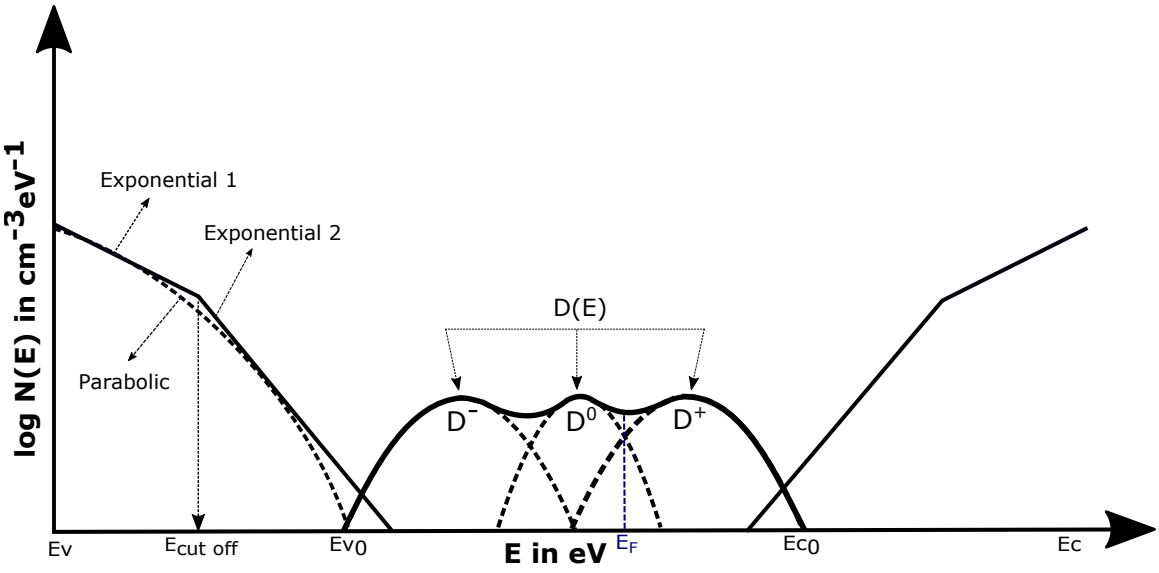

Figure 4-5: The density of states using the improved defect-pool model. The total density of states $D(E)$ is divided into components of D^-, D^0, and D^+. The band tail state distributions are considered as in standard DOS model, either a single or two exponential distribution function is used.

with

$$\rho = \frac{2kT_V}{2kT_V + ikT} \tag{4.42}$$

The above equations are applicable for the calculation of density of states at equilibrium, which is maintained for temperatures above the equilibrium temperature, T_{eq}. The energy dependence of the density of states comes from Eq. (4.40) where γ represents a scaling factor towards the absolute value. The energy distribution of the density of deep states depends on i through ρ. Since the defect-pool function $P(E)$ is a Gaussian, the Eq. (4.40) represents a Gaussian shifted by the presence of the occupancy of neutral defects $f^0(E)$.

In the calculation of the density of states, we should estimate the correlation energy E_U, which is positive and must be greater than 0.1 eV [77]. Some measurement results suggested a value of E_U ranging from 0.2-0.3 eV [78]. The most commonly used value is 0.2 eV [72], [79].

In order to divide $D(E)$ into three different charge densities, D^+, D^0, and D^-, we should multiply it with its corresponding occupancy functions as denoted in Eq. (4.27). Hence, the distributions of different charge densities can be written:

$$D^+(E) = D(E)f^+(E) \tag{4.43a}$$
$$D^0(E) = D(E)f^0(E) \tag{4.43b}$$
$$D^-(E) = D(E)f^-(E) \tag{4.43c}$$

From Fig. 4-5 it can be seen that the defect-pool density is centered on the D^0 states, whereas the peaks of $D(E)$ at lower and higher energies consist of D^- and

D^+, respectively. The energy separation between the peaks of the negatively charged defects and the positively charged defects is defined by $2\rho\sigma^2_{Pool}/kT_V$. The energy separation between the doubly occupied D^- states and the empty D^+ states is given by Δ, which can be denoted as:

$$\Delta = \frac{2\rho\sigma^2_{Pool}}{kT_V} - E_U \tag{4.44}$$

The relationship between E_F and E_P is $E_P = E_F + \Delta/2$, thus the peak of D^+ states coincides with E_P.

Calculation of the absorption coefficient from the defect-pool model DOS

The calculation of the absorption coefficient using the defect-pool model is based on Eq. (4.1). The absorption coefficient is calculated from the electronic transitions as defined in the previous section, which are transitions A, B_1, B_3, C_1, and C_2 (see Fig. 4-1). Since in the defect-pool model DOS we use the same distribution functions as in the standard DOS model for the extended states and the band tails, which is a parabolic function for the extended band states and exponential function for the band tail states, the band-to-band transition (transition A) and the band tail to extended band transition (transitions B_1 and B_3) calculated using Eqs. (4.17) and (4.19) (in the case of two exponential distribution functions for band tail states) are still valid.

For the transition C_1, we need to consider that in the defect-pool model the localized states consist of three states of charge, D^-, D^0, and D^+. The electronic transitions from the extended states of the valence band are only possible toward an empty or almost empty localized states. It means that the possible transitions are either towards D^0 or D^+ states, since D^- is filled with two electrons while D^0 carries one electron and none for D^+ . Hence, we can denote the absorption coefficient as:

$$\alpha(h\nu) = \frac{1}{h\nu}\int_{E_V-h\nu-E_U}^{E_V} C^{opt}_{VB}\ N_{EV}\sqrt{E_{V0}-E}\ C^{opt}_{D^0}\ D^0(E-E_U+h\nu)\,dE \tag{4.45}$$

for the electronic transition towards D^0 states. Note that since an electron is already present in the D^0 states at an energy E, an electron from the extended states of valence band will have to arrive at an energy $E+E_U$ in the D^0 states to transform it into a D^-. For the transition C_1 towards D^+ states, we can calculate the absorption coefficient as follows:

$$\alpha(h\nu) = \frac{1}{h\nu}\int_{E_V-h\nu}^{E_V} C^{opt}_{VB}\ N_{EV}\sqrt{E_{V0}-E}\ C^{opt}_{D^+}\ D^+(E+h\nu)\,dE \tag{4.46}$$

Transition C_2 represents an electronic transition from the localized states in the band gap towards the extended states of the conduction band. Knowing that the D^+ states contains no electron, the transition C_2 is only possible either from D^- or D^0 states. For the transition from the D^- states, we need to note that the electron at the energy E will remain in its state while the electron at energy $E+E_U$ is available for the transition towards the extended states. Hence, we can calculate the absorption

coefficient as:

$$\alpha(h\nu) = \frac{1}{h\nu} \int_{E_C - h\nu - E_U}^{E_C} C_{D^-}^{opt}\ D^-(E)\, C_{CB}^{opt}\, N_{EC} \sqrt{E + h\nu + E_U - E_{C0}}\, dE \qquad (4.47)$$

for transition from D^- states, and :

$$\alpha(h\nu) = \frac{1}{h\nu} \int_{E_C - h\nu}^{E_C} C_{D^0}^{opt}\ D^0(E)\, C_{CB}^{opt}\, N_{EC} \sqrt{E + h\nu - E_{C0}}\, dE \qquad (4.48)$$

for transition from D^0 states.

In the numerical simulation of DOS using DeOSt, the defect-pool DOS model parameters that were chosen to be varied are shown in Table 4.2. Note that in the defect-pool DOS model, we use two exponential distribution functions for the band tail states. The optical matrix coefficient C_{pool}^{opt} is set constant for all the defect-pool states. It means that this value is chosen identical for $C_{D^-}^{opt}$, $C_{D^0}^{opt}$, and $C_{D^+}^{opt}$.

Table 4.2: List of the defect-pool model DOS parameters chosen to be manipulated using DeOSt.

Extended band states	N_{EV}, N_{EC}, E_G
Band tail states	$N_V^{EXT}, N_C^{EXT}, T_{V2}, T_{C2}, E_V^{cutoff}, E_C^{cutoff}, C_{VBT}^{opt}, C_{CBT}^{opt}$
Defect-pool states	$H, E_P, E_U, \sigma_{Pool}, C_{pool}^{opt}$

From the model density of states parameter tables, Tabs. 4.1 for the standard model and 4.2 for the defect-pool model, the extended states for both conduction and valence band are constructed through Eq. (4.2). The parameters T_V and T_C were calculated with the band tail state distributions. E_{cutoff} and $N^{exp}(E_{cutoff})$ is the intersection point of the two exponential band tail state distribution functions, hence the value of T_V and T_C can be extracted since all the other band tail state parameters are defined initially. By knowing these values, the exponential band tail state distributions can be calculated using Eqs. (4.14) and (4.15) for the first and second exponential distributions, respectively.

For simplicity, the optical matrix coefficient for the band tail state distributions and the defect states are set identical for the valence and conduction band side, $C_{VBT}^{opt} = C_{CBT}^{opt}$ and $C_{don}^{opt} = C_{acc}^{opt}$. To model the density of states using the standard model using DeOSt, 17 parameters are to be defined. The defect-pool DOS model has 15 parameters to be defined. The set of parameters are used to construct the density of states and calculate the absorption coefficient.

4.2 Extraction of DOS parameters using Teacher Learner Based Optimization

Earlier, the extraction of the DOS parameters from the absorption coefficient was proposed by quantifying the light induced changes in the derivative of the absorption

coefficient spectra. This method has been used in a-Si:H samples characterized using DBP. The derivative of the absorption coefficient spectrum represents the density of electron occupied states, which contains a number of defect states in the sub gap region fitted with a sum of Gaussian functions [31,32]. When calculating the derivative of the absorption coefficient, one should be aware that numerical differentiation is a common problem in computational mathematics [80]. Hence, the noise variation of the absorption coefficient due to the noise in the FTPS measurement may lead to errors in the calculated derivative. To obtain a good approximation of the true and noise free derivatives, it is necessary to apply a regularisation method [81]. A correct derivative of the absorption coefficient then takes a long calculation time.

A similar approach was proposed by Melskens *et al.* [82] to quantify changes in the sub gap FTPS-EQE spectrum. However, they suggested a fitting by the sum of error functions. An error function was chosen as it is the primitive of a Gaussian function. By using the error function the calculated derivative is no longer needed, thus the fitting is obtained more quickly. Although the error function can be calculated faster, it does not have a direct physical equivalence as compared to the Gaussian functions as these functions are assumed to correspond to physical quantities such as the defect distributions. For example, when fitting the defect states using Gaussian functions, the different distributions can be easily distinguished while it is not the case for the error functions. Nevertheless, due to the mathematical equivalence of the two approaches, the fitting parameters (amplitude, position, and width) contain the same information about the sub gap defect states.

As we can see in the previous section, the relation between the absorption coefficient and the DOS model parameters are indirect and nonlinear, thus the DOS parameters direct contribution to the absorption coefficient spectrum cannot be obtained so easily. In a nonlinear problem, numerical techniques are widely used, especially the ones involving a certain mathematical algorithm, like curve fitting algorithm to fit all the points of the given result to extract the unknown parameters. Using such technique, we can get a more reliable result since all the points of the given result are utilized. However, the accuracy of this technique is dependent on the type of fitting algorithm, the fitting criterion, objective function and the starting values of the parameters [83]. Moreover, the application of these techniques to extract the DOS parameters becomes very complicated because the fitting function is an integral of the convolution of DOS and the occupation probability over a given range of energy. It means that for each given energy range a specific fitting function has to be applied. In addition, we need to take into consideration that for a given energy, the absorption coefficient involves two types of electron transitions, the one leaving the valence band and the one arriving in the conduction band. Hence, for a given energy range, there is a significant amount of possible fitting functions and these have to be carefully chosen.

In this work, the DOS model is calculated neither through the derivative nor the error functions. Due to its complexity, the numerical fitting approach was not chosen either. In fact, in this work we looked back at the origin of the absorption coefficient as a contribution of electron transitions in the DOS. Thus, our approach is to model the DOS. DeOSt is used as a platform to model the DOS and to calculate

the absorption coefficient from the DOS. It means that for a given DOS model, a given distribution of electronic states is defined. When a given photon energy is selected, electron transitions occur using the photon energy. To be in agreement with the FTPS principles, only the electron transitions leaving the extended states of valence band or arriving to the conduction band will be used to calculate the absorption coefficient. In this way, the calculated absorption coefficient is obtained directly from the contribution of all possible electron transitions in the DOS. Hence, DeOSt is a powerful tool for DOS modeling and absorption coefficient calculation. Despite this advantage, the DOS model has many parameters. The adjustment of the DOS parameters is tedious and can take a very long time if the effect of the change of DOS parameters on the absorption coefficient spectrum is not very well understood.

Due to this difficulty, a numerical evolutionary algorithm (EA) is proposed for the extraction of the DOS parameters. In recent years, EA have been used for the solar cell parameters extraction because of their effectiveness and flexibilities [84], [85]. Among the EAs, genetic algorithm (GA) has been extensively used for the solar cell parameters extraction [86], [87]. Particle swarm optimization (PSO) also has been used to investigate the solar cell parameters [88], [89]. Recently, teaching–learning-based optimization (TLBO) algorithm was introduced by Rao *et al.* [90], emerging as new promising global optimization algorithm capable of solving a wide range of optimization problems. Some features of the TLBO algorithm are ready to use so that it makes it a very effective algorithm. As an example, the implementation of the algorithm is simple and easy, requiring very few control variables. The only control variables are population size and number of iterations in order to reach the global optimum solution. TLBO has been proposed by Patel *et al.* [57] to extract solar cell parameters from single illuminated I–V characteristic using LabVIEW program. It was demonstrated in their paper that the TLBO algorithm can be a very effective and useful tool to extract the information about all the five important solar cell parameters from a single I–V characteristic measured under illumination. The limitation of numerical methods and conventional optimization algorithms in solar cell parameters extraction problem was significantly overcome with the help of the TLBO approach.

So far, the TLBO algorithm has not been investigated for the extraction of DOS parameters. Hence, here we report a study on the effectiveness of the TLBO algorithm for the extraction of DOS parameters. We applied the algorithm to extract all the DOS parameters which result in a good agreement of the absorption coefficient obtained through the calculation and the FTPS measurement. The algorithm is implemented through MATLAB as a programming tool. The details about these DOS parameters extraction are explained in the next subsection.

4.2.1 Description of the TLBO algorithm

The TLBO algorithm uses the basic principles of teaching–learning process in a classroom. The optimization algorithm in TLBO uses a population of solutions to reach the global optimum based on the real numbers. A population is considered as a group of learners in the classroom. In the case of the DOS extraction parameters, a population contains a group of sets of DOS parameters, each set being a learner. TLBO

algorithm is inspired by knowledge passing within a classroom, where firstly, learners obtain their knowledge from a teacher and the interaction between learners is done to propagate the knowledge. The learners are evaluated using a specific objective function called "fitness function". The value of the fitness function then represents the performance of a learner. Thus, the fitness of a population of learners is improved by the propagation of knowledge through two phases: teacher phase and learner phase.

Teacher phase

Teacher phase is the first phase of the TLBO algorithm. In this stage, learners learn from the teacher who is considered as a highly learned person in the population. Teacher shared the knowledge with the learners in the classroom. A good teacher trains learners to get a better result or fitness. In this phase, the algorithm tries to improve the fitness of the learners by moving their position (X_i) towards the position of the teacher ($X_{teacher}$). The position is moved using the mean value of the learner (X_{mean}). The modification of learners value by the teacher is performed using the equation below :

$$X_{new} = X_i + r.(X_{teacher} - (T_F \cdot X_{mean})) \tag{4.49}$$

where, $i = 1, 2, 3..., N$, N being the number of learners in the classroom. X_{new} is the modified learner which will modify the X_i only if it has a better result or fitness compared to X_i. r defines a random number between 0 and 1 which represents the fraction of knowledge sharing between the teacher and learner. 0 corresponds to no knowledge sharing, meaning that learner does not learn anything from the teacher and 1 when learner learns everything from the teacher. When the value of r is low, it corresponds a low knowledge transfer and slow convergence but it creates a better exploration of the search space. Teaching factor, T_F, is given to determine how much of the mean value (X_{mean}) has to be changed. Rao and Patel [90] suggested that the algorithm performance is better when the value of T_F is set either at 1 or 2. In this TLBO algorithm, the value of T_F is determined by:

$$T_F = round(1 + rand[0, 1]) \tag{4.50}$$

where *rand* is a random number between 0 and 1.

Learner phase

In the learner stage, learners learn by having interaction between learners. Each learner ($X_i, i = 1, 2, 3..., N$) interact with a randomly selected other learner ($X_j, j = 1, 2, 3..., N$) in the classroom, where the selected learner X_j must be different of the X_i. If X_i has a better fitness value, f, than X_j, the position of X_j is moved towards X_i using Eq. (4.51)a. In the other hand, if X_j is better than X_i, X_i is moved towards X_j using Eq.(4.51)b.

$$X_{new} = X_i + r.(X_i - X_j), \quad \text{if } f(X_i) > f(X_j) \tag{4.51a}$$
$$X_{new} = X_i + r.(X_j - X_i), \quad \text{if } f(X_i) < f(X_j) \tag{4.51b}$$

where $i \neq j$. In this learner phase, X_{new} will only be taken into account if it has a better fitness value than X_i.

4.2.2 Implementation of the TLBO algorithm for DOS parameters extraction

The extraction of the DOS parameters is carried out using the experimental absorption coefficient spectrum obtained through FTPS measurement or with the DeOSt program (for example to create the synthetic absorption coefficient spectrum in the case of the TLBO program validation). The performance of the extracted DOS parameters is evaluated using the fitness function which is calculated for each iteration of the TLBO process. In this program, the fitness function is defined using the calculated root-mean-square error of the absorption coefficient given by the FTPS measurement (α_{FTPS}) and the DeOSt calculation ($\alpha DeOSt$) used during TLBO algorithm:

$$RMSE_\alpha(X) = \sqrt{\frac{\sum_{i=1}^{k} \left(\frac{\alpha_{FTPS}(\lambda_i) - \alpha_{DeoSt,X}(\lambda_i)}{\alpha_{FTPS}(\lambda_i)}\right)^2}{k}} \tag{4.52}$$

where k is the number of wavelength steps in the absorption coefficient spectrum and α_{DeOSt} is calculated using the set of DOS parameters X inputted in DeOSt. The value of $RMSE_\alpha$ ideally should become zero when the exact values of DOS parameters are found. But, in reality we rather expect a small finite difference between the experimental and calculated absorption coefficient spectra. Hence, a lower value of fitness function represents a better agreement between the absorption coefficient spectrum calculated by DeOSt and measured by FTPS.

However, the value of the fitness function is set very high if the DOS model sets in DeOSt result in a non tolerable value of activation energy measured using the steady state photoconductivity measurement (SSPC), $E_a = E_G - E_F$. It means that even though the RMSE is very small, if the deviation of E_a is high, the RMSE will be set in a higher value, i.e 9999. In this way, the activation energy measured by SSPC becomes a critical parameter for the fitting of α and introduces a strengthful constraint that should help to refine the determination of DOS parameters.

In this work, a set of DOS parameters is defined as a learner X_i. An individual DOS parameter is considered as a subject. Thus, a learner X_i learns a number of defined subjects, which depends on the type of DOS model used. For instance, if the DOS model is the standard one, learner will learn 17 subjects and 15 when using defect-pool DOS model. The overall performance of X_i is determined using the value of the fitness function, which depends on each DOS parameter (subject). The values of these parameters are modified through continuous evolution using the TLBO algorithm via teacher and learner phases by taking into account the fitness of X_i. The adjustment of the values of DOS parameters is done in such a way that the fitness function in Eq. (4.52) is minimized.

The TLBO algorithm is executed using primarily three control variables which are population size, number of iterations and the search space, which is the range of

value for each DOS parameter. These control variables are set as input parameters in the program, although the number of iterations can be excluded in the control variables if the minimum value of fitness is prioritized. The flow chart detailing the TLBO algorithm for the extraction of DOS parameters is shown in Fig. 4-6.

4.2.3 Results and discussion

The accuracy and reliability of the TLBO algorithm for the DOS parameters extraction was verified using a synthetic absorption coefficient spectrum calculated through the DOS modeling in DeOSt. The synthetic absorption coefficient curve is calculated from a DOS model, which is defined by the DOS parameters in the DeOSt software. The DOS parameters used are the ones of typical a-Si:H thin films as proposed by O. Saadane in [91]. The accuracy of the program is validated through the evaluation of the DOS parameters values obtained as well as the form of the absorption coefficient spectrum. The control variables of the program are the population size, number of iterations, and the search space (the range of values of a DOS parameter of a typical a-Si:H thin film). The population size was fixed at 100 and the iteration number was set at 10000. After the validation of the program, the TLBO algorithm can be applied to model the DOS linked to an absorption coefficient experimentally obtained by FTPS measurement.

In order to propose a systematic approach for the DOS parameters extraction, first we should suggest an approximation of the search space of the DOS parameters from the absorption coefficient spectrum. From the absorption coefficient spectrum, we can estimate characteristic values such as: the band gap energy (E_G), temperature of the valence band tail exponential distribution (T_{V2}), and the difference of the density of states in the band tail and defect region ($\Delta N(E)$). The standard deviation (σ) of the defect states can also be estimated if the region in the absorption coefficient which corresponds to the defect states is visible. As in DeOSt only the second band tail exponential distribution can be set, for the reading simplicity, from this point the T_{V2} and T_{C2} will be denoted as T_V and T_C.

For a given absorption coefficient, the one of the synthetic absorption coefficient in Fig. 4-7, we can estimate the search space of those four DOS parameters using the procedures explained in the following paragraph.

The E_G value can be estimated from the energy where the exponential band tail joins the parabolic extended band. In the absorption coefficient spectrum, this energy is where the exponentially increasing part of the spectrum starts becoming more parabolic. Using Fig. 4-7, the estimated E_G is 1.74 eV. The T_V can be estimated from the Urbach slope of the absorption coefficient spectrum. The relation between the exponentially decaying band tail state with the Urbach energy is described by :

$$\alpha = \alpha_0 \exp\left(\frac{E - E_0}{E_{Urbach}}\right) \tag{4.53}$$

where

$$E_{Urbach} = kT_v \tag{4.54}$$

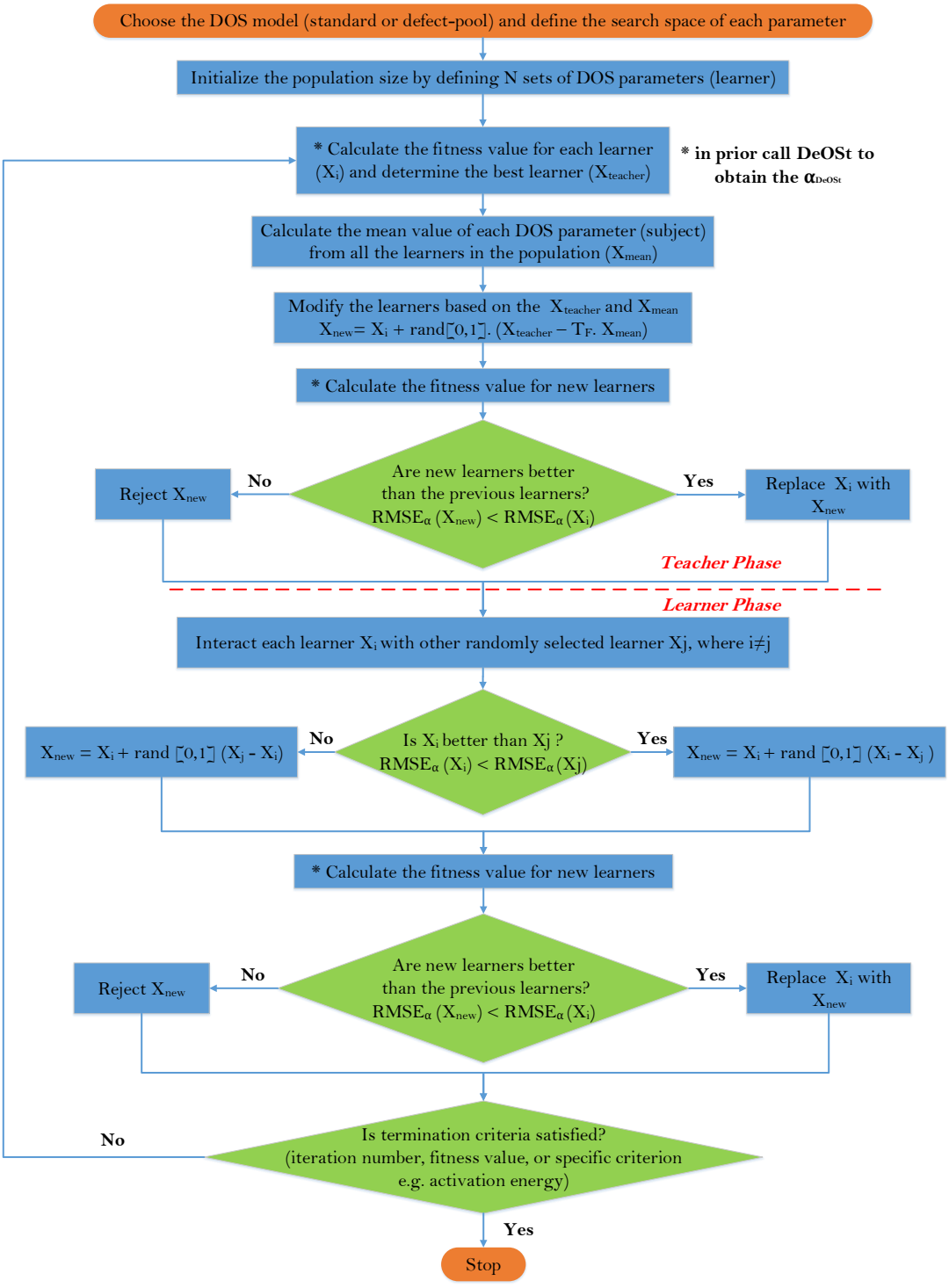

Figure 4-6: The flow chart of the extraction of DOS parameters using the TLBO algorithm.

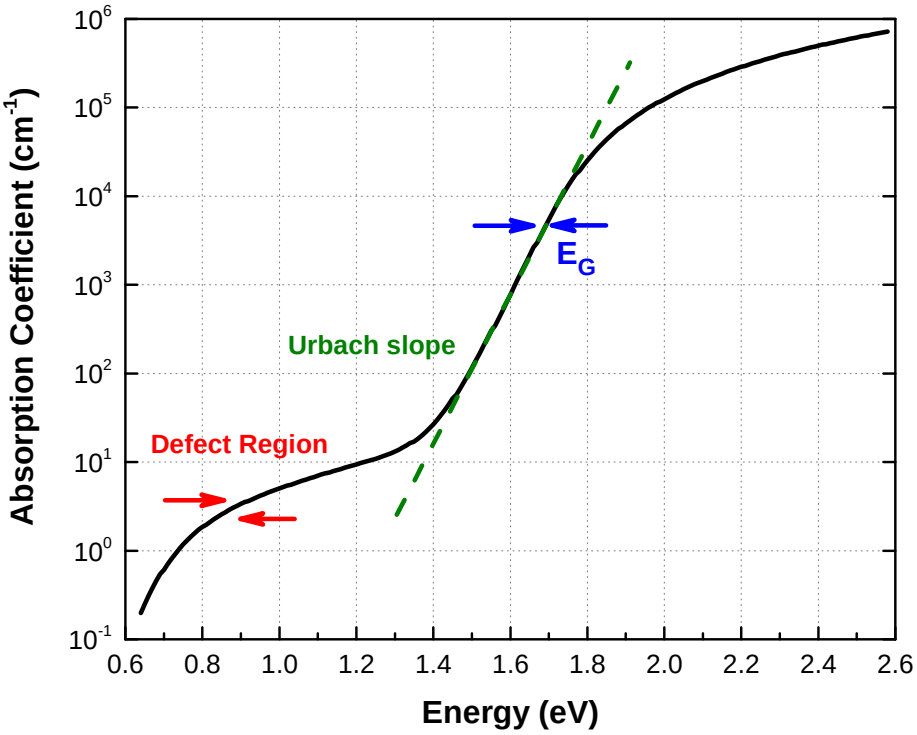

Figure 4-7: Synthetic absorption coefficient calculated from a designed DOS model in DeOSt software with an activation energy E_a=0.705 eV.

k being the Boltzmann constant.

Hence, from Fig. 4-7, we obtained 53 meV of Urbach energy, which corresponds to a value of the valence band tail temperature of 614 K. The difference of the density of the band tail and defect states can be estimated using the ratio of the absorption coefficient value where we obtain the band gap energy and the defect region. From Fig. 4-7 we obtain the ratio of $\simeq 10^4$. Hence, if we set a certain density of states value in the band tail states, the density of the defect states has to be at least 10^4 times lower. The value of the σ of the defect state distributions were estimated around 0.1 to 0.3 eV. These four parameter values were set in the DOS model with a narrow search space, whereas the other parameters were set with a rather wider search space.

From the four parameters that were estimated, the estimated value of T_V cannot be used directly as the real T_V in the DOS model. The difference between the estimated and real T_V is explained using Fig. 4-8.

An over estimation value of T_V is due to the fact that the extended conduction band state distribution is parabolic. The electron transitions from the valence band tail states for a given energy reach a higher value of the extended states of conduction band when the transition is conducted by the electrons in the higher energy of the valence band tail states. These electrons will arrive in the parabolic extended conduction band state, and the calculated absorption coefficient, which is the convolution product of the initial and final state, is higher. Due to this fact, we finally perceive a higher T_V (slower slope) in the synthetic absorption coefficient spectrum. Thus, it can

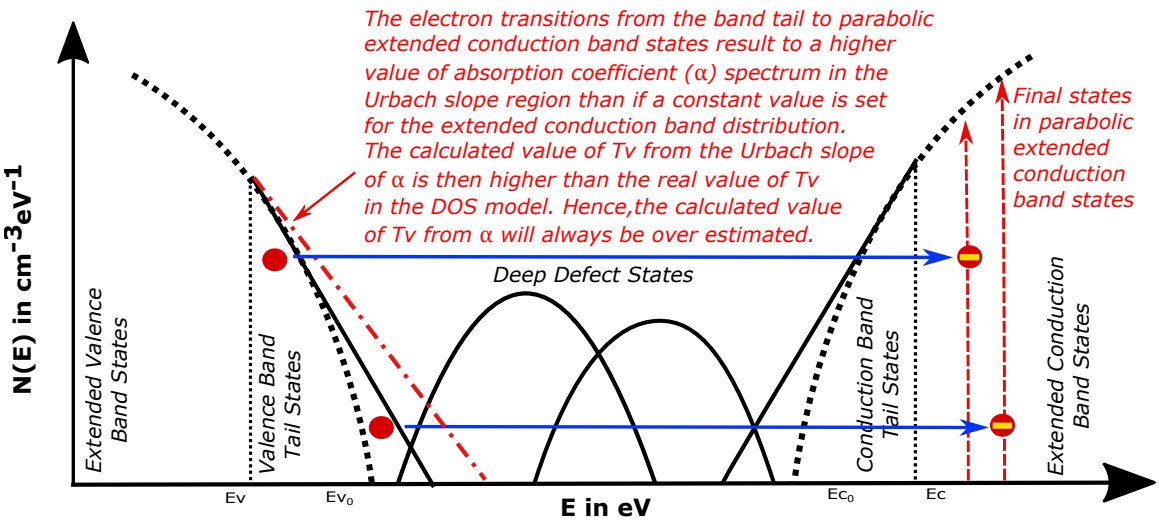

Figure 4-8: Illustration of the electron transitions from the valence band tail states which cause an over estimation of T_V calculated from absorption coefficient spectrum.

be concluded that the value of T_V which is estimated from the synthetic absorption coefficient will always be over estimated, if the contribution of the parabolic extended conduction band states is neglected. Hence, by taking into consideration these possible transitions, a lower value of T_V (than the one estimated from the Urbach slope) is expected to give a more accurate DOS model of the measured sample.

Determination of standard DOS parameters using the TLBO algorithm

The synthetic absorption coefficient in Fig. 4-7 was calculated from a standard DOS model using the parameters as in Table 4.3 (see page 115), hence involving two defect states with Gaussian distributions and two exponential distributions for the band tail states. The band tail states which were modeled in DeOSt consist of two exponential distribution functions (for each band side; valence and conduction) with a rather similar slope. It means that although there are two exponential functions, the slopes of these two functions are nearly the same, so that it resembles very much as if there was only one exponential function.

The DOS parameters' search space is represented in Table 4.3 (see page 115). The search spaces of the four previously estimated parameters are narrower than the other parameters, because the deviation of these parameters values should respect the values which have been calculated using the concepts of physics. With these DOS parameters, the TLBO algorithm is executed to find the best suited DOS model for the synthetic absorption coefficient presented in Fig. 4-7.

Fig. 4-9A shows the evolution between the fitness value of the teacher set of the DOS parameters in the population and the individual DOS parameter with the standard model, as function of the iteration number. Fitness value is calculated from the fitness function, which described the matching of the synthetic and calculated absorption coefficient, and the matching of the activation energy (see Fig. 4-10 for

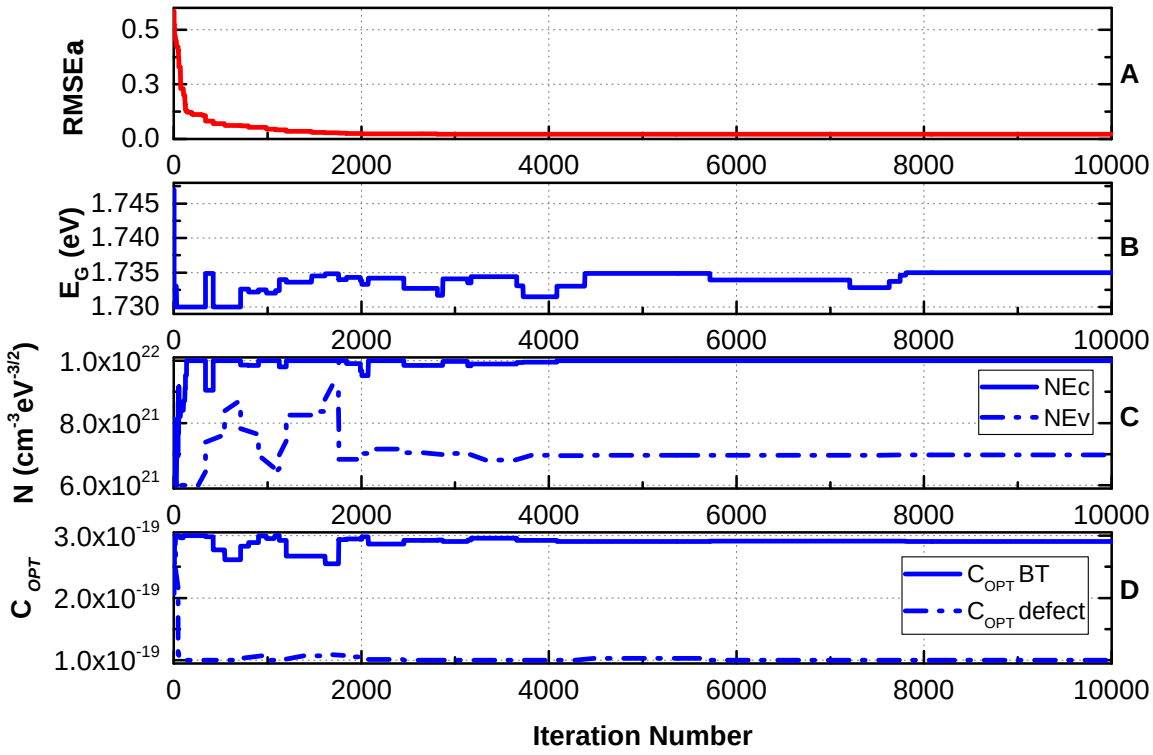

Figure 4-9: Evolution of the (A) fitness value (RMSE_α), (B) band gap energy, E_G, (C) density of exponential valence and conduction band tail state distributions, N_{EV} and N_{EC}, and (D) optical matrix element of band tail and defect state distributions, C_{BT}^{opt} and C_{Def}^{opt}, in the TLBO program.

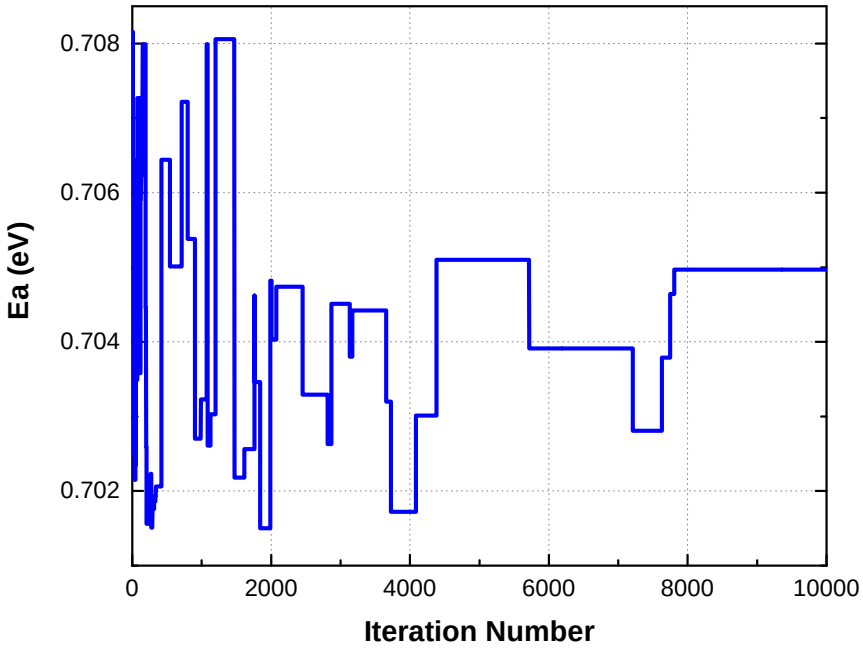

Figure 4-10: Evolution of the activation energy, E_a, in the TLBO program.

the evolution of the activation energy values). The low value of fitness thus represents a good agreement of the absorption coefficient spectra shape and the activation energy value.

As seen in Fig. 4-9A, the fitness value at the first iteration is 0.5845 and then this value sharply decreases to 0.050 at iteration number 1000. This value keeps decreasing to 0.025 at the iteration number 2000, which can be seen as the end of the transient response of the fitness value. After iteration 2000, the fitness value decreases steadily with the progress of the iteration number. By the last iteration, 10000, the fitness value is down to 0.021.

The evolution of the fitness value is driven by the evolution of the DOS parameters. In Figs. 4-9B to 4-9D, the evolution of five DOS parameters, E_G, N_{EV}, N_{EC}, C_{BT}^{opt} and C_{Def}^{opt}, in the TLBO program are presented. When the fitness value tends to decrease in the transient region, the value of E_G follows an extreme decrease and then continues to rise until 2000 iterations (see Fig. 4-9B). The value of E_G beyond 2000 iterations oscillates very slightly, and finally converges at 1.735 eV.

For the N_{EC} and N_{EV} parameters, the evolution of their values is as E_G. However, in the transient region, below 2000 iterations, the value of N_{EC} as presented in Fig. 4-9C is rather more stable than the N_{EV} value. The value of N_{EC} starts to stabilize at 1400 iterations, and finally the value converges at 1.000×10^{22} $cm^{-3}.eV^{-3/2}$. The value of N_{EV} keeps increasing up to 2000 iterations, after its downfall at 100 iterations. A rapid decay is present at 1800 iterations, and then from this iteration the N_{EV} value remains quite stable and converges at 6.978×10^{21} $cm^{-3}.eV^{-3/2}$.

The drop of the fitness value in the early iteration number translates a sharp increase of the optical matrix parameters values for the band tail distributions, C_{BT}^{opt}, and a sharp decrease of the same parameter for the defect distributions, C_{Def}^{opt}, as depicted in Fig. 4-9D. The value of C_{BT}^{opt} tends to oscillate in the upper bound region of its search space up to 4000 iterations, then it starts to stabilize and converge at 2.906×10^{-19} in the end of the iteration. In the other hand, a sharp decrease is present at the C_{Def}^{opt} value in the early iteration numbers, followed by a rather stable oscillation in the lower bound of the search space region. The C_{Def}^{opt} value is slightly increasing up to 2000 iterations then it drops and is steadily converging to 1.004×10^{-19}.

The band tail DOS parameters evolution during the TLBO program is presented in Fig. 4-11. Compared to the evolution of the fitness value in the first 2000 iterations, the conduction band tail distribution temperature, T_C, shows a similar transient response as the fitness value, with a reciprocal evolution (see Fig. 4-11B). The T_C starts to increase when the fitness value decreases, while both of these parameter values tends to stay stable after 2000 iterations. At the end of the iterations, T_C is converging toward 392.1 K. In response to the fitness value evolution, the value of T_V remains quite stable at around 530 K throughout the iteration process and converges at 536.28 K at the end of the iterations.

In the very beginning of the iterations, both of the densities of the second exponential band tail distributions are increasing, while only after the 100 first iterations, the value of N_V^{ext} dropped, as can be seen in Fig. 4-11C. N_V^{ext} value starts to increase again after 740 iterations while N_C^{ext} remains decreasing up to 2000 iterations. Both

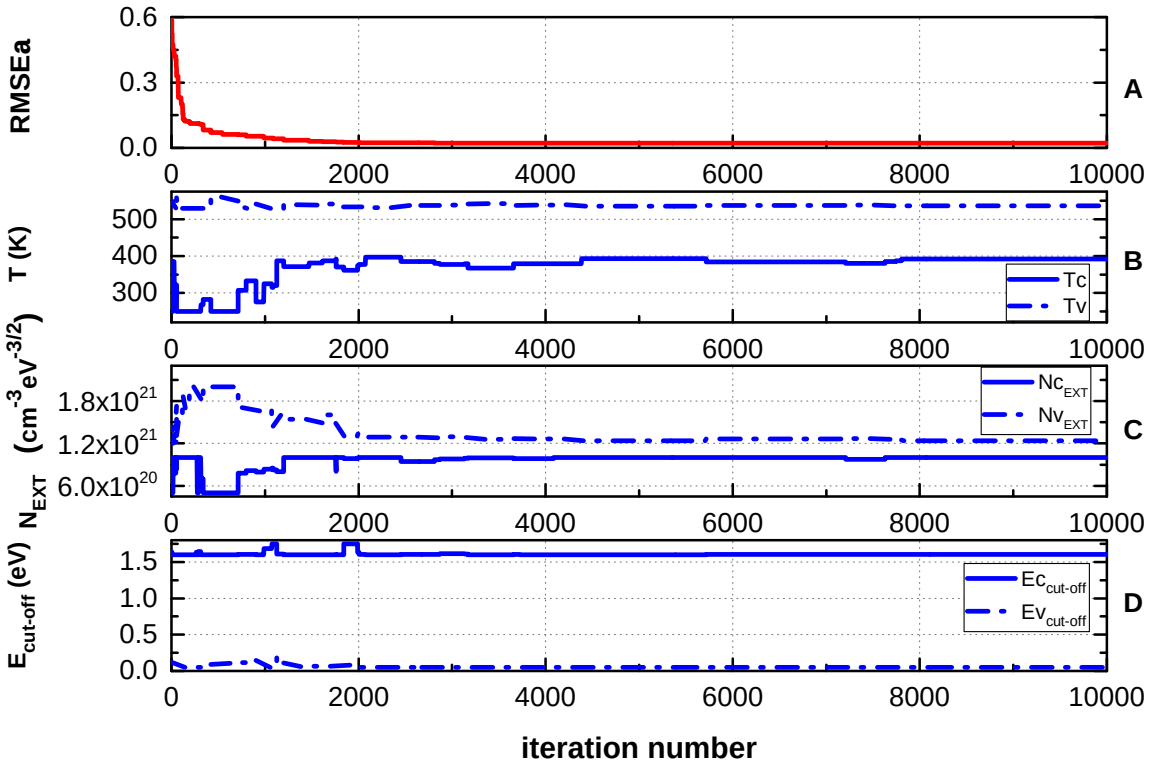

Figure 4-11: Evolution of the (A) fitness value, RMSE_α (B) valence and conduction band tail temperature, T_V and T_C, (C) density of the second exponential valence and conduction band tail state distribution, N_V^{ext} and N_C^{ext}, and (D) cut-off energy where the two exponential band tail distributions meet. $E_V^{cut-off}$ stands for the valence band tail and $E_C^{cut-off}$ for the conduction band tail side, in the TLBO program.

of the parameters stabilise and converge quite rapidly afterwards at 1.239×10^{21} and 1.000×10^{21} $cm^{-3}.eV^{-1}$, for N_V^{ext} and N_C^{ext} respectively.

As two exponential band tail distributions are present in the DOS model, an energy where these two distributions meet has to be defined, $E^{cut-off}$. The search space of these two parameters as in Table 4.3 (see page 115) is chosen to agree with the band positioning in the DOS model, where $E_C^{cut-off}$ is towards the conduction band side closer to the band gap energy and $E_V^{cut-off}$ is closer to the valence band side, close to 0 eV. The value of $E_C^{cut-off}$ in Fig. 4-11D starts to rise up to 1000 iterations and slowly decreases up to 2000 iterations. Afterwards, $E_C^{cut-off}$ still decreases very slightly throughout the whole iteration and finally converges toward 1.604 eV. For the $E_V^{cut-off}$, the evolution is quite stable despite a few extreme drops and rises between the 1000 and 1800 iterations. These instabilities stop at 2000 iterations and then stabilizes (see Fig. 4-11D). $E_V^{cut-off}$ was found at 0.050 eV at the last iteration.

Fig. 4-12 represents the evolution of the deep-defect states distribution parameters in the DOS model during the TLBO program. A sharp decay in the first 200 iterations of the maximum donor density, N_{Don}^{max} (Fig. 4-12B), value is followed by the lowering of the fitness value. While throughout the iteration process the fitness value

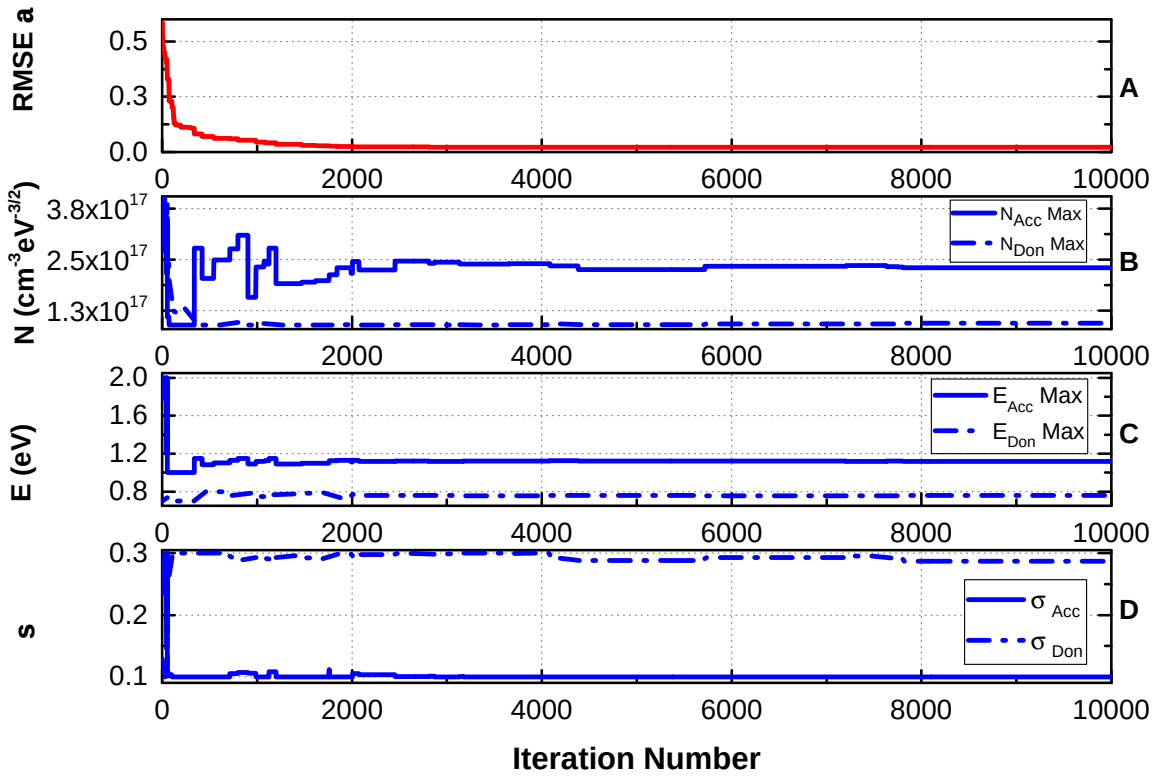

Figure 4-12: Evolution of the (A) fitness value, RMSE_α (B) maximum density of the acceptor and donor in the defect distributions, N_{acc}^{max} and N_{don}^{max}, (C) energy position where the density of the defect is at maximum, E_{acc}^{max} and E_{don}^{max}, and (D) standard deviation of the defect Gaussian distributions, σ_{acc} and σ_{don}, in the TLBO program.

keeps decreasing, the evolution of N_{Don}^{max} value is quite steady after 600 iterations and converges at 9.463×10^{16} $cm^{-3}.eV^{-1}$ at the end. For the acceptor side, the N_{Acc}^{max} drops at 200 iterations and slowly rises to almost the double of its value until the 2000 iterations, and then stabilizes. N_{Acc}^{max} was found at 2.303×10^{17} $cm^{-3}.eV^{-1}$ at the lowest fitness value.

The value of E_{Acc}^{max} is close to the band gap energy value initially and then it falls after the 15^{th} iteration, as presented in Fig. 4-12C, followed by slow rise until 2000 iterations and finally set at 1.120 eV at the lowest fitness value. For the donor distribution, the value of E_{Don}^{max} follows a small increase from the beginning of the iteration and remains steady around 0.760 eV throughout the iteration process.

The evolution of the standard deviations of the Gaussian defect distributions, σ, is presented in Fig. 4-12D. The search space of this two parameters are set the same. In the first iteration, the value of σ_{Acc} and σ_{Don} of the teacher set was found at 0.274 and 0.129 eV, respectively. These values changed quite drastically in the first 20 iterations. σ_{Acc} value is decreased while σ_{Don} value is increased drastically. After this extreme change of value, both of these parameters stays stable although tiny oscillations occur throughout the iteration process. Finally, at the end of iterations, the value of both of these parameters are converging toward 0.100 and 0.287, for σ_{Acc}

Table 4.3: Comparison of the standard DOS model parameter values by the TLBO algorithm with the values set in DeOSt (for the synthetic absorption coefficient, α).

Parameter	Search Space	Estimated Value	Real Value in DeOSt (for synthetic α)	Value by TLBO	Relative Error (%)	Fitness Value
E_G	[1.730; 1.750]	1.740	1.730	1.735	0.02	
N_{EV}	$[6.000 \times 10^{21}; 1.000 \times 10^{22}]$	$10^4 \times N_{defect}^{max}$	6.850×10^{21}	6.978×10^{21}	1.87	
N_{EC}	$[6.000 \times 10^{21}; 1.000 \times 10^{22}]$		9.810×10^{21}	1.000×10^{22}	1.94	
C_{BT}^{opt}	$[1.000 \times 10^{-19}; 3.000 \times 10^{-19}]$		3.000×10^{-19}	2.906×10^{-19}	3.12	
C_{Def}^{opt}	$[1.000 \times 10^{-19}; 3.000 \times 10^{-19}]$		1.000×10^{-19}	1.0044×10^{-19}	0.44	
T_V	[530.00; 560.00]	614.00	530.00	536.28	1.18	
N_V^{EXT}	$[5.000 \times 10^{20}; 2.000 \times 10^{21}]$		1.070×10^{21}	1.239×10^{21}	15.74	
$E_V^{cut-off}$	[0.050; 0.300]		0.050	0.0502	0.30	
T_C	[250.00; 400.00]		400.00	392.10	2.20	0.021
N_C^{EXT}	$[5.000 \times 10^{20}; 1.000 \times 10^{21}]$		1.290×10^{21}	1.000×10^{21}	22.48	
$E_C^{cut-off}$	[1.600; 1.750]		1.700	1.604	5.64	
N_{don}^{max}	$[9.000 \times 10^{16}; 4.000 \times 10^{17}]$		1.022×10^{17}	9.463×10^{16}	7.40	
E_{don}^{max}	[0.700; 0.800]		0.730	0.759	3.96	
σ_{don}	[0.100; 0.300]	[0.100; 0.300]	0.290	0.287	0.90	
N_{acc}^{max}	$[9.000 \times 10^{16}; 4.000 \times 10^{17}]$		2.065×10^{17}	2.303×10^{17}	11.53	
E_{acc}^{max}	[1.000; 2.000]		1.110	1.120	0.89	
σ_{acc}	[0.100; 0.300]	[0.100; 0.300]	0.100	0.100	0	

and σ_{Don} respectively.

The DOS parameters values of the teacher set which were found at the lowest fitness value are summarized in Table 4.3. In this Table, the relative error value is the relative error of each parameter value obtained by TLBO with respect to the value set previously in DeOSt to model the synthetic absorption coefficient, α, spectrum. The value of relative error varies in the range 0-22.48 %. The four highest relative error values are found for density related parameters, in the band tail and defect states distributions, N_V^{EXT} ,N_C^{EXT}, N_{don}^{max}, and N_{acc}^{max} . The explanation of why this value of relative error is acceptable will be explained in the following paragraphs. For the other parameters, the relative error varies in the range 0-5.64 %, which is in the range of acceptable margin of error and moreover this level of error still yields a very small, 0.021 cm^{-1}, error in the final result for α as depicted in Fig. 4-13A. A good agreement between the synthetic absorption coefficient spectrum and the one calculated from the DOS parameters found by TLBO algorithm can be seen in Fig. 4-13A. At the lowest fitness value, identical absorption coefficient spectrum shape and activation energy between the synthetic and TLBO spectra are obtained.

In Fig. 4-13B, the DOS model of each corresponding absorption coefficient is presented. It can be seen that despite a good agreement of the absorption coefficient, the DOS model found using TLBO differs very slightly from the designed DOS model for synthetic absorption coefficient spectrum. From both DOS model, it can be seen that a steeper slope in the valence band tail side for the TLBO DOS is compensated by a slower slope in the conduction band side. Hence, the convolution product of possible electronic transitions in these energies range should be very similar. In this case, it can be seen that in the α comparison (in Fig. 4-13A) at the energy range of 1.2-1.6 eV, the TLBOα and synthetic α have almost identical values. In the deep-defect region, the same phenomenon occurs for the donor and acceptor distributions. A lower density of donor in the TLBOα DOS model is compensated by a higher density of acceptor type defect, resulting in similar values of α at the energy below 1 eV. Due to these compensations, a high relative error value of these parameters does not affect very much the final result, i.e. α.

Determination of defect-pool DOS parameters using the TLBO algorithm

As the TLBO algorithm was successful to reproduce the absorption coefficient with a standard DOS model, similar effort was done to reproduce the absorption coefficient using a defect-pool DOS model. The same procedure of DOS parameter estimation is applied to the synthetic absorption coefficient spectrum using defect-pool model as shown in Fig. 4-18A with red points. The estimated parameters calculated from that spectrum are E_G at 1.72 eV, T_V at 615 K, difference of the density between the band tail and defect states of the order of 10^4, and σ_{Pool} of the defect states at 0.1-0.3 eV. The value of T_V was found to be over estimated from the spectrum itself as in the case of the standard DOS model. Hence, -5 % of the estimated value of T_V will rather be an upper bound in term of the search space of T_V in the TLBO algorithm. The extraction of the defect-pool model DOS parameters was conducted using the same population size, 100, as for the standard model. A lower iteration number, 5000,

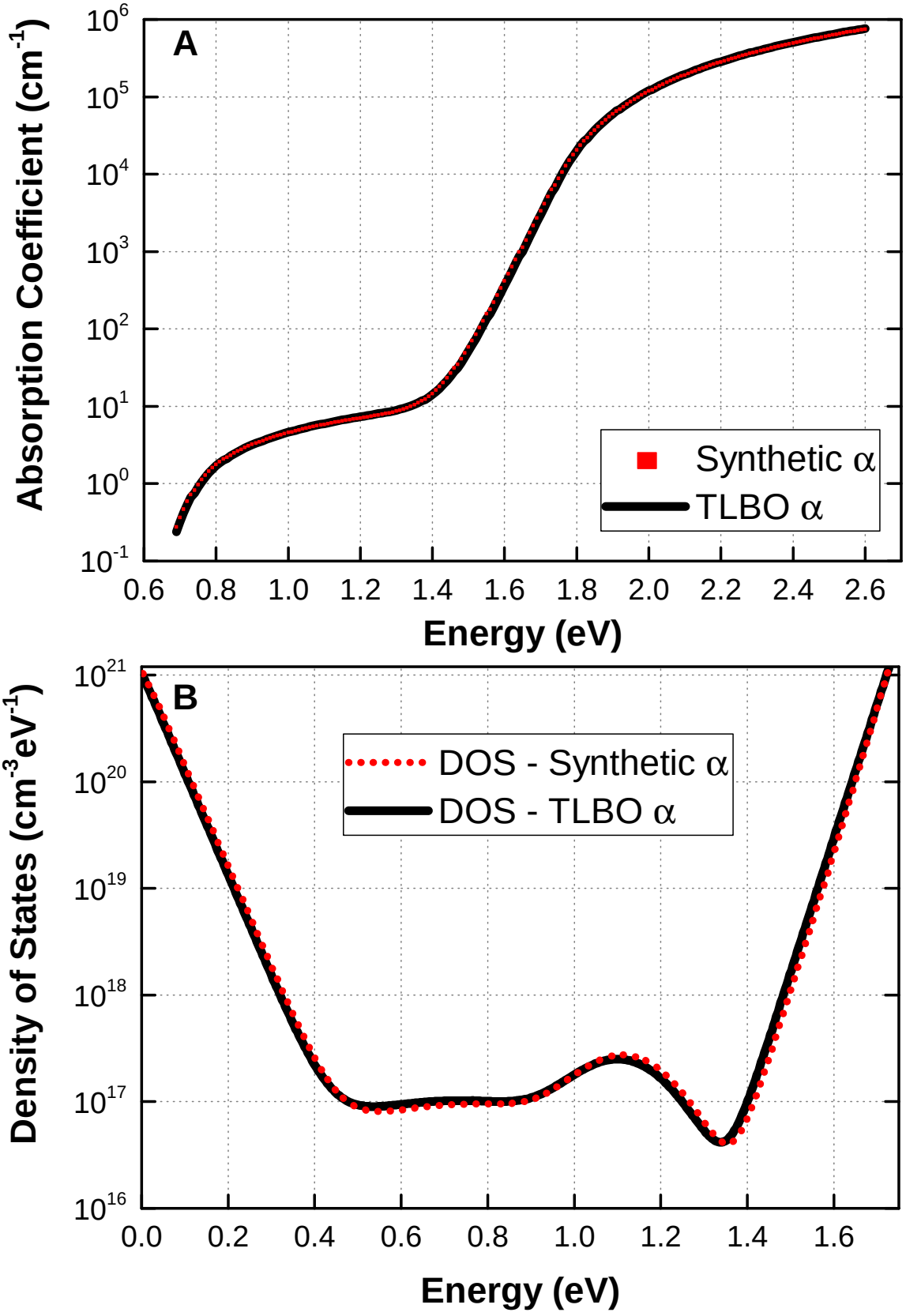

Figure 4-13: Comparison of the A.) Synthetic and TLBO-driven absorption coefficient spectra B.) DOS models corresponding to the absorption coefficient spectra.

was chosen due to the convergence of parameter values after 4000 iterations in the standard DOS model. A lower iteration number is chosen due to the convergence of parameter values after 4000 iterations in the standard DOS model. Note that the number of DOS parameters in the defect-pool model is 15.

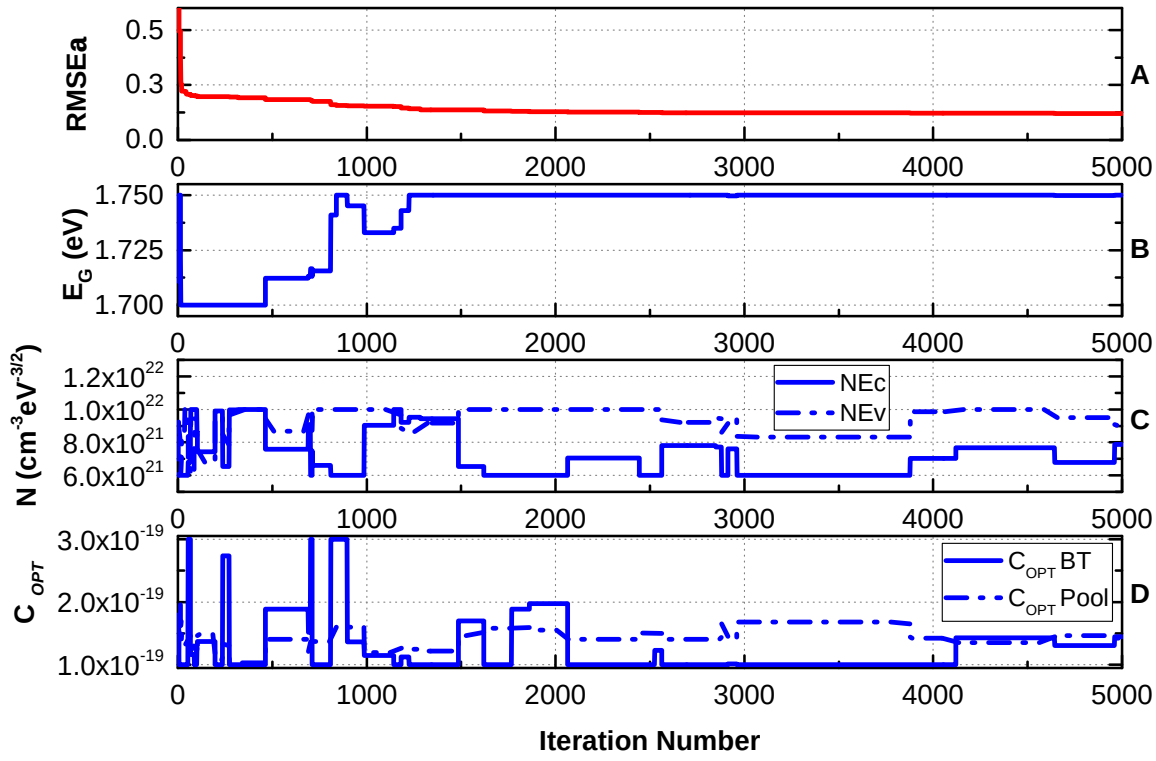

Figure 4-14: Evolution of the (A) fitness value (RMSE_α), (B) band gap energy, E_G, (C) density of exponential valence and conduction band tail state distribution, N_{EV} and N_{EC}, and (D) optical matrix element of band tail and defect state distributions, C_{BT}^{opt} and C_{Pool}^{opt}, in the TLBO program using the defect-pool DOS model.

The evolution of the extended bands distribution parameters and the α fitness value are presented in Fig. 4-14. From the figure, it can be seen that the fitness value is constantly decreasing until the end of the iteration numbers. When the fitness value drops, the E_G value drops from 1.750 to 1.700 eV until 500 iterations and then it starts to increase to 1.750 eV. As the fitness value stays quite stable at 2000 iterations, the E_G tends to remain steady, and converges at 1.750 eV by the end of iteration numbers. The density of the extended valence band distributions, N_{EV}, as shown in Fig. 4-15C shows a more stable evolution compare to that of the conduction band, N_{EC}. By the end of the iteration number, the N_{EV} converges at 9.042×10^{21} and N_{EC} at 7.875×10^{21} $cm^{-3}eV^{-3/2}$. Though the search space of the optical matrix coefficient of the band tail and deep defect distributions are set the same, during the early iteration numbers the value of that of the deep defect tends to oscillate towards its upper bound while for the band tail it remains at its lower bound value. Since then, the value of these optical matrix coefficients remain very

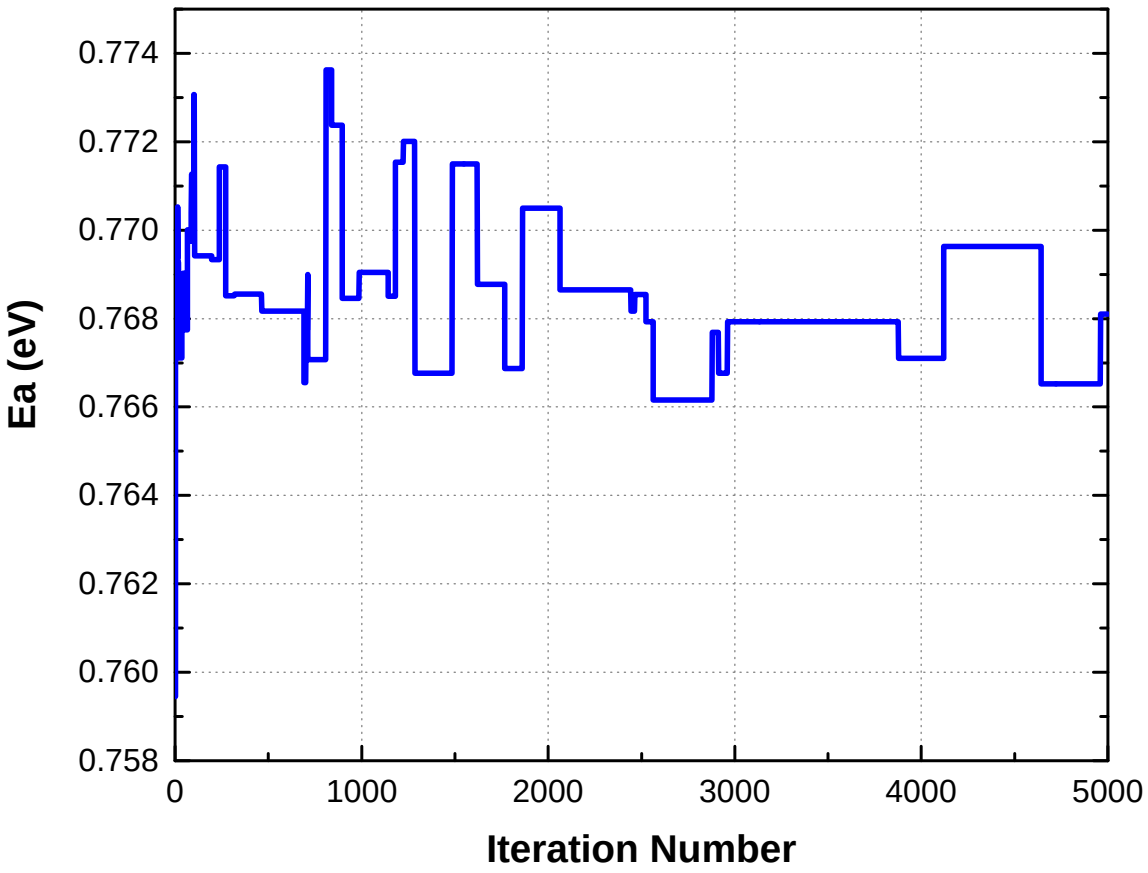

Figure 4-15: Evolution of the activation energy, E_a, in the TLBO program using defect-pool DOS model.

steady. C_{OPT}^{BT} and C_{OPT}^{Pool} were set at 1.425×10^{-19} and 1.447×10^{-19}, respectively by the end of the iteration numbers.

The activation energy for this respective absorption coefficient spectrum was given at 0.770 eV, and as the number of iteration increases, E_a first dropped at 0.758 eV and not long afterwards it stays in the range of 0.767-0.772 eV (see Fig. 4-15), which yields 0.2-0.4% of error from the given value.

The evolution of the band tail distribution parameters using the defect pool DOS model as a function of iteration number is represented in Fig. 4-16. The T_V remains steady at its lower bound from the first iteration, as the search space of this parameter is quite narrow due to the previously estimated value using the Urbach slope of the absorption coefficient. The increase of T_C in the beginning of the iteration numbers and frequent small oscillations of its value can be understood as the search space of this parameter is quite large compare to T_V. T_V and T_C are found at 551.68 and 393.41 K, respectively, at the end of iterations. In Fig. 4-16C, the evolution of N_V^{EXT} and N_C^{EXT} is presented. Between these two parameters, N_C^{EXT} yields more instability compare to N_V^{EXT}, which can be caused by the evolution of T_C. N_V^{EXT} and N_C^{EXT} are found at 9.638×10^{20} and 2.000×10^{21} $cm^{-3}eV^{-1}$ at the lowest fitness value. For the cut-off energy which defines where the two exponential band tail distributions meet,

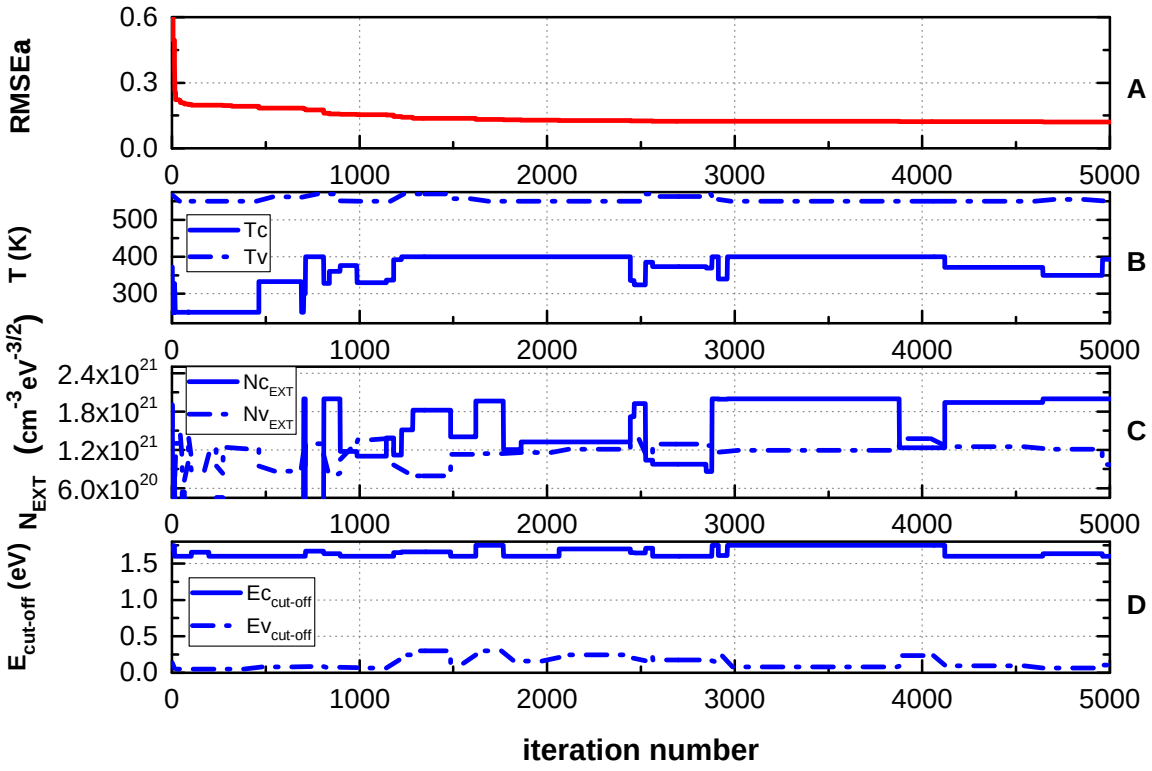

Figure 4-16: Evolution of the (A) fitness value, RMSE_α (B) valence and conduction band tail temperature, T_V and T_C, (C) density of the second exponential valence and conduction band tail state distribution, N_V^{ext} and N_C^{ext}, and (D) cut-off energy where the two exponential band tail distributions meet. $E_V^{cut-off}$ stands for the valence band tail and $E_C^{cut-off}$ for the conduction band tail side, in the TLBO program using defect-pool DOS model.

the changes throughout the iteration number are very stable. This is mainly caused by a very narrow search space of these parameters and also because of the constraints put into the DeOSt program that the first and second exponential should vary very slightly. At the lowest fitness value, 0.103 and 1.601 eV are found for $E_V^{cut-off}$ and $E_C^{cut-off}$, respectively.

The evolution of the deep defect distribution parameters using the defect-pool DOS model is represented in Fig. 4-17. The hydrogen concentration proceed an increasing trend when the fitness value is decreasing. In the early iterations, the H is varied between 2.000×10^{21} and 5.0×10^{21}, and then its value started to increase to 8.000×10^{21} at the 1600 iterations. From this time on, the H stays in the range of 4.000×10^{21} to 8.000×10^{21} cm^{-3}, and at the end of iteration it is set at 7.494×10^{21} cm^{-3}. The correlation energy does not vary much through the iteration numbers, as the search space is limited by the proposed physical value by Powell and Deane [56]. The same steady trend is followed by the E_{Pool} which defines the energy of the maximum of D^+ distribution. At the lowest fitness value, E_U and E_{Pool} are found at 0.112 and 1.049 eV, respectively. The evolution of the standard deviation of the deep

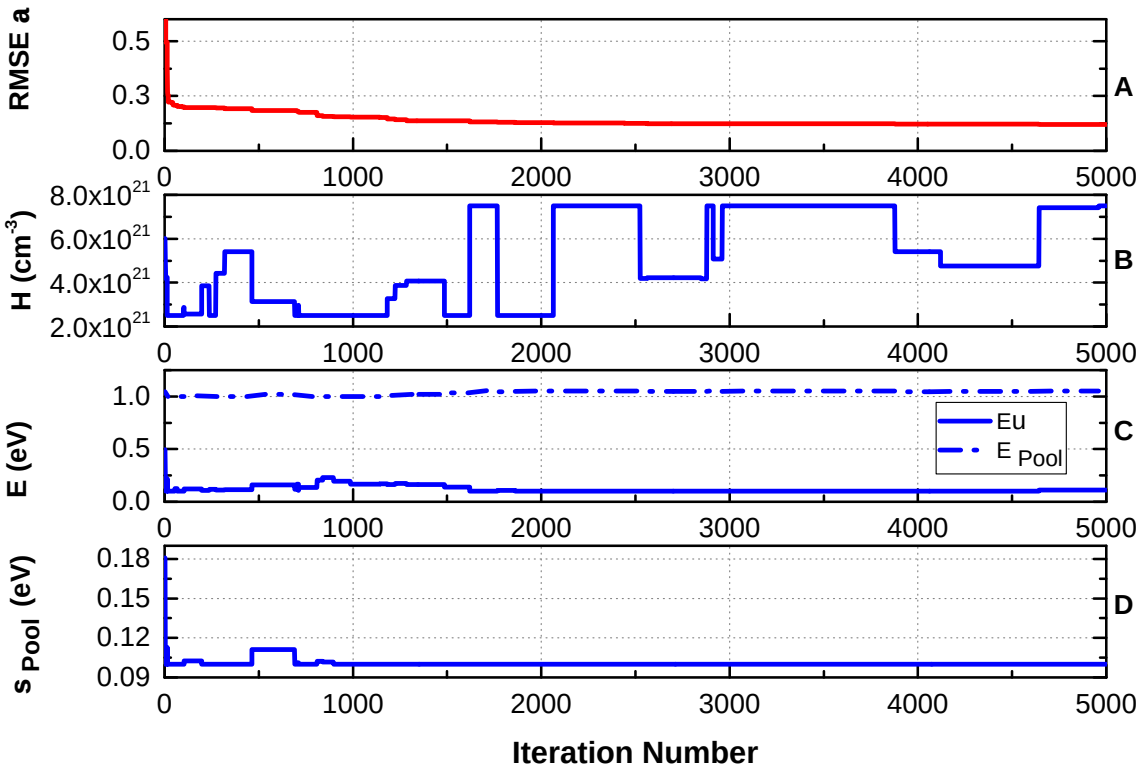

Figure 4-17: Evolution of the (A) fitness value, RMSE_α, (B) concentration of hydrogen, H, (C) energy position of the potential defect-pool sites and correlation energy, E_{Pool} and E_U, and (D) standard deviation of the defect-pool Gaussian distributions, σ_{Pool}, in the TLBO program using defect-pool model DOS.

defect distribution using the defect-pool DOS model is shown in Fig. 4-17D. As can be seen, the variation tends to stay in the lower range of the search space although in the beginning of the iteration number the value is set at 0.18 eV. Starting at 1000 iterations, the value of σ_{Pool} is very steady and finally it converges to 0.10 eV by the end of the iterations.

Table 4.4 is given to summarize the performance of the TLBO algorithm to determine the defect-pool DOS model parameters. From the calculated relative error between the real value set in DeOSt and given by the TLBO algorithm, TLBO algorithm yields 0-4.67 % of error for the defect-pool DOS model, which is lower than when using the standard DOS model. The fitness value is found at 0.120 cm^{-1} at the 5000 iteration. This fitness value corresponds to the results given in the Fig. 4-18. From the results, it can be remarked that the TLBO algorithm has successfully reproduced the synthetic α that was previously constructed using the given set of defect-pool DOS model in DeOSt. A good agreement of α is not very surprising as can be seen from the comparison of the defect-pool DOS models in Fig. 4-18B, which are very similar to each other. A slight difference between the synthetic and TLBO defect-pool DOS model lies mainly at the D^- distribution at 0.6-0.8 eV. This slight disagreement may be caused by the diminution of the iteration numbers and hence

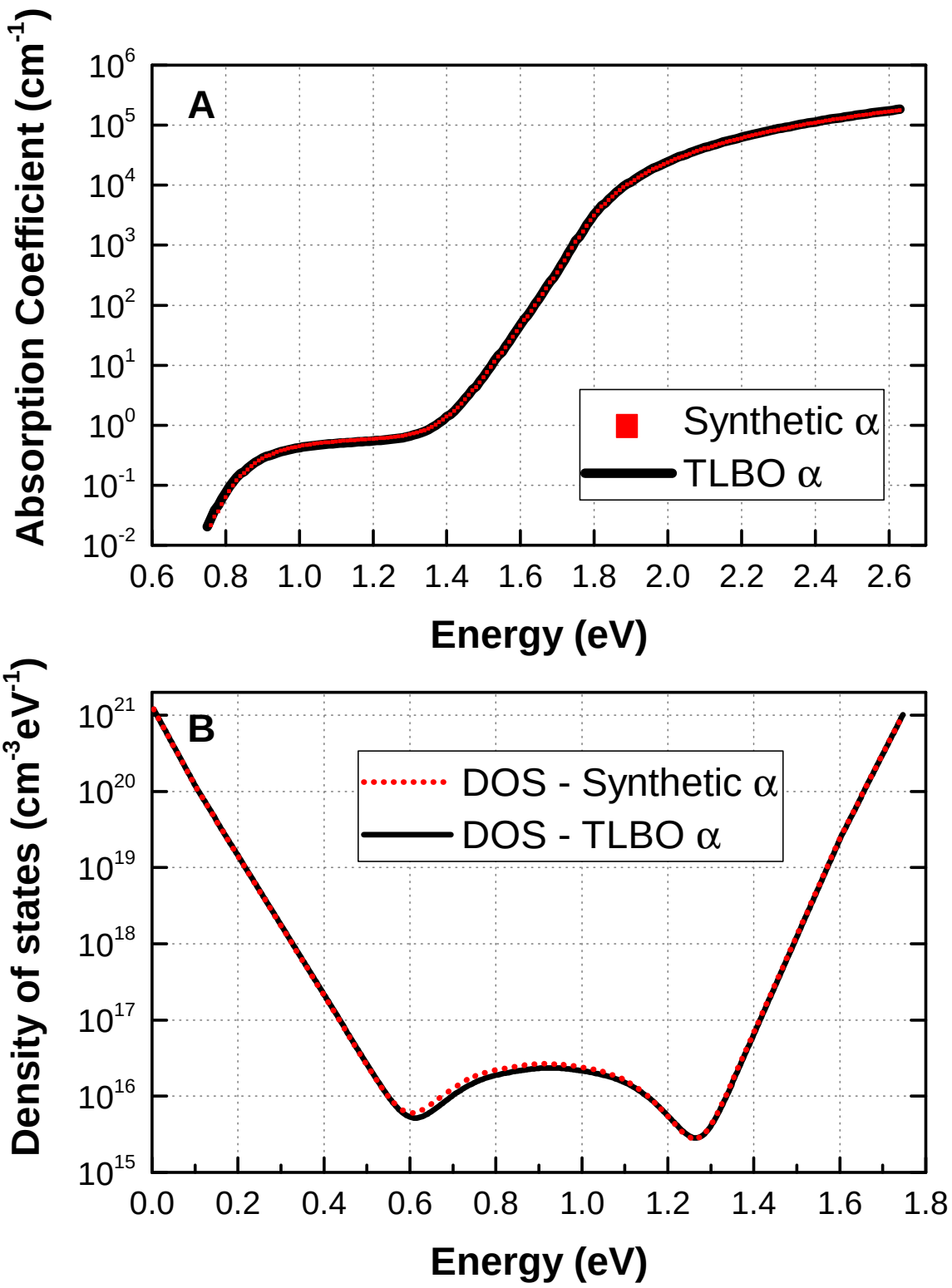

Figure 4-18: Comparison of the A.) Synthetic and TLBO-driven absorption coefficient spectrum B.) DOS model corresponding to the absorption coefficient spectrum using defect-pool DOS model.

Table 4.4: Comparison of the defect-pool model DOS parameter values by the TLBO algorithm with the values set in DeOSt (for the synthetic absorption coefficient, α).

Parameter	Search Space	Estimated Value	Real Value in DeOSt (for synthetic α)	Value by TLBO	Relative Error (%)	Fitness Value
E_G	[1.700; 1.750]	1.720	1.750	1.750	0.00	
N_{EV}	$[6.000 \times 10^{21}; 1.000 \times 10^{22}]$	$10^4 \times N_{defect}^{max}$	9.000×10^{21}	9.042×10^{21}	4.67	
N_{EC}	$[6.000 \times 10^{21}; 1.000 \times 10^{22}]$		7.900×10^{21}	7.875×10^{21}	3.16	
C_{BT}^{opt}	$[1.000 \times 10^{-19}; 3.000 \times 10^{-19}]$		1.400×10^{-19}	1.425×10^{-19}	1.78	
C_{Pool}^{opt}	$[1.000 \times 10^{-19}; 3.000 \times 10^{-19}]$		1.450×10^{-19}	1.447×10^{-19}	0.21	
T_V	[550.00; 570.00]	615.00	551.00	551.68	0.12	
N_V^{EXT}	$[1.000 \times 10^{20}; 2.000 \times 10^{21}]$		9.680×10^{20}	9.683×10^{20}	0.03	
$E_V^{cut-off}$	[0.050; 0.300]		0.100	0.103	0.03	0.120
T_C	[250.00; 400.00]		395.00	393.41	0.40	
N_C^{EXT}	$[1.000 \times 10^{20}; 2.000 \times 10^{21}]$		1.950×10^{21}	2.000×10^{21}	2.56	
$E_C^{cut-off}$	[1.600; 1.750]		1.600	1.601	0.06	
H	$[2.500 \times 10^{21}; 7.500 \times 10^{21}]$		7.450×10^{21}	7.494×10^{21}	0.59	
E_{Pool}	[1.000; 1.300]		1.050	1.049	0.09	
σ_{Pool}	[0.100; 0.300]	[0.100; 0.300]	0.100	0.100	0.00	
E_U	[0.100; 0.500]		0.110	0.112	1.81	

for a better agreement, a higher iteration numbers is advised to yield better results.

From the Tabs. 4.3 and 4.4, we can see that there are good agreements between the values that were set in DeOSt to produce the synthetic absorption coefficient and the values obtained by the TLBO algorithm. The results of the final absorption coefficients in Figs. 4-13 and 4-18 also demonstrate that the set of DOS parameters obtained by TLBO algorithm has successfully reproduced the synthetic absorption coefficient by constantly evolving the value of the DOS parameters linked to the absorption coefficient. The algorithm also showed very good performances for both standard and defect-pool model DOS. Hence, TLBO program can be validated for the determination of DOS parameters from the absorption coefficient as demonstrated with the above results.

By looking at the evolution of DOS parameters throughout the iteration number in the TLBO program, it can be remarked that each parameter evolves very differently. The evolution of the parameter in the TLBO program to yield a minimum fitness value though cannot be used as the reference of how the DOS parameters should be modified to obtain a good agreement with the given absorption coefficient. It should rather be considered that each parameter does not have the same significance toward the final result and that the absorption coefficient is mainly linked to the four parameters estimated from given absorption coefficient spectrum, which can be obtain from the FTPS measurement. Indeed, some parameters may influence significantly the final result and some are not very critical. In the next section, the importance of individual DOS parameter is studied and explained in detailed manner using the sensitivity analysis.

4.3 Sensitivity Analysis of DOS Parameters

As we can see from the results of the best set of DOS parameters using TLBO algorithm in the previous Section, each parameter evolved differently to lower the fitness value. These different ways of evolution of each parameter can be due to the different degree of influence or contribution of that parameter on the final result, which is the absorption coefficient spectrum. The degree of sensitivity is usually analyzed using a sensitivity analysis technique. The sensitivity analysis technique approached in this Section is based on one variable at time (OAT) method which is one of the variance based sensitivity analysis as introduced in [92]. OAT method studies the effect of one parameter change at a time, while keeping the other parameters constant. Sensitivity analysis methods are also used as a guide to assess scientific models and experiments as reported by Saltelli *et al.* in [93].

In the application of the sensitivity analysis of DOS parameters on the absorption coefficient spectrum, the study is conducted by: 1.) analyzing the impact of the change of each parameter value on the modification of the absorption coefficient spectrum shape, 2.) identifying the sensitivity of each DOS parameter using a quantification of the span of changes in the absorption coefficient value when a parameter value is changed, 3.) identifying the sensitivity of a parameter using the degree of freedom of each DOS parameter on the absorption coefficient. The following paragraphs

will further explain these three sensitivity analysis approaches.

The analysis of the impact of the modification of a parameter value on the change of the absorption coefficient spectrum shape is done first by setting a range of percentage of change in the parameter value. In this study, the parameter value is changed by +/- 30 % of its initial value. When one parameter value is changed, the initial DOS model is updated and used to calculate the absorption coefficient. The change of absorption coefficient spectrum shape is quantified using the percent of change of the absorption coefficient value at four different regions; 1.) defect region, 2.) Urbach slope region, 3.) high absorption region, 4.) below 0.8 eV region, this last region being important mainly in the defect-pool model DOS. The change of absorption coefficient value is calculated using Eq. (4.55).

$$\Delta\alpha = \sum_{i=1}^{k} \left| \frac{\alpha_m - \alpha_{init}}{\alpha_{init}} \right| \times 100 \ , \tag{4.55}$$

where k is the number of data points, α_m and α_{init} are the modified (using one modified DOS parameter value) and initial absorption coefficient, respectively. The change of absorption coefficient value at a specific region is calculated using the data points that only correspond to that region. The percent of change of the absorption coefficient value at four different regions of absorption coefficient can be finally calculated using Eq. (4.56), which is the ratio of the change of absorption coefficient value at each region and all regions.

$$\%\Delta\alpha_{\ at\ region\ x} = \frac{\sum_{i=1}^{n} \left| \frac{\alpha_m - \alpha_{init}}{\alpha_{init}} \right|}{\Delta\alpha} \times 100 \tag{4.56}$$

where x is the specific region in absorption coefficient spectrum ($x = 1, 2, 3, 4$) and n is the number of the data points in region x.

The identification of the sensitivity of each DOS parameter, using the quantification of the span of change in the absorption coefficient value when a parameter value is changed, is represented in a shape of a Tornado diagram as firstly proposed in [94]. Tornado diagrams are constructed using the techniques in [95]. In this study, one DOS parameter value is varied at a certain value of percentage (e.g. +/- 30 %) and the RMSE of the modified absorption coefficient is calculated. The RMSE is calculated using Eq. (4.57).

$$RMSE_\alpha = \sqrt{\frac{\sum_{i=1}^{k} \left(\frac{\alpha_m - \alpha_{init}}{\alpha_{init}} \right)^2}{k}} \tag{4.57}$$

This value of RMSE is calculated when one parameter is changed at its minimum and maximum percentage of change. The difference between these two RMSE_α values defines the span of changes of RMSE_α value in the calculation of the absorption coefficient. In the case of a quantification of RMSE_α at a specific region in the absorption coefficient spectrum, the number of data points k should correspond to the number of data points in that region. Parameters that have wider span compare

to the others can be considered as the parameters which give sufficient amount of contribution towards the final observed results according to [95]. Nevertheless, to qualify the most important DOS parameters to the change in the absorption coefficient spectrum, the method of sorting will not be based on the width of change of RMSE_α value. The reason of which is that the change of absorption coefficient value will depend on the region of the change. For example if the change occurs in the low energy region, the change of α will be very small and that cannot be compared directly with the change of α in the high energy region where the α value is quite high. To qualify the sensitivity of DOS parameters using Tornado plot, firstly the mean value of the width of RMSE_α when a parameter is varied to +/- 30% is calculated. This mean value is summed with the minimum value of the RMSE_α, or the minimum of the change. The DOS parameters are then sorted descending. Hence, in the following results of Tornado plots we will see that even if a DOS parameter does not yield a wide span of change in the RMSE_α, yet if the mean of the RMSE_α is higher, it will be categorized as a more important DOS parameter than the one with wider span of change.

The identification of the sensitivity to parameters using the degree of freedom of each DOS parameter on the absorption coefficient is represented using Spider plots as in [94]. One DOS parameter values is varied within a certain range of value, e.g. +/- 30 % and the RMSE_α is calculated using Eq. (4.57). When the value of RMSE_α of each DOS parameters as function of change of parameter is plotted together in the same graph, the most influential parameters should result into a high RMSE_α value due to a small change of the parameter value. In the other hand, there exists some parameters whose values are modified but still result in a low RMSE_α value.

The sensitivity analysis of the DOS parameters brings the advantage to better understand the behavior of each DOS parameters on the absorption coefficient spectrum. For example, when the DeOSt program is used to model the DOS parameters, the sensitivity analysis can serve as a guide to find the best fit of the DOS model to the corresponding absorption coefficient. The first sensitivity analysis represented using the stacked bar plot is very beneficial to know which region of the absorption coefficient spectrum will change and its proportion of change with respect to the other regions if a specific DOS parameter is varied. By using this analysis, user can first have a global overview of the influence of DOS a parameter on the absorption coefficient spectrum. The second sensitivity analysis represented using the Tornado plot is useful to know the amount of change in a specific region of the absorption coefficient when a DOS parameters is varied to a certain percentage from its optimum value. By quantifying the amount of change induced by each DOS parameter on the absorption coefficient, the most influential parameter can be determined. The more influential parameters yield significant change in the absorption coefficient when it is varied to a certain value. This type of sensitivity analysis can help the user to choose which parameter should be modified in order to correct the error that persists in a specific region of the absorption coefficient during the fitting process. The third sensitivity analysis represented using the Spider plot has similar advantage as the second method, where user can understand which parameter is the most important and influential on the absorption coefficient calculation. This sensitivity analysis is

beneficial to know which parameter should really be set to its optimum value to yield a good fit of absorption coefficient, and that a tiny deviation from its optimum value will bring a significant change in each specific region of the absorption coefficient. In the case where user can quantify the error in the absorption coefficient, this third method brings even more advantage. For example, when user determines the quantity of error, by reading at this sensitivity analysis, he can know exactly how much does each DOS parameter deviate from its optimum value. These analyses using the above methods for the DOS parameters will be explained further in 4.3.1 and 4.3.2, respectively for standard and defect-pool models.

4.3.1 Sensitivity of standard model DOS Parameters

Stacked bar plots of the standard DOS model

The impact of the change of the standard model DOS parameters on the shape of the absorption coefficient, α, is presented in Figs. 4-19, 4-20, and 4-21. In these figures, the change of α when a parameter value is changed is partitioned into four different regions of α. For example, in Fig. 4-19A, when the value of E_G is varied to -30 % of its optimum value, the change of value in α shows an extreme exponential increase starting from -10 % change of E_G. During this exponential increase, over 60 % of the change in α occurs in the Urbach slope region, 30 % in the defect region, and the rest in the other two regions. Fig. 4-19B is a closer look of the evolution of α before the exponential increase. It can be seen that the change of α increases up to 58 % at the +10 % of E_G initial value, and then very slightly decreases to 56 % at the +30 % of E_G initial value.

The impacts of changes of the extended band state distributions parameters, N_{EV} and N_{EC} are represented in Figs. 4-19D and 4-19E respectively. Both of these parameters when their values are varied +/- 30 % of their initial value, produce a significant change in the high absorption region of α. The change of these parameters affects the changes in extended states distributions which impact the number of band-to-band transitions that contributes to high absorption (or energy) region in α.

Figs. 4-19C and 4-19F show the impact of the variation of optical matrix element, C_{Def}^{OPT} and C_{BT}^{OPT} values for defect and band tail distributions, respectively. Both of these parameters affect the increase in the change of α value when varied +/- 30 % of their initial value, with the majority of change in the defect region for C_{Def}^{OPT} and in the high α region for C_{BT}^{OPT}, as expected.

The impact of band tail state distribution parameters variation on the α shape is represented in Fig. 4-20. As can be seen from the figure, band tail related parameters mostly impact the Urbach slope region in α. Contribution to the change in the high absorption region can also be seen, which is due to the increased possibility of band-to-band electron transitions when high energy photons are absorbed. The change of the valence band tail temperature results in a higher percentage of change in α than the change of the conduction band tail temperature. This can be understood as the Urbach slope region of α is mainly dominated by the electron transitions from the valence band tail states towards the extended states of the conduction band, rather

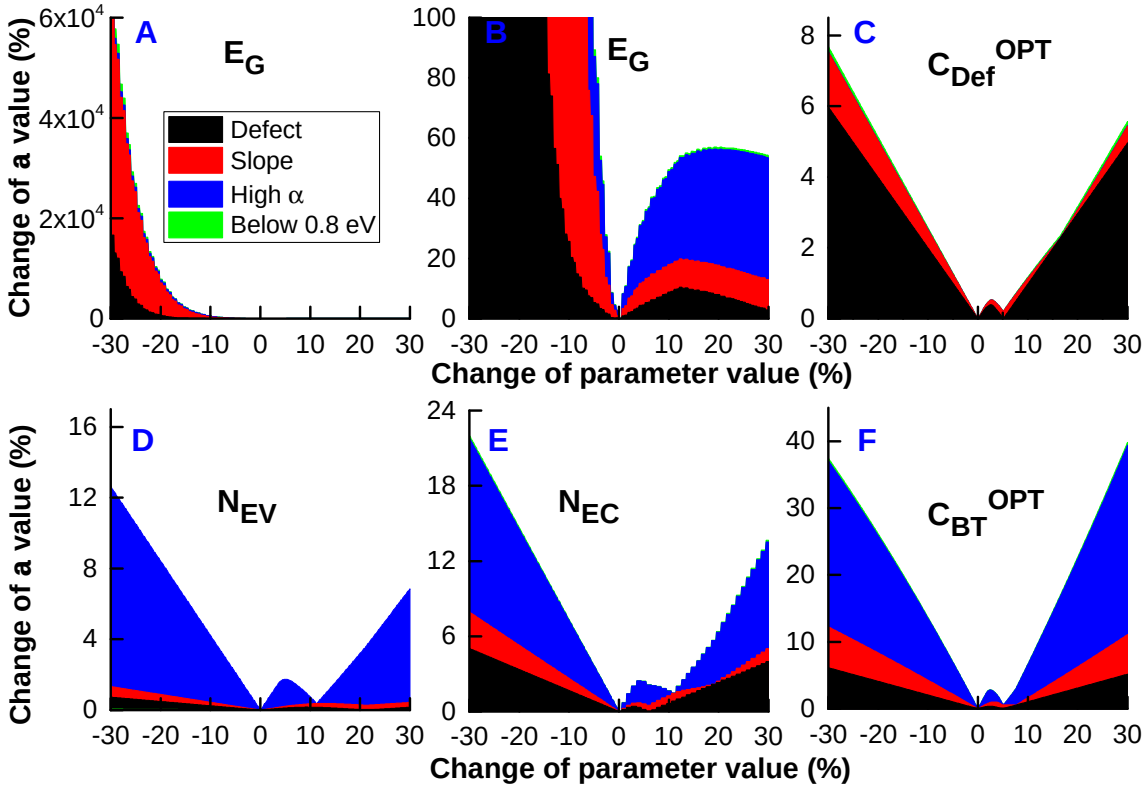

Figure 4-19: The analysis of the impact of the change of (A) E_G (presented with a lower Y-scale in B), (C) C_{Def}^{OPT}, (D) N_{EV}, (E) N_{EC}, and (F) C_{BT}^{OPT} using the standard model, on the evolution of the absorption coefficient spectrum shape.

than the hole creation in the extended states of the valence band coming from an electronic transition toward the conduction band tail states.

The influences of the second exponential distributions of valence and conduction band tail distributions in term of their N_V^{EXT} and N_C^{EXT}, is presented in Fig. 4-20B and 4-20E, respectively. It can be seen that the variation of these parameters results in a similar behavior and degree of change both in the Urbach slope and high absorption region in α, except that the variation of N_C^{EXT} to +30 % of its initial value does not bring any change in the value of α. The similarity of the degree of change in the high absorption and the Urbach slope region in α, when these parameters are varied to their upper range, is basically due to the particularity of these parameters which define the extension of the density of exponential distributions of band tail states toward the extended band states (which is related to the number of possible band-to-band electron transitions).

The variations of the cut-off energies of the two exponential band tail state distributions, $E_V^{cut-off}$ and $E_V^{cut-off}$ and their impact on the change of α shape are presented in Figs. 4-20C and 4-20F. It can be seen that the change of α follows a stair-like progress, which is due to the small step of change of these parameters values which becomes beyond the precision of the DeOSt program. Hence, this small change of value can be considered as constant as it does not literally change the value of

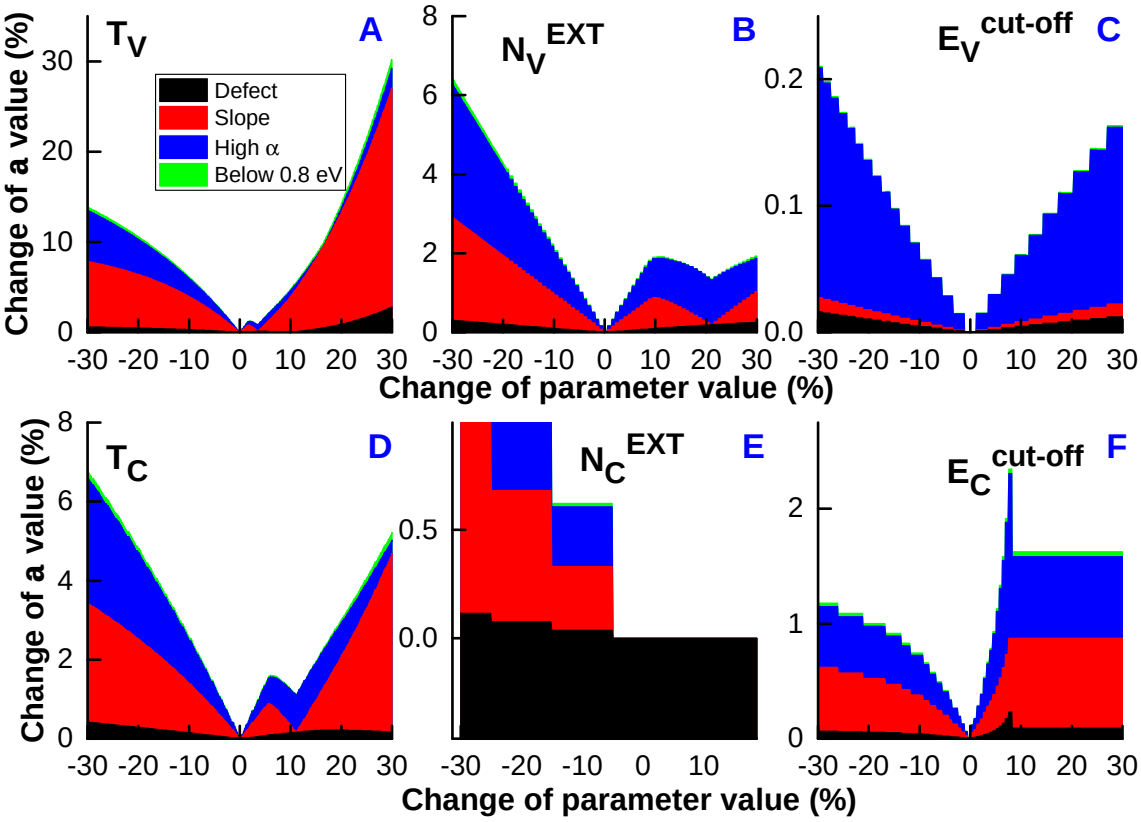

Figure 4-20: The analysis of the impact of the change of band tail parameters values, (A) T_V, (B) N_V^{EXT}, (C) $E_V^{cut-off}$ for valence band, and (D) T_C, (E) N_C^{EXT}, (F) $E_C^{cut-off}$ for conduction band, using the standard model DOS, on the evolution of the absorption coefficient spectrum shape.

the parameter set in DeOSt. As can be seen, the variation of $E_V^{cut-off}$ mostly yields change in the high absorption region of α. In the case of the variation of $E_C^{cut-off}$, the degrees of change in the Urbach slope and high absorption region of α are very similar. In Fig. 4-20F, it can be seen that after +10 % of $E_C^{cut-off}$ variation, the change of α is constant which is due to the fact that $E_C^{cut-off}$ was chosen close to the conduction band edge and with a decrease of 10 % $E_C^{cut-off}$ becomes too small to have any influence on the α spectrum.

The change of value in the defect region of α is mostly affected by the variations of defect-related parameters as shown in Fig. 4-21. The donor-type defect distribution parameter, N_{Don}^{MAX}, E_{Don}^{MAX}, and σ_{Don} variations can be seen to be impacting the deep-defect region of α more than the acceptor-related DOS parameters. This can be understood as the defect region of α is mainly coming from the electron transitions from defect states to the conduction band side instead of hole creation in the valence band side.

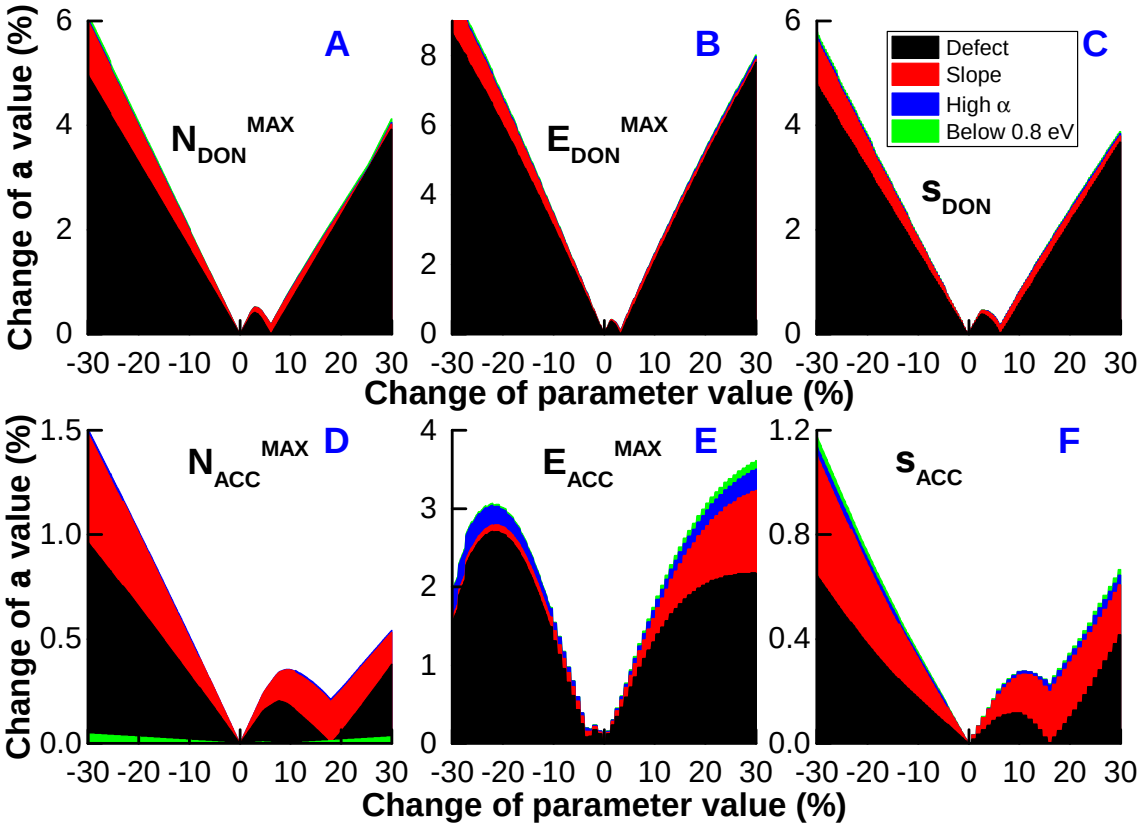

Figure 4-21: The analysis of the impact of the change of deep defect parameters values, (A) N_{don}^{max}, (B) E_{don}^{max}, (C) σ_{don} for donor-type defect and (D) N_{acc}^{max}, (E) E_{acc}^{max}, (F) σ_{acc} for acceptor-type, using the standard model DOS on the evolution of the absorption coefficient spectrum shape.

Tornado plots of the standard DOS model

The Tornado plots which give the span of changes in α when each parameter is varied to +/- 30% from their optimum values, sorted by the mean value of their span of change in α are presented in the following paragraphs and figures. From these Tornado plots we can get information on the most influential DOS parameters in specific regions of α and also in the E_a value. The Tornado plots for all regions of α are presented in Fig. 4-22, whereas the changes in a specific region are presented in Fig. 4-23 for the defect region, 4-24 for the Urbach slope region, and 4-25 for the high absorption region. The Tornado plot representing the effect of the change in Ea is presented in Fig. 4-26.

From Fig. 4-22, the parameters that significantly contribute to the change of α are E_G, T, C_{BT}^{OPT}, N_{EC}, E_{Don}^{MAX}, and N_{EV}. From the results, it can be seen that the most important parameters contributing to the change of α come from all the states, i.e. extended band states: E_G, N_{EV} and N_{EC}, exponential band tail states: T_V, C_{BT}^{OPT}, and defect states: E_{Don}^{MAX}. E_G plays a major role because it controls the band to band transitions that contribute to the higher values of α. Then, it can be

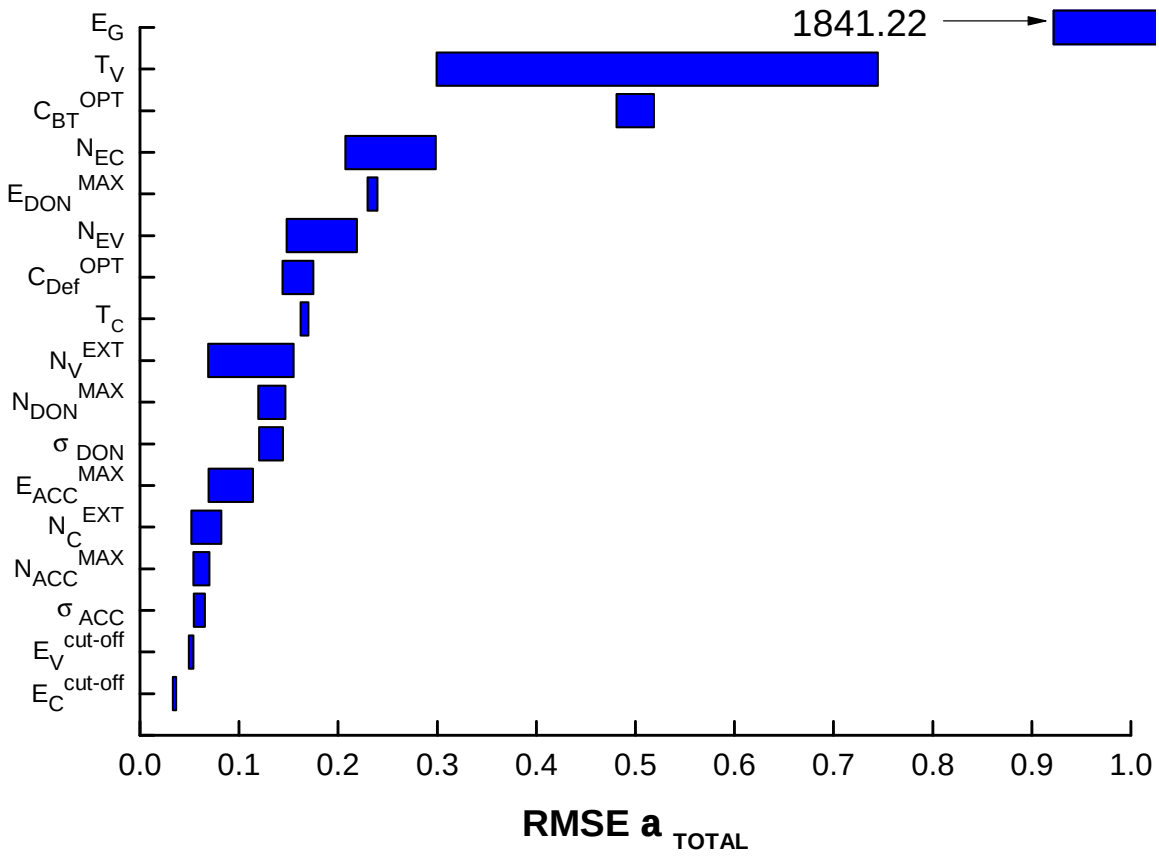

Figure 4-22: Tornado diagram of the influence of the standard model DOS parameters on the evolution of the value of the absorption coefficient spectrum.

seen that the change of α is dominated by the change in the Urbach slope region for which the dynamic range of α is the greatest. Finally, the change of α becomes significant when some of the parameters of the region of high absorption are changed. Hence, the exponential band states parameters are of some importance, mainly the valence band tail states, which fix the electronic transitions from these states towards the extended conduction band states, and then secondly, in terms of influence, the extended band states, defining the band to band type electronic transitions.

The changes of the deep defect region of α, as identified from the Tornado plot in Fig. 4-23 are mainly linked to: E_G, E_{Don}^{MAX}, C_{BT}^{OPT}, C_{Def}^{OPT} N_{EC}, N_{Don}^{MAX}, and σ_{Don}. It can be seen that the changes in the deep defect region are mostly dominated by the parameters that directly affect this region, i.e. E_{Don}^{MAX}, N_{Don}^{MAX}, σ_{Don}. The change of the deep-defect parameters will affect the possible number of electronic transitions from the donor states towards the extended conduction band states. Meanwhile, this region of α is also impacted by the valence band tail states that depend on E_G and C_{BT}^{OPT}, notably E_G which define the energy range of possible electronic transitions. Finally, since the electronic transitions contributing to α from this region can occur towards the extended conduction band states, we see that N_{EC} also plays an important role.

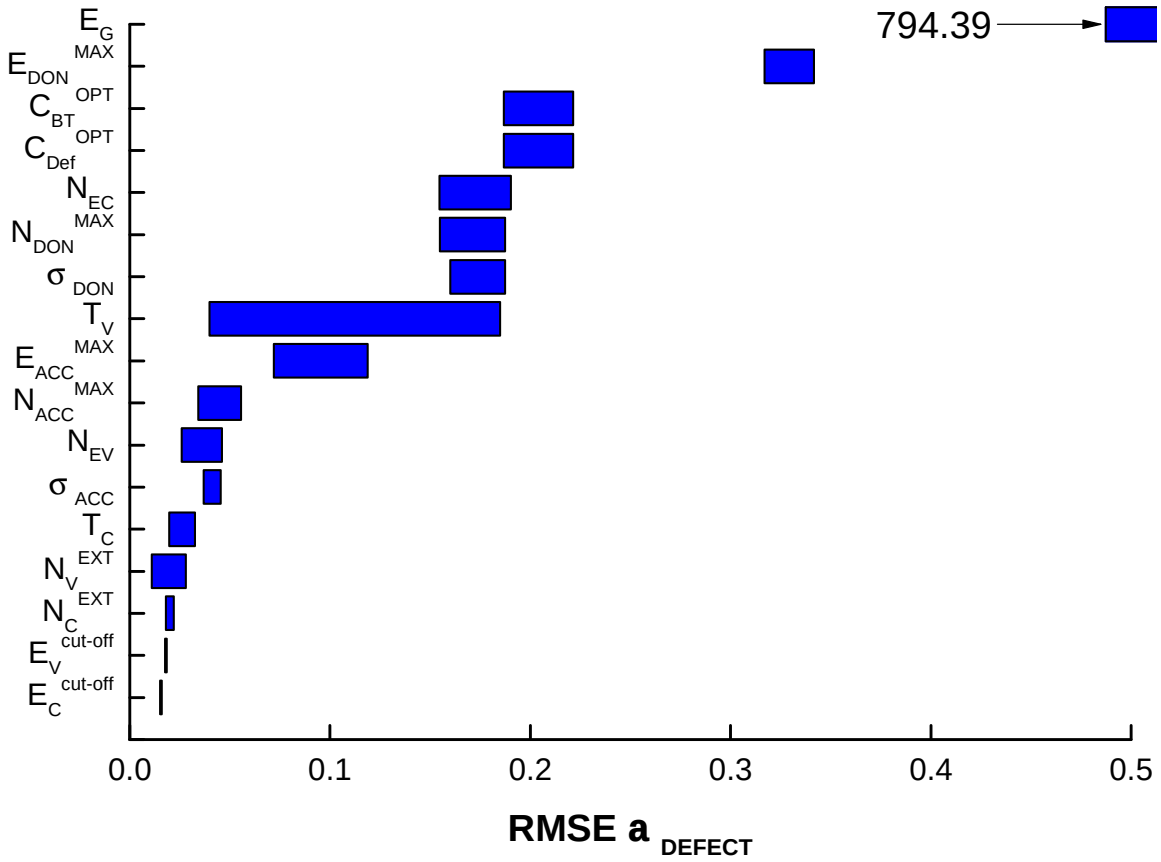

Figure 4-23: Tornado diagram of the influence of the standard model DOS parameters on the evolution in the deep defect region of absorption coefficient spectrum.

The Urbach slope region in α is most sensitive to band tail related parameters, i.e: E_G, T_V, C_{BT}^{OPT}, T_C, and extended band distributions, i.e. N_{EC} and N_V^{EXT}, as depicted in Fig. 4-24. The contribution of the extended band states can be explained since the possible electronic transitions using the range of energy in the Urbach slope region of α, i.e 1.4-1.8 eV, may induce transitions from the extended valence band states to the conduction band tail states, as well as from the valence band tail states towards extended conduction band states.

In the high absorption region of α, the change of value is mostly due to the variation of E_G, C_{BT}^{OPT}, N_{EC}, N_{EV}, T_V, and N_V^{EXT}, as shown in the Tornado plot in Fig. 4-25. As can be seen from the α spectrum, the high absorption region, where the absorption is greater than 10^4 cm^{-1}, is a mixture of an Urbach slope and a parabolic extended states contribution. Hence, the influential parameters as analyzed with the Tornado plot, are mostly the parameters that have a direct contribution to the α spectrum: the parabolic extended states, i.e. E_G, N_{EC}, N_{EV}, and the exponential band tail states, i.e.:C_{BT}^{OPT} , T_V, and N_V^{EXT}.

The change of value of the activation energy is mostly impacted by the change of E_G, E_{Acc}^{MAX}, E_{Don}^{MAX}, σ_{Don}, σ_{Acc}, N_{Don}^{MAX}, and N_{Acc}^{MAX} as represented in Fig. 4-26. The activation energy is obtained by the difference of the band gap energy E_G and the

energy of Fermi level, E_F, defined by the charge neutrality. From the classical DOS model, it can be seen that the deep defect states occupy most of the energy range in the middle of DOS distribution, thus the parameters of the deep defect region are dominating the change of value in Ea.

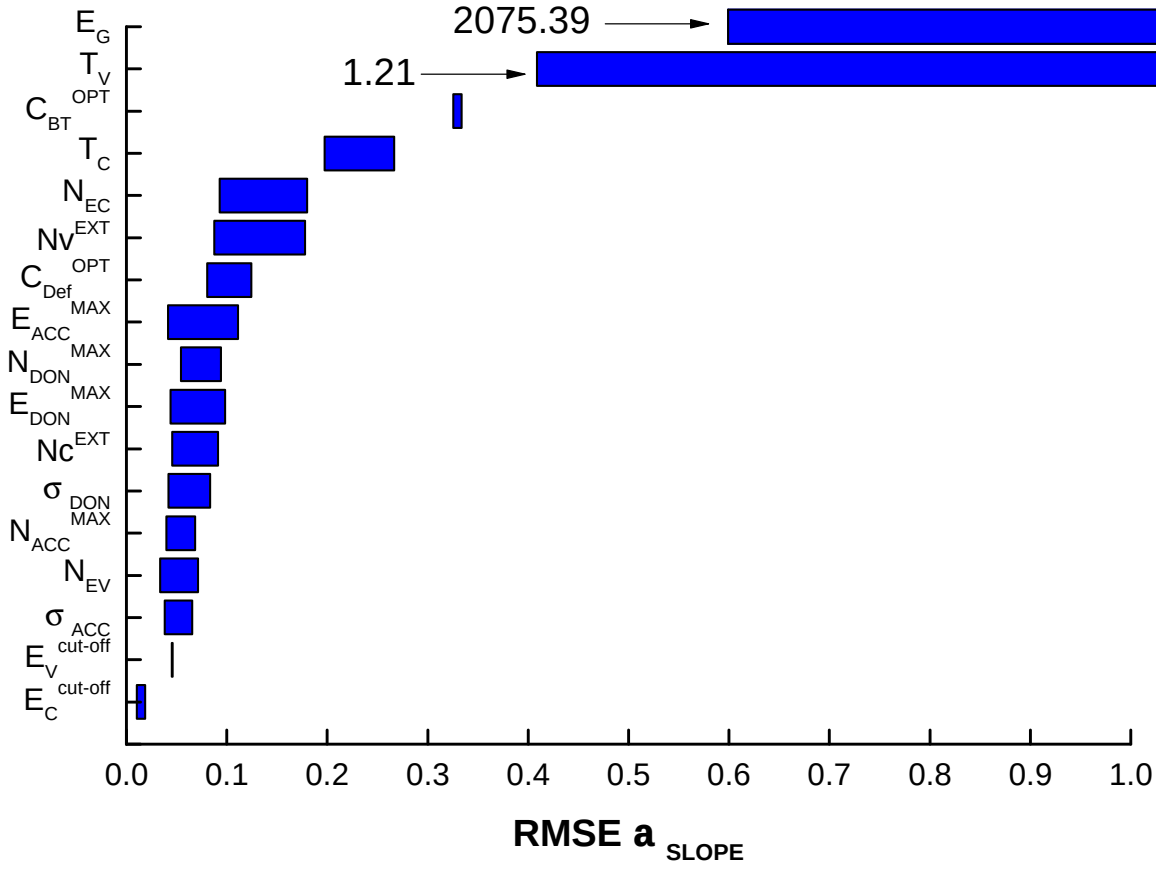

Figure 4-24: Tornado diagram of the influence of the standard model DOS parameters on the evolution in the Urbach slope region of absorption coefficient spectrum.

Spider plots of the standard DOS model

The sensitivity analysis of standard model DOS parameters can also be represented by means of spider plots, as shown in Fig. 4-27. A spider plot has a greater complexity than the Tornado diagram because the latter only shows the impact of the change of α or E_a at the extremities of a spider plot curve. On the other hand, a spider plot depicts the limit for each independent DOS parameter of the change of α or E_a. The slopes in the spider plot curves depict the relative change in α or E_a for a unit of change of a given independent DOS parameter. The shape of the spider plot curve also shows whether a linear or nonlinear relationship is present between the change of α or E_a and the individual DOS parameters.

The changes in the absorption coefficient spectrum and activation energy in Figs. 4-27 are mainly influenced by the band gap energy, E_G, as can be seen from the slopes

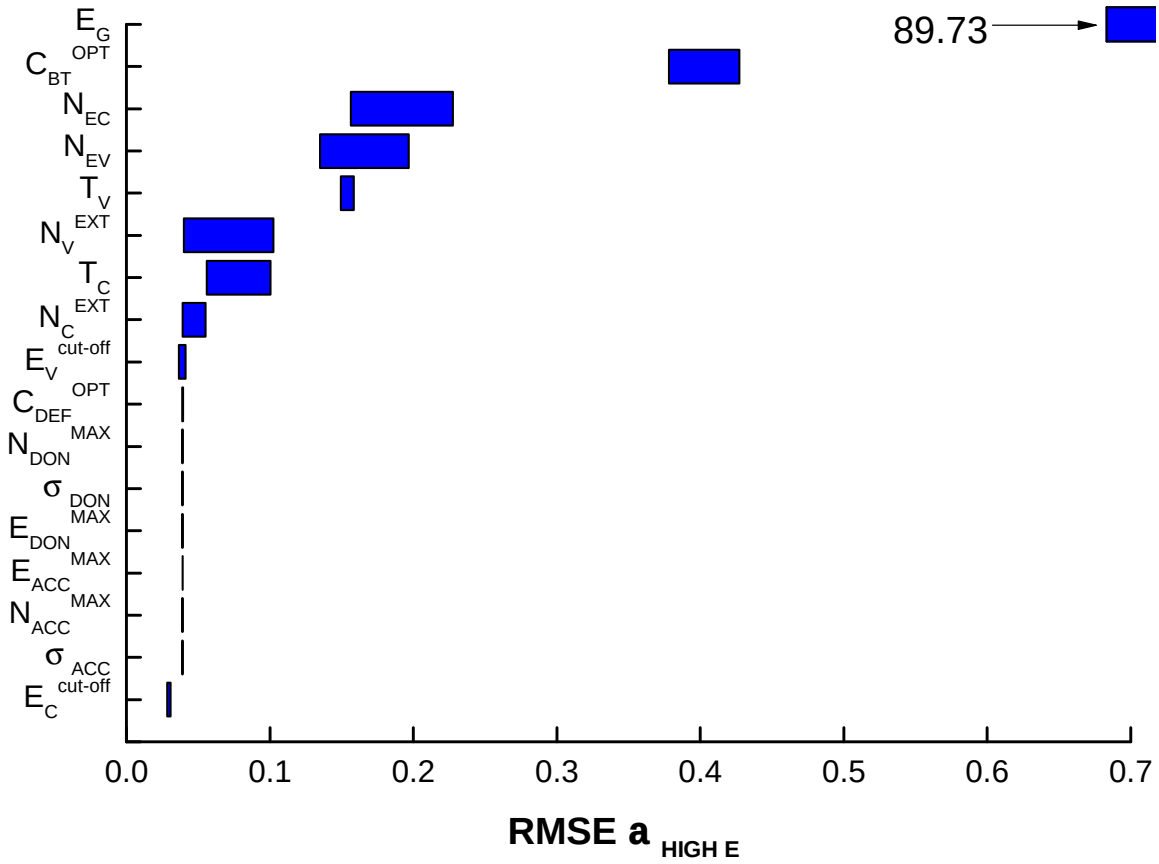

Figure 4-25: Tornado diagram of the influence of the standard model DOS parameters on the evolution in the high absorption region of absorption coefficient spectrum.

representing the relative changes of α in all regions (see Figs. 4-27A, B, C, and D), or the relative changes of E_a (Fig. 4-27E). The great influence of E_G on the changes of α and E_a was also observed previously using Tornado diagrams in Figs. 4-22 to 4-26.

In Fig. 4-27D, it can be seen that the second most influential parameter for the changes of α is T_V followed by C_{BT}^{OPT}. Both of these parameters are great contributors to the change of α in the Urbach slope region, as this region dominates α, and as already seen in Figs. 4-20A and 4-19F, these parameters are critical to define the Urbach slope region. In the Urbach slope region of α, after E_G the change of value are secondarily influenced by T_V, as confirmed using the results in Fig. 4-24, C_{BT}^{OPT}, and T_C, which are all band tail distributions related parameters. The order of sensitivity of these parameters has a very good agreement with the corresponding Tornado plot, previously presented in Fig. 4-24. For the changes in E_a, the second most influential parameters are E_{Acc}^{MAX} and E_{Don}^{MAX}, which is in a good agreement with the result given by the Tornado diagram in Fig. 4-26.

The deep defect region of α is most sensitive to E_{Don}^{MAX}, C_{Def}^{OPT}, and σ_{Don}. As can also be seen from Figs. 4-21A and 4-19C, these parameters mainly affect the change of value in the defect region of α. The importance of these parameters were as well

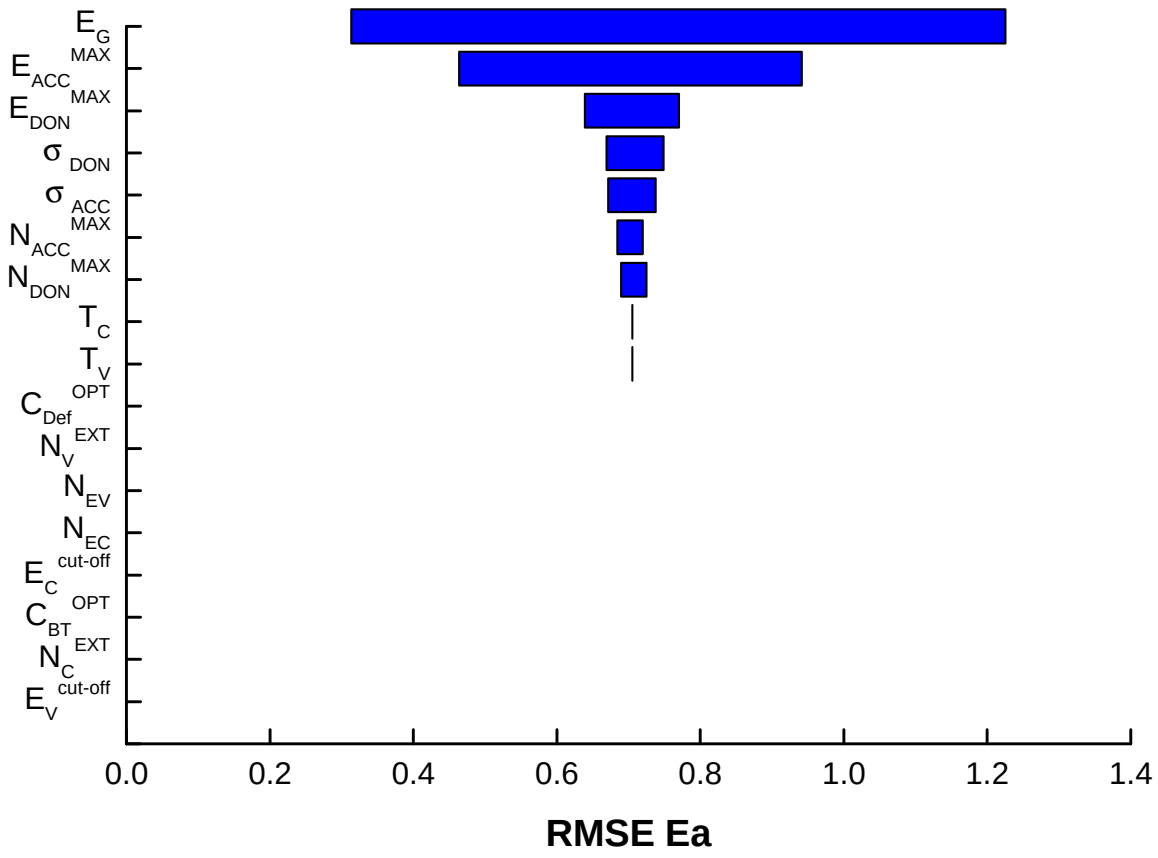

Figure 4-26: Tornado diagram of the influence of the standard model DOS parameters on the evolution in the activation energy, E_a.

demonstrated by the Tornado plot in Fig. 4-23.

The change of value of α in the high energy region is due to a significant contribution of C_{BT}^{OPT}, N_{EC}, and N_{EV}, as can be confirmed using Figs. 4-19C, D, and E, by looking at the significant change in the high absorption region due to the variation of these parameters. The order of the degree of sensitivity is almost as given in the Tornado plot in Fig. 4-25, except that the second most influential parameter is C_{Def}^{OPT}, instead of C_{BT}^{OPT}. The order of the degree of sensitivity is almost as given in the Tornado plot in Fig. 4-25.

From the results of the sensitivity analysis of the standard DOS parameters, it can be seen that the evolution of each parameter on α is variable. It can be remarked that the degree of sensitivity of parameters for different regions of α is not always the same, except for E_G. The following subsection will explain the results of sensitivity analysis of the defect-pool model DOS parameters on α.

4.3.2 Sensitivity of the defect-pool model DOS Parameters

In this subsection, a similar study of sensitivity analysis is presented for the defect-pool model DOS parameters. From the previous study, the optical matrix coefficient

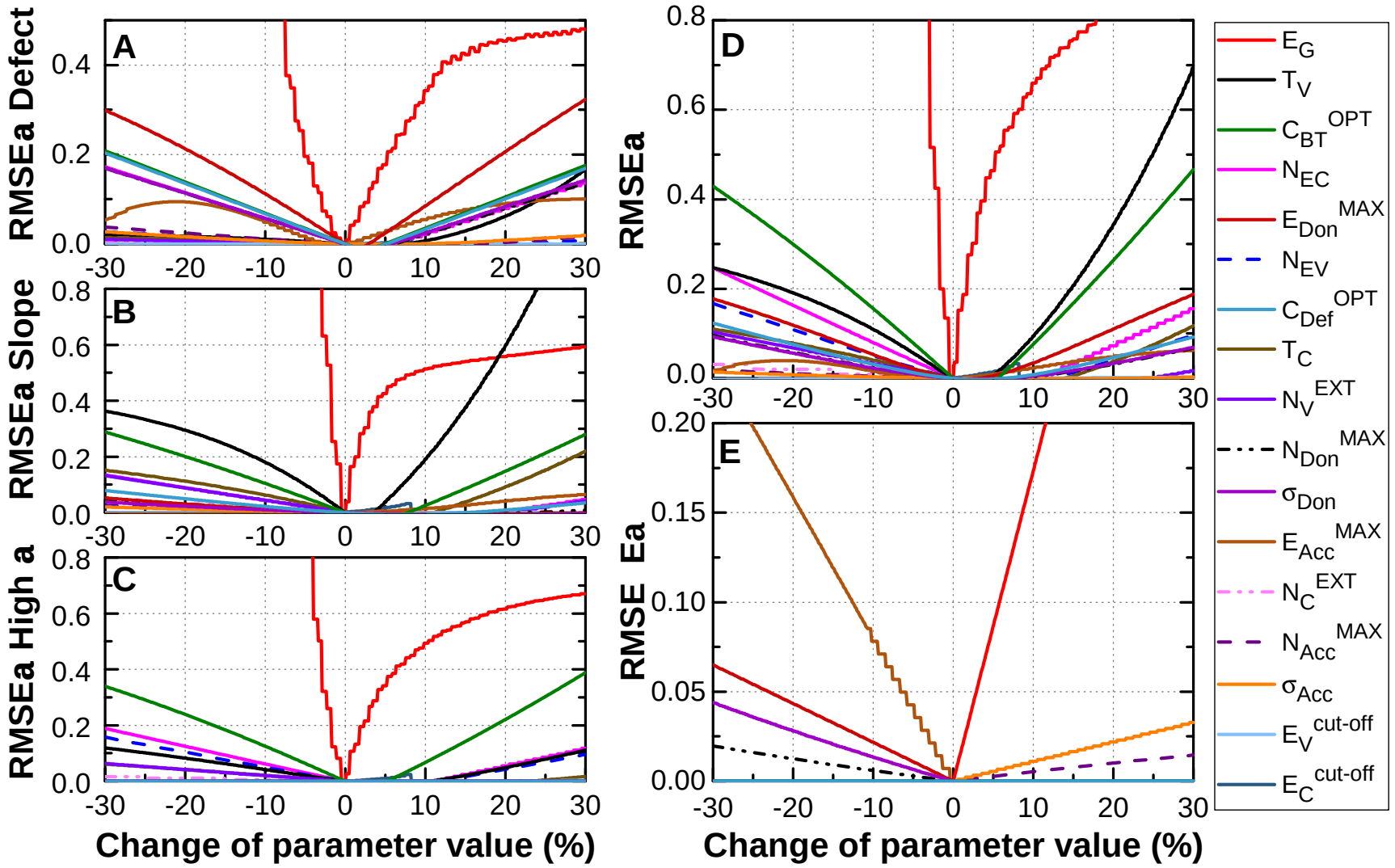

Figure 4-27: Spider plots of standard model DOS parameters influence, describing the change of value in (A) α in the deep defect region, (B) α in the Urbach slope region, (C) α in the high absorption region, (D) RMSE of the absorption coefficient, α, and (E) RMSE of the activation energy, Ea.

C^{OPT} for the band tail and defect distribution in the standard DOS model should be varied. However, the optical matrix coefficient for the band tail distribution in the defect-pool model DOS was kept constant as the contribution of this parameter can be seen as a multiplication constant of the band tail related parameters for the calculation of α. Nevertheless, since the impact of the defect-pool type defect distribution is the interest of the study with this particular DOS model, the optical matrix coefficient of the defect-pool distribution, C_{Def}^{OPT}, is varied.

Stacked bar plot of the defect-pool DOS model

As previously seen, the impact of band gap energy change in the standard model DOS brings significant change in the value of α. In the case of the defect-pool model DOS, the change of E_G extremely impact the change of value in α, mostly in the Urbach slope region (see Fig. 4-28A). As we can see from the figure, the change of α is mostly impacted by in the lower end of the E_G variations. Figure 4-28B shows the same information as in 4-28A, except that the Y-axis is lowered in scale in order to see the transient response of the exponential rise in the change of α. An exponential increase of α in the Urbach slope region can be seen when E_G is varied up to -8 % of its initial value. Then, the change in α proceeds a drastic drop before starting to increase exponentially again up to the lower end of the E_G variation. This behavior is due to the fact that from 0 to -8% $E_C^{cut-off}$ is below E_G and α in the high energy region increases because more transitions are possible due to the decrease of E_G. When E_G reaches $E_C^{cut-off}$ everything happens as if the extended states band edge was modified since only one exponential conduction band tail has to be considered. This results in a drop of α due to the change of slope. For larger modifications, from -8% and below, α increases again because of the increase of the possible transitions due to the lowering of E_G.

The extended band state distributions parameters, N_{EV} and N_{EC}, variations result in a change of α up to 8 % and 12 %, respectively (see Figs. 4-28C and D). The variation of N_{EC} to +/-30 % of initial value yields almost a similar proportion of increase in the value of α in the high absorption, defect, and below 0.8 eV region, while only very little change occurs in the Urbach slope region.

The optical matrix coefficient of the defect-pool defect distributions variation to +/- 30 % from its initial value promotes 6.4 % of change in α value. The change of α as shown in Fig. 4-28E is mostly caused by the deviation of α in the defect region accompanied with a small proportion of change in the Urbach slope region.

The influence of the band tail distribution parameters variations on the change of α is presented in Fig. 4-29. The variation of band tail temperatures bring significant change to α notably for T_V variation. T_V variation to + 30 % yields 102 % of change in α, mainly at the defect and Urbach slope region. When varied to -30 %, T_V produces 24 % of change in α, for which 54 % occurs in the defect region, 38 % in the Urbach slope region, and the rest in the high absorption and below 0.8 eV regions (see Fig. 4-29A). The variation of T_C, as in Fig. 4-29D, to +30 % of its initial value yields up to 30 % of change in α, with 64 % of the change in the Urbach slope region and 25 % in the high absorption region.

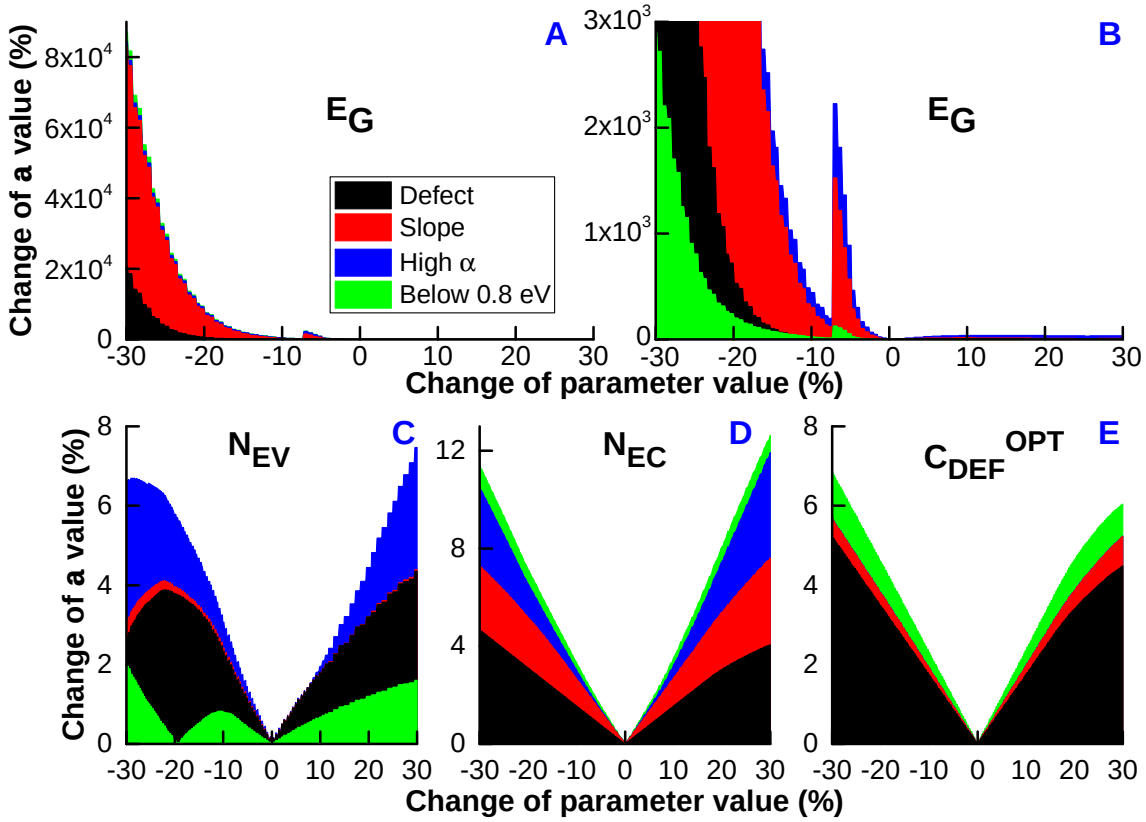

Figure 4-28: The analysis of the impact of the change of (A) E_G (presented with lower Y-scale in (B), (C) N_{EV}, (D) N_{EC}, and (E) C^{OPT} values, using the defect-pool model DOS on the evolution of the absorption coefficient spectrum shape.

The density of the second valence exponential band tail distribution, N_V^{EXT}, yields relatively higher change in α compare to the variations of N_C^{EXT}. The variation of N_V^{EXT} up to +30 % of its value results in 15 % of change in alpha at the lower end of N_V^{EXT} variation and 13 % of change in the higher end of the variation. The change when N_V^{EXT} is varied to -30 % mostly occurs in the defect region of α followed by the change in the Urbach slope region, then in the below 0.8 eV region, and finally in the high absorption region. When varied to +30 %, change in the defect region is slightly lower compare to the change in the Urbach slope region. In opposition to the impact of variation of N_V^{EXT}, the variation of N_C^{EXT} brings less significant change on α and the change in α mostly occurs in the Urbach slope and high absorption region. In Fig. 4-29E it can be seen that the change of α becomes quite constant and steady after the variation of N_C^{EXT} to +/- 7.85 % of its value.

A similar phenomenon as previously depicted in Fig. 4-28C and F happens in the variation of the cut-off energies for defect-pool model DOS due to the lack of precision in DeOSt, as presented in Figs. 4-29C and F. The variation of the cut-off energy in the valence band side produces up to 1.35 % of change in α, primarily in the defect region (see Fig. 4-29C). Meanwhile, the variation of the cut-off energy in the conduction band side brings significant change in α when varied up to +10% of

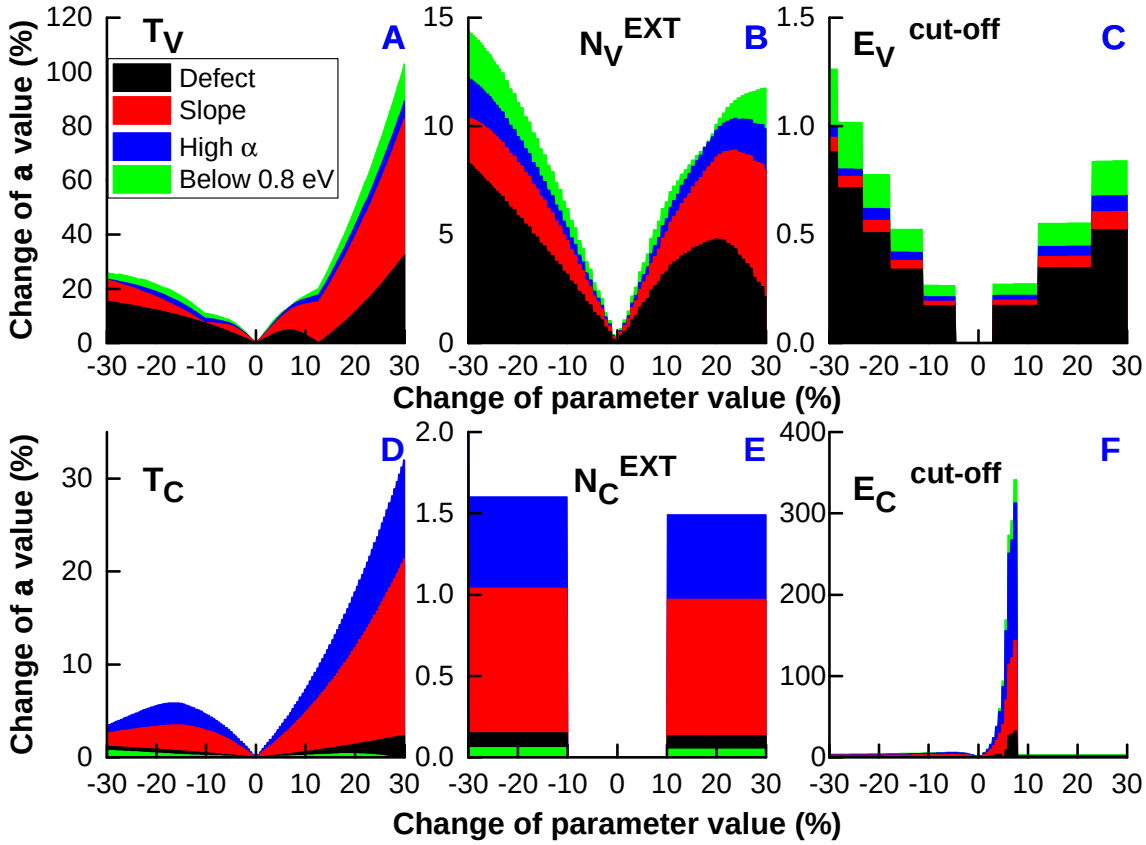

Figure 4-29: The analysis of the impact of the change of band tail parameters values, (A) T_V, (B) N_V^{EXT}, (C) $E_V^{cut-off}$ for valence band, and (D) T_C, (E) N_C^{EXT}, (F) $E_C^{cut-off}$ for conduction band, using the defect-pool model DOS, on the evolution of the absorption coefficient spectrum shape.

its initial value. The rapid exponential rise in the change of α is due to the shift of the cut-off energy closer to the extended conduction band states, whereas after +10 % of variation in $E_C^{cut-off}$ there is no change in α because the value of $E_C^{cut-off}$ has surpassed the value set for the band gap energy E_G since the value of E_G is set as the upper bound of $E_C^{cut-off}$ in the calculation with DeOSt.

Fig. 4-30 represents the impact of the variation of the defect-pool defect distribution parameters on the change of α. As can be seen from the figure, the variation of those parameters result in change of α notably in the defect region, where E_P brings the most significant change in α than the other parameters (see Fig. 4-30C). The variation of the defect-pool energy E_P as represented in Fig. 4-30C, yields a quite significant change in the value of α up to 1425 %, where the change mainly lies in the defect region. The variation of the hydrogen concentration to +/- 30 % of its initial value yields 3.65 % of change in α, as shown in Fig. 4-30A. Correlation energy, E_U, variation does not affect α as much as H, and the change in alpha occurs mostly at the below 0.8 eV region. When the value of the correlation energy is increased, the possibility of the electron transitions from the defect states below 0.8 eV is increased

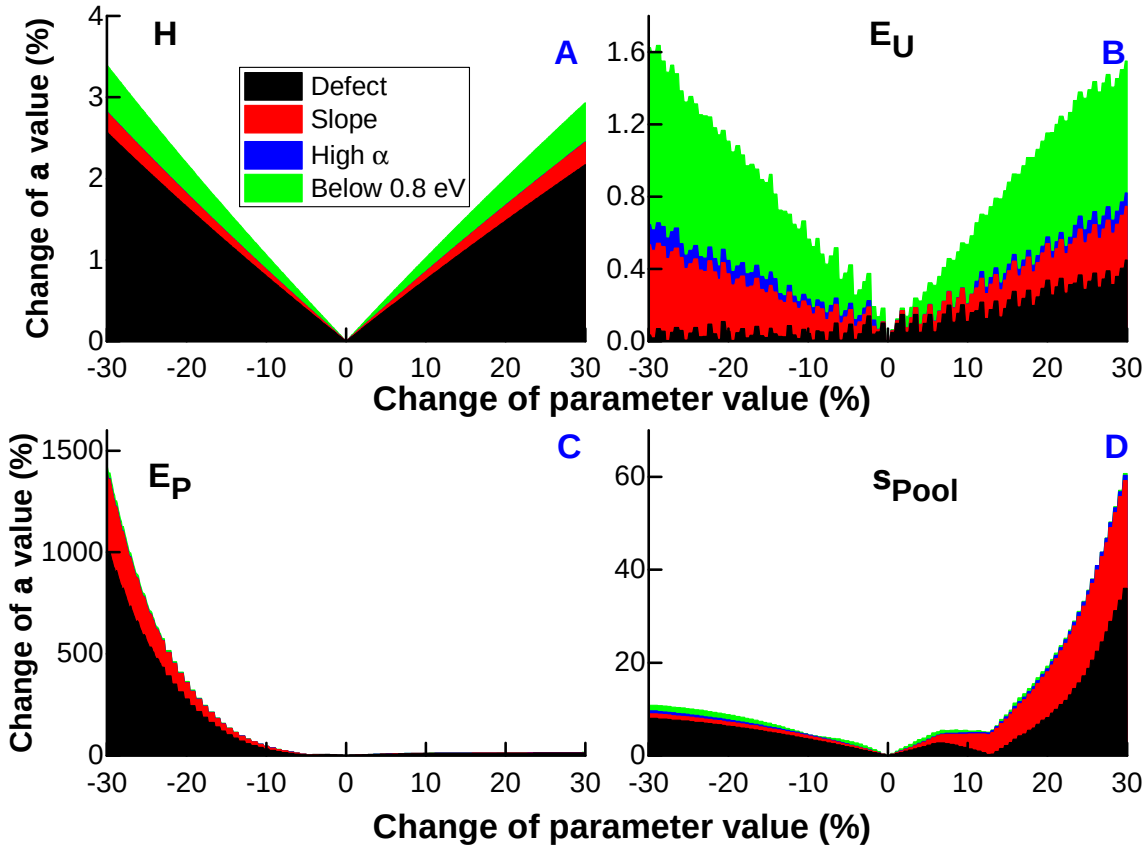

Figure 4-30: The analysis of the impact of the defect-pool parameters values, (A) H, (B) E_U, (C) E_P, (D) σ_{Pool}, using the defect-pool model DOS on the evolution of the absorption coefficient spectrum shape.

hence the value of α in the defect and below 0.8 eV is heightened, as shown in Fig 4-30B. In the lower end of E_U variation, it can be seen that the change of α at below 0.8 is dominating the total change. This is due to the lower possibility of electron transitions as correlation energy is decreased, hence the value of α typically in the below 0.8 eV and defect regions is now lower than the α with the initial value of E_U. Therefore, the change of value in α in this region is quite significant during the variation of E_U.

The last defect-pool parameter to be analyzed is the standard deviation of the defect-pool Gaussian distribution, σ_{Pool}. This parameter when its value is varied to +30 % yields 60.45 % of change in value of α, where the changes lie mostly in the defect and Urbach slope region. The variation to the lower end of σ_{Pool} result in 17 % change of value in α, where the changes persist mostly in the defect region.

Tornado plots of the defect-pool DOS model

As the impact of change of individual DOS parameters were quantified, the change in α can also be quantified when a DOS parameter is varied to its lower and higher end with the following Tornado diagrams. The change of value of α in all regions is

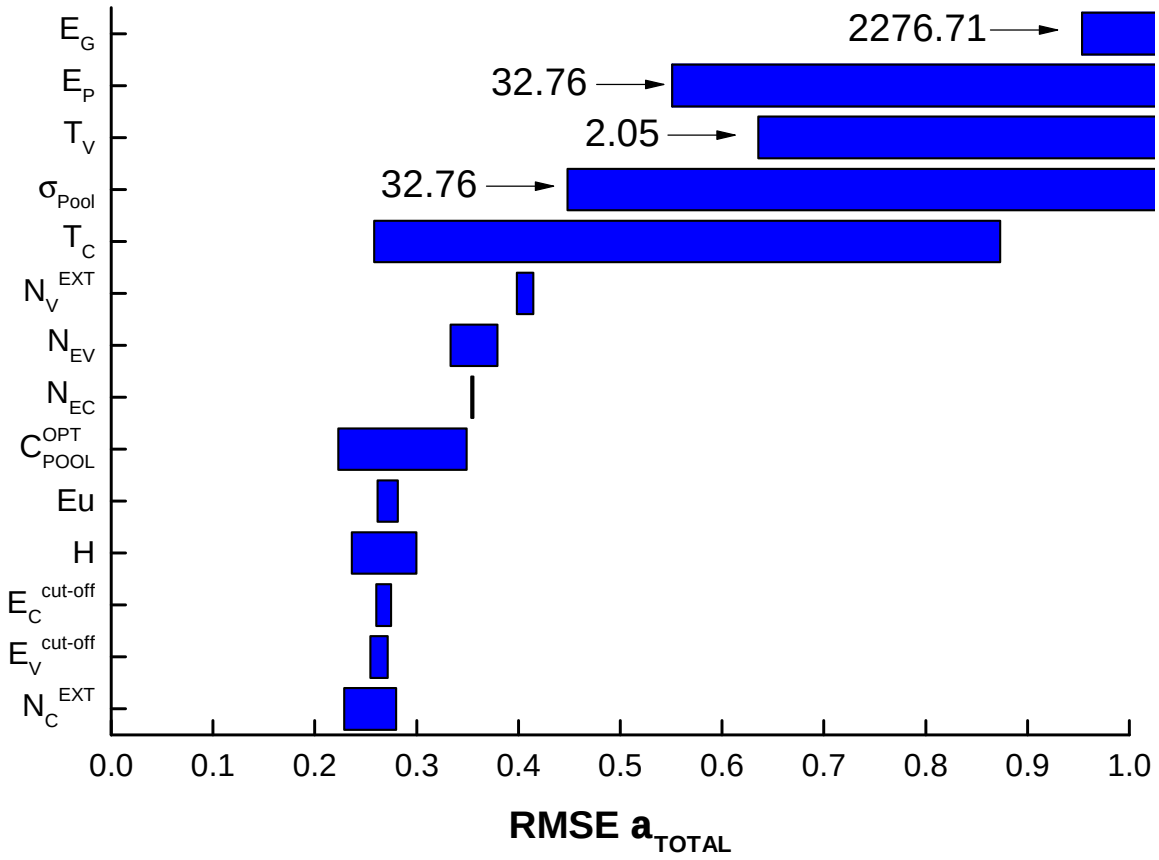

Figure 4-31: Tornado diagram of the influence of the defect-pool model DOS parameters on the evolution in the absorption coefficient spectrum.

mostly affected by E_G and E_P, as previously remarked using the analysis of impact of individual DOS parameter (in Figs. 4-19- 4-21). Following E_G and E_P, α is sensitive to T_V, σ_{Pool}, T_C, and N_V^{EXT}, for all regions of α, as represented in Fig. 4-31. It can be seen that, in addition to E_G, α calculated using the defect-pol DOS model is mostly sensitive to the deep-defect and exponential band tail parameters, as the α is dominated by the deep-defect and Urbach slope region.

The Tornado diagram for the defect region of α is represented in Fig. 4-32. It can be seen that this region is directly sensitive to the defect-pool parameters E_P and σ_{Pool}, followed by the band tail states parameters T_V, N_V^{EXT}, and C_{pool}^{OPT}. It can be remarked that the band tail parameters contributing to the change in the defect region of α are of the valence band side. The reason of which is that the contribution of the deep defect density near the valence band tail can be modified by the contribution of the density of the deeper valence band tail states.

The changes in the Urbach slope region are mostly influenced by the parameters of the band tail states, as represented by the Tornado plot in Fig. 4-33. Following E_G and E_P, this region is impacted by the change in T_V, σ_{Pool}, T_C and N_V^{EXT}. The Urbach slope of α is linked to the possible electronic transitions which are generally between 1.2-1.75 eV, where the upper limit of the photon energy involved in these

transitions can goes up to the band gap energy, E_G. It is then possible to have transitions from the valence band tail states towards the extended conduction band states, as well as transitions leaving the valence band extended states and arriving to the conduction band tail states. This is why we can see the influence of T_V, T_C, and N_V^{EXT}. In addition, a large σ_{Pool}, which defines the width of the deep-defect density of states, can result in the creation of states towards the valence band tail region and hence modify the density of states in the valence band tail side of defects.

As represented in Fig. 4-34, the high energy region of α is affected primarily by the change of the extended states related parameters. The order of the influence following E_G is T_C, T_V, N_{EC}, N_{EV}, and E_P. As can be seen, E_P appears as the least influential among the six most influential parameters in the high energy region of α because in the high energy region of α, the influence of the deep-defect states are almost negligible, except that it is still important to note that E_P defines the position of the D^+ state of the defect-pool type defect states, acting as an acceptor. Hence, the position of D^+ will affect the number of possible transitions from the extended valence band states towards D^+ states.

E_G and E_P stay as primary and secondary influential parameters for the activation energy, E_a, as represented in Fig. 4-26. The subsequent most influential parameters are σ_{Pool}, T_V, E_U, and N_{EV}. The influence of the deep-defect parameters, i.e.: E_P, σ_{Pool}, and E_U, on the change of E_a has been previously found when a standard DOS model is used, as it accounts for the equality of charges defined by E_F.

Spider plots of the defect-pool DOS model

The sensitivity analysis of the defect-pool model DOS parameter can also be represented with Spider plots as shown in Fig. 4-36, constructed using the technique as previously used for the standard DOS parameters. From the Fig. 4-36, the change of value in α, leading to the deformation of its shape, is mostly affected by E_G and E_P as previously seen using the Tornado diagrams. The shape of the valence band tail as defined by T_V also gives significant change of shape in α when varied to +20 % of its optimum value. The other three most influential parameters on α are σ_{Pool}, T_C, and N_V^{EXT}. It can be seen that the order of the influence of the DOS parameters on α corresponds to the order given by the Tornado diagram in Fig. 4-31, and the reason why these parameters are influential has been explained previously. The change of α is also very sensitive to $E_C^{cut-off}$ when its value is varied to +/- 7.85 % as previously reported in Fig. 4-20F. The influence of $E_C^{cut-off}$ appears similar for the defect and Urbach slope regions of α as depicted in Fig. 4-36A and B. The reason of this sudden increase in α when the $E_C^{cut-off}$ is varied is because the α is changed more particularly in the high energy region, hence the calculated $RMSE_\alpha$ becomes very high. The sudden decrease just after this increase corresponds to the fact that $E_C^{cut-off}$ becomes too close to E_G. In this case there is no more distinction between the first and second exponential distribution of the conduction band tail. Hence, when $E_C^{cut-off}$ is superior to E_G, it does not have any more impact on the conduction band tail state distribution. This effect is not seen in the Tornado plot as the Tornado plot only takes into account the change in α when a parameter is varied

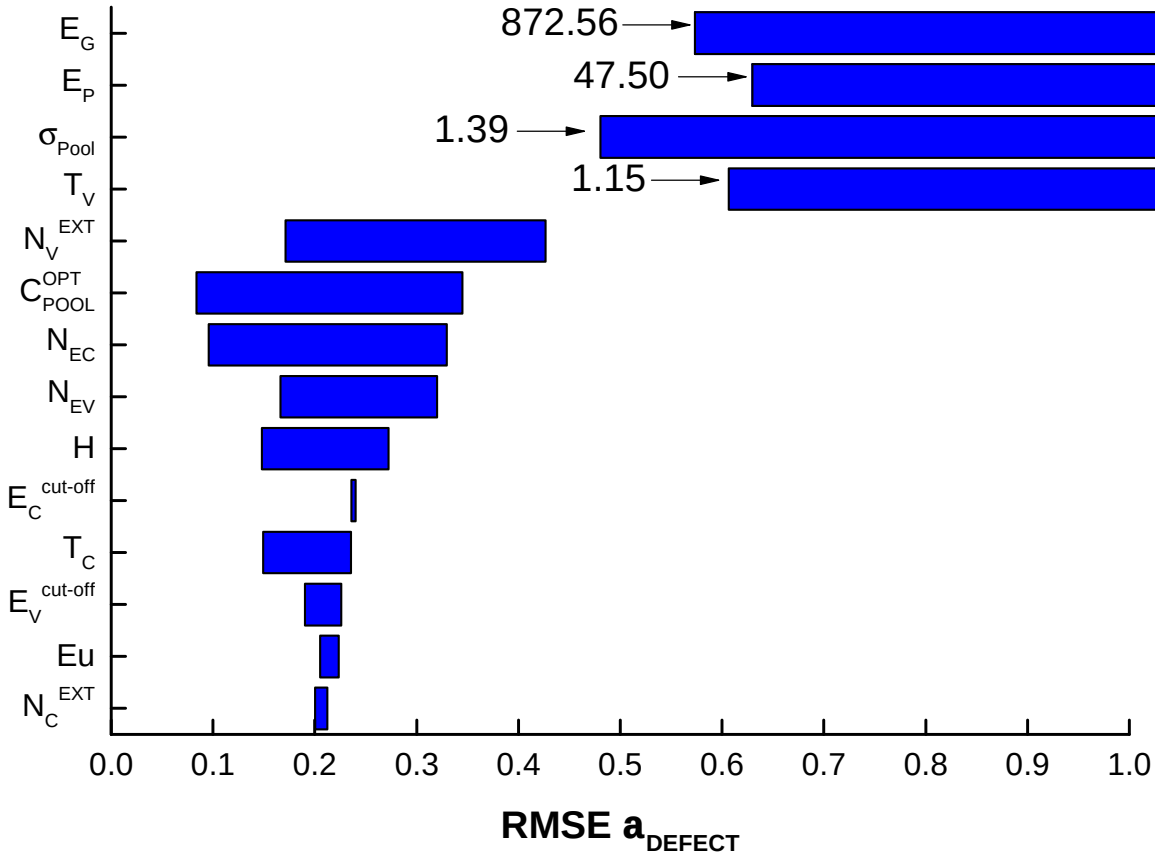

Figure 4-32: Tornado diagram of the influence of the defect-pool model DOS parameters on the evolution in the deep-defect region of the absorption coefficient spectrum.

to +/- 30% of its initial value, whereas the major change of α due to $E_C^{cut-off}$ only happens when it is varied to below 10% of its initial value.

In the defect region of α, the influence of E_G and E_P on α are very similar, except that the variation of E_G to +30 % of its value brings 25 % less change in the defect region of α than in all the other regions of α (see Fig. 4-36A). In the case when it is varied to -4.5 % of its value, E_G yields a high deformation of α in the defect region. At the variation of -7.85 % of the E_G initial value, the change in the defect regions of α drops significantly to 0.2%. The drop does not occur long until the value of E_G is varied again. The reason of the sudden increase is due to the $E_C^{cut-off}$. When the band gap energy is set to be lower than its optimum value, the parabolic extended states of the conduction band is then lower than initially. Hence, we can see the sudden increase of change in α. When the band gap energy is down to the cut-off energy, there is no more second exponential conduction band tail distribution, and the parabolic extended conduction band states joins directly the first exponential conduction and distribution. In this case, the extended conduction band tail is then higher than when the band gap energy is just slightly above the cut-off energy. In the α spectrum, we perceive a good agreement between the initial α and the α with this change of band gap energy, and thus the error drops. The variation of E_P to +30 %

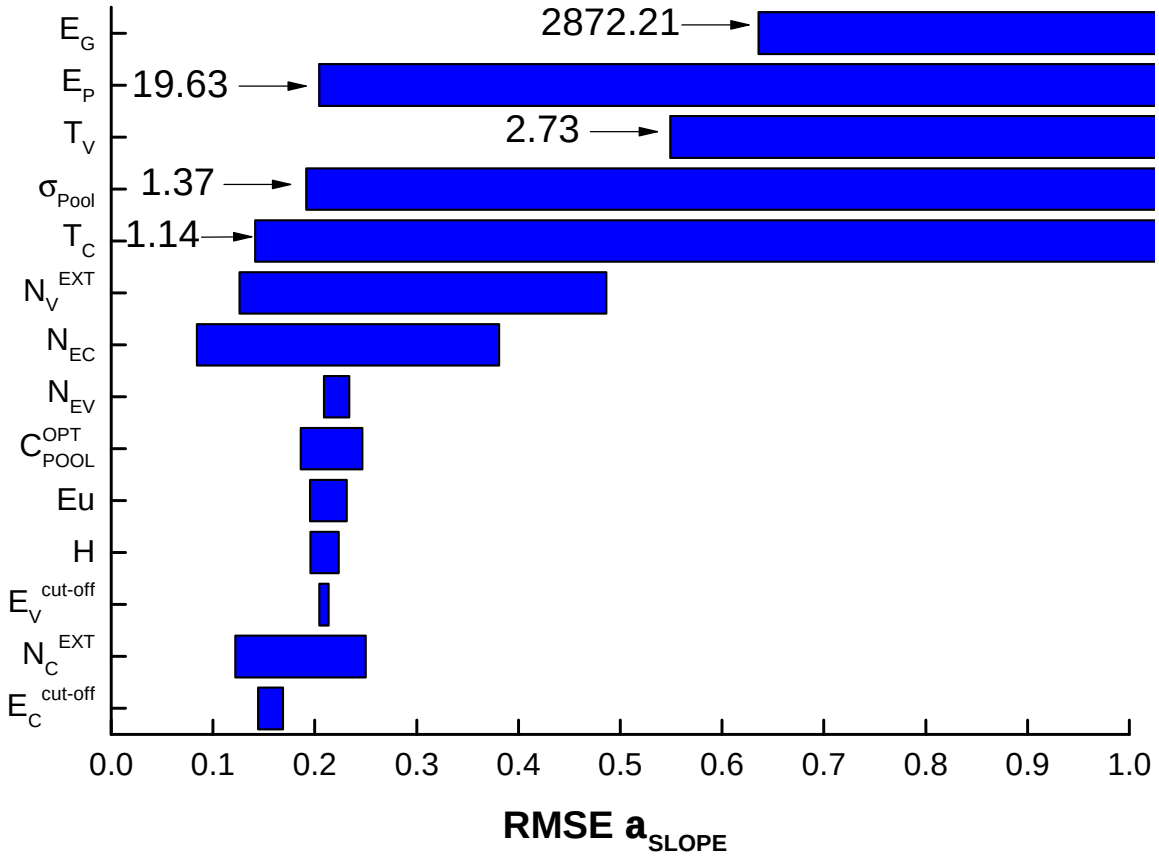

Figure 4-33: Tornado diagram of the influence of the defect-pool model DOS parameters on the evolution in the Urbach slope region of the absorption coefficient spectrum.

of its initial value also yields 0.13 % less change in the defect region of α than in the all region in α. It can be also studied in the Fig. 4-36 that the parameters such as T_V and σ_{Pool} are very influential in the defect region of α. The variation of N_V^{EXT} and C_{Pool}^{OPT} are also more important than any other defect-pool parameters even though, from the Spider plot, these are not very visible. In conclusion, the influence of the defect-pool DOS parameters on α given by the Spider plot has a good agreement with the one given by the Tornado diagram in Fig. 4-32.

The Urbach slope region of α is mostly sensitive to E_G, T_V, and E_P as can be seen in Figs. 4-28 to 4-30. These three parameters are very influential because their variations to +/- 30 % of their initial value bring change in the Urbach slope region, notably when varied to +30 %. E_G is mostly influential on the Urbach slope when varied to -30 %, while T_V is the most influential when varied to +30 % of its initial value. The other parameters influence such as E_P and σ_{Pool} are also important in the Urbach slope region. E_P is very influential when varied to -10 % while the variation to its upper end does not give significant change in the Urbach slope region. In the other hand, σ_{Pool} yields an exponential increase in the change of the Urbach slope region when varied to +30 % of its initial value. Following σ_{Pool}, T_C and N_V^{EXT} are

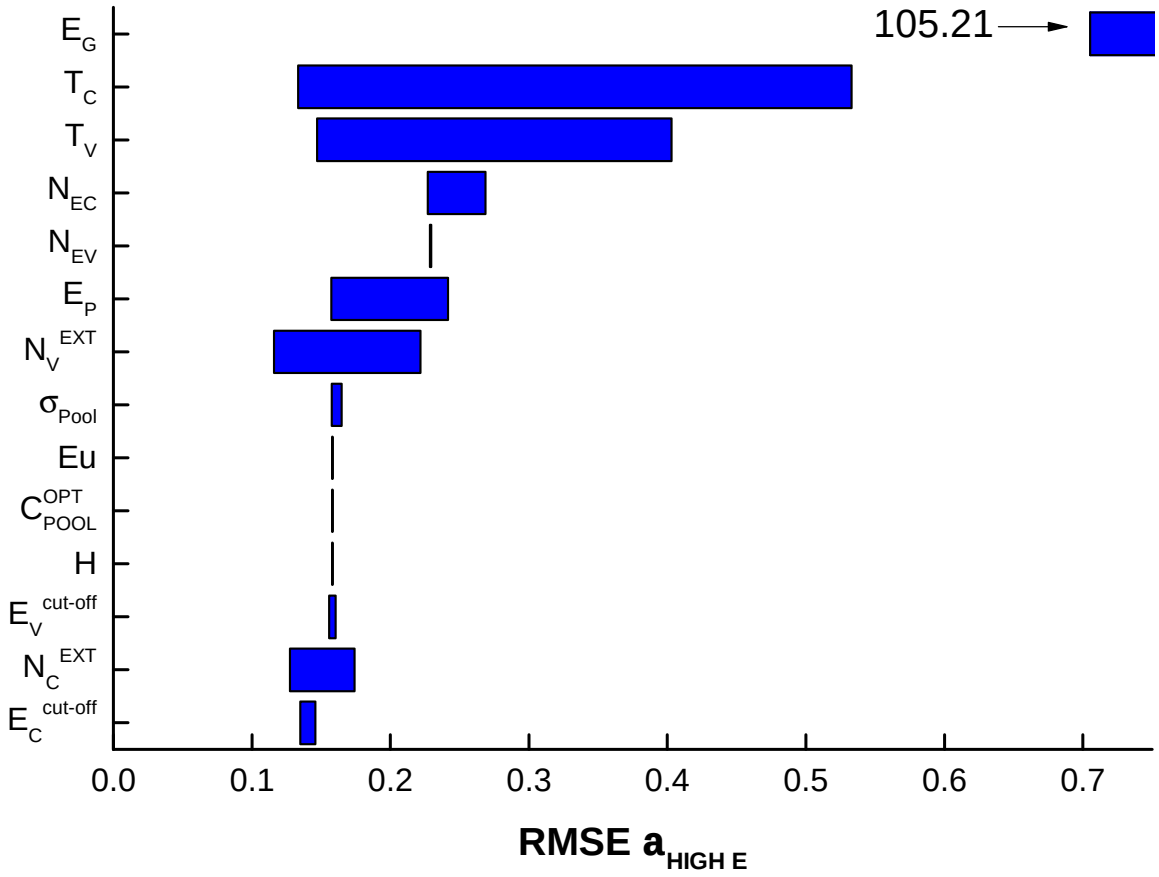

Figure 4-34: Tornado diagram of the influence of the defect-pool model DOS parameters on the evolution in the high absorption region of the absorption coefficient spectrum.

quite influential although their contributions are not as dominant as the other above listed parameters. Hence, the previously presented degree of importance of defect-pool parameters to the Urbach slope region of α using Tornado diagram in Fig. 4-33 can be confirmed with the Spider plot in Fig. 4-36B.

As can be seen in Fig. 4-36C, the number of parameters that are influential on the high absorption region are less compared to the other regions of α. Nevertheless, the influence of E_G and $E_C^{cut-off}$ appears very similar, although the change of α in the high absorption region due to E_G is 18 % higher than in the Urbach slope region by the upper end of its variation. As we can see in the right-hand side of Fig. 4-36C, the band tail parameters such as T_C for conduction and T_V for valence band play an important role in the change of α in the high absorption region, although it can be seen that this influence is not very significant. Following these two parameters, on the bottom of the spider plot in Fig. 4-36C we can remark that some extended band states parameters such as N_{EV} and N_{EC} seem to give similar impact on the change of α in the high energy region. It can be concluded that the degree of sensitivity of the defect-pool DOS parameter for this region agrees with the previously given results in

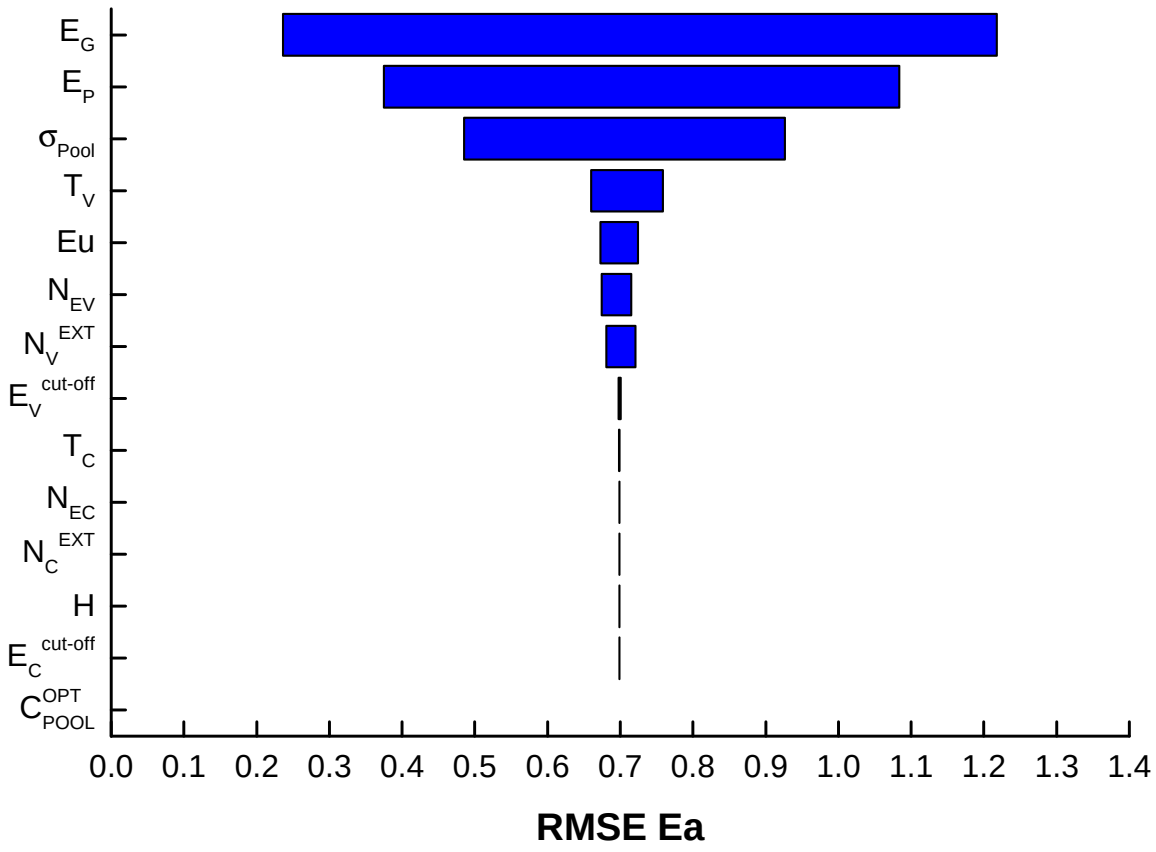

Figure 4-35: Tornado diagram of the influence of the defect-pool model DOS parameters on the evolution in the activation energy, E_a, value.

Fig. 4-34.

Finally, the sensitivity of the activation energy, E_a, in the defect-pool model DOS parameters is represented in Fig. 4-36E. From this spider plot, the influence of the defect-pool DOS parameters on E_a is not symmetrical. It means that in most cases the parameters are mainly influential when varied only to their upper or lower end of variation. Parameters such as E_G, σ_{Pool}, and N_{EV} are most influential to E_a when varied to their upper end, while others such as E_P, T_V, E_U, and N_V^{ext} are mostly influential when varied to the lower ends of their variation. However, among these parameters, only E_G, σ_{Pool}, and E_P are very influential and bring significant change to the value of E_a. Overall, the defect-pool DOS parameters that bring significant modification to E_a given by the Spider plot were previously observed in the Tornado diagram in Fig. 4-35.

Conclusions

Sensitivity analysis using the stacked bar plots have given useful information related to the impact of each DOS parameter towards specific regions of α, which is a necessary knowledge to properly perform the α fitting from the DOS model. Both sensitivity analysis performed using the Tornado and the Spider plot are quite useful to asses the

impact of uncertainty. These two methods can be used to improve decision-making in the determination of DOS parameters for α, and, most importantly, to point out which parameters need more refined estimated value. The tornado diagrams highlight the parameters that merit further attention and summarize the total impact of the parameters. However, only spider plot can show which of the high-impact parameters needs further data gathering to refine the value estimation, and to derive the reasonable limits of change for most influential parameters. The order of sensitivity of α and E_a on the standard and defect-pool DOS parameters are summarized in Tab. 4.5.

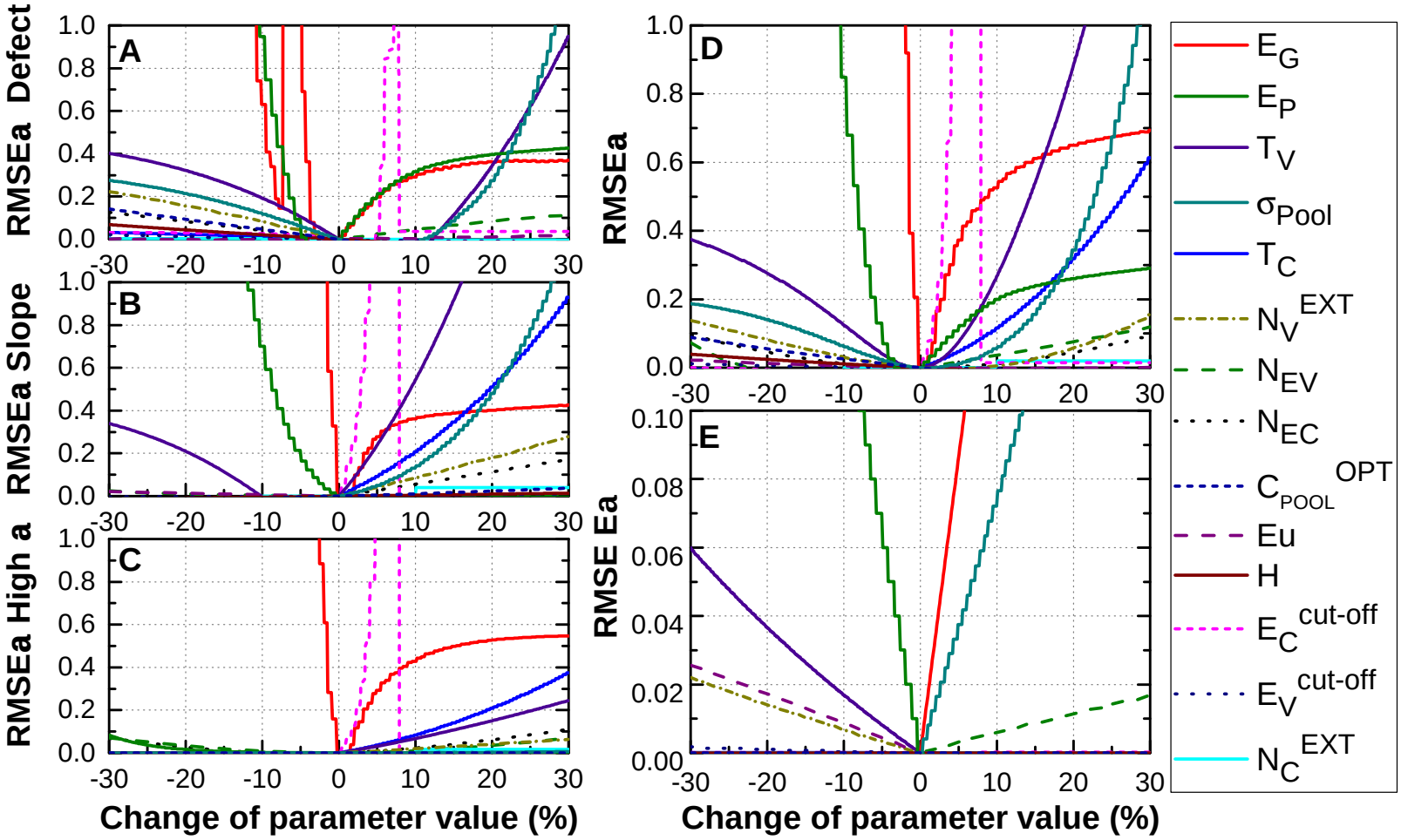

Figure 4-36: Spider plot of defect-pool model DOS parameters influence, towards the change of value in (A) α in the deep defect region, (B) α in the Urbach slope region, (C) α in the high absorption region, (D) RMSE od the absorption coefficient, α, and (E) RMSE of the activation energy, Ea.

Table 4.5: Sensitivity order of α and E_a to standard and defect-pool DOS parameters. The order of the DOS parameters influence on α is sorted using the results given by the Tornado plots. Using this order, the influence of each DOS parameter to the other specific regions of α is then numbered with respect to the order of influence given by the Tornado plots of these specific regions.

DOS parameters	α	High α	Slope	Defect	E_a	DOS parameters	α	Defect	Slope	High α	E_a
Standard DOS						Defect-pool DOS					
E_G	1	1	1	1	1	E_G	1	1	1	1	1
T_V	2	5	2	8	9	E_P	2	2	2	6	2
C_{BT}^{OPT}	3	10	3	3	15	T_V	3	4	3	3	4
N_{EC}	4	3	5	5	13	σ_{Pool}	4	3	4	8	3
E_{Don}^{MAX}	5	13	10	2	3	T_C	5	11	5	2	9
N_{EV}	6	4	14	11	12	N_V^{EXT}	6	5	6	7	7
C_{Def}^{OPT}	7	2	7	4	10	N_{EV}	7	8	8	5	6
T_C	8	7	4	13	8	N_{EC}	8	7	7	4	10
N_V^{EXT}	9	6	6	14	11	$C_{Pool}^{OPT} = C_{BT}^{OPT}$	9	6	9	10	14
N_{Don}^{MAX}	10	11	9	6	7	E_U	10	13	10	9	5
σ_{Don}	11	12	12	7	4	H	11	9	11	11	12
E_{Acc}^{MAX}	12	14	8	9	2	$E_C^{cut-off}$	12	10	14	14	13
N_C^{EXT}	13	8	11	15	16	$E_V^{cut-off}$	13	12	12	12	8
N_{Acc}^{MAX}	14	15	13	10	6	N_C^{EXT}	14	14	13	13	11
σ_{Acc}	15	16	15	12	5						
$E_V^{cut-off}$	16	9	16	16	17						
$E_C^{cut-off}$	17	17	17	17	14						

Chapter 5

Experimental Results

5.1 Example of DOS parameters determination of a-Si:H thin films using the TLBO algorithm

In this Section, three a-Si:H thin films samples as previously used for the R/T measurement in Sec. 3.5, were measured using FTPS to obtain their absorption coefficient spectrum as a function of photon energy, $\alpha(h\nu)$. The $\alpha(h\nu)$ obtained from the FTPS measurements were calibrated using the calculated $\alpha_{optics}(h\nu)$, as previously presented in Fig. 3-12, in the high energy region in order to provide the absolute value of $\alpha(h\nu)$ from FTPS. The results of the calibrated $\alpha(h\nu)$ and the $\alpha_{optics}(h\nu)$ of these samples are presented in Fig. 5-1. From the figure, it can be seen that the measured $\alpha(h\nu)$ of all the three samples yield a good agreement in term of the shape of α with the $\alpha_{optics}(h\nu)$ in the high energy region.

From the $\alpha(h\nu)$ of these samples, one can see that these samples have similar Urbach energy, E_{Urbach} as their slopes are very similar. The E_{Urbach} values can be calculated from the $\alpha(h\nu)$ using Eq. (4.53), and their values are presented in Tab. 5.1. Sample 1604211 yields the lowest E_{Urbach} as its slope is the steepest compare to the others and the last sample, 1604213 yields the highest E_{Urbach} as it provides the lowest slope compared to the other samples. The band tail temperatures are calculated from the E_{Urbach} using Eq. (4.54). The band gap energy E_G of these samples are identified in the region where the exponential distribution in the Urbach slope region of α is merged with the parabolic distribution in the high energy region of α. 1604211 provides the smallest E_G at 1.71 eV, whereas 1604212 possesses the highest E_G at 1.75 eV. Table 5.1 provides the information regarding the above mentioned parameters of α and in addition the activation energies E_a which were obtained through the steady state photocurrent spectroscopy (SSPC).

From the results of α and its calculated characteristic summarized in Tab. 5.1, we can estimate several DOS parameters to model the DOS of these samples. Firstly, the value of T_V has to be lowered as the value calculated through α will always be over estimated, as explained in Fig. 4-8. Hence, the T_V at -5% of its calculated value from α is set as the upper bound of the T_V of the DOS model. From Fig. 5-1, we can also estimate the density of defect as it is approximately 10^{-4} lower than the

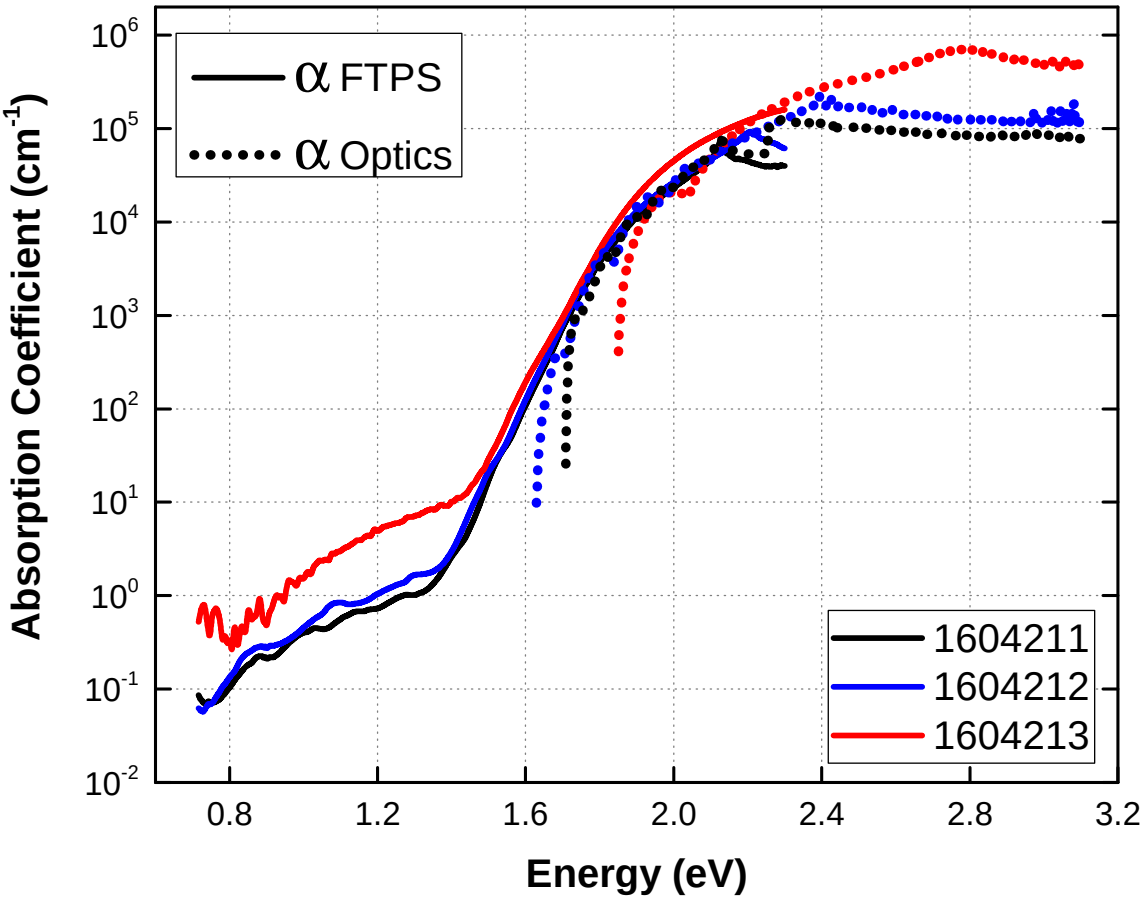

Figure 5-1: Absorption coefficient of a-Si:H thin films: 1604211 (black full line), 1604212 (blue full line), and 1604213 (red full line), obtained through FTPS and optical measurements.

Table 5.1: DOS parameters determined from the absorption coefficient spectrum. *Ea* is obtained from steady state photocurrent spectroscopy (SSPC).

Sample names	*Ea* (from SSPC) in eV	Urbach energy in meV	T_V in K	E_G in eV
1604211	0.75	51	591.85	1.71
1604212	0.77	53	615.06	1.75
1604213	0.69	58	673.09	1.74

density of the parabolic extended valence band set in the DOS model. The standard deviation of the defect states distribution, σ_{Def}, of these samples are quite similar, as can be seen from the deep defect region in α at below 1.3 eV. The estimated values of σ_{Def} are in the range of 0.1-0.3 eV. The approximated values of the DOS parameters obtained through α are summarized in Tab. 5.2.

Table 5.2: Approximated values of DOS parameters for DOS modeling, based on the absorption coefficient spectrum.

Sample names	T_V DOS model (-5%) in K	N_{Def} in $cm^{-3}eV^{-1}$	$\sigma_{Def}(eV)$
1604211	562.26		
1604212	584.31	$N(E_V) \times 10^{-4}$	0.1-0.3
1604213	639.43		

The absorption coefficient spectra of these samples were used to model their DOS using the TLBO algorithm, with a population size of 50 and for 5000 iterations. Two type of DOS models are used, i.e. standard and defect-pool models, to find the absorption coefficient as the one given from the FTPS measurements. Some DOS parameters values such as E_G, T_V, N_{Def}, and σ_{Def} are approximated from the α_{FTPS} as in Tab. 5.2. The value of the other DOS parameters are set so that the E_a corresponds to the measured value by SSPC (See. Tab. 5.1).

The other physical boundary is that the first and second exponential band tail distributions should have rather similar slopes. In order to obtain similar slopes, the temperatures of the first exponential band tail distributions, T_{V1} and T_{C1}, should be constrained in the range of the values of T_V and T_C to for example +10% of T_V and T_C values. The percentage of deviation, n, as stated above e.g. +10%, is a variable. This deviation can be set freely by the users of DeOSt, depending on how much similarity of these two exponential band tail distributions they want to set. As in DeOSt the values of T_{V1} and T_{C1} cannot be set, these values can be fixed by setting the range of values of N_V^{EXT} and N_C^{EXT} using the Eqs. (5.1) and (5.2):

$$N_{Vmin}^{EXT} = N_{EV}\sqrt{\frac{kT_V}{2}} \tag{5.1a}$$

$$N_{Vmax}^{EXT} = N_{EV}\sqrt{\frac{kT_V(1+n)}{2}} \tag{5.1b}$$

$$N_{Cmin}^{EXT} = N_{EC}\sqrt{\frac{kT_C}{2}} \tag{5.2a}$$

$$N_{Cmax}^{EXT} = N_{EC}\sqrt{\frac{kT_C(1+n)}{2}} \tag{5.2b}$$

where the N_{EV}, N_{EC}, T_V, and T_C parameters are not given as constant values, but rather given in range of values, N_{min}^{EXT} should be calculated with the given lower and N_{max}^{EXT} with the given upper limit of values of these parameters.

The results of the absorption coefficient fitting using DeOSt to model the DOS and TLBO algorithm to find the best values of the DOS parameters of the DOS model for each sample are presented in the following subsections.

Results of DOS fitting for the sample 1604211

The result of the absorption coefficient fitting using the TLBO algorithm is presented in Fig. 5-2A. It can be seen that both the absorption coefficients. α found by the TLBO algorithm using the standard and defect-pool DOS model have a very good agreement with the α_{FTPS}. The evolution of the $RMSE_\alpha$ as a function of the iteration number is presented in Fig. 5-3A. Significant drops of $RMSE_\alpha$ arrive almost simultaneously for both DOS models, which is at 7 iterations. Their $RMSE_\alpha$ by the end of the iterations were obtained at 0.192 and 0.188 for standard and defect-pool model, respectively. The DOS parameters search of both models also took into consideration the value of the activation energy, E_a, which was obtained at 0.750 eV using SSPC. During the fitting process, E_a evolves between 0.747 and 0.753 eV, as can be seen in the Fig. 5-3B. In term of the fit of calculated and measured α, the defect-pool DOS model has given a better fit in all regions of α compare to the standard DOS model, as can be seen from the Fig. 5-2A. Nevertheless, both of these DOS models have yield a quite low and acceptable fitness value, as one can evaluate that the disagreement with the measured α lies mainly in the region where the remaining of the interference fringes exists.

The DOS models which corresponds to the calculated α are presented in Fig. 5-2B. These DOS models were found by TLBO using the search space as presented in Tab. 5.3 for the standard DOS model and 5.4 for the defect-pool DOS model. These tables also present the DOS parameter values which finally yield a good agreement with the α_{FTPS}. From that figure, one can see that both DOS models have very similar band tail temperatures at the valence as well as conduction band side. Yet, in the valence band side, a higher N_{EV} is set for the standard DOS model than for the defect-pool model. N_{EV} for the standard DOS model was set at 1.179×10^{22} $cm^{-3}eV^{-1}$, which was higher than the value that was found for the defect-pool DOS model, i.e. 1.000×10^{21}. The major difference of these DOS models can be pinpointed at the deep defect region, where one can find that the defect-pool DOS model has a lower deep defect density compare to the standard DOS model.

The difference of the density of states in the valence band tail and deep defect regions nevertheless is still giving a very good agreement with the measured α. This is because the final product of convolution of these two DOS models are very similar. In the standard DOS model, the optical coefficient of the band tail and defect states, C_{BT}^{OPT} for band tail and C_{Def}^{OPT} for defect states, are lower than in the defect-pool model. The C_{BT}^{OPT} was found at 1.002×10^{-19} for standard DOS model and at 2.029×10^{-19} for the defect-pool model. Whereas the C_{Def}^{OPT} of the standard DOS model was found at 1.002×10^{-19} and that of the defect-pool DOS model at 2.138×10^{-19}. It can be seen that the optical matrix coefficients of the standard DOS model are generally lower than those of the defect-pool DOS model for this sample. This means that if similar α are expected from both of these models, the density of states of the defect-pool model has to be lower than that of the standard DOS model.

Actually, these results illustrate the limits of the research of the DOS parameters starting from an experimental curve. Indeed, the calculation of α is a convolution product between the states from which the electron is extracted and the states where

the electron is arriving. Besides, one has to take into account the optical coefficients that are involved in these transitions. We can compare the results of the calculations of α using DeOSt and the TLBO algorithm for both models, standard and defect pool, both giving a quite good fit whatever the region that can be considered (high energy, Urbach tail and deep defects).

If we consider the transitions in the high energy region, and taking account of the differences obtained for the valence band tail we could expect different fits for the defect pool model and the standard one, because for the latter the valence band tail is higher than for the defect pool by a factor of the order of 11 (see the values of N_{EV}). However, it can be noted that the conduction band tail of the defect pool is higher by a factor of the order of 3 (see the values of N_{EC}) and that the optical coefficient for the band tail of the defect pool model is approximately twice the value of that of the standard model. It means that, considering the states of arrival times the optical coefficient for departure and arrival states, we have a factor of 3x2x2 = 12 which is of the same order of the factor of 11 found for the ratio of the density of states at the valence band side. Hence, for the defect pool model what is lost on one side (less states in the valence band side) is gained on the other (more states on the conduction band side) and also compensated by higher optical coefficients. At the end this leads to equivalent convolution products giving the same variation of α in the high energy region.

The same approach can be used to explain the discrepancies found for the band tails at the origin of the Urbach slope as well as for the deep states on the valence band side (below the Fermi level). Indeed, the defect pool deep states are also found much lower that these of the standard model. However, as for the high energy region the lower density of states on the valence band side is compensated by a higher density of states on the conduction band side as well as by higher optical coefficients.

To obtain the same order of magnitude for the DOS for both models we should have fixed the optical coefficients at the same values instead of using them as a free parameter that can be adjusted by the TLBO algorithm.

The last point of discrepancy concerns the deep states above the Fermi level. These states are found much higher for the standard model than for the defect pool model. However, their influence on the final value of α is very limited as shown in the previous chapter. Indeed, transitions from the valence band toward these states creates holes the contribution of which to the current measured by FTPS is rather limited since holes are the minority carriers (low mobility). Besides, there are no transitions of electrons from these states toward the conduction band since these states are empty, being above the Fermi level. This high value of the deep defect density above the Fermi level in the standard model is mainly found for it is this value that fixes the position of the dark Fermi level at the position recorded experimentally by SSPC.

We will see in the following that these types of behaviors are also found with the other samples that we have studied.

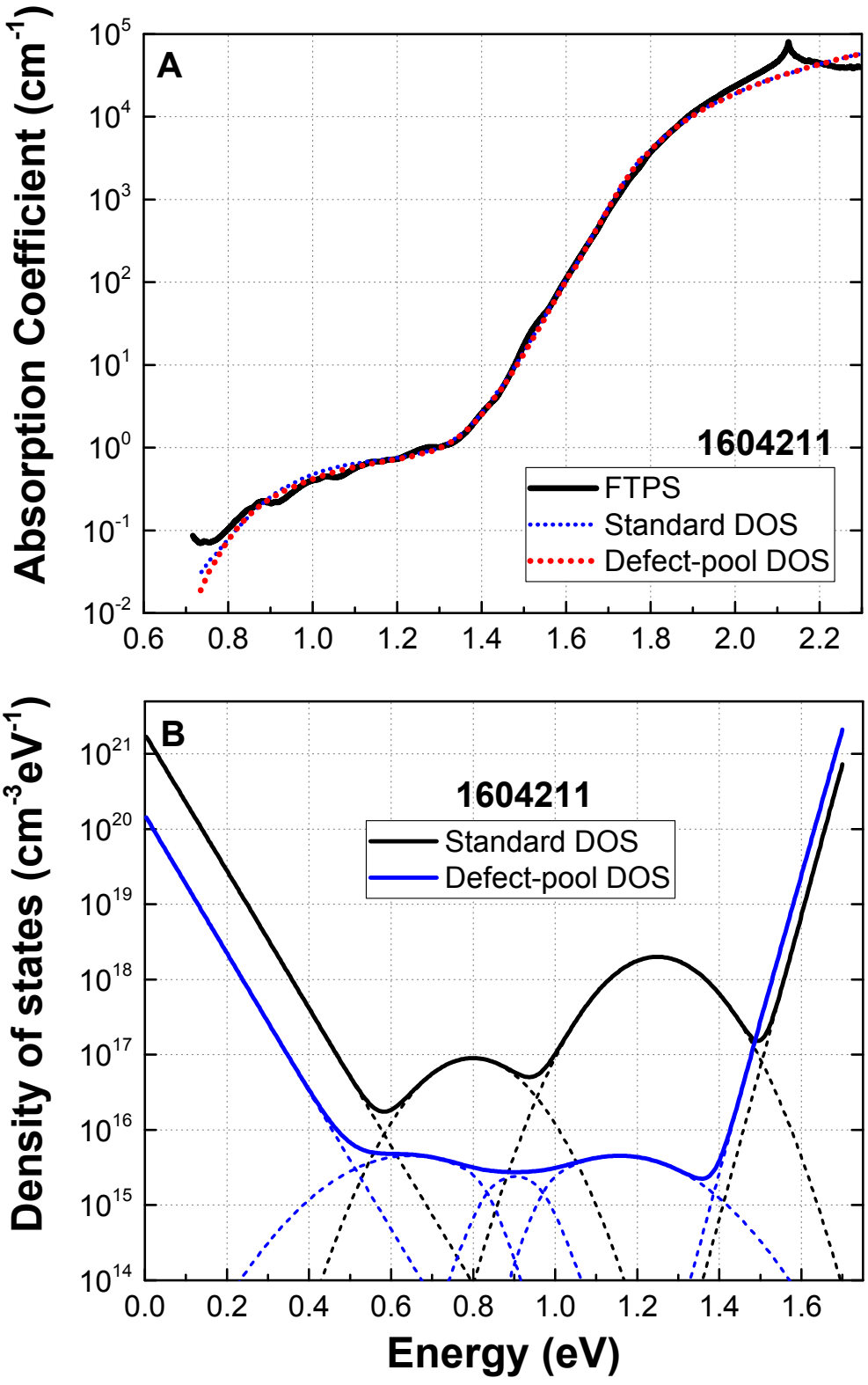

Figure 5-2: (A) Comparison of the absorption coefficient spectra obtained from the FTPS measurements and from the calculated DOS models (standard and defect-pool models) found by the TLBO algorithm and (B) comparison of the standard and defect-pool DOS models reproducing the absorption coefficient spectrum measured by FTPS on the sample 1604211.

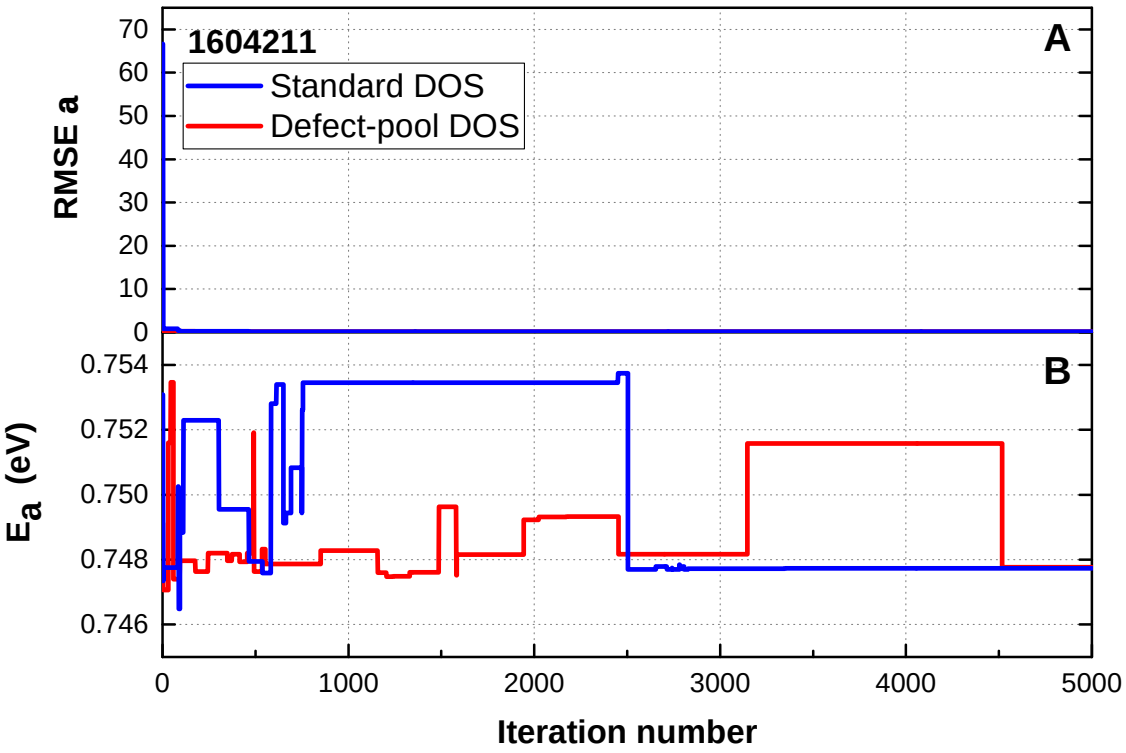

Figure 5-3: The evolution of the (A) $RMSE_\alpha$ and (B) activation energy, E_a, during the DOS model fitting of the sample 1604211 using the TLBO algorithm.

Results of DOS fitting for the sample 1604212

The results of the absorption coefficient fitting of the sample 1604212 using the TLBO algorithm is presented in Fig. 5-4A. It can be seen that the fitting using both standard and defect-pool DOS models had very good agreement with the spectrum obtained from the FTPS measurement. Nevertheless, the α given by the standard DOS model has a better fit compare to the α given by the defect-pool DOS model, particularly in the deep defect region below 1 eV. The quality of the fitting of α can be seen from the calculated values of the $RMSE_\alpha$ by the end of the iteration, which were found at 0.115 and 0.159 for the standard and defect-pool models, respectively. The evolution of the $RMSE_\alpha$ as a function of the iteration number is presented in Fig. 5-5A. Significant drop of $RMSE_\alpha$ value occurred earlier for the defect-pool DOS model, which is at 15 iterations, than for the standard DOS model which is at 150 iterations. The fitting of α should also consider the value of the activation energy E_a which was previously measured using SSPC, which is 0.770 eV for the sample 1604212. During the fitting process, the value of E_a oscillates between 0.766 and 0.774 eV, as can be seen in the Fig. 5-5B, which is around the measured value from SSPC.

The DOS models giving the calculated absorption coefficient spectra as in Fig. 5-4A are drawn in Fig. 5-4B. The parameter values of the DOS models are presented in Tabs. 5.5 and 5.6 for the standard and defect-pool DOS models, respectively. The standard and defect-pool DOS models have very similar valence band tail slopes,

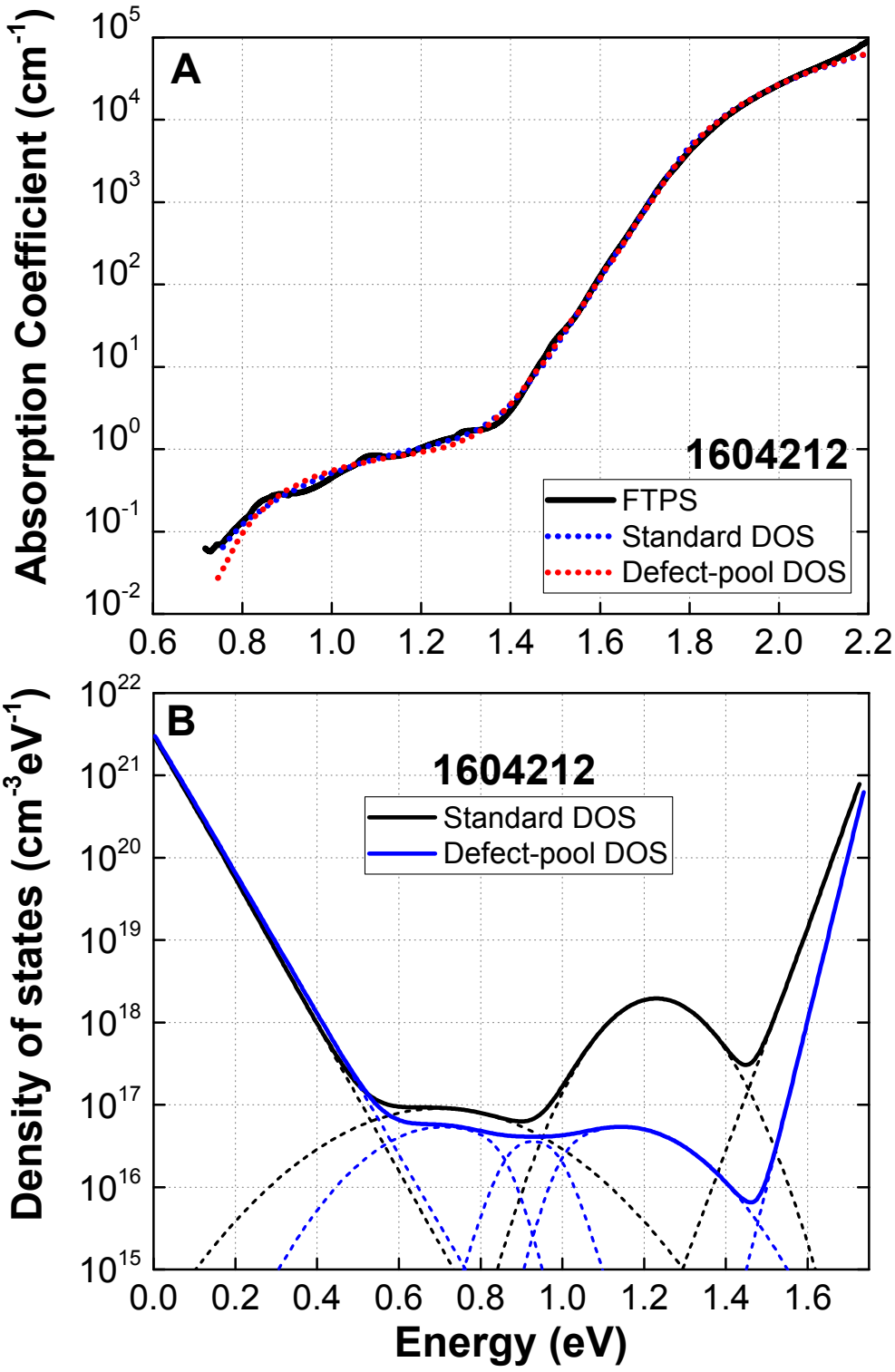

Figure 5-4: (A) Comparison of the absorption coefficient spectra obtained from the FTPS measurements and from the calculated DOS models (standard and defect-pool models) found by the TLBO algorithm and (B) comparison of the standard and defect-pool DOS models reproducing the absorption coefficient spectrum measured by FTPS on the sample 1604212.

Table 5.3: The search space and the corresponding DOS parameter values found by the TLBO algorithm giving the best fit to the given α_{FTPS} for sample 1604211, using the standard DOS model.

DOS parameters	Search space	Values by TLBO	$RMSE_\alpha$
Standard DOS			
E_a (SSPC)	0.750	0.748	0.192
N_{EV}	$[7.000 \times 10^{21}; 2.000 \times 10^{22}]$	1.179×10^{22}	
N_{EC}	$[7.000 \times 10^{21}; 2.000 \times 10^{22}]$	7.002×10^{21}	
E_G	[1.700; 1.740];	1.700	
C_{BT}^{opt}	$[1.000 \times 10^{-19}; 3.010 \times 10^{-19}]$	1.000×10^{-19}	
T_V	[550.00; 575.00]	550.05	
N_V^{EXT}	$[1.064 \times 10^{21}; 3.302 \times 10^{21}]$	1.922×10^{21}	
$E_V^{cut-off}$	[0.050; 0.300]	0.266	
T_C	[250.00; 400.00]	250.10	
N_C^{EXT}	$[7.174 \times 10^{20}; 2.754 \times 10^{21}]$	7.293×10^{20}	
$E_C^{cut-off}$	[1.600; 1.740]	1.606	
C_{Def}^{opt}	$[1.000 \times 10^{-19}; 3.000 \times 10^{-19}]$	1.002×10^{-19}	
N_{don}^{max}	$[9.000 \times 10^{16}; 2.000 \times 10^{18}]$	9.003×10^{16}	
E_{don}^{max}	[0.700; 0.800]	0.799	
σ_{don}	[0.100; 0.300]	0.102	
N_{acc}^{max}	$[9.000 \times 10^{16}; 2.000 \times 10^{18}]$	2.000×10^{18}	
E_{acc}^{max}	[1.000; 2.000];	1.249	
σ_{acc}	[0.100; 0.300]	0.101	

although a slightly lower slope is obtained for the defect-pool model. These slopes corresponds to the valence band tail temperatures, T_V, of 567 and 589 K for standard and defect-pool DOS models, respectively. In the deep defect region, it can be seen that the defect-pool DOS model for this sample has higher deep-defect density compare to the standard DOS model. Between 0.6 and 0.9 eV, the defect-density of the standard DOS model is 9.346×10^{16} which is twice higher than the defect-pool one. Closer to the conduction band region at the energy between 1 and 1.4 eV, the maximum density of the deep defect in the standard DOS model is found at 2.022×10^{18} corresponds to 50 times of the defect density found in the defect-pool DOS model. The conduction band tail of the standard DOS model appears to be lower than that of the defect-pool one. The lower slope corresponds to a conduction band tail temperature, T_C of 372 K. On the other hand, the defect-pool DOS model has a T_C of 250 K.

Table 5.4: The search space and the corresponding DOS parameter values found by the TLBO algorithm giving the best fit to the given α_{FTPS} for sample 1604211, using the defect-pool DOS model.

DOS parameters	Search space	Values by TLBO	$RMSE_\alpha$
Defect-pool DOS			
E_a (SSPC)	0.750	0.753	0.188
N_{EV}	$[1.000 \times 10^{21}; 5.000 \times 10^{22}]$	1.000×10^{21}	
N_{EC}	$[1.000 \times 10^{21}; 5.000 \times 10^{22}]$	2.000×10^{22}	
E_G	[1.700; 1.750];	1.700	
C_{BT}^{opt}	$[1.000 \times 10^{-19}; 3.000 \times 10^{-19}]$	2.029×10^{-19}	
T_V	[550.00;575.00]	550.03	
N_V^{EXT}	$[1.520 \times 10^{20}; 3.302 \times 10^{21}]$	1.520×10^{20}	
$E_V^{cut-off}$	[0.050; 0.30]	0.303	
T_C	[250.00; 400.00]	250.02	
N_C^{EXT}	$[1.025 \times 10^{20}; 2.754 \times 10^{21}]$	2.754×10^{21}	
$E_C^{cut-off}$	[1.500; 1.770]	1.500	
C_{Def}^{opt}	$[1.000 \times 10^{-19}; 3.000 \times 10^{-19}]$	2.138×10^{-19}	
H	$[1.500 \times 10^{21}; 9.000 \times 10^{21}]$	1.500×10^{21}	
E_{pool}	[0.950; 1.600]	1.160	
σ_{pool}	[0.100; 0.300]	0.149	
E_U	[0.100; 0.300]	0.100	

Again, the results of the fit using either the standard model or the defect pool model illustrate one of the limits of the accuracy of the method. Indeed, though the densities of the tail states on the valence band side are rather similar, one can see that the characteristic temperature of the valence band tail for the standard model is slightly lower than that of the defect pool model. This lower T_V is compensated by a higher T_C so that the final convolution products are quite identical giving very close fits of the Urbach region of α for both models. The reader may note also that the influence of T_C on the final result is rather weak, as seen in the previous chapter. It explains why though we have a large variation of T_C (372 K instead of 250 K) we finally obtained the same convolution product with a small variation of T_V (566 K instead of 589 K).

Results of DOS fitting for the sample 1604213

The results of the DOS parameter research of sample 1604213 using its measured absorption coefficient are presented in Fig. 5-6. From Fig. 5-6A, one can see that the

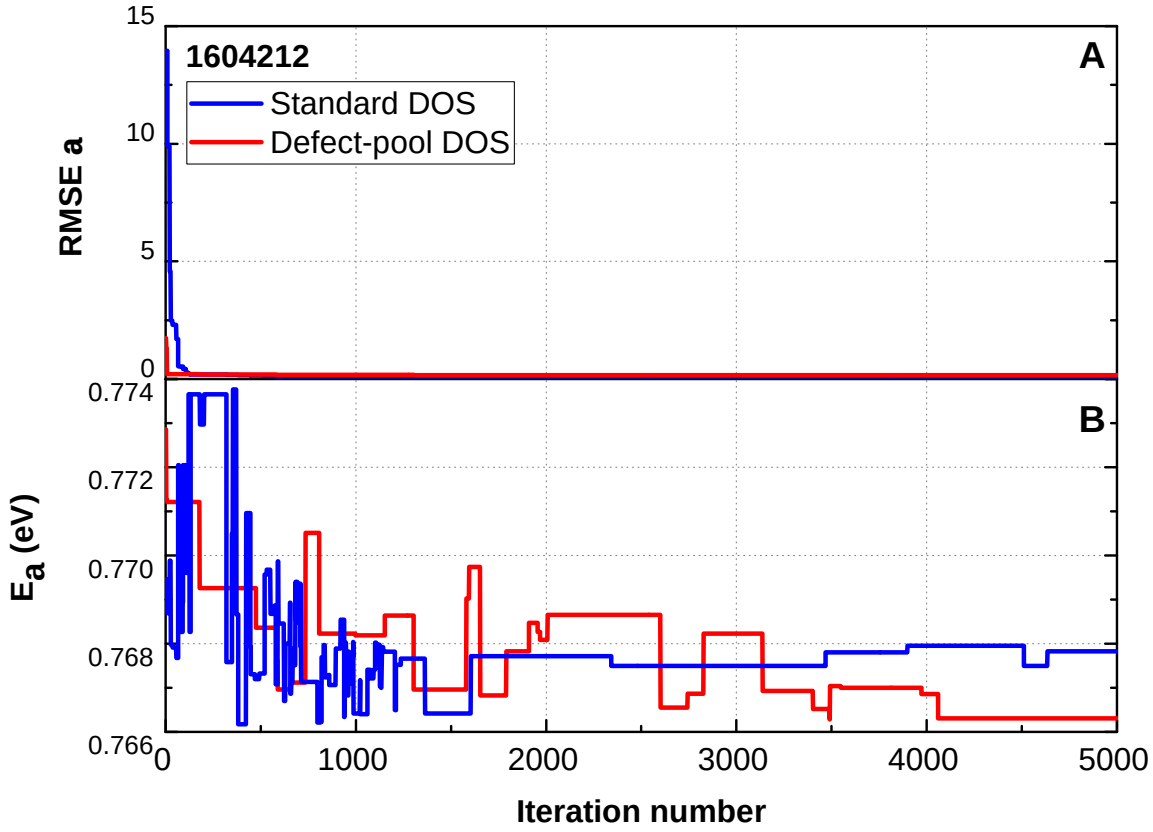

Figure 5-5: The evolution of the (A) $RMSE_\alpha$ and (B) activation energy, E_a, during the DOS model fitting of the sample 1604212 using the TLBO algorithm.

absorption coefficient calculated from the DOS models in 5-6B yields quite a good fit with the measured α_{FTPS}, notably from the standard DOS model. Meanwhile, the absorption coefficient calculated from the defect-pool DOS model, represented in red dots, did not succeed to reproduce the shape of α_{FTPS} at the region of 1-1.4 eV, as can be seen that the calculated α from defect-pool DOS model is lower than the α_{FTPS}. Despite of this slight disagreement, from Fig. 5-7, the $RMSE_\alpha$ of the defect-pool DOS model is still very low and acceptable, i.e. 0.227. Additionally, this model reproduced a good agreement in term of its E_a that has been measured by SSPC.

A good agreement of α in the high energy region is obtained despite of different DOS between the standard and defect-pool DOS models, notably in the conduction band tail region. The reason of which can be explained using the values of the DOS parameters of these DOS models presented in Tabs. 5.7 for the standard and 5.8 for the defect-pool DOS model. From these tables, it can be seen that the value of N_{EC} is 3.5 times higher for the defect-pool DOS model, whilst the C_{BT}^{opt} of this DOS model is two times lower than the standard DOS model. Hence, the integral of the convolution product of band-to-band transitions of these two DOS models are very similar. In the other hand, the defect-pool DOS model of sample 1604213, as can be seen from Fig. 5-6B, presents a lower density of deep-defect compared to the standard DOS model.

Table 5.5: The search space and the corresponding DOS parameter values found by the TLBO algorithm giving the best fit to the given α_{FTPS} for sample 1604212, using the standard DOS model.

DOS parameters	Search space	Values by TLBO	$RMSE_\alpha$
Standard DOS			
E_a (SSPC)	0.770	0.768	0.115
N_{EV}	$[7.000 \times 10^{21}; 2.000 \times 10^{22}]$	1.901×10^{22}	
N_{EC}	$[7.000 \times 10^{21}; 2.000 \times 10^{22}]$	7.002×10^{21}	
E_G	[1.730; 1.770];	1.735	
C_{BT}^{opt}	$[1.000 \times 10^{-19}; 3.000 \times 10^{-19}]$	1.003×10^{-19}	
T_V	[564.00; 604.00]	566.92	
N_V^{EXT}	$[1.077 \times 10^{21}; 3.384 \times 10^{21}]$	3.379×10^{21}	
$E_V^{cut-off}$	[0.050; 0.300]	0.171	
T_C	[250.00; 400.00]	372.6	
N_C^{EXT}	$[7.174 \times 10^{20}; 2.754 \times 10^{21}]$	8.170×10^{20}	
$E_C^{cut-off}$	[1.600; 1.740]	1.611	
C_{Def}^{opt}	$[1.000 \times 10^{-19}; 3.000 \times 10^{-19}]$	1.001×10^{-19}	
N_{don}^{max}	$[9.000 \times 10^{16}; 2.000 \times 10^{18}]$	9.003×10^{16}	
E_{don}^{max}	[0.700; 0.800]	0.702	
σ_{don}	[0.100; 0.300]	0.199	
N_{acc}^{max}	$[9.000 \times 10^{16}; 2.000 \times 10^{18}]$	1.950×10^{18}	
E_{acc}^{max}	[1.000; 2.000];	1.228	
σ_{acc}	[0.100; 0.300]	0.101	

In this case, one can see the compensating effect of the density of deep defect and the C_{Def}^{opt}. The value of C_{Def}^{opt} for the defect-pool DOS model is three times higher than that of the standard DOS model. Therefore, similar α can only be obtained with lower density of defect in the defect-pool DOS model.

Conclusions

Again, these results underline the limits of the fitting of the α experimental curves with the TLBO algorithm. Using the same optical coefficients for both models, standard and defect pool, we would have obtained closer densities of states.

To check this last assumption and to illustrate the influence of the optical coefficients on the determination of the density of states we have performed a new calculation with the TLBO algorithm for the determination of the DOS parameters

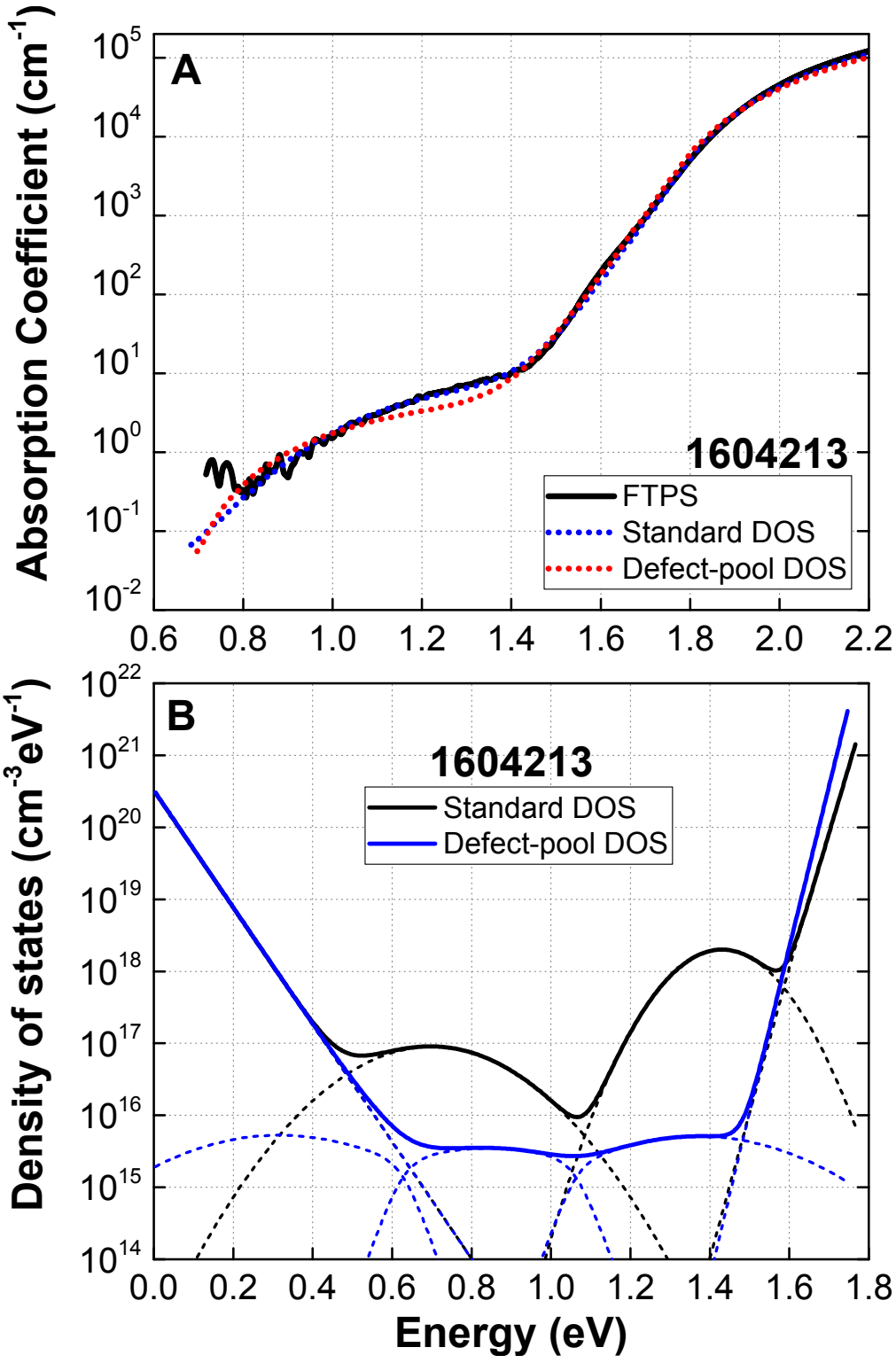

Figure 5-6: (A) Comparison of the absorption coefficient spectra obtained from the FTPS measurements and from the calculated DOS models (standard and defect-pool models) found by the TLBO algorithm and (B) comparison of the standard and defect-pool DOS model reproducing the absorption coefficient spectrum measured by FTPS on the sample 1604213.

Table 5.6: The search space and the corresponding DOS parameter values found by the TLBO algorithm giving the best fit to the given α_{FTPS} for sample 1604212, using the defect-pool DOS model.

DOS parameters	Search space	Values by TLBO	$RMSE_\alpha$
Defect-pool DOS			
E_a (SSPC)	0.770	0.766	0.159
N_{EV}	$[7.000 \times 10^{21}; 2.000 \times 10^{22}]$	1.994×10^{22}	
N_{EC}	$[7.000 \times 10^{21}; 2.000 \times 10^{22}]$	7.059×10^{21}	
E_G	[1.730; 1.770];	1.745	
C_{BT}^{opt}	$[1.000 \times 10^{-19}; 3.000 \times 10^{-19}]$	1.001×10^{-19}	
T_V	[564.00;604.00]	589.26	
N_V^{EXT}	$[1.077 \times 10^{21}; 3.384 \times 10^{21}]$	3.380×10^{21}	
$E_V^{cut-off}$	[0.050; 0.30]	0.106	
T_C	[250.00; 400.00]	250.02	
N_C^{EXT}	$[7.174 \times 10^{20}; 2.754 \times 10^{21}]$	7.172×10^{20}	
$E_C^{cut-off}$	[1.600; 1.750]	1.601	
C_{Def}^{opt}	$[1.000 \times 10^{-19}; 3.000 \times 10^{-19}]$	1.228×10^{-19}	
H	$[2.500 \times 10^{21}; 7.500 \times 10^{21}]$	4.628×10^{21}	
E_{pool}	[0.800; 1.500]	1.150	
σ_{pool}	[0.100; 0.300]	0.142	
E_U	[0.100; 0.300]	0.105	

for sample 1604211, a calculation based on the defect pool model DOS. In this determination we have fixed the optical coefficients at the same values as the ones we have used for the calculation based on the standard defect pool model: the optical coefficients were allowed to vary only in the range 1.000 – 1.005×10^{19} $cm^{-5/2}eV^{-1}$.

The results of this calculation are presented in Fig. 5-8. In Fig. 5-8A it can be seen that the reconstructed α are all in good agreement with the experimental measurement. However, it can be seen in Fig. 5-8B that the DOS distributions found in the case of the defect pool model are really different one from another, when determined with different optical coefficients. The most striking differences are a much higher valence band tail, though with almost the same characteristic temperature, and a much higher density of deep states, the deep defect density below the Fermi level being very close to that of the DOS distribution calculated with the standard DOS model, for which we have used the same optical coefficients. The parameters that we have found to create the DOS reproducing the experimental results are presented in Tab. 5.9. One can see that most of them are close to the parameters used to

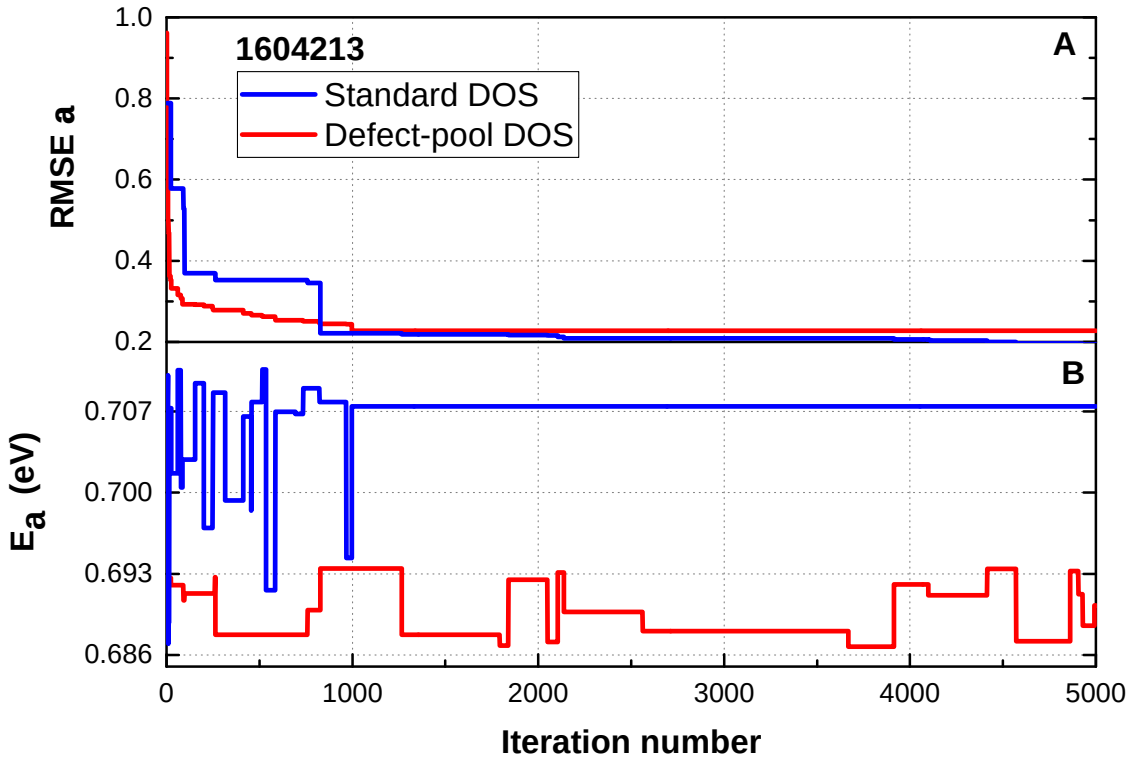

Figure 5-7: The evolution of the (A) $RMSE_\alpha$ and (B) activation energy, E_a, during the DOS model fitting of the sample 1604213 using the TLBO algorithm.

reproduce α using the standard DOS model by looking at Tab. 5.3.

These results underline again the influence that the capture coefficients can have on the calculation of the DOS distributions used to reproduce the experimental results. Their involvement in the convolution product with which we calculate α is really important and uncontrolled range of variation of these parameters could lead to unrealistic values for the distribution of states. Since these optical coefficients are unknown we can only make assumptions on their values. A guide for a proper estimate can be the hydrogen content of the film. Indeed, the hydrogen content H is one of the parameters used to calculate the deep defect distribution in the defect pool model. In our last calculation we have found a value of the order of $H = 9 \times 10^{21}$ cm^{-3} corresponding to a percentage of 18 % of hydrogen. This value, though a little too high, corresponds to the value expected in our samples. Therefore, we believe that the estimate of $1 \times 10^{19} cm^{-5/2} eV^{-1}$ for the capture coefficient is rather satisfying.

In addition, a look at the density of states above the Fermi level underlines that the determination of the density of states above the Fermi level cannot be achieved accurately simply because, as already mentioned above, this part of the density of states as only little influence on the final calculation of α. Other experiments, like modulated photocurrent are needed to investigate on this part of the DOS.

In conclusion, the TLBO algorithm combined with DeOSt appears to be a powerful tool to estimate the DOS distribution in a-Si:H from the experimental results

Table 5.7: The search space and the corresponding DOS parameter values found by the TLBO algorithm giving the best fit to the given α_{FTPS} for sample 1604213, using the standard DOS model.

DOS parameters	Search space	Values by TLBO	$RMSE_\alpha$
Standard DOS			
E_a (SSPC)	0.690	0.690	0.193
N_{EV}	$[2.000 \times 10^{21}; 2.000 \times 10^{22}]$	2.000×10^{21}	
N_{EC}	$[2.000 \times 10^{21}; 2.000 \times 10^{22}]$	1.534×10^{22}	
E_G	[1.730; 1.770];	1.768	
C_{BT}^{opt}	$[1.000 \times 10^{-19}; 3.000 \times 10^{-19}]$	3.000×10^{-19}	
T_V	[620.00; 645.00]	620.00	
N_V^{EXT}	$[3.228 \times 10^{20}; 3.497 \times 10^{21}]$	3.250×10^{20}	
$E_V^{cut-off}$	[0.050; 0.300]	0.051	
T_C	[250.00; 400.00]	250.06	
N_C^{EXT}	$[2.050 \times 10^{20}; 2.754 \times 10^{21}]$	2.650×10^{21}	
$E_C^{cut-off}$	[1.600; 1.750]	1.604	
C_{Def}^{opt}	$[1.000 \times 10^{-19}; 3.000 \times 10^{-19}]$	1.01×10^{-19}	
N_{don}^{max}	$[9.000 \times 10^{16}; 2.000 \times 10^{18}]$	9.006×10^{16}	
E_{don}^{max}	[0.700; 0.800]	0.703	
σ_{don}	[0.100; 0.300]	0.161	
N_{acc}^{max}	$[9.000 \times 10^{16}; 2.000 \times 10^{18}]$	2.000×10^{18}	
E_{acc}^{max}	[1.000; 2.000];	1.431	
σ_{acc}	[0.100; 0.300]	0.101	

providing that some parameters, such as the optical coefficients, are handle with caution in order to obtain realistic DOS distribution. Besides, though it is possible to evaluate the conduction band tail shape since it is involved in the calculation of the Urbach energy, it seems rather difficult to have a correct estimate of the deep defect density above the Fermi level since this part of the DOS has only little influence on the final calculation of α.

5.2 Comparison of FTPS performed on thin films and solar cells

In the previous section, we have performed FTPS on a-Si:H thin films deposited on a transparent non conductive substrate, i.e. glass. In this section, the discussion will

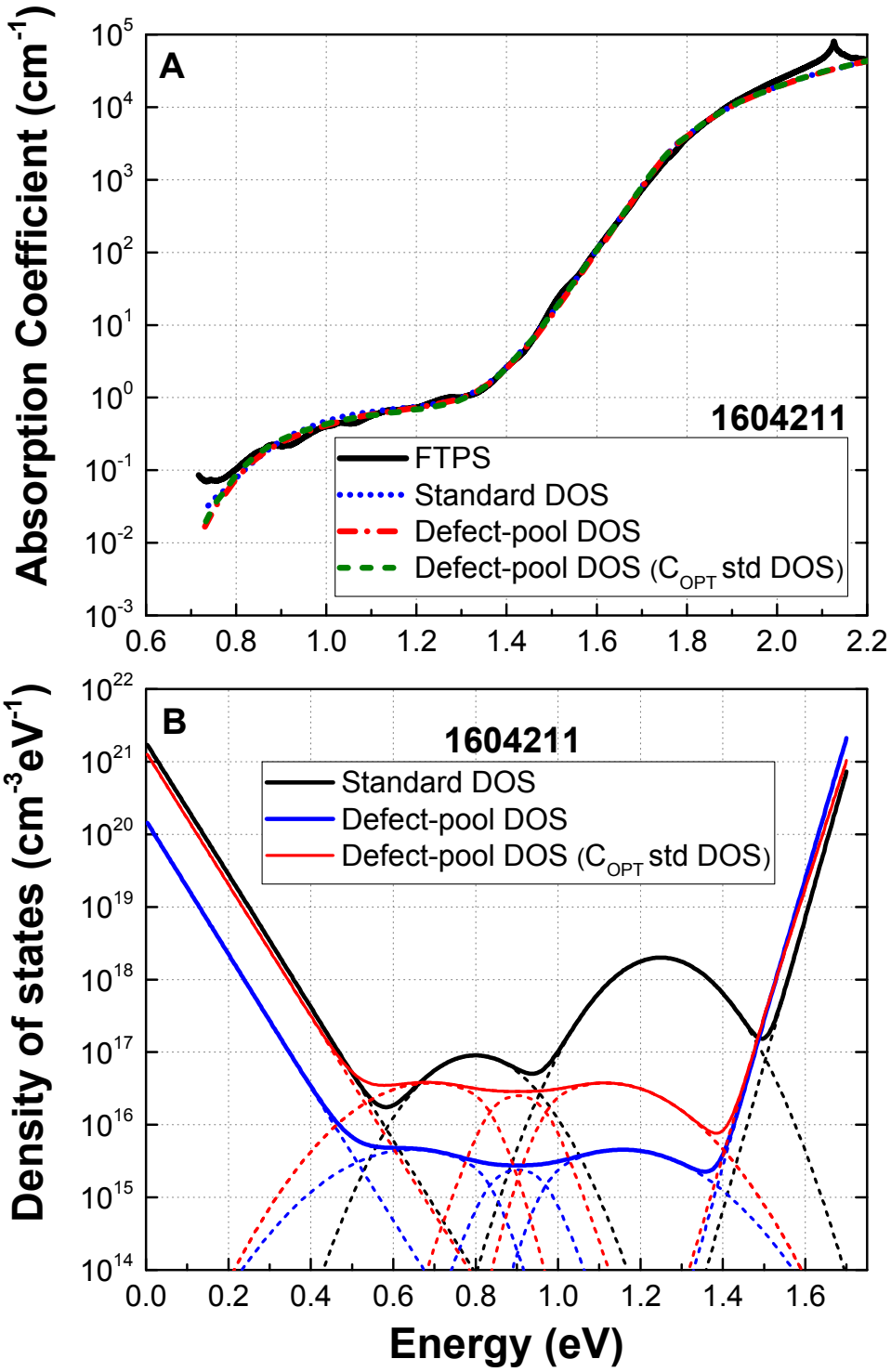

Figure 5-8: (A) Comparison of the absorption coefficient spectra obtained from the FTPS measurements and from the calculated DOS models (standard, defect-pool, and defect-pool DOS models using the C^{opt} of the standard DOS model) found by the TLBO algorithm and (B) comparison of the standard, defect-pool, and defect-pool DOS model using the C^{opt} of the standard DOS model, reproducing the absorption coefficient spectrum measured by FTPS on the sample 1604211.

Table 5.8: The search space and the corresponding DOS parameter values found by the TLBO algorithm giving the best fit to the given α_{FTPS} for sample 1604213, using the defect-pool DOS model.

DOS parameters	Search space	Values by TLBO	$RMSE_\alpha$
Defect-pool DOS			
E_a (SSPC)	0.690	0.707	0.227
N_{EV}	$[2.000 \times 10^{21}; 5.000 \times 10^{22}]$	2.004×10^{21}	
N_{EC}	$[2.000 \times 10^{21}; 5.000 \times 10^{22}]$	4.998×10^{22}	
E_G	[1.740; 1.760];	1.753	
C_{BT}^{opt}	$[1.000 \times 10^{-19}; 3.000 \times 10^{-19}]$	1.528×10^{-19}	
T_V	[620.00;645.00]	620.00	
N_V^{EXT}	$[3.228 \times 10^{20}; 8.742 \times 10^{21}]$	3.228×10^{20}	
$E_V^{cut-off}$	[0.050; 0.30]	0.005	
T_C	[250.00; 400.00]	220.04	
N_C^{EXT}	$[1.923 \times 10^{20}; 5.656 \times 10^{21}]$	5.656×10^{21}	
$E_C^{cut-off}$	[1.600; 1.760]	1.600	
C_{Def}^{opt}	$[1.000 \times 10^{-19}; 3.000 \times 10^{-19}]$	3.000×10^{-19}	
H	$[2.500 \times 10^{21}; 7.500 \times 10^{21}]$	5.000×10^{21}	
E_{pool}	[0.500; 1.600]	1.372	
σ_{pool}	[0.100; 0.300]	0.21982	
E_U	[0.100; 0.400]	0.400	

concern the results of FTPS measurements on thin films of a-Si:H on glass and solar cells using our *3-in-1* measurement bench as presented in Sec. 2.2.1.

Results of FTPS measurement on solar cells were published by Poruba *et al.* and FTPS was reported as a fast and sensitive quality assessment for photovoltaics thin films [42]. They demonstrated how to utilize the FTPS for measurement of micro crystalline silicon films grown on conductive TCO covered glass substrate, as it is the case for solar cells, in order to put into evidence that the properties of this material strongly depend on the substrate used. In their publication, they also showed a possibility to interpret the FTPS data on cells as the quantum efficiency (spectral response) measurement extended from near IR over the whole visible region. In another publication [44], the appropriate measuring conditions and evaluation procedures for a correct data interpretation of various thin films and solar cell structures were presented. They showed how the measured and the final evaluated α spectra differ in case of single junction amorphous and micro crystalline silicon solar cells as well as for a micromorph tandem. From their results, they found that the key issue

Table 5.9: The search space and the corresponding DOS parameter values found by the TLBO algorithm giving the best fit to the given α_{FTPS} for sample 1604211, using the defect-pool DOS model with the C^{opt} of the standard DOS model.

DOS parameters	Search space	Values by TLBO	$RMSE_\alpha$
Defect-pool DOS			
E_a (SSPC)	0.750	0.747	0.186
N_{EV}	$[1.000 \times 10^{21}; 5.000 \times 10^{22}]$	8.753×10^{21}	
N_{EC}	$[1.000 \times 10^{21}; 5.000 \times 10^{22}]$	9.403×10^{21}	
E_G	[1.700; 1.750];	1.700	
C_{BT}^{opt}	$[1.000 \times 10^{-19}; 1.005 \times 10^{-19}]$	1.000×10^{-19}	
T_V	[550.00;575.00]	554.88	
N_V^{EXT}	$[1.520 \times 10^{20}; 3.302 \times 10^{21}]$	1.335×10^{21}	
$E_V^{cut-off}$	[0.050; 0.30]	0.052	
T_C	[250.00; 400.00]	264.07	
N_C^{EXT}	$[1.025 \times 10^{20}; 2.754 \times 10^{21}]$	1.526×10^{21}	
$E_C^{cut-off}$	[1.500; 1.770]	1.502	
C_{Def}^{opt}	$[1.000 \times 10^{-19}; 1.005 \times 10^{-19}]$	1.000×10^{-19}	
H	$[1.500 \times 10^{21}; 9.000 \times 10^{21}]$	9.000×10^{21}	
E_{pool}	[0.950; 1.600]	1.122	
σ_{pool}	[0.100; 0.300]	0.137	
E_U	[0.100; 0.300]	0.100	

of the tandem structure diagnostics is a separation of FTPS signals from amorphous and micro crystalline parts of a stacked structure and their correct interpretation of the absorption coefficient spectra. In order to provide the correct interpretation, they have built a computer model cell using the simulation of the light propagation within the structure of the solar cell stack, and compared the model cell α spectra with the measured spectra from FTPS.

The experimental studies related to the influence of the pressure used during the deposition of individual a-Si:H films and absorber layers in p–i–n solar cells on the films and solar cells absorption using FTPS were investigated by Melskens *et al.* [30]. It was found that the deposition pressure influences the structural phase of the Si:H films; below a certain threshold pressure a phase transition from the amorphous to the micro crystalline phase is observed. On the other hand, this phenomenon did not appear from the measurement results on solar cells. They also used the FTPS results on solar cells to evaluate the quality of Si:H films and solar cell absorber layers, since from the obtained sub-band gap absorption coefficient spectrum the

defect concentration can be estimated.

In his thesis [48], Python presented the influence of the properties of the substrate used for the deposition of the solar cell's intrinsic layer (i-layer) on the values of α obtained from FTPS measurement. In this study, he demonstrated that three characteristics (doping, thickness, and surface morphology) of the ZnO, as the substrate of the i-layer, modify the light intensity that enters in the silicon solar cell leading to an inexact evaluation of the α spectrum. However, the substrate morphology only weakly affects the FTPS results compared to the doping and substrate thickness. From the various measurements, he found that the measurement of FTPS signal does not give the real α of the i-layer because of the additional absorption due to the wavelength dependent light scattering of the i-layer's substrate. To be able to compare the quality of the i-layer of cells deposited on different substrates, two methods were proposed to suppress the influence of the substrate on the measurements of the solar cell's intrinsic layer absorption.

In this section, we exemplify the use of our 3-in-1 characterization tool to study both intrinsic a-Si:H thin films deposited on glass and n-i-p solar cells. The intrinsic i-layers of the solar cells were deposited using the same deposition parameters as the a-Si:H thin films. The aim of this study is to answer the following questions: (i) Is it really possible to probe the deep defect density of a material by applying FTPS to a solar cell incorporating this material? (ii) How the $\alpha(h\nu)$ curve obtained by FTPS on a device compares with the same curve obtained on a thin film? Indeed, previous attempts to compare film and devices using CPM provided interesting results [22]. Thanks to our 3-in-1 technique we can now obtain more accurate results which reveal a parasitic absorption by TCO in the solar cells.

5.2.1 Experimental details

Deposition of a-Si:H films and solar cells

The deposition of the thin a-Si:H films and transparent solar cells was performed using a radio-frequency plasma enhanced chemical vapor deposition (RF-PECVD) reactor system [96]. Two sample groups were used in these experiments. Each group of samples consists of a thin a-Si:H sample deposited on glass and n-i-p type transparent solar cells with the i-layer deposited using the same deposition parameters as the thin film on glass (See Fig. 5-9). The deposition parameters of the thin films and transparent solar cells are summarized in Tab. 5.10.

The thin films on glass were fitted with two parallel ohmic contacts on top, which were 1 cm long and separated by 1 mm. These electrodes were used for the FTPS. On these thin film on glass samples, a space was kept free of reflective metallic contacts to be able to perform the R/T measurements.

For the solar cells, the back TCO was deposited on glass with a thickness of 1000 nm followed by an n-type layer of $\mu c - SiOx$ deposited with a thickness of 20 nm. On top of these layers, the i-layer is a 200 nm thick a-Si:H layer, covered with a 20 nm thick p-layer of a-SiC. The TCO layer was then deposited on top of the p-layer with a thickness of 80 nm. The first group of samples contains two solar cell devices

Table 5.10: Deposition parameters of the thin a-Si:H films and transparent solar cell stacks used in the experiments

Deposition Parameters	Group I.	Group II.
Electrodes' distance	17 mm	17 mm
Pressure	280 mTorr	260 mTorr
SiH_4 flow	35 sccm	35 sccm
RF power	4 W	4 W
Deposition time	1 hour 34 mins	3 hours

with two types of TCO layers, i.e. ZnO and ITO, whereas the second group has only one solar cell with ZnO as the TCO layer, as represented in Fig. 5-9.

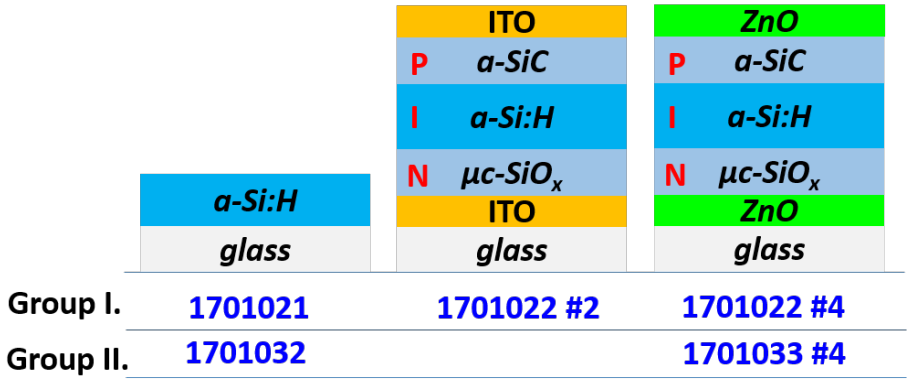

Figure 5-9: Thin a-Si:H films and transparent solar cell stacks used in these experiments. Sample names are denoted in blue.

System configuration for measurements

The R/T and FTPS measurements of the thin films deposited on glass were performed using the basic principles of photocurrent measurements and experimental setup as explained in Chap. 2, Fig. 2-25. For the FTPS we used the parallel ohmic contacts deposited on the coplanar samples and a voltage of 60 V was applied in between. Meanwhile, the FTPS measurement of the transparent solar cells is based on Eq. 5.3, using exactly the same principles of FTPS measurements for thin films, except that no bias voltage is applied. The setup of the R/T and FTPS measurement of the transparent solar cells is presented in Fig. 5-10. We have:

$$\alpha(\nu) \sim \frac{J_{solarcells}(\nu)}{F_{transmitted}(\nu)} \tag{5.3}$$

where the $J_{solarcells}$ is the photocurrent density generated by the solar cells in A.cm^{-2}, and $F_{transmitted}$ is the flux transmitted by the transparent solar cells measured by a

calibrated photodiode placed behind the transparent solar cells. For the SR and EQE

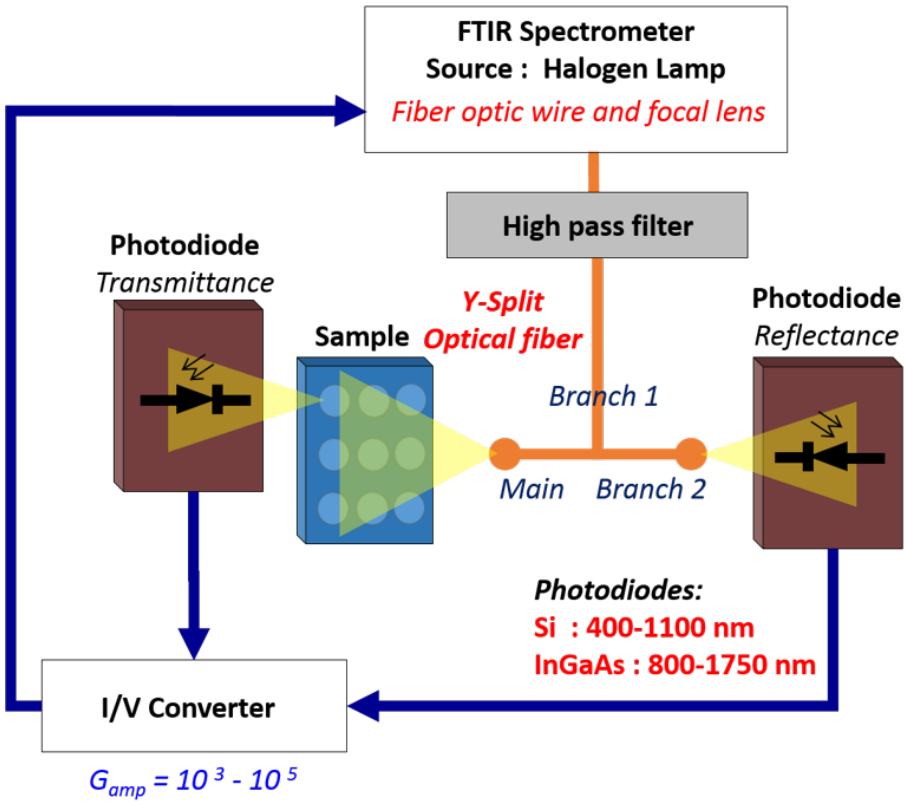

Figure 5-10: System configuration of R/T and FTPS measurements on a transparent solar cell.

measurements, the light source of the FTIR spectrometer was modified by adding blue LEDs because often the cell responses are quite weak in the blue light region. Fig. 5-10 presents a schematic of the setup designed for SR and EQE measurements.

Photocurrent measurements using an FTIR

In the transmittance measurement, we measure the ratio of the photocurrent density generated by the photodiodes when the sample is placed in front of the photodiode and the photocurrent density when no sample is placed, which is proportional to the incident flux (see Eq. (2.26)). The second measurement is used for the reference measurement. For the reflectance measurement, we measured with a photodiode the photocurrent density due to the light reflected by the sample and the photocurrent density due to the light reflected by an aluminum mirror as a reference (see Eq. (2.28)).

The absorption coefficient and the intensity of the light impinging the sample are calculated as described in Eq. (2.40). The interest of using the transmitted light instead of the incident light in the calculation of α is to remove the interference fringes in the final α spectrum as shown in the transmission CPM (TCPM) reported by Sasaki

et al. [23]. In order to get the absolute value of the α spectrum, we calibrated the α values using the procedures in Chap. 3 from the results of the R/T measurements.

The FTPS measurement on a transparent solar cell is based on Eq. (5.3). The spectral response (SR) is obtained by calculating the ratio of the photocurrent generated by the solar cell under illumination and the power of the incident light impinging the solar cell. Knowing the spectral response, we are able to obtain the EQE of the solar cell using Eq. (2.45). The short circuit current density J_{SC} is calculated using the product of SR and the power density of a sun at AM1.5G for each wavelength, as denoted in Eq. (2.46). The total J_{SC} of the solar cell in A/m^2 under AM1.5G is the integrated J_{SC} over all the wavelengths, calculated using Eq. (2.47).

R/T results for thin films

The R/T measurement results of the thin films 1701021 and 1701032 are presented in Fig. 5-11. We observe classical R/T of a-Si:H. The reflectance measurement from the film side yields $R = 0.38$ and $R = 0.34$ at 500 nm for the samples 1701021 and 1701032, respectively. On the other hand, the reflectance measurement from the substrate side yields $R = 0.25$ and $R = 0.22$ at 500 nm for the samples 1701021 and 1701032, respectively.

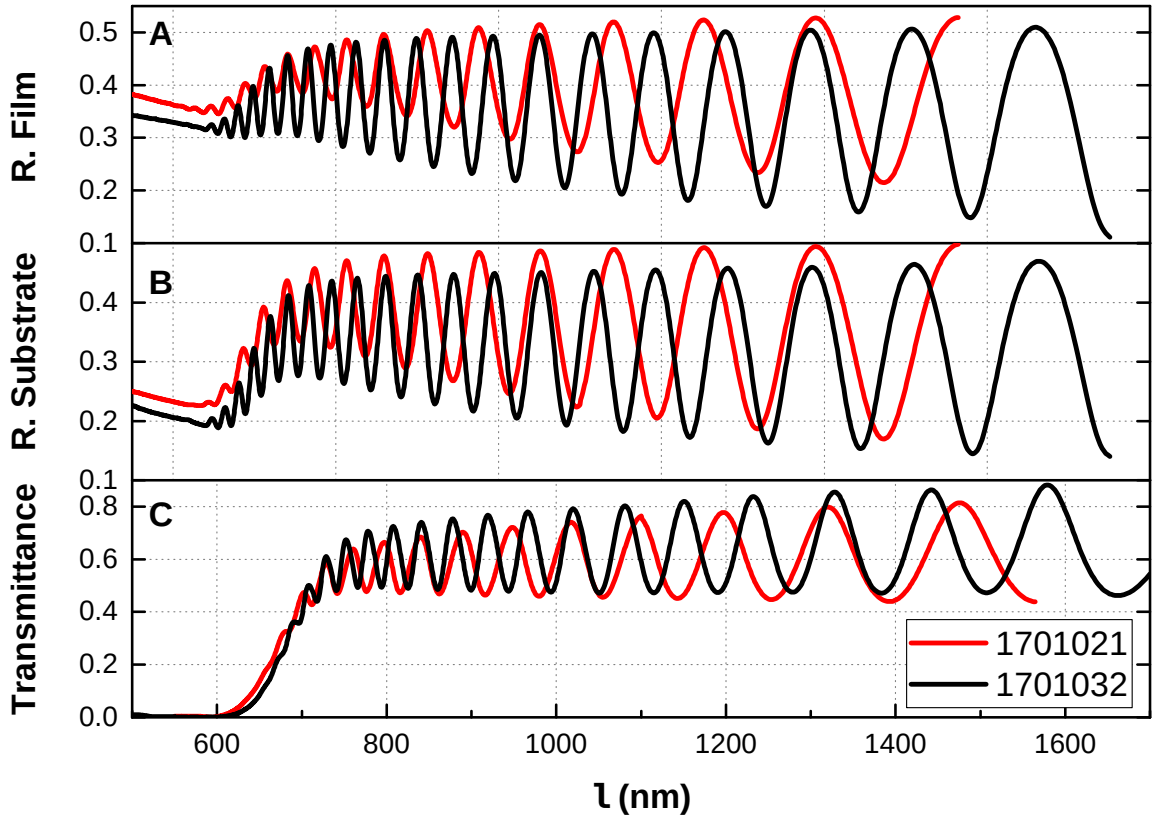

Figure 5-11: (A) Reflectance from the film side, (B) reflectance from the substrate side, and (C) transmittance of the 1701021 and 1701032 films.

From these R/T results, an optical modeling as in [51] was used to calculate the refractive index, n_f, and thickness at 550 nm. Refractive indices of 4.29 and 3.97 were found for the samples 1701021 and 1701032, respectively. The thicknesses of the samples 1701021 and 1701032 were found equal to 1.01 μm and 2.05 μm, respectively, corresponding well with the deposition times of these two samples (the second sample is deposited twice as long as the first one and has roughly twice the thickness).

FTPS results of films and solar cells

The FTPS measurements of the thin films and the solar cells were normalized to the EQE measurements of the solar cell in order to compare the α spectra of these samples. The α spectra of the thin films can be obtained in absolute value using the Ritter-Weiser formula (Eq. (2.42)) with their R/T results. On the other hand, this method cannot be used yet for the α spectra of the solar cells because an optical modeling taking into account the multiple reflections and transmissions in the whole solar cell's film stack, e.g. using the transfer matrix method (TMM), is necessary to obtain the true α spectra of solar cells with multiple stacks.

From Fig. 5-12 it can be remarked that the FTPS spectra of the thin films and solar cells have a good agreement in the Urbach slope region (1.6-1.8 eV), whereas in the deep defect region (below 1.4 eV), the α is lower for the solar cells.

In addition, it can be noted that at 0.8 eV, α of solar cells produce a sharp increase indicated by the arrows in Fig. 5-12. In this case, we looked back at the origin of how the α is measured using our system. α is obtained using Eq. (5.3), thus the increase of α in solar cells can be caused either by the increase of photocurrent generated by the solar cells due to an increased reflectance of the back TCO, or the decrease of transmittance, as it is reciprocal to α. Hence, R/T measurements were performed on the transparent solar cells. The results of these measurements are presented in Fig. 5-13. In this figure, the expected R/T results causing the increase in α are obtained. In the long wavelength region, a decreasing transmittance and an increasing reflectance are found.

Correction of the FTPS-EQE of solar cells

The increase of R and the decrease of T from the R/T measurement results of the solar cells were further investigated using the R/T measurements of their TCO layers deposited on glass, and are presented in Figs. 5-14 and 5-15. The results of the R/T measurements on ZnO is presented in Fig. 5-14. From the reflectance spectra measured from the film and substrate sides (see Fig. 5-14A), a sharp increase is remarked in the long wavelength region. On the other hand, the transmittance spectrum in Fig. 5-14B shows a decreasing trend in the long wavelength region. For the R/T measurements of ITO-type TCO as represented in Fig. 5-15, a sharp increase in the long wavelength region was not found for the reflectance. Nevertheless, the same behavior of the transmittance spectrum in the long wavelength region as the one from the ZnO is found for the ITO.

The R/T results of the TCO layer are used to calculate their absorptance as

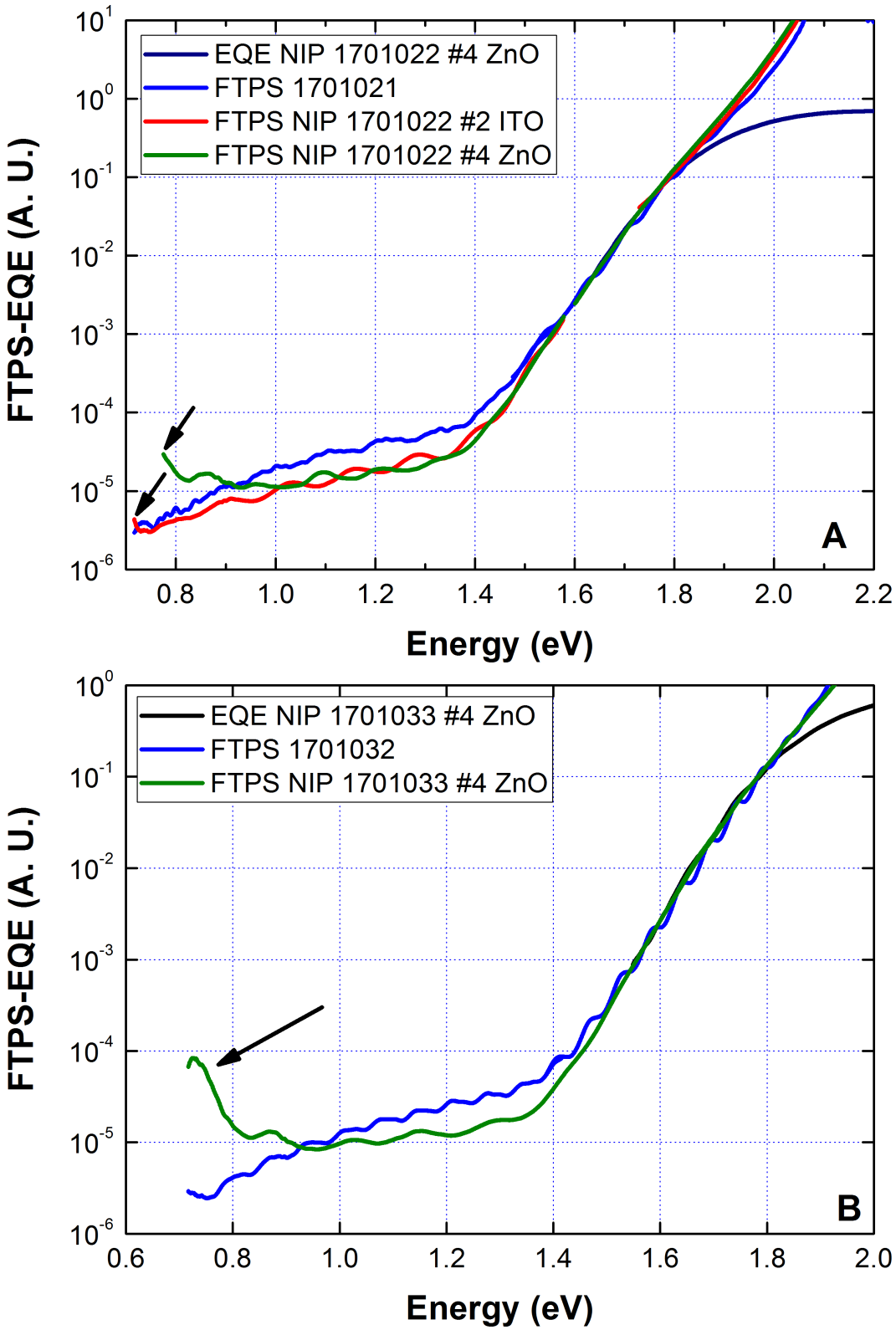

Figure 5-12: FTPS spectra of the thin films and the solar cells as well as their EQE for (A) the first sample group, and (B) the second sample group.

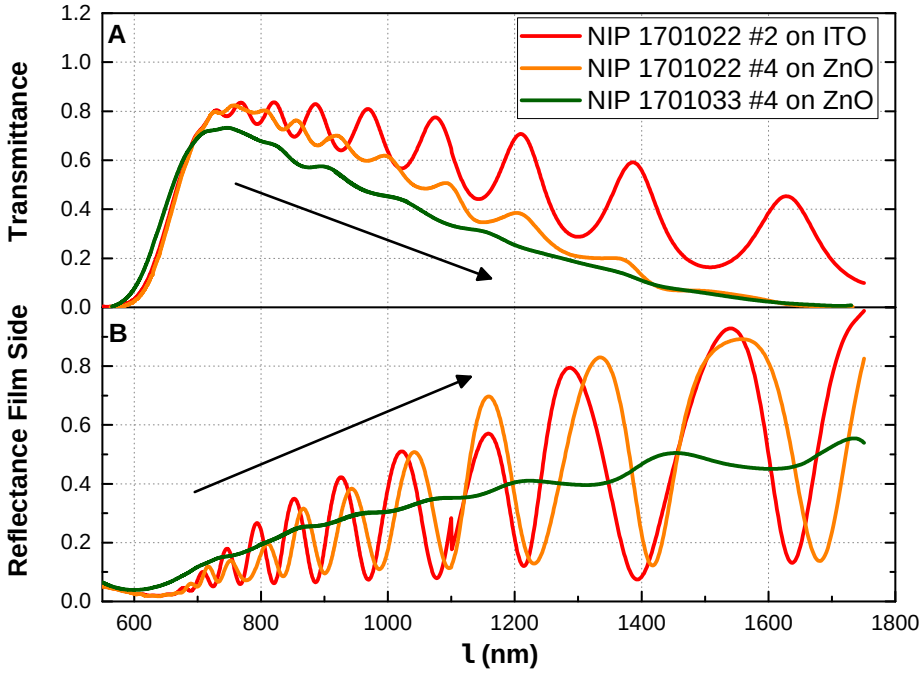

Figure 5-13: (A) Transmittance, and (B) reflectance of the transparent solar cells from the R/T measurements.

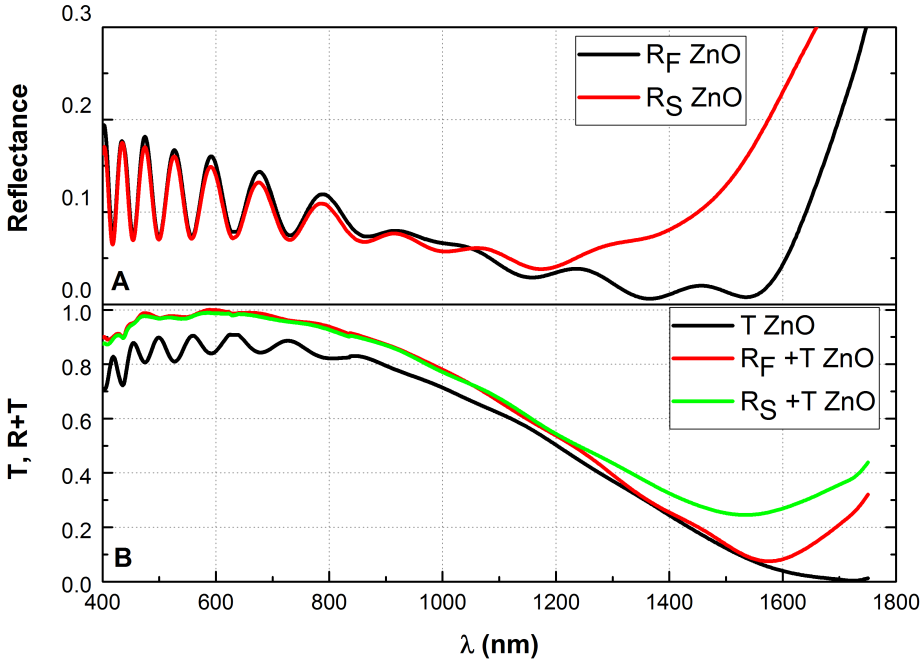

Figure 5-14: (A) Reflectance from the film (R_F) and substrate side(R_S), and (B) transmittance and the R+T=1-A of the ZnO film deposited on glass acting as the TCO in the solar cells

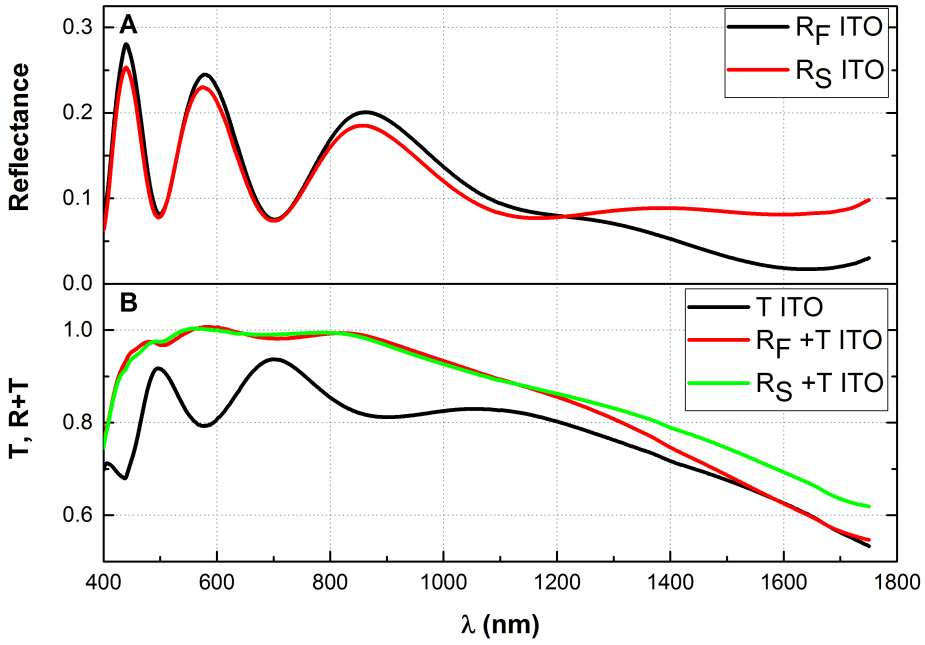

Figure 5-15: (A) Reflectance from the film (R_F) and substrate (R_S) sides, and (B) Transmittance and the R+T=1-A of the ITO deposited on glass acting as the TCO in the solar cells.

presented in Fig. 5-16. For these two different TCO layers, the same absorptance behavior is found in the long wavelength region. Both ZnO and ITO show a higher absorption in the long wavelength region. All these results are linked to the *metallic* behavior of the TCO layers in the long wavelength region. Indeed, in this region reflection, transmission, and absorption are linked to the interaction of the photons with the electrons of the extended states of the TCO and could be explained via a Drude model [97], [98].

As mentioned previously, the increase in α can be caused either by an increase in the generated photocurrent due to the back TCO reflectance or a decrease of the transmittance. To correct α using the reflectance of the back TCO, we could have used a sample built as a cell but without the top TCO layer to calculate the reflectance of the back TCO. Unfortunately, this kind of sample was not available and thus the correction using back TCO reflectance will not be provided for the moment. On the other hand, a correction due to the decrease of the transmittance spectrum can be provided. To perform this correction, one must understand how the transmittance spectrum is obtained experimentally. A schematic diagram showing how the transmitted flux through the sample is measured by the photodiode is presented in Fig. 5-17.

The transmitted flux through the transparent solar cell measured by the photodiode is the transmitted flux through all the layers in the solar cells, denoted by T_{FTPS} in Fig. 5-17. The α obtained from the FTPS measurements is obtained through the ratio of photocurrent and T_{FTPS}, whereas to obtain the true α of the solar cells' i-layer, the transmittance of the i-layer, T_{True} , should have been used. To obtain

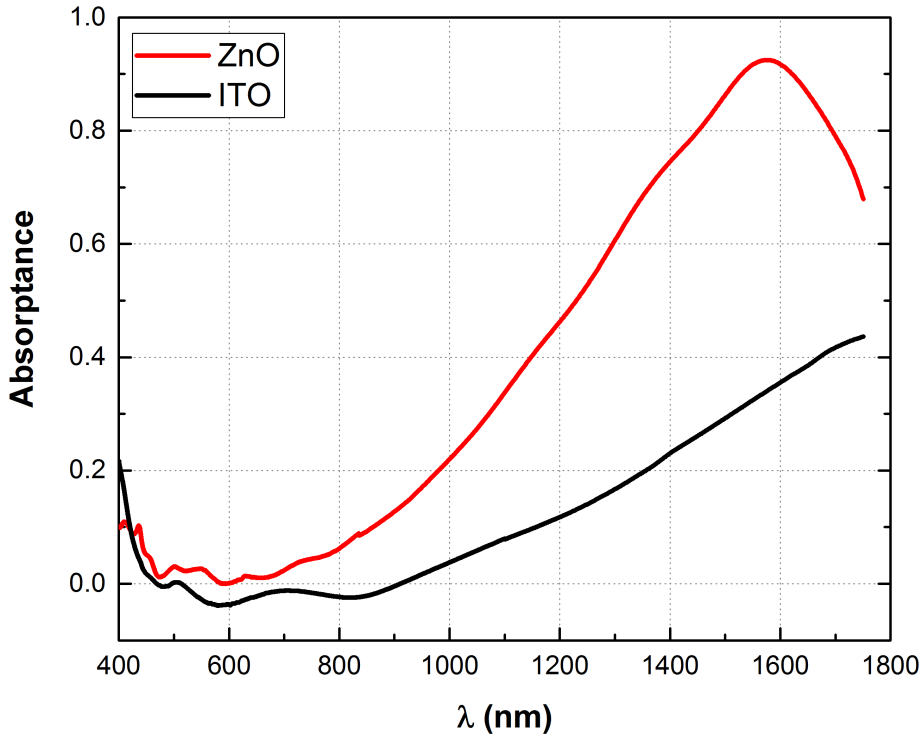

Figure 5-16: Absorptance of the TCO layers of the solar cells (ZnO and ITO) deposited on glass calculated from their respective R/T spectra.

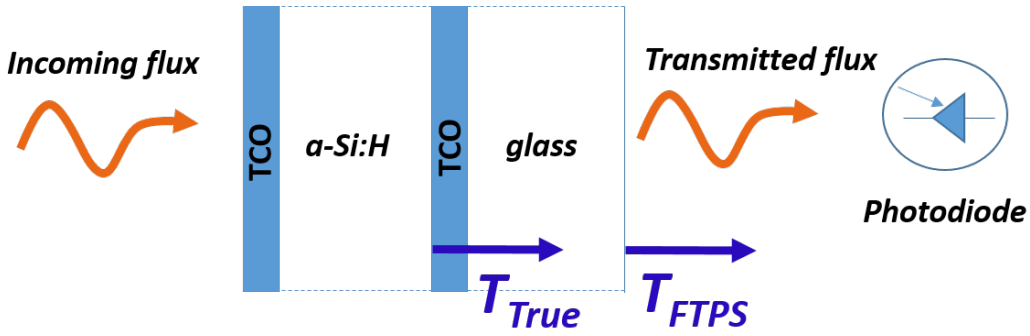

Figure 5-17: Schematic diagram of the measurement of the transmitted flux through the solar cells fitted with transparent electrodes. The photodiode placed behind the sample is measuring the transmitted flux through the whole transparent solar cell film stack, T_{FTPS}, and the transmittance of the sole i-layer is denoted by T_{True}.

the T_{True}, T_{FTPS} needs to be corrected with the absorptance of the back TCO layer, A_{TCO}, using Eq. (5.4).

$$T_{FTPS} = T_{True} \times (1 - A_{TCO}) \tag{5.4}$$

Hence, the α of the solar cells' i-layer can be calculated as:

$$\alpha_{True} = \alpha_{FTPS} \times (1 - A_{TCO}) \tag{5.5}$$

where :

$$1 - A_{TCO} = R_{TCO} + T_{TCO} \tag{5.6}$$

where R_{TCO} and T_{TCO} were obtained previously using the R/T measurement of the TCO layers deposited on glass.

The corrected FTPS-EQE spectra of solar cells using the above methods are presented in Fig. 5-18 with arrows underlying the correction influence. After the correction we can remark that the α spectra of the solar cells are following the same trends as the thin films except that lower values are found in the deep defect region. We can propose an explanation based on the deposition conditions.

Indeed, in the case of cells the absorber is deposited onto a conductive oxide whereas the thin film is deposited onto an insulating substrate. We can then think that the potential at the deposition surface is not the same in both cases. Therefore, the ion bombardment energy may be different and, in the case of the conductive oxide, the deposition is smoother leading to a slightly lower deep defect density.

On the other hand, the fact that the deep defect density is found lower is due to the normalization of the FTPS curves to the EQE of the cells. This normalization is done by adjusting the curves in the Urbach region. After correction of the absorptance of the TCO, if we align the curves by adjusting the deep defect density parts we shall find the same Urbach energy (i.e. same slope) but with a shift between the FTPS-EQE measured on films on glass and on solar cells. This shift would imply that the band gap is larger for films than for the solar cells, the FTPS-EQE spectra of the cells being above that of the films. We cannot rule out this possibility that would suggest for instance that the hydrogen content of the films is larger than that of the cells. Why the hydrogen content of the a-Si:H layer would be different in the case of films on glass and cells is unclear, that is why we favor the first hypothesis of a lowering of the deep defect density.

In any case it seems that the density of states of films deposited on glass and of the same films incorporated in solar cells, though both being deposited under the same conditions, present some slight differences.

It can be noted that differences in the absorption spectra of thin films and the related devices were already reported by Poruba *et al.* [99] for micro crystalline silicon material. Thus, more investigations are clearly needed to understand the origin of these differences.

Finally, whatever is the origin of these differences, an increase around 0.8 eV in the α spectra of the solar cells can still be remarked showing that the correction we have used should be refined, at least in this region.

5.2.2 Conclusions

We have designed a system based on an FTIR with which we can perform three kinds of measurements: R/T, FTPS and SR-EQE, yielding high resolution spectra simply

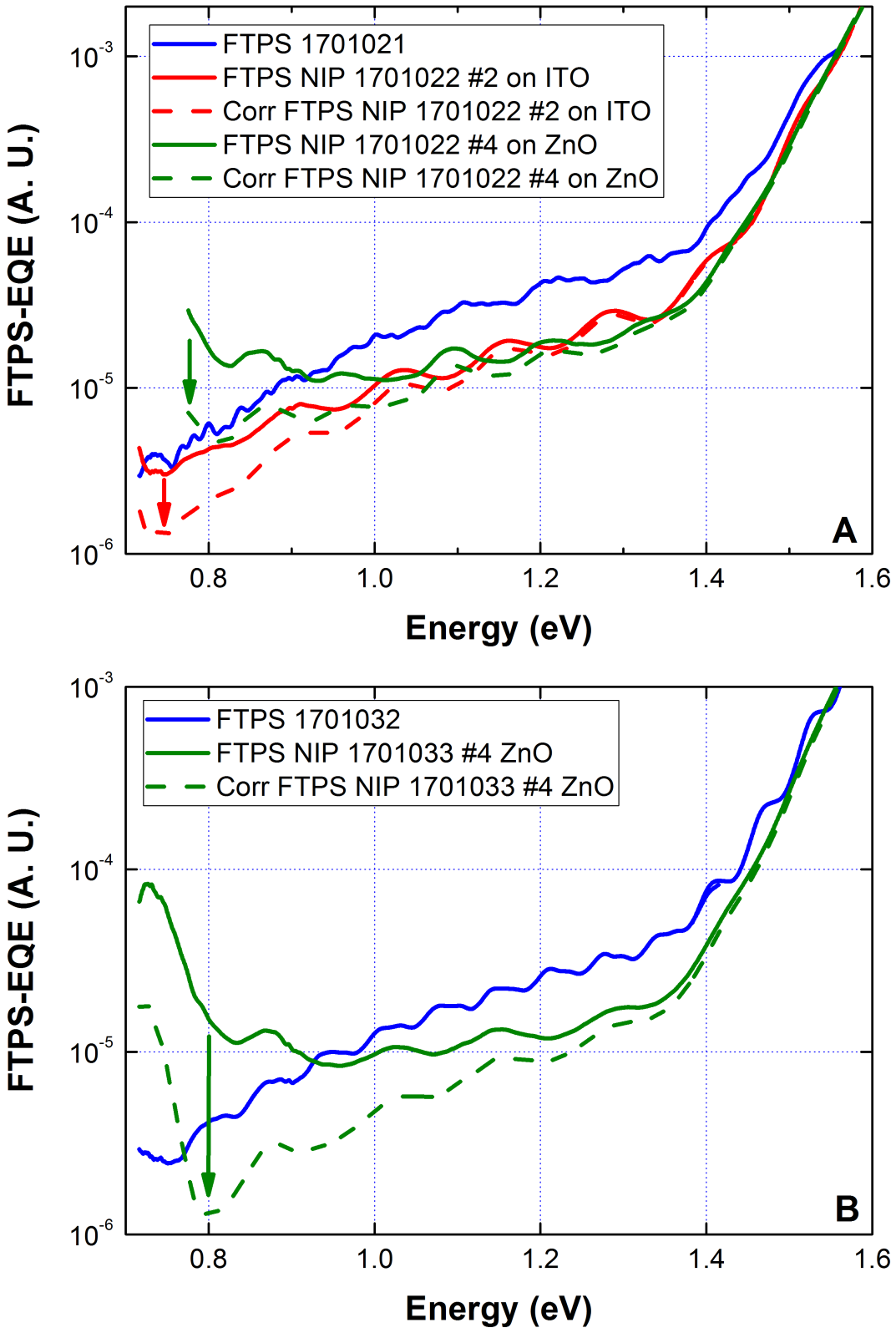

Figure 5-18: Corrected FTPS spectra of the thin films and solar cells of (A) the first sample group, and (B) the second sample group, using the absorptance of their TCO layers.

and rapidly. Some thin film parameters such as refractive index and thickness can be deduced using R/T measurements and an optical model proposed by Poruba *et al.* [51]. Our FTPS concept allows the suppression of the interference fringes in the $\alpha(h\nu)$ without the need of any optical modeling.

The measured $\alpha(h\nu)$ spectra of the i-layer of transparent solar cells show a good agreement with the one of the corresponding a-Si:H thin films, notably in the Urbach slope region. However, an over-estimation occurs in the deep defect region of the solar cells' $\alpha(h\nu)$ spectra. The cause of this over-estimation was investigated using the R/T measurements of the solar cell TCO deposited on glass: ZnO and ITO. We propose a simple method based on these R/T measurements to correct this over-estimation.

Chapter 6

Conclusions

In this project, we have developed three types of photocurrent measurements, i.e. R/T, FTPS, and spectral response (SR) - EQE measurement for thin film semiconductor deposited on transparent non-conductive substrate and solar cell devices . We have used the principles of the Fourier transform infrared spectroscopy to perform these photocurrent measurements to characterize optical and electrical performances of samples, using an FTIR spectrometer equipped with an optical fiber to deliver the light source. Our characterization techniques bring more advantages in comparison to other classical measurements for two reasons : 1.) only an FTIR spectrometer with a very simple experimental setup is needed to perform these three photocurrent measurements, and 2.) a faster measurement rate for high precision and resolution results is obtained using our characterization setup.

The R/T measurements using an FTIR spectrometer are performed to characterize the optical properties such as the reflectance and transmittance. These R/T results are introduced in an optical model proposed by Poruba *et al.* [51] to determine the refractive index, film thickness, and roughness. In addition to those properties, R/T results are used to calculate the optical absorption coefficient using the formula proposed by Ritter-Weiser [38]. The calculated optical absorption coefficient is useful to calibrate the absorption coefficient measured by FTPS to its absolute value.

FTPS is used to characterize the absorption coefficient of thin film semiconductors deposited on transparent non-conductive substrate as well as transparent solar cell devices. Our FTPS measurement setup is based on the principles of the ACPM proposed by Vanecek in [21]. By using this setup, the interference fringes in the absorption coefficient can be suppressed without any optical modeling and by using the previously calculated optical absorption coefficient we obtained the absorption coefficient measured by FTPS in absolute value.

The spectral responsivity measurements is useful to measure the spectral responsivity of a solar cell device and calculate its EQE. In addition to the EQE, we can use the power density of the AM 1.5G in $W/cm^2/nm$ to yield the short circuit current density, J_{SC}, of the solar cell device for each wavelength. By integrating the J_{SC} over all the wavelengths, we obtained the total J_{SC} of the solar cell device. The total J_{SC} of the solar cell calculated from our measurement bench has been confirmed using the classical I-V measurement with a solar simulator.

In order to characterize the electrical performance and quality, notably the presence of defects in the thin film semiconductor materials, we have used the absorption coefficient measured by FTPS to model their density of states, DOS. The DOS is modeled using DeOSt software, in which two type of DOS model can be chosen, i.e. standard and defect-pool DOS model. By taking the possible electronic transitions between the states in the DOS model, we can calculate the variations of the absorption coefficient. The DOS is modeled so that it reproduces the absorption coefficient spectrum versus the photon energy as the one measured by FTPS.

The modeling of the DOS is quite complicated and tedious since for each chosen DOS model, 15-17 numbers of DOS parameter values have to be adjusted. Due to this reason, we have proposed an artificial intelligence algorithm called Teacher and Learner Based Optimization (TLBO) algorithm to find the values of these DOS parameters. This algorithm was chosen because of its simplicity combined with good performances. There are only three types of input variables that have to be set, i.e. the search space of each DOS parameters, the number of sets of DOS parameters, and the iteration number. In the search of the optimum value of the DOS parameters, we have also taken into account the range of values that corresponds to their physical boundaries. It has been shown that the TLBO algorithm yields a very good performance in determining the values of DOS parameters for both standard and defect-pool models, as this algorithm provided a very low error between the modeled and measured absorption coefficient.

However, the evolution of each DOS parameter as a function of the iteration number using the TLBO algorithm cannot be used as a straight forward manner to adjust the value of each DOS parameter to give a good agreement with the measured absorption spectrum from FTPS. Understanding the influence of each DOS parameter on the evolution of the absorption coefficient is of primary importance as if a manual adjustment method was used to obtain the optimum values of DOS parameters using DeOSt software, without the TLBO algorithm. The understanding of the DOS parameters influence is approached using a sensitivity analysis based on one variable at a time (OAT) method.

To understand the impact of the change of each DOS parameter on the change in specific regions of the absorption coefficient spectrum, i.e. deep-defect, Urbach slope, and high energy region, DOS parameters values are varied to +/- 30% of their initial values and the change of absorption coefficient at each region is quantified. This study is useful to give a global overview on how each DOS parameters impacts the absorption coefficient. When this problem is understood, and that the absorption coefficient spectrum given by the DOS model set in DeOSt still does not give a good fit with the measured value, the degree of importance of each DOS parameters towards the specific region in α has to be understood. In this sensitivity analysis, we have used Tornado and Spider plots to look for the most influential DOS parameters for specific regions of the absorption coefficient spectrum.

The Tornado plots were used to understand the evolution of the absorption coefficient when a parameter is varied to +/- 30% of its optimum value, and the parameters were sorted by their influence on α. DOS parameters that bring significant change to the absorption coefficient spectrum are categorized as the most influential ones.

In addition to Tornado plots, the Spider plots give the degree of change in a specific region of the absorption coefficient when the parameter values are swept to +/- 30% from their optimum values. It means that the given quantified change in the absorption coefficient given by a Tornado plot only reflects the left and right-end sides of a Spider plot. With the Spider plot, we can more easily understand the influence of each DOS parameter and know which parameters give a significant change in the absorption coefficient, and thus in case of a manual fitting the values of these parameters could be very carefully chosen. Indeed, a more detailed quantification of the degree of change of the absorption coefficient is proposed with Spider plot, so that when the error between the modeled and measured absorption coefficient spectrum is known, one can readily know how much each DOS parameters have to be adjusted to give a better fit. From the results of the Tornado and Spider plots, we have put into evidence the most important DOS parameters for specific regions of the absorption coefficient.

In the experimental work related to the research of the DOS model of the thin films, we have chosen three samples of a-Si:H thin films. These samples have gone through the FTPS and R/T measurements with which their absorption coefficients and R/T spectra are obtained. Their absorption coefficients were used to estimate some of the density of states parameters such as the band gap energy, valence band temperature, and the dynamic range and width of the deep defect density of the studied samples. The TLBO algorithm was used to run their corresponding density of states modeled in DeOSt. Standard and defect-pool DOS models were used during the search and all the DOS parameters were set as uncontrolled variable. The results showed that the two DOS models are very dependent on the chosen value of optical matrix coefficient of the respective model, which is true according to the equation used to calculate the absorption coefficient. As an example, the standard DOS model may result in a higher deep defect density level compared to the defect-pool model due to a lower optical matrix coefficient chosen for the standard DOS model. The difference DOS levels due to the different values of optical matrix coefficients resulted in a more complicated at comparison of these DOS models that could not be done at a glance. To resolve this particular issue, we simulated the defect-pool DOS model of one sample using the optical matrix coefficient of the standard DOS model. The result showed that both DOS models appeared to be very similar in term of their DOS level. Therefore, it can be concluded that the optical matrix coefficients values have to be set as controlled variables if a more comprehensive comparison between these two DOS models is desired.

In this project, we also studied whether the FTPS measurements performed to thin film semiconductor materials deposited on glass and transparent solar cell devices incorporating an intrinsic layer having the same properties as the thin films deposited on glass give the same absorption coefficient spectra results or not. From the results, we have seen that the measured absorption coefficient on transparent solar cell follows the same trend as those of thin films deposited on glass. However, the absorption coefficient on transparent solar cell devices had to be corrected using their transparent conducting oxide (TCO) optical properties to ensure the same perception of reflectance and transmittance as the ones measured on thin films deposited

on glass.

We have also observed that the deep defect density of the intrinsic material incorporated in the solar cell was lower than that of the corresponding layer deposited on glass and we have proposed an explanation for this behavior.

In conclusion, we have both designed a new bench with which we can perform three different types of experiments: the FTPS technique, R/T measurements for thin films deposited in on transparent substrates and spectral response measurements of devices.

We have also develop programs for the exploration of the experimental results. In particular, we have develop a program to deduce the density of states of the studied material from the experimentally measured absorption coefficient variations.

We believe that all these novelties will actively participate to the optimization of materials and devices dedicated to the solar energy conversion.

Appendix A

Comparison of FTPS performed on thin films and solar cells

pss-Header will be provided by the publisher

Comparison of FTPS performed on thin films and solar cells

Nastiti Puspitosari[*,1,2], Christophe Longeaud[,1,2], Raphaël Lachaume[1,2], Li Zeyu[3,4], Rusli[4], Pere Roca i Cabarrocas[3]**

[1] GEEPS (UMR 8507 CNRS), Centrale-Supélec, Université Paris Sud XI, Université Pierre et Marie Curie, 11 rue Joliot Curie, 91190 Gif sur Yvette, France
[2] IPVF, Institut Photovoltaïque d'Ile de France, 8 rue de la Renaissance, 92160 Antony, France
[3] LPICM, (UPR0258 CNRS), Ecole Polytechnique, 91128 Palaiseau, France
[4] NOVITAS, Nanoelectronics Centre of Excellence, School of Electrical and Electronic Engineering, Nanyang Technological University, 50 Nanyang Avenue, 639798, Singapore.

Received ZZZ, revised ZZZ, accepted ZZZ
Published online ZZZ(Dates will be provided by the publisher.)

Keywords FTPS, absorption coefficient, thin films, solar cells, transparent conductive oxide.

* Corresponding author: e-mail nastiti.puspitosari@geeps.centralesupelec.fr, Phone: +00 999999 999, Fax: +33 1 69 41 83 18
** e-mail christophe.longeaud@geeps.centralesupelec.fr, Phone: +33 1 69 85 16 45, Fax: +33 1 69 41 83 18

Fourier Transform Photocurrent Spectroscopy (FTPS) has been used to investigate on the absorption coefficient vs. photon energy ($\alpha(h\nu)$) spectroscopy of thin film semiconductors. We have developed an FTPS experiment to study the $\alpha(h\nu)$ spectrum of hydrogenated amorphous silicon (a-Si:H) thin films, to subsequently deduce information on the density of states in the sub bandgap region. In this work we studied whether the same $\alpha(h\nu)$ spectroscopy could be found both for coplanar a-Si:H films deposited on glass and for NIP diodes incorporating the same material as the intrinsic layer. The back and front contacts of the diodes are made of transparent conductive oxides, either ITO or ZnO. The results show that the Urbach tails of both coplanar and NIP diodes are very similar but that α at low photon energy is slightly lower for the diodes than for the coplanar samples. In addition, we noticed that the diode with ZnO contacts presents a rapid increase of α below 0.95 eV. Transmission-reflection measurements performed on the diodes show that the diode with ZnO contacts exhibits a weaker transmission in the same wavelength range where we observed an increase of α, though the reflection with both types of contacts remains the same, indicating a parasitic absorption of the back ZnO layer. These results show that FTPS measurements performed on diodes must be taken very cautiously and that one has to take into account the optical properties (e.g. absorption) of the contacts to properly deduce reliable $\alpha(h\nu)$ spectroscopy.

u line will be provided by the publisher

1 Introduction In the search of the best performing materials for solar cells, characterization techniques to identify the optical and electrical properties of solar cell absorber layers become very important. Optical characterization techniques allow the determination of the optical properties such as the transmittance (T), reflectance (R), and absorptance (A) of the material as a function of photon energy ($h\nu$). Electrical characterization techniques on the other hand can yield the photosensitivity and the presence of defects in the materials as a function of energy. The quality of the materials and solar cell devices can thus be assessed using these characterization techniques. By understanding the properties, behaviour, and defects in these materials, researches related to the improvement of the materials performance can be more easily pushed forward to yield a better absorber layer for a higher efficiency of solar cells.

Optical characterization techniques for materials such as UV-Visible spectroscopy can yield the R, T, and A as function of $h\nu$. Techniques based on photocurrent spectroscopy e.g. constant photocurrent method (CPM) [1-3] and Fourier transform photocurrent spectroscopy (FTPS) [4] have been reported to reliably yield the absorption coefficient (α) as a function of $h\nu$, which can also provide information on the deep defect density of materials. For solar cell devices, the most commonly performed characterization is the spectral responsivity (SR) measurement which

yields the external quantum efficiency (EQE) as function of hv and the short-circuit current density (J_{SC}).

In this work, we have developed a *3-in-1* characterization technique for thin film materials and solar cell devices based on photocurrent spectroscopy using a single Fourier transform infrared spectrometer (FTIR) [5]. This technique can yield (i) R, T, and A, (ii) α of thin film materials and solar cells deposited on transparent substrates as function of hv, and (iii) SR, EQE, and J_{SC} of solar cell devices.

From the measurements of R, T, we can also determine the refractive index and the thickness of the thin film material deposited on a transparent substrate using the optical modelling proposed by Poruba *et al.* [6]. In the case of the α measurements using FTIR on thin film materials deposited on transparent substrates, we have used the principle of absolute CPM (ACPM) proposed by Vanecek *et al.* [3]. Based on the ACPM technique, the suppression of interference fringes in α is done without any optical modelling. The J_{SC} is classically obtained by coupling the SR measurements and the measured solar spectrum at AM1.5G.

The main advantages of this *3-in-1* characterization tool are that (i) only an FTIR spectrometer is necessary to perform all the measurements, (ii) the measurement is obtained much faster and with a higher resolution and precision compared to the classical methods using either UV-Visible spectrometer or SR technique using a light source and a monochromator.

In this paper, we exemplify the use of our *3-in-1* characterization tool to study both intrinsic a-Si:H thin films deposited on glass and NIP solar cells. The intrinsic *i*-layers of the solar cells were deposited using the same deposition parameters as the a-Si:H thin films. The aim of this study is to answer the following questions: (i) Is it really possible to probe the deep defect density of a material by applying FTPS to a solar cell incorporating this material ? (ii) How the $\alpha(hv)$ curve obtained by FTPS on a device compares with the same curve obtained on a thin film ? Indeed, previous attempts to compare film and devices using CPM provided interesting results [7]. Thanks to our *3-in-1* technique we can now obtain more accurate results which reveal a parasitic absorption by TCO in the solar cells.

2 Experimental details

2.1 Deposition of a-Si:H films and solar cells

The deposition of the a-Si:H thin films and the NIP transparent a-Si:H solar cells has been performed using a radio-frequency plasma enhanced chemical vapour deposition (RF-PECVD) reactor [8].

Two sets of deposition parameters for the intrinsic a-Si:H layer have been investigated in this study, constituting two groups of samples (group I and group II). The different deposition parameters are summarized in Table 1. Each group of samples comprises both intrinsic a-Si:H thin films deposited on glass and NIP a-Si:H solar cells fitted with transparent electrodes (See Fig. 1). The *i*-layer in the NIP cells has been deposited using the same deposition parameters as the thin film on glass in the same group.

Intrinsic a-Si:H thin films deposited on glass (herein after called coplanar samples) are fitted with two parallel ohmic contacts on top, which are 1 cm long and separated by 1 mm.These electrodes are used for the FTPS. On these coplanar samples, a space is kept free of reflective metallic contacts to be able to perform the R/T measurements.

Concerning the solar cells, the back and front contacts have been exclusively made of transparent conductive oxides (TCO), either ITO or ZnO, to keep the solar cell transparent. The back side TCO, deposited on glass, is *1* µm thick. On top of it is a *20* nm thick n-type layer of µc-SiO_x. Then, a *200* nm thick intrinsic a-Si layer is deposited, covered with a *20* nm thick a-SiC *p*-layer. To finish the solar cell, a *80* nm top contact TCO layer is deposited above the *p*-layer.

Table 1 Deposition parameters of the intrinsic a-Si:H films used for the fabrication of the two groups of samples.

Deposition Parameters	Group I.	Group II.
Electrodes distance	17 mm	17 mm
Pressure	280 mTorr	260 mTorr
SiH_4 flow	35 sccm	35 sccm
RF power	4 W	4 W
Deposition time	1 hour 34 mins	3 hours

Group I comprises two different solar cell designs, *i.e.* with two types of TCO layers (ZnO and ITO). Group II contains only one solar cell design, with ZnO as for the TCO layers, as depicted in Fig. 1.

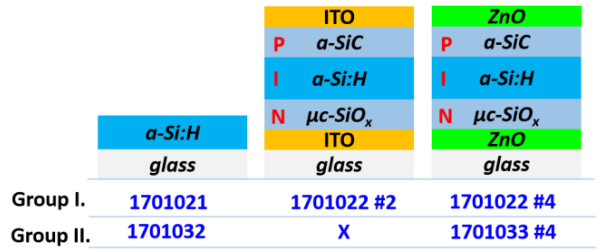

Figure 1. a-Si:H thin films and transparent solar cell stacks used in this study. Sample names are denoted in blue.

2.2 System configuration for measurements The setup of R/T and FTPS experiments is shown in Fig. 2A. In this setup, the FTIR spectrometer, a Thermo Scientific Nicolet IS50R, has a range of wavelengths extending from *400* to above *2500* nm, with a halogen lamp as a light source and a quartz plate as a beam splitter. Measurements are conducted in an external sample chamber, the light of the FTIR being collected by a setup specially designed and placed in the sample compartment of the FTIR. This setup is made of a silica lens, 5 cm in diameter and a focal length

of 5 cm (*f*/1), focusing the light of the Michelson interferometer onto the entrance of one branch of a bifurcated optical fibre bundle. In between the lens and the fibre, we have inserted an optical filter wheel to select the wavelength range of interest (see Fig. 2B).

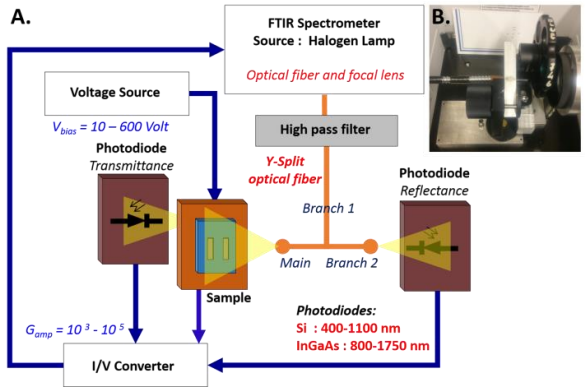

Figure 2. (A) System configuration of the R/T and FTPS measurement on thin film materials deposited on a transparent non-conductive substrate. (B) Optical filter wheel and lens mounted in the sample compartment of the FTIR spectrometer focusing the light on a bifurcated optical fibre bundle.

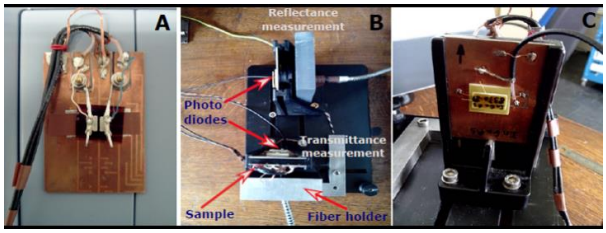

Figure 3. (A) The electronic plate holding the sample with coplanar contacts. Two springs maintain the sample onto the plate and also play the role of electrical contacts. (B) The electronic plate is inserted in a substrate holder, which has two slots to facilitate the measurement of *T*, one for the plate holding the sample in front of the optical fibre, and another for the photodiode holder placed behind the sample. For the measurement of *R*, another substrate holder is placed away from the sample, maintaining a photodiode in front of the fibre branch carrying the reflected light from the sample. (C) The InGaAs photodiode placed in the substrate holder behind the sample for the measurement of *T*.

The main output of the optical fibre is placed on a fibre holder in front of and perpendicularly to the sample maintained on an electronic board inserted in a slit of a substrate holder. For the FTPS we use the parallel ohmic contact deposited on the coplanar samples (Fig. 3A) and a voltage of *60* V was applied in between. A hole was made through the electronic plate behind the sample and a photodiode can be set behind and very close to it (~*6* mm) to measure the light transmitted through the film (Figs. 3.B and C). The same photodiode can be used to measure the incident light impinging the sample. Two photodiodes with different spectral ranges were chosen, a silicon photodiode for the range *400-1100* nm and an InGaAs photodiode for the range *800-1750* nm. The other branch of the optical fibre bundle is used to collect the light reflected by the sample, this light being sent to a photodiode fixed on another substrate holder for the measurement of the reflectance *R* (Fig. 3.B). Photocurrents generated by either the sample or photodiodes are amplified by an I/V converter before being sent back to the FTIR for treatment.

2.3 Photocurrent measurements using a FTIR

In an FTIR, the spectrum of an interferogram as a function of the optical path difference δ, $S(\delta)$, is the integral of the product of the transfer function of the measurement line $B(\omega)$ times the sample's response $I(\omega)$, as function of the wavenumber ω, over all the wavenumbers of the continuum source. $S(\delta)$ can be represented using Eq. (1).

$$S(\delta) = \int_0^{+\infty} B(\omega) I(\omega) \cos 2\pi\omega\delta d\omega \qquad (1)$$

Before any treatment, the current generated by the sample is converted into voltage and amplified by a I/V converter. The signal is then sent back to the FTIR to obtain the $B(\omega)I(\omega)$ spectrum by fast Fourier transform using Eq. (2).

$$B(\omega) I(\omega) = \int_{-\infty}^{+\infty} S(\delta) \cos 2\pi\omega\delta d\delta \qquad (2)$$

To correct for the background of the measurement line, an acquisition of the baseline is performed with no light shone onto the sample, leading to:

$$B(\omega)[I(\omega) - I_{baseline}(\omega)] = B(\omega) I_{sample}(\omega) \qquad (3)$$

Equation 3 shows that with a single measurement we can suppress the baseline influence but the contribution of $B(\omega)$ still exists, hence the real spectrum generated by the sample cannot be extracted directly from one measurement. The effect of $B(\omega)$ can be suppressed using a reference measurement. This reference measurement is generally a photocurrent measurement using a photodiode, measuring for instance the flux of the incoming light source, which is used to normalize the photocurrent measured with the sample. The normalization can be done using the following equation:

$$\frac{B(\omega) I_{sample}(\omega)}{B(\omega) I_{reference}(\omega)} = \frac{I_{sample}(\omega)}{I_{reference}(\omega)} \qquad (4)$$

where $I_{sample}(\omega)$ is the real spectrum of the sample measured using the FTIR spectrometer. In conclusion, the real spectrum measured from a given sample was normalized to

a reference spectrum for each measurement we performed with the FTIR spectrometer.

2.4 R/T measurements using FTIR In the transmittance measurement, we measure the ratio of the photocurrent generated by the photodiodes when the sample is placed in front of the photodiode, $I_{transmitted}$, which is proportional to the transmitted flux, and the photocurrent when no sample is placed, $I_{incident}$, which is proportional to the incident flux (see Eq. (5)). The measurement of the photodiode current due to the incident light is used for the reference measurement.

$$\frac{B(\lambda)J_{sample}(\lambda)}{B(\lambda)J_{reference}(\lambda)} = \frac{J_{transmitted}(\lambda)}{J_{incident}(\lambda)} \tag{5}$$

Note that in Eq. (5) we have chosen to use the wavelength λ instead of the wavenumber ω as the main variable, and it will be the same in the following. For the reflectance measurement, we measured with a photodiode the photocurrent due to the light reflected by the sample and collected by the second branch of the optical fibre, $I_{reflected}$, and the photocurrent due to the light reflected by an aluminium mirror inserted in place of the sample. Correcting this latter photocurrent by the reflectance of the aluminium mirror gives the reference photocurrent $I_{reference}$. Both these currents being proportional either to the light reflected by the sample or to the incident light, we have :

$$\frac{B(\lambda)I_{sample}(\lambda)}{B(\lambda)I_{reference}(\lambda)} = \frac{I_{reflected}(\lambda)}{I_{aluminium}(\lambda)} = R(\lambda) \tag{6}$$

2.5 FTPS measurements using FTIR for thin films The absorption coefficient α is proportional to the ratio of the photocurrent generated by the sample under illumination, I_{sample} and the intensity of the light impinging the sample. However, in that case the $\alpha(h\nu)$ curve is altered by interference fringes. That is why we have preferred to plot the ratio of the generated photocurrent and the light intensity transmitted by the sample, $F_{transmitted}$. This latter is proportional to the photocurrent measured by a photodiode placed behind the sample, $I_{transmitted}$, that we shall use as the reference measurement.

$$\frac{B(\lambda)I_{sample}(\lambda)}{B(\lambda)I_{reference}(\lambda)} = \frac{I_{sample}(\lambda)}{I_{transmitted}(\lambda)} \sim \alpha(h\nu) \tag{7}$$

The interest of using the transmitted light instead of the incident light in the calculation of α is to remove the interference fringes in the final α spectrum as shown in the transmission CPM (TCPM) reported by Sasaki *et al.*[2].

The spectrum obtained using the above equation gives us the trend and the dynamic range of the α spectrum, but not its absolute value. In order to get the absolute value of the α spectrum, we need to calibrate the α values using the result of the R/T measurement, or only T if R is already known as in the calculation of α with the absolute constant photocurrent method proposed by Vanecek *et al.* [3] for a-Si:H using the Ritter-Weiser formula [9]:

$$\alpha d = ln\left(0.5\left\{\left(1-R_1\left(1+\frac{A}{T}\right)+\left[(1-R_1)^2\times\left(1+\frac{A}{T}\right)^2+4R_1\right]^{0.5}\right)\right\}\right) \tag{8}$$

where d is the thickness of the film and R_1 is the reflectivity of the back interface of the film, the approximations of which for a-Si:H are given in [3].

2.6 FTPS, Spectral response, and EQE measurements using FTIR for solar cells The FTPS measurement on a transparent solar cell is based on Eq. (9), using exactly the same principles of FTPS measurements as for thin films, except that no bias voltage is applied to the solar cell, taking advantage of its internal field to collect the generated carriers:

$$\frac{B(\lambda)I_{sample}(\lambda)}{B(\lambda)I_{reference}(\lambda)} = \frac{I_{solar\ cell}(\lambda)}{I_{transmitted}(\lambda)} \sim \alpha(\lambda), \tag{9}$$

where $I_{solarcell}$ is the photocurrent generated by the solar cell.

The spectral response (SR) is obtained by calculating the ratio of the photocurrent generated by the solar cell under illumination and the power of the incident light impinging the solar cell :

$$SR(\lambda) = \frac{I_{solar\ cell}(\lambda)}{P_{light}(\lambda)}, \tag{10}$$

where P_{light} is measured by means of a calibrated photodiode. Knowing the spectral response, we are able to obtain the EQE of the solar cell using Eq. (11).

$$EQE(\lambda) = SR(\lambda)\ \frac{1240}{\lambda\ (nm)} \tag{11}$$

To obtain an estimate of the short circuit current density J_{SC} we have used the power density of a sun at AM1.5G. For each wavelength we can write:

$$J_{SC}(\lambda) = SR(\lambda)\,P_{AM1.5G}(\lambda) \tag{12}$$

where $J_{SC}(\lambda)$ is in A/m^2/nm and $P_{AM1.5G}(\lambda)$ is the power density of AM1.5G in W/m^2/nm. The total J_{SC} of the solar cell in A/m^2 under AM1.5G is calculated by integrating Eq. (12) over the whole range of wavelengths investigated.

The bases of the experimental setup we used for FTPS measurement on solar cells are the same as those presented in Fig. 2A. The main difference with the standard FTPS being that no bias is applied to the device.

For the SR and EQE measurements, the light source of the FTIR spectrometer was modified by adding blue LEDs because in the blue region of the light spectrum both the halogen lamp spectrum and often the cell response are quite weak. Blue LEDs with wavelengths of *405*, *420*, *450*, *470*, and *525* nm were mounted on a LED holder with sliding axes in the FTIR spectrometer, before the Michelson interferometer, to enhance the blue part of the light spectrum. To measure the power of the incident light we used a calibrated silicon photodiode with a spectral range of *400-1100* nm. Figure 4 presents a schematic of the set-up designed for spectral response measurements.

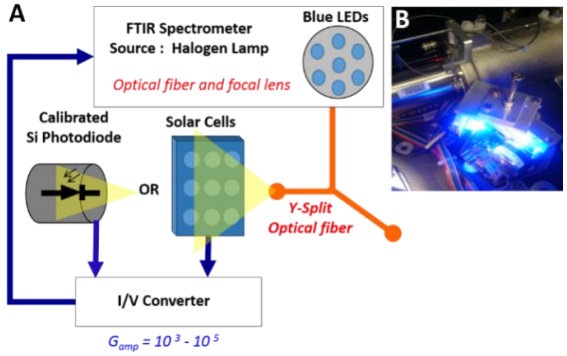

Figure 4. (A) System configuration of SR and EQE measurements of transparent solar cells, (B) Blue LEDs were mounted inside the FTIR spectrometer in order to amplify the flux intensity in the blue region

3 Experimental results In this section, the measurement results of R/T, FTPS, SR and EQE of the two groups of samples are presented and compared.

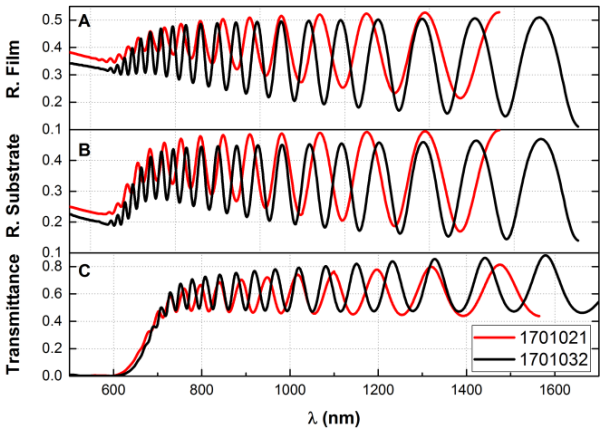

Figure 5. (A) Reflectance from the film side, (B) reflectance from the substrate side, and (C) transmittance of 1701021 and 1701032 films.

3.1 R/T results of thin films The R/T measurement results of thin films 1701021 and 1701032 are presented in Fig. 5. We observe the classical behaviour for a-Si:H R/T. The reflectance measurements at *550* nm from the film side yields *0.38* and *0.34* for the films 1701021 and 1701032, respectively. On the other hand, the reflectance measurement at *550* nm from the substrate side yields *0.25* and *0.22* for the films 1701021 and 1701032, respectively.

From these R/T results, the same optical modelling as in [6] was used to calculate the refractive index at *550* nm, n_f, and the thickness. n_f is found to be *4.29* and *3.97* for the films 1701021 and 1701032, respectively. The thicknesses of these films are *1.01* µm and *2.05* µm, respectively, which are in good agreement with the deposition times of these two samples (see Table 1). Indeed, the deposition time of the second film is twice as long as for the first one, leading to a film with twice the thickness of the first film.

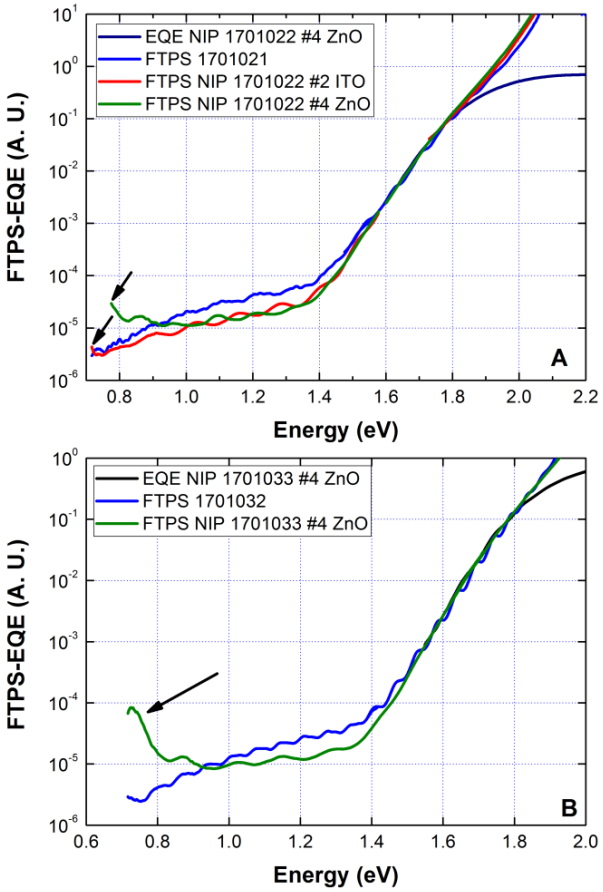

Figure 6. FTPS spectra of the thin films and the solar cells as well as their EQE for (A) the first sample group, and (B) the second sample group.

3.2 FTPS results of films and solar cells As previously explained, the absolute α spectra of the thin films could be obtained using the Ritter-Weiser formula (Eq. (8)) and the R/T results. However, this method cannot be used to obtain the true α spectrum of a solar cell because a more complex optical modelling is needed to take

into account the multiple reflections and transmission throughout the whole solar cell film stack (e.g. using the transfer matrix method (TMM)). Instead, in order to compare the α spectra of these samples, we chose to normalize the FTPS measurements of both the thin films and the solar cells by the solar cells EQE. The comparison of the FTPS-EQE spectra is displayed in Fig. 6.

From Fig. 6 it can be remarked that the FTPS spectra of the thin films and solar cells are very similar in the Urbach slope region (*1.5-1.8* eV), whereas in the deep defect region (below *1.4* eV), the FTPS-EQE spectra of the solar cells are slightly lower. It can be noted that from *1* eV and below, the FTPS-EQE spectra of solar cells present a clear increase underlined by arrows. To explain this behaviour, we have to go back to the way these spectra are calculated. They are obtained using Eq. (9). Thus the increase for solar cells can be caused either by an increase of the photocurrent generated by the solar cells due to an increased reflectance of the back TCO, or a decrease of the transmittance. To investigate further, R/T measurements were performed on the transparent solar cells. The results of these measurements are presented in Fig. 7. As it can be observed, the increase of the FTPS-EQE spectra in the deep defect region is actually due to both a decreasing transmittance and an increasing reflectance in the long wavelength region.

The observed increase of *R* and decrease of *T* from the R/T measurements performed on solar cells were further investigated using R/T measurements of their TCO layers deposited on glass, which are presented in Figs. 8 and 9.

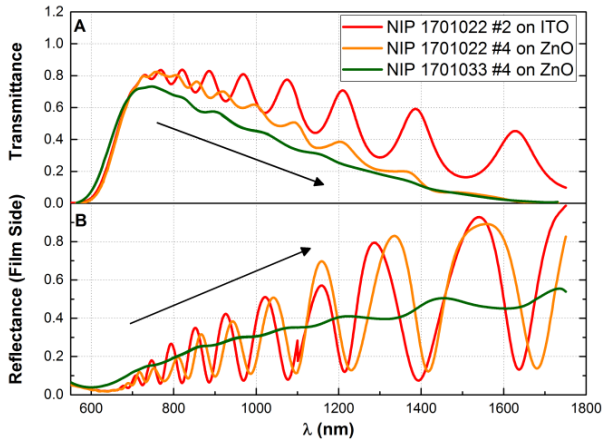

Figure 7. (A) Transmittance, and (B) reflectance of the transparent solar cells from the R/T measurements.

The results of the R/T measurements on ZnO are presented in Fig. 8. From the reflectance spectra measured from the film and substrate sides (see Fig. 8A), a sharp increase can be noted in the long wavelength region, which underlines a metallic behaviour of the ZnO, doped with aluminium. On the other hand, the transmittance spectrum in Fig. 8B shows a decreasing trend in the long wavelength region.

Concerning the R/T measurements of ITO represented in Fig. 9, a sharp increase in the long wavelength region is not found in the *R* spectra. Nevertheless, the same behaviour as for the ZnO is found for the transmittance spectrum in the long wavelength region.

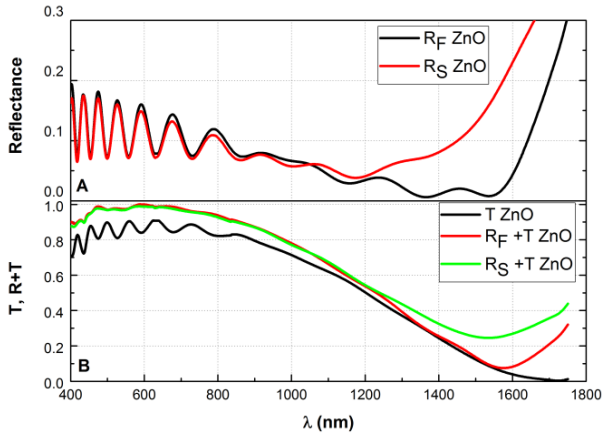

Figure 8. (A) Reflectance from the film (R_F) and substrate (R_S) sides, and (B) Transmittance and the R+T=1-A of the ZnO deposited on glass acting as the TCO in the solar cells.

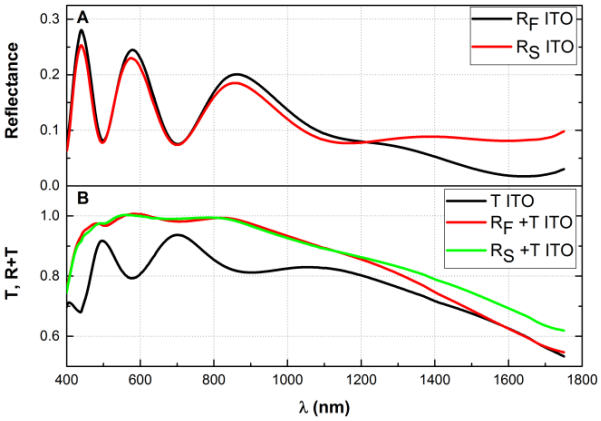

Figure 9. (A) Reflectance from the film (R_F) and substrate side(R_S), and (B) transmittance and the R+T=1-A of the ITO film deposited on glass acting as the TCO in the solar cells.

The R/T results of the TCO layer were used to calculate their absorptance as presented in Fig. 10. From these two different TCO layers, the same absorptance behaviour is found in the long wavelength region where both ZnO and ITO present a higher absorption.

3.3 Correction of the FTPS-EQE of solar cells

Using the above results on transmittance and absorptance of the TCO we may try to correct the FTPS-EQE spectra.

However, correcting them using the reflectance of the back TCO is rather difficult and would need a treatment by TMM of the reflectance of the complete a-Si:H/TCO/glass stack to get the proper variations of $R_{\text{a-Si:H/TCO}}$. Besides, such a sample was not available when we performed our study. On the other hand, a correction linked to the decrease of the transmittance spectrum can be provided.

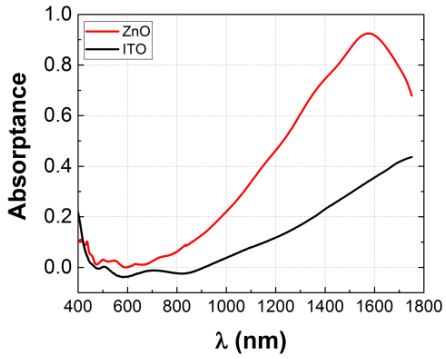

Figure 10. Absorptance of the TCO layers of the solar cells (ZnO and ITO) deposited on glass calculated from their respective *R/T* spectra.

To perform this correction, one must understand how the transmittance spectrum is obtained experimentally. A schematic diagram showing how the transmitted flux through the sample is measured by the photodiode is presented in Fig. 11.

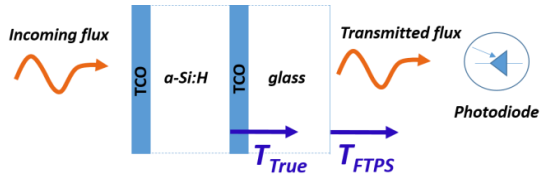

Figure 11 Schematic diagram of the measurement of the transmitted flux through the solar cells fitted with transparent electrodes. The photodiode placed behind the sample is measuring the transmitted flux through the whole transparent solar cell film stack, T_{FTPS}, and the transmittance of the sole *i*-layer is denoted by T_{True}.

The photon flux transmitted by the transparent solar cell is denoted by T_{FTPS} in Fig. 11. The FTPS-EQE obtained from the FTPS measurements is calculated through the ratio of photocurrent and T_{FTPS} , whereas to obtain the 'true' FTPS-EQE of the solar cells' *i*-layer, the transmittance of the *i*-layer, T_{True}, the transmittance at the a-Si:H/TCO interface, should have been used. To obtain the T_{True}, T_{FTPS} can be corrected, at least partly, with the absorptance of the TCO layer, A_{TCO}, using Eq. (13).

$$T_{FTPS} = T_{True}\,(1-A_{TCO}) \tag{13}$$

Hence, the α of the solar cells' *i*-layer can be calculated as:

$$\alpha_{True} = \alpha_{FTPS}\,(1-A_{TCO}) \tag{14}$$

where :

$$1-A_{TCO} = R_{TCO}+T_{TCO} \tag{15}$$

where R_{TCO} and T_{TCO} were obtained previously using the *R/T* measurement of the TCO layers deposited on glass.

The corrected FTPS-EQE spectra of solar cells using the above methods are presented in Fig. 12 with arrows underlying the correction influence. After correction, we can remark that the spectra of the solar cells in the deep defect region follows the same trend of those of thin films except that their value is lower. Nevertheless, an increase at *0.8* eV can still be noted indicating that the correction taking account of the transmittance and reflectance of the back TCO has to be refined for the deepest states. However, with the simple method presented here, and without any optical modelling, it seems possible to correct the FTPS-EQE variations for the deep defect down to *0.8* eV and to obtain the same variations as those observed from FTPS measurements performed on a thin film deposited on glass.

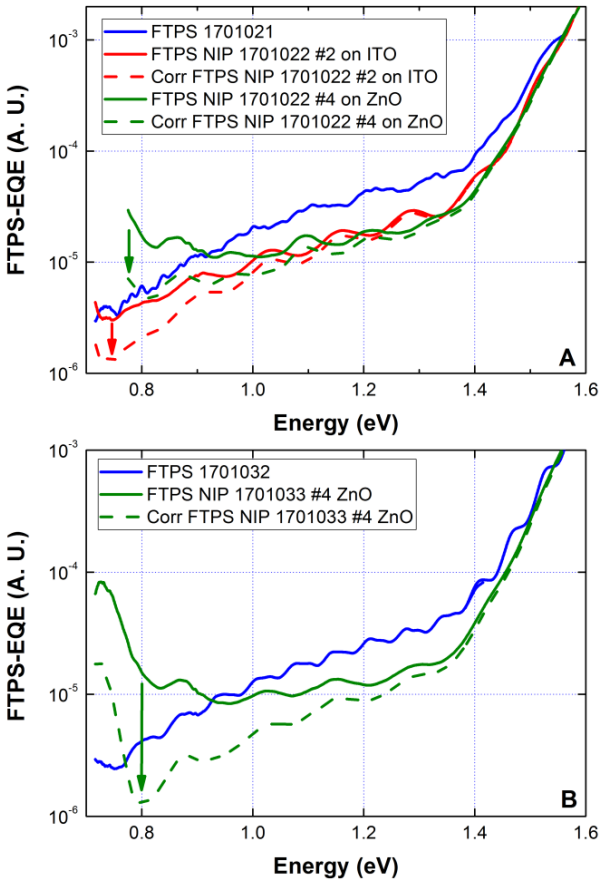

Figure 12. Corrected FTPS spectra of the thin films and solar cells of (A) the first sample group, and (B) the second sample group, using the absorptance of their TCO layers.

As mentioned above, we can see that the deep defect density probed in the cells, though presenting the same variations as that of the thin films, seems to be lower by a factor around *3* than that of the thin films. We can propose an explanation based on the deposition conditions. Indeed, in the case of cells the absorber is deposited onto a conductive oxide whereas the thin film is deposited onto an insulating substrate. We can then think that the potential at the deposition surface is not the same in both cases. Therefore, the ion bombardment energy may be different and, in the case of the conductive oxide, the deposition is smoother leading to a slightly lower deep defect density.

On the other hand, the fact that the deep defect density is found lower is due to the normalization of the FTPS curves to the EQE of the cells. This normalization is done by adjusting the curves in the Urbach region. After correction of the absorptance of the TCO, if we align the curves by adjusting the deep defect density parts we shall find the same Urbach energy (i.e. same slope) but with a shift between the FTPS-EQE measured on films on glass and on solar cells. This shift would imply that the band gap is larger for films than for the solar cells, the FTPS-EQE spectra of the cells being above that of the films. We cannot rule out this possibility that would suggest for instance that the hydrogen content of the films is larger than that of the cells. Why the hydrogen content of the a-Si:H layer would be different in the case of films on glass and cells is unclear, that is why we favour the first hypothesis of a lowering of the deep defect density.

In any case it seems that the density of states of films deposited on glass and of the same films incorporated in solar cells, though both being deposited under the same conditions, present some slight differences.

4 Conclusions We have designed a system based on a FTIR spectrometer with which we can perform three kinds of characterizations using an optical fibre: R/T, FTPS and SR-EQE, yielding high resolution spectra simply and rapidly. With this system it is possible to achieve a complete study of thin film materials in terms of optical properties (refractive index, reflectance, transmittance...) as well as in terms of defect density by means of the measurement of the $\alpha(h\nu)$ variations using absolute FTPS. In addition, the properties of cells made of a stacking of different thin films can be investigated.

Measuring the absolute variations of $\alpha(h\nu)$ for the *i*-layer of a solar cell is rather tricky since the absolute FTPS theory cannot be applied easily. Nevertheless, after normalization of all the curves, for cells and films, to the EQE of the cells, the FTPS-EQE variations measured in the *i*-layer of transparent solar cells show a good agreement with the ones of the corresponding a-Si:H thin films, notably in the Urbach slope region. However, an increase of the FTPS-EQE values occurs in the deep defect region of the solar cells spectra. The cause of this increase was investigated using the *R/T* measurements of the TCOs deposited on glass: ZnO and ITO. We proposed a simple method based on these *R/T* measurements to correct this parasitc influence of the back TCOs. After correction, the deep defect density of the absorber layer of the cells is found lower by a factor of the order of *3* than that of the corresponding thin film. We suggest that the deposition conditions of a thin a-Si:H film onto a conductive substrate favour the growth of a less defective layer compared to when it is deposited on an insulating substrate such as glass.

References

[1] B. Monemar, and H. G. Grimmeiss, Prog. Cryst. Growth Charact **5**(1-2), pp 47-88, (1982).
[2] M. Sasaki, S. Okamoto, Y. Hishikawa, S. Tsuda, and S. Nakano, Sol. Energy Mater. Sol. Cells **34**(1-4), pp 541-547 (1994).
[3] M. Vaněček, J. Kočka, A. Poruba, and A. Fejfar, J. of Appl. Phys. **78**(1), pp 6203-6210 (1995).
[4] A. Poruba, J. Holovsky, A. Purkrt, and M. Vaněček, Journal of Non-Crystalline Solids **354**(19-25), pp 2421-2425 (2008).
[5] N. Puspitosari, and C. Longeaud, Submitted to Rev. Sci. Instrum.
[6] A. Poruba, A. Fejfar, Z. Remeš, J. Špringer, M. Vaněček, J. Kočka, J. Meier, P. Torres, and A. Shah, J. of Appl. Phys. **88**(1), pp 148-160 (2000).
[7] P. Sladek, P. St'ahel, P. Roca i Cabarrocas, and P. Morin, Phil. Mag. B **77**, 1049 (1998).
[8] P. Roca i Cabarrocas, J. B. Chévrier, J. Huc, A. Lloret, J.Y. Parey, and J. P. M. Schmitt, J. of Vac. Sci. and Technol. A**9**, 2331 (1991).
[9] D. Ritter and K. Weiser, Optics Comm. **57**(5), pp 336-338 (1986).

Appendix B

Modification of an FTIR spectrometer for optoelectronic characterizations

Note: Modification of an FTIR spectrometer for optoelectronic characterizations

N. Puspitosari, and C. Longeaud

Citation: Review of Scientific Instruments **88**, 086112 (2017); doi: 10.1063/1.5000057
View online: http://dx.doi.org/10.1063/1.5000057
View Table of Contents: http://aip.scitation.org/toc/rsi/88/8
Published by the American Institute of Physics

Note: Modification of an FTIR spectrometer for optoelectronic characterizations

N. Puspitosari and C. Longeaud[a)]
GeePs, CNRS (UMR 8507 CNRS), CentraleSupelec, Université Paris Sud XI, Université Pierre et Marie Curie, 11 rue Joliot Curie, 91190 Gif sur Yvette, France and IPVF, Institut Photovoltaïque d'Ile de France, 8 rue de la Renaissance, 92160 Antony, France

(Received 28 March 2017; accepted 13 August 2017; published online 25 August 2017)

We propose a very simple system to be adapted to a Fourier Transform Infra-Red (FTIR) spectrometer with which three different types of characterizations can be done: the Fourier transform photocurrent spectroscopy, the recording of reflection-transmission spectra of thin film semiconductors, and the acquisition of spectral responses of solar cells. In addition to gather three techniques into a single apparatus, this FTIR-based system also significantly reduces the recording time and largely improves the resolution of the measured spectra compared to standard equipments. *Published by AIP Publishing.* [http://dx.doi.org/10.1063/1.5000057]

Optoelectronic characterizations of thin film semiconductors and devices for photovoltaic applications are still a matter of research for materials and conversion efficiency optimization. Among these techniques, we can quote the Fourier Transform Photocurrent spectroscopy (FTPS) first proposed by Poruba *et al.*[1,2] and largely detailed since then.[3] FTPS was developed to replace the Constant Photocurrent Method (CPM) proposed earlier by Vaněček *et al.*[4] The great advantages of FTPS over CPM are the speed and high resolution at which the same spectroscopy can be achieved. These advantages are due to the fact that all the wavelengths are present at the same time in the Fourier Transform Infra-Red (FTIR) light, the respective sample response to each wavelength being analyzed by applying an inverse fast Fourier transform to the sample signal to eventually obtain the complete spectrum. The use of an FTIR spectrometer as a light source for the analysis of sample responses was also proposed by Tomm *et al.*[5] to study the aging of high power light emitting devices (LEDs). Earlier, Hennies *et al.*[6] had proposed to build a Fourier transform spectrometer specially dedicated to the study of spectral responses of solar devices. All these experiments suggest that the principles of an FTIR spectrometer could be used in many cases as soon as a one seeks to measure a "spectral response" of a material or a device. In this note, we describe a very simple system to be adapted to a standard FTIR spectrometer to perform FTPS, fast reflection-transmission (R/T) measurements, and fast spectral response (SR) measurements of photovoltaic devices, gathering in a single bench three different experiments that are usually performed with three different apparatus.

Detailed descriptions of different setups for FTPS can be found in Refs. 2 and 3. These setups have the major drawback to be very rigid since the positions of the sample and optical components are fixed. To be more versatile, we propose the setup described in Fig. 1 that allows three types of characterization with almost no modifications of the system.

For this setup, we have used a Nicolet IS50R FTIR spectrometer from Thermo Scientific. To work in the visible part of the light, the light source is a halogen lamp, all the mirrors are covered with aluminum, and the beam splitter of the Michelson interferometer is a quartz plate. With such a system, we easily cover a range of wavelengths from 390 nm to 1800 nm. The beam of light exiting the Michelson interferometer, 2.4 cm in diameter, and focused in the standard FTIR spectrometer to the film position in the sample compartment, is even more focused by a silica lens, 5 cm in diameter and approximately 5 cm of focal length ($f/1$), onto the input of one of the two branches of a bifurcated optical fiber bundle from Newport Corp. (input diameter 3.2 mm, numerical aperture NA = 0.22). This branch of the optical fiber bundle was fixed onto an XYZ mount to optimize the collection of the light coming out of the FTIR spectrometer. A filter wheel is set in between the lens and the optical fiber entrance to select appropriate wavelength ranges if needed. In this way, the light of the FTIR spectrometer can be easily shone onto a sample or photodiode set close and perpendicular to the common output of the fiber bundle (output diameter 4.7 mm, NA = 0.22). The system we have designed to collect the light of the FTIR spectrometer is compact and can be easily inserted into the sample compartment of the FTIR as shown in Fig. 2.

In all the experiments, the responses of the samples or photodiodes to the FTIR illumination have to be amplified. We chose a low noise, broadband, and high gain current/voltage converter, DLPCA200 from FEMTO. With a mirror velocity of 0.158 cm/s and a data spacing of 3.58 cm^{-1}, each spectrum is recorded in 1 s with a high resolution, 5500 data points between 390 and 1750 nm, and a maximum modulation frequency of 8 kHz at 390 nm, much lower than the bandwidth of DLPCA200 (50 kHz at a gain of 10^7). The signal is subsequently injected in an external input of the FTIR (see Fig. 1) to be treated by fast Fourier transform to obtain the final spectrum.

For the FTPS experiment, the sample is a thin film deposited on glass and fitted with two ohmic and parallel electrodes (1 cm height, 2 mm apart). It is fixed onto an electronic

a)Author to whom correspondence should be addressed: longeaud@geeps.centralesupelec.fr.

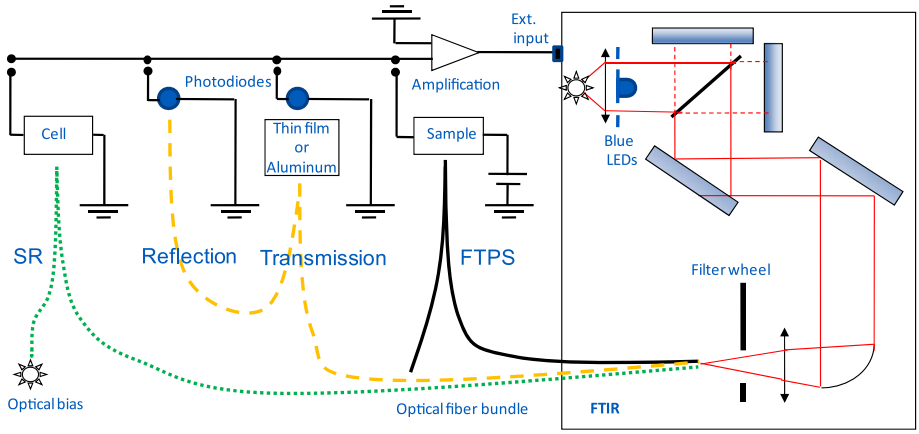

FIG. 1. Schematic of the setup designed to illuminate the sample with the light coming from the Michelson interferometer of an FTIR spectrometer. The *same* optical fiber bundle can be used to perform FTPS acquisition (black full line), reflection-transmission measurements (yellow dashed line), and spectral response (green dotted line) with a minimum of modification of the system holding the sample to be studied.

circuit plate by two springs that both maintain the sample in position and play the role of electrical connections. BNC cables allow the connection to the amplifier and to a bias source. A very thin hole, of 0.8 mm width and 5 mm height, was drilled through the substrate holder behind the sample to let the light pass through it and to deduce the transmittance of the film by placing a photodiode just behind the sample. Two types of photodiodes are used: a crystalline silicon (c-Si) one for the range 390–1100 nm and an InGaAs one for the range 800–1750 nm. The variations of the absorption coefficient vs photon energy, $\alpha(h\nu)$, can be deduced from the FTPS spectra and the transmittance spectra, measured at the same position of the sample, following the procedure proposed by Vaněček *et al.* for the "absolute" CPM.[7]

The same transmittance measurement can be performed on a thin film without electrodes. Besides, the fiber bundle being bifurcated, the light reflected by the film enters back into the fiber and can be measured at the output of the other branch by means of the photodiodes at our disposal. For the reflectance measurement, the flux of incident light can be estimated by replacing the sample by an aluminum mirror and taking into account the aluminum reflectance to correct the measured spectrum. From these R/T measurements, one can deduce some parameters of the film such as the index, thickness, and $\alpha(h\nu)$ in the high photon energy region using the theoretical developments proposed by Poruba *et al.*[8] The measured $\alpha(h\nu)$ can also be used to set the FTPS curves to their absolute value if needed.

For both the FTPS and R/T measurements, the final spectra are the average of 30–40 acquisitions to improve the signal to noise ratio. However, the acquisition time of all the spectra for the FTPS or R/T study does not exceed a few minutes (5 to 8 min).

To measure the SR in a single shot, we can modify the light source of the FTIR by inserting in the beam, before the interferometer (see Fig. 1), a plate in which we have fixed 5 blue LEDs surrounded by two semi-circular apertures to let a part of the halogen light pass through it [see Fig. 3(a)]. These

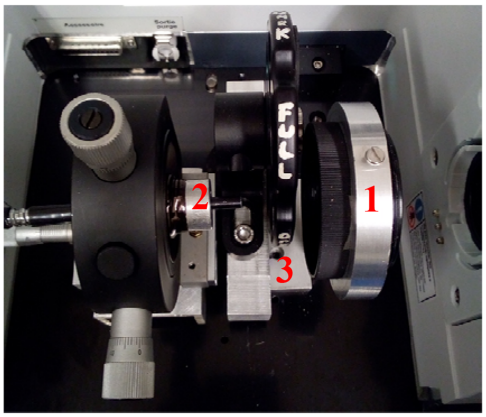

FIG. 2. System designed to collect the light from the Michelson interferometer of the FTIR: (1) a silica lens concentrating the light on the entrance of one leg of a bifurcated optical fiber bundle (2) and a filter wheel in between to select different ranges of wavelengths (3).

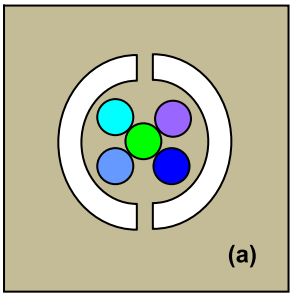

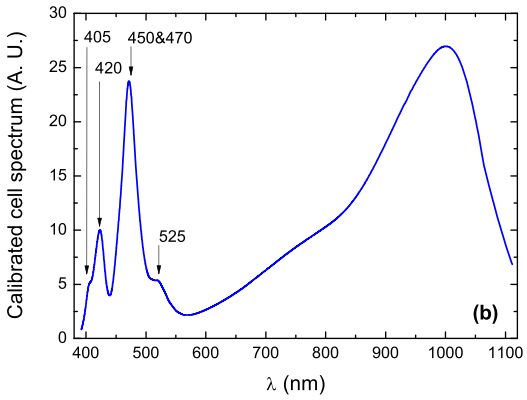

FIG. 3. (a) Design of the LEDs and semicircular apertures set in an electronic plate to enhance the light emission of the source in the range 390–550 nm and (b) spectrum of the modified light source measured with a calibrated c-Si photodiode. The wavelengths corresponding to the LED emission peaks are indicated in the figure in nm.

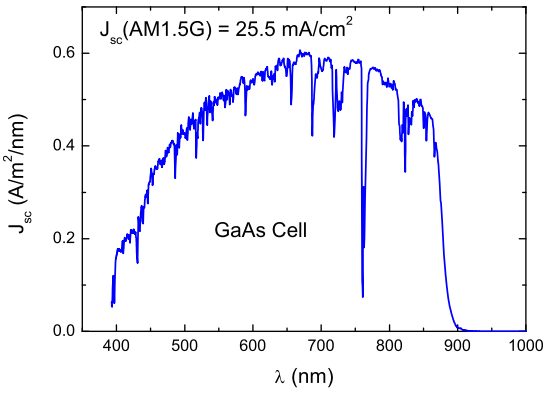

FIG. 4. Spectrum of the short circuit photocurrent density that would flow in a GaAs cell under AM1.5G illumination. The integral of this curve gives a short circuit photocurrent density of 25.5 mA/cm^2.

blue LEDs compensate the weak emission of the halogen lamp in the blue region of its spectrum, a region where the responses of the cells are also often weak. An example of the spectrum of this modified light source is presented in Fig. 3(b). Without these blue LEDs, the SR appears very noisy in the blue region of the spectrum. To determine the cell SR, the output of the fiber has to be set close to it so that all the light exiting the fiber is shone onto the device when measuring the current spectrum. The incident power is deduced from the same type of measurement performed on a large area c-Si photodiode, the SR of which is calibrated. From the SR, one can deduce the external quantum efficiency and the short circuit current density under AM1.5G power density [W/(m^2/nm)], $J_{sc}(\lambda)$ = SR × AM1.5G. An example of a $J_{sc}(\lambda)$ spectrum for a GaAs cell is shown in Fig. 4. The total short circuit current density is J_{sc}(AM1.5G) = 25.5 mA/cm^2, in good agreement with the value provided by the fabricant (24.9 mA/cm^2).

The SR measurements are usually done with an excellent signal to noise ratio (>100) even when one records a single spectrum. The spikes in the curve of Fig. 4 do not reveal any noise problem but come from the spikes of the sun AM1.5G spectrum, these latter resulting mainly from absorption from molecules of the atmosphere. This behavior underlines the excellent resolution with which the acquisition is done. Since a single spectrum can be recorded within 1 s, it opens the possibility to achieve a mapping of large area cells, up to 15.6 × 15.6 cm^2, with the resolution of the output of the optical fiber (~5 mm) within a "reasonable" acquisition time. The last advantage of our system is that it is possible to add an optical bias on the other branch of the optical fiber when studying tandem cells (see Fig. 1).

As a conclusion, we have designed a very simple system to be inserted into the sample compartment of an FTIR spectrometer to collect the light at the exit of the Michelson interferometer. With this system, it is possible to perform three types of optoelectronic characterizations of thin film semiconductors and solar devices with a single apparatus: FTPS, acquisition of R/T spectra on thin films, and SR measurements of solar cells. These acquisitions are fast and with an excellent resolution giving the opportunity to achieve systematic evaluations of some of the properties of a thin film material. Indeed, it takes between 10 and 15 min of acquisition to obtain a rather complete overview of a particular thin film material potentialities by performing characterizations on the thin film alone (FTPS and R/T) and when incorporated as an absorber in a solar device (SR). It is therefore easy and fast to achieve a comparative study of several thin film materials with one particular characterization technique, or the three of them, for optimization of the deposition parameters to improve the device conversion efficiency. In terms of future developments, the setup we designed also offers the possibilities to study tandem cell performances as well as to achieve mappings of large area cells to check their homogeneity within a reasonable time of acquisition. Finally, the system we presented is easy to use and no special training is required except mastering the operating procedure of the FTIR. It could be then developed in any laboratory working in the photovoltaic domain, seeking for ready-to-use characterization techniques and in which an FTIR apparatus is available.

[1] A. Poruba, M. Vaněček, J. Rosa, L. Feitknecht, N. Wyrsch, J. Meier, A. Shah, T. Repmann, and B. Rech, in *Proceedings of the 17th European Photovoltaic Solar Energy Conference* (WIP, Munich, Germany, 2001), Vol. 2981.
[2] M. Vaněček and A. Poruba, Appl. Phys. Lett. **80**, 719 (2002).
[3] J. Holovsky in *Fourier Transforms-New Analytical Approaches and FTIR Strategies*, edited by G. Nikolic (IntechOpen, 2011), Chap. 13, available at http://www.intechopen.com/books/fourier-transforms-new-analytical-approaches-and-ftir-strategies/fourier-transform-photocurrent-spectroscopy-on-non-crystalline-semiconductors.
[4] M. Vaněček, J. Kočka, J. Stuchlík, and A. Tříska, Solid State Commun. **39**, 1199 (1981).
[5] J. W. Tomm, A. Jaeger, A. Bärwolff, T. Elsaesser, A. Gerhardt, and J. Donecker, Appl. Phys. Lett. **71**, 2233 (1997).
[6] M. Hennies, A. Zastrow, and V. Wittwer, Measurements **7**, 93 (1989).
[7] M. Vaněček, J. Kočka, A. Poruba, and A. Fejfar, J. Appl. Phys. **78**, 6203 (1995).
[8] A. Poruba, A. Fejfar, Z. Remes, J. Springer, M. Vaněček, J. Kocka, J. Meier, P. Torres, and A. Shah, J. Appl. Phys. **88**, 148 (2000).

Appendix C

Résumé en français

La recherche dédiée à l'étude de matériaux de type semi-conducteurs en couche mince reste un sujet d'actualité notamment pour le développement de l'industrie photovoltaïque. Plusieurs types de matériaux peuvent être incorporés comme absorbeur dans des cellules solaires. Ces matériaux comprennent les fameux matériaux inorganiques comme le silicium amorphe hydrogéné (a-Si:H), le CIGS, et le CdTe, mais aussi des nouveaux matériaux organiques comme les mélanges P3HT-PCBM et les pérovskites. Les méthodes de caractérisations sont d'une grande importance dans l'étude des performances de ces matériaux avant qu'ils soient incorporés dans des cellules solaires. En effet, ces méthodes de caractérisation sont nécessaires et fondamentales pour l'optimisation de nouveaux matériaux et enfin des cellules solaires qui les incorporent.

Au laboratoire GeePs, plusieurs types de méthode de caractérisation avancée pour les matériaux de type semi-conducteur en couche mince ont été et sont toujours développées. Le développement de ces méthodes de caractérisation est focalisé sur l'amélioration de méthodes existantes et aussi l'implémentation de nouvelles méthodes pour l'étude des paramètres de transport des matériaux. Le laboratoire GeePs est aussi un des partenaires de l'Institut Photovoltaïque d'Ile de France (IPVF), dans lequel plusieurs laboratoires académiques et industries sont impliquées. Dans ce cadre, le GeePs est l'acteur principal dans le Projet H en tant que développeur de bancs de caractérisation pour matériaux semi-conducteur en couche mince, notamment d'expériences qui n'ont pas encore été introduites dans la communauté photovoltaïque française jusqu'à présent.

En ce qui concerne les méthodes de caractérisation avancée, dans cette thèse nous proposons une méthode qui peut être utilisée pour la caractérisation des performances optiques et électriques de matériaux semi-conducteurs en couche mince. Cette méthode possède aussi l'avantage de pouvoir caractériser les défauts dans les matériaux, défauts qui déterminent leurs performances, avant leur intégration dans la cellule solaire. Dans cette méthode, les défauts du matériau sont étudiés en mesurant le photo-courant engendré dans ce matériau sous éclairement. Ce matériau est déposé sur un substrat transparent et non-conducteur, par exemple du verre. Le photocourant est mesuré en éclairant la surface entre deux électrodes coplanaires et parallèles déposées sur le film du matériau semi-conducteur. Une électrode est utilisée

pour polariser l'échantillon et l'autre pour récupérer le photo-courant généré. Derrière ce matériau, une photodiode est installée pour mesurer le flux lumineux transmis à travers le matériau et son substrat. Le ratio entre le photo-courant mesuré et le flux lumineux transmis est proportionnel au coefficient d'absorption. Finalement, cette mesure donne le coefficient d'absorption en fonction de la longueur d'onde ou de l'énergie des photons. Le photo-courant généré est le résultat des transitions optiques possible entre les états localisées (défauts) et les états étendus de la densité d'états du matériau semi-conducteur en couche mince. La variation du coefficient d'absorption est donc liée à la densité de défauts dans le matériau. La partie de la densité d'états la plus intéressante est celle liée à la partie de faible absorption dans la courbe du coefficient d'absorption, qui se trouve dans la plage de longueurs d'onde où l'énergie des photons est inférieure à l'énergie du gap de ce matériau.

La méthode de caractérisation que l'on utilise est la spectroscopie de photo-courant en utilisant la transformée de Fourier ou Fourier Transform Photocurrent Spectroscopy (FTPS). Historiquement, la FTPS a été précédée par une autre technique qu'on appelle la méthode de photo-courant constant ou Constant Photocurrent Method (CPM). La CPM était utilisée pour mesurer le photo-courant d'un matériau semi-conducteur en l'éclairant sous lumière monochromatique et en gardant le photo-courant engendré constant. Cette technique utilise un monochromateur et mesure le photo-courant pour une seule énergie de photon à la fois. A chaque changement d'énergie de photon, le flux de la source lumineuse doit être réglé pour que le photo-courant reste constant. La réalisation de cette expérience est donc assez longue puisqu'une mesure sur une plage de longueurs d'onde de 400 à 1800 nm peut atteindre jusqu'à 17 heures. Ce désavantage de la mesure du CPM peut être corrigé dans la technique FTPS par l'utilisation de la spectroscopie infrarouge à transformée de Fourier ou Fourier Transform Infrared Spectrometer (FTIR). Le FTIR utilise une source poly-chromatique, par exemple la lumière blanche provenant d'une lampe halogène, qui remplace la source monochromatique utilisée pour la mesure de CPM. Le principe de mesure de la FTPS est très similaire à celui de la CPM. Pendant la mesure FTPS, le photo-courant est mesuré en une fois. Il est donc maintenu constant comme pendant la mesure CPM. Néanmoins, l'utilisation de la transformé de Fourier nous permet de décomposer les contributions de chaque photo-courant correspondant à chaque longueur d'onde. Enfin, avec la FTPS on est aussi capable d'obtenir le coefficient d'absorption en fonction de la longueur d'onde ou de l'énergie des photons et ceci dans un temps de mesure beaucoup plus court qu'avec la CPM. Une mesure du coefficient d'absorption en utilisant la FTPS ne dure que quelques minutes au maximum.

Notre banc de mesure de FTPS est conçu en utilisant un système optique simple installé dans le compartiment d'échantillon du FTIR. Ce banc de mesure opère dans la plage de longueurs d'onde de 390 à 1750 nm. L'installation dans le compartiment d'échantillon utilise une lentille qui focalise la lumière provenant du Michelson du FTIR sur l'entrée d'une branche d'une fibre optique en Y qui conduit la lumière du FTIR jusqu'au matériau étudié. Dans le compartiment du FTIR, une roue tournante portant plusieurs filtres optiques est placée entre la lentille et la fibre optique. Ces filtres sont principalement utilisés pour éliminer la partie des photons donnant la

plus grande réponse de photo-courant. En éliminant cette partie, la précision de la plage de longueurs d'onde où le signal est faible peut être améliorée et ainsi la gamme dynamique de la mesure peut être augmentée. La plage où le signal est faible comprend la partie de faible absorption et donc l'utilisation de ce filtre nous permet de mieux mesurer les défauts profonds du matériau étudié. En principe, le matériau semi-conducteur étudié est utilisé en tant que photo-détecteur et son signal de photo-courant doit être envoyé vers un convertisseur courant-tension avant d'être renvoyé au FTIR pour traitement. Ce convertisseur permet d'amplifier le signal de photo-courant qui est généralement assez faible et cette conversion est importante car le FTIR lit uniquement la tension. Le signal envoyé vers le FTIR est traité ultérieurement en utilisant la transformation de Fourier rapide (FFT) donnant enfin un spectre en fonction de la longueur d'onde. Pour calculer le coefficient d'absorption, la mesure du flux transmis par le matériau semi-conducteur doit être effectuée. Cette mesure est faite en utilisant deux types de photodiodes, ayant deux différentes gammes de sensibilité de longueur d'onde, placées derrière le matériau semi-conducteur. Ces deux photodiodes sont de type silicium (390-1100 nm) et InGaAs (800-1750 nm). Une fois que les spectres de mesure du flux ont été faits, on peut lancer le calcul du coefficient d'absorption en utilisant le ratio du spectre de photo-courant et du flux.

Le principe de la mesure du flux au travers le matériau semi-conducteur en utilisant le FTIR a aussi été développé pour la mesure de la réflexion et transmission (R/T) du matériau semi-conducteur en couche mince déposé sur un substrat transparent. Cette mesure de R/T en utilisant le FTIR peut remplacer la mesure classique qui utilise un spectromètre UV-Visible. L'utilisation d'une lumière poly-chromatique et le traitement du signal en utilisant la FFT dans la mesure R /T réduit considérablement le temps de mesure par rapport à une mesure utilisant un spectromètre UV-Visible, comme c'est le cas lorsqu'on compare la CPM et la FTPS. La mesure de la réflexion est faite en mesurant le flux réfléchi par le matériau semi-conducteur. La mesure du flux réfléchi est réalisée grâce à l'utilisation de la fibre optique à deux branches (fibre optique en Y). Une des branches est utilisée pour envoyer la lumière venant du FTIR vers le matériau et la lumière réfléchie par l'échantillon est collectée par l'autre branche et envoyée vers une photodiode qui mesure le flux réfléchi. La réflexion est calculée par le ratio du flux réfléchi par le matériau et du flux réfléchi par une référence qui est un matériau parfaitement réfléchissant comme un miroir aluminium. La mesure de la transmission se fait comme pour la FTPS. Une photodiode est placée derrière le matériau et mesure le flux traversant le matériau. La transmission est obtenue par le ratio du flux au travers le matériau et le flux incident, ce dernier étant mesuré par une photodiode à la sortie de la fibre optique. Par la suite, les résultats de mesure R/T peuvent être utilisés pour la modélisation optique des matériaux qui nous donnera les valeurs de ses paramètres optiques comme l'indice de réfraction, l'épaisseur, la rugosité, et le coefficient d'absorption optique dans la plage des hautes énergies de photons. Le coefficient d'absorption optique donné par la simulation optique à partir de la mesure R/T est donc très utile pour valider et calibrer les résultats donnés par la mesure FTPS notamment sur la partie de haute absorption. La validité de la simulation optique qu'on utilise pour la détermination de quelques paramètres optiques d'un matériau a aussi été réalisée en mesurant les R/T

d'un set de matériaux semi-conducteurs type silicium a-Si :H ayant des paramètres optiques connus.

Le banc de mesure de FTPS a aussi été développé pour la mesure de la réponse spectrale (RS) en fonction de la longueur d'onde d'un dispositif solaire. La mesure de la RS est faite en calculant le ratio entre le photo-courant généré par la cellule solaire en court circuit et la puissance du flux incident mesuré à l'aide d'une photodiode étalonnée. Connaissant la RS, on peut en déduire l'efficacité quantique externe (EQE) de la cellule solaire en fonction de la longueur d'onde. La mesure de la RS peut nous donner aussi le spectre de la densité de courant court-circuit de la cellule solaire en fonction de la longueur d'onde, $J_{SC}(\lambda)$, que l'on obtiendrait sous AM1.5G. Ces valeurs peuvent être obtenues en multipliant la RS par le spectre de densité de puissance solaire sous AM 1.5 G. L'intégrale de la courbe $J_{SC}(\lambda)$nous donne enfin la densité totale de courant de court-circuit sous AM1.5G, J_{SC}, du dispositif solaire étudié.

En conclusion, notre banc de mesure de FTPS est un banc 3-en-1. Ce banc a l'avantage de conduire trois types de mesure avec un seul banc : FTPS, R/T, et RS. Un autre avantage est le temps de mesure réduit par rapport aux mesures classiques comme la CPM, un spectromètre UV-Visible et les mesures de RS classiques. En utilisant un FTIR, les résultats de mesure enregistrés sont aussi obtenus avec une très haute résolution, par exemple 5500 points de données sur la plage de 390-1750 peuvent être mesurés, et ceci seulement en quelques minutes.

Plus loin dans cette thèse, le coefficient d'absorption mesuré par FTPS est utilisé pour mesurer la densité de défauts dans le matériau. La mesure de la densité d'états à partir du coefficient d'absorption est faite par une modélisation numérique en utilisant un logiciel qui s'appelle DeOSt. Ce logiciel nous permet de concevoir une modèle de densité d'états pour un matériau. Le modèle de la densité d'états peut être construit en définissant la forme des états étendus, des queues de bandes, des états localisées ou états de défaut. La forme de la densité d'états est construite par la définition des paramètres de densité d'états comme l'énergie du gap, la température de la queue de bande, la forme de la distribution de défauts, etc. La densité d'états d'un matériau défini alors le nombre des états disponibles pour effectuer les transitions électroniques dans ce matériaux. A partir de ce modèle de densité d'états, on peut définir les types de transition électronique qui contribuent au coefficient d'absorption. Ce coefficient d'absorption est calculé à partir du produit de convolution des transitions électroniques définies. Dans cette modélisation, deux types de modèle de densité d'états sont utilisés : un modèle classique ou standard, et un modèle basé sur un réservoir de défauts ou Defect-Pool. Ces deux modèles sont similaires au niveau de la distribution des états étendus et des états des queues de bande. La différence entre ces deux modèles est liée à la distribution des états localisés ou défauts. Le modèle standard comprend 17 paramètres différents pour définir la densité d'états, tandis que le modèle Defect-Pool n'a besoins que de 15 paramètres. Le réglage de ces paramètres à la main n'est pas impossible mais un peu compliqué étant donné leur nombre. Néanmoins, certains paramètres peuvent être estimés à partir de la courbe du coefficient d'absorption, par exemple : l'énergie du gap, la température caractéristique de la queue de bande de valence, et l'amplitude de la distribution de défauts profonds par rapport aux distributions des états étendus. La détermination de ces valeurs doit

être faite pour que le calcul du coefficient d'absorption corresponde avec les résultats obtenus par FTPS. Donc, pour avoir un modèle parfait, le processus de réglage et d'ajustement des valeurs de paramètre de densité d'états devient très fastidieux.

Pour surmonter ce problème, nous proposons un algorithme évolutif qui s'appelle Teacher and Learner Based Optimization (TLBO), pilotant le logiciel DeOSt. Cet algorithme a été utilisé par Rao et al. pour la recherche des paramètres électriques d'une cellule solaire à partir de sa courbe I(V). En utilisant un modèle analytique, cet algorithme est capable de retrouver les valeurs des paramètres optiques donnés par le fabricant de cette cellule solaire. Pour l'instant, cet algorithme n'a jamais été utilisé pour la recherche de paramètres de densité d'états. L'algorithme TLBO a été réalisé dans le langage Matlab. Cet algorithme minimise l'erreur entre les courbes du coefficient d'absorption calculé par DeOSt et celle obtenue par FTPS. Dans cet algorithme, on peut aussi fixer la plage physique des valeurs de chaque paramètre de densité d'états, et donner un set de valeurs des paramètres de densité d'états comme point de départ de leur recherche. Ce choix de départ peut venir de l'ajustement manuel du modèle de densité d'états dans DeOSt donnant une courbe du coefficient d'absorption proche de celle donnée par la FTPS. La fiabilité de cet algorithme a été aussi validée en reproduisant une courbe du coefficient d'absorption qui était déjà modélisé par DeOSt. Le résultat du modèle de densité d'états trouvé par TLBO était très similaire au modèle de départ.

Dans la pratique, cet algorithme est très simple car on peut juste donner les plages de valeur de chaque paramètre et définir le nombre d'itérations. Pendant la recherche de valeur de ces paramètres, cet algorithme aussi prendre en compte la cohérence de l'énergie d'activation mesurée par SSPC et calculée par DeOSt. Cet algorithme typiquement peut atteindre l'erreur minimum à partir de 2000 itérations, voire moins de 200 itérations si les paramètres de départ sont astucieusement choisis.

La façon dont évoluent les différents paramètres pendant la minimisation d'erreur en algorithme de TLBO ne peut pas être utilisée comme base de recherche des paramètres de la densité d'états lorsque cette recherche se fait manuellement. En effet, tous les paramètres, parmi les 17 ou 15 selon le modèle, ne peuvent pas avoir le même impact pour le calcul du coefficient d'absorption. Pour cette raison, nous avons mené une analyse de la sensibilité du coefficient d'absorption aux différents paramètres de la densité d'états. Cette étude a été menée pour mettre en évidence les paramètres de la densité d'états qui sont les plus importants pour le calcul du coefficient d'absorption. L'analyse de la sensibilité a été réalisée par: 1.) L'analyse de l'impact de la modification d'une valeur de paramètre de +/- 30% de sa valeur initiale sur le changement de la forme du spectre de coefficient d'absorption, 2.) l'identification de l'influence de chaque paramètre de la densité d'états en donnant une quantification de plage de changement des valeurs du coefficient d'absorption lorsque la valeur du paramètre est modifiée de +/- 30% de sa valeur initiale, quantification représentée en diagramme Tornado, et 3.) l'identification de l'influence d'un paramètre en mesurant le degré de liberté de chaque paramètre de la densité d'états sur le coefficient d'absorption, représenté en diagramme de Spider. Le changement de la forme du coefficient d'absorption dans cette étude est découpé et analysé en trois parties différents: la partie des hautes absorptions, la partie correspondant à la pente

d'Urbach, et les défauts profonds. Les résultats de l'analyse de sensibilité montrent que pour la modèle standard, le coefficient d'absorption dépend essentiellement : de l'énergie du gap, de la température caractéristique de la queue de bande de valence et de son coefficient optique, de la densité d'états étendus de la bande de conduction, de l'énergie où la densité de défaut type donneur est maximale, et de la densité d'états de la bande de valence. Cependant, l'énergie d'activation dans ce modèle standard dépend : de l'énergie où la densité de défauts type accepteur est maximale et de sa valeur à cette énergie, de l'énergie où la densité de défauts type donneur est maximale, et des 'largeurs' (écarts-type) de la distribution de donneurs et d'accepteurs. Pour le modèle de Defect-Pool, le coefficient d'absorption est influencé par l'énergie du gap, l'énergie du Defect-Pool, la température caractéristique de la queue de band de valence, la 'largeur' (Ecart-type) du Defect-Pool, et la température de la queue de bande de conduction. En utilisant ce même modèle, l'énergie d'activation est très influencée par l'énergie du gap, l'énergie du Defect-Pool et son écart-type, la température caractéristique de la queue de bande de valence, l'énergie de corrélation, et la densité d'états étendus de la bande de conduction.

Nous avons appliqué cette technique TLBO à l'étude de différents films minces de a-Si :H pour lesquels leurs coefficients d'absorption avaient été mesurés par FTPS. De bons accords ont été obtenus entre les coefficients d'absorption calculés et expérimentaux. Toutefois, ces résultats ont également soulignés les limites de l'ajustement des paramètres pour reproduire les courbes expérimentales des coefficients d'absorption par l'algorithme TLBO. Nous avons pu montrer par exemple que, malgré l'excellent accord entre les courbes de coefficient d'absorption expérimentales et calculées, soit par l'utilisation d'un modèle de densité d'états standard soit par l'utilisation d'un Defect-Pool, les densités d'états pouvaient être très différentes si on utilise des coefficients optiques très différents d'un modèle à l'autre. Nous avons également retrouvé que certains paramètres n'avaient que peu d'influence sur le résultat final comme dans l'étude de sensibilité.

Dans la partie expérimentale de cette thèse, nous avons également étudié si le même coefficient d'absorption pouvait être trouvé à la fois pour des films coplanaires de a-Si:H déposés sur verre et pour des diodes NIP incorporant le même matériau comme couche intrinsèque. Les contacts arrière et avant des diodes étaient constitués d'oxydes conducteurs transparents, ITO ou ZnO. Les résultats montrent que les queues d'Urbach des échantillons coplanaires et des diodes NIP sont très similaires mais que le coefficient d'absorption à faible énergie est légèrement plus faible pour les diodes que pour les échantillons coplanaires. De plus, nous avons remarqué que la diode à contacts ZnO présente une augmentation rapide du coefficient d'absorption au-dessous de 0,95 eV. Les mesures de R/T effectuées sur les diodes montrent que la diode à contacts ZnO présentent une transmission plus faible dans la même gamme de longueur d'onde où l'on observe une augmentation du coefficient d'absorption, bien que la réflexion avec les deux types de contacts reste la même, indiquant une absorption parasite de la couche de ZnO arrière. Ces résultats montrent que les mesures FTPS effectuées sur les diodes doivent être prises avec beaucoup de prudence et qu'il faut prendre en compte les propriétés optiques (par exemple l'absorption) des contacts pour déduire correctement la spectroscopie du coefficient d'absorption à faible

énergie dans des dispositifs solaires.

Notre banc de mesure, rapide et facile à utiliser, peut être finalement appliqué pour une étude systématique de certains paramètres du matériau et des dispositifs, ainsi que pour des études comparatives de mesures FTPS effectuées sur un film et sur un dispositif incorporant le même film en tant qu'absorbeur. Enfin, la possibilité d'effectuer des expériences 3-en-1 avec un seul banc ainsi qu'une étude enrichie de la densité d'états des matériaux font de cette thèse un outil qui pourrait s'avérer utile pour l'optimisation des matériaux et des cellules solaires à l'avenir

Bibliography

[1] NREL. efficiency-chart rev.04-14-2017.

[2] M. Vanecek, J. Kocka, J. Stuchlik, and A. Triska. Direct measurement of the gap states and band tail absorption by constant photocurrent method in amorphous silicon. *Solid State Communications*, 39(11):1199 – 1202, 1981.

[3] M. Vanecek, J. Kocka, J. Stuchlik, Z. Kozisek, O. Stika, and A. Triska. Density of the gap states in undoped and doped glow discharge a-si: H. *Solar Energy Materials*, 8(4):411–423, 1983.

[4] J Kocka, M Vanecek, and A Triska. Amorphous silicon and related materials (pp. 297-327). *Amorphous Silicon and Related Materials*, page 297, 1989.

[5] N. Wyrsch, F. Finger, T.J. McMahon, and M. Vanecek. How to reach more precise interpretation of subgap absorption spectra in terms of deep defect density in a-si:h. *Journal of Non-Crystalline Solids*, 137:347 – 350, 1991.

[6] Warren B. Jackson and Nabil M. Amer. Direct measurement of gap-state absorption in hydrogenated amorphous silicon by photothermal deflection spectroscopy. *Phys. Rev. B*, 25:5559–5562, Apr 1982.

[7] S. J. Pearton. Hydrogenated amorphous silicon, by r. a. street, cambridge university press, cambridge 1991, xiv, 417 pp., hardcover, £ 65.00; isbn 0-521-37156-2. *Advanced Materials*, 4(4), 1992.

[8] D. L. Staebler and C. R. Wronski. Optically induced conductivity changes in discharge produced hydrogenated amorphous silicon. *Journal of Applied Physics*, 51(6):3262–3268, 1980.

[9] Christopher R. Wronski and Ronald E. Daniel. Photoconductivity, trapping, and recombination in discharge-produced, hydrogenated amorphous silicon. *Phys. Rev. B*, 23:794–804, Jan 1981.

[10] Warren B Jackson and Nabil M Amer. Direct measurement of gap-state absorption in hydrogenated amorphous silicon by photothermal deflection spectroscopy. *Physical Review B*, 25(8):5559, 1982.

[11] A. V. Gelatos, K. K. Mahavadi, J. D. Cohen, and J. P. Harbison. Transient photocapacitance and photocurrent studies of undoped hydrogenated amorphous silicon. *Applied Physics Letters*, 53(5):403–405, 1988.

[12] Karin Jahn, Reinhard Carius, and Walther Fuhs. Photoluminescence and photoconductivity of a-si: H at high electric fields. *Journal of Non-Crystalline Solids*, 97:575–578, 1987.

[13] M. S. Ablova, G. S. Kulikov, and S. K. Persheev. Gamma-irradiation-induced metastable states of undoped amorphous hydrogenated silicon. *Semiconductors*, 36(8):936–940, Aug 2002.

[14] Daewon Kwon, Hao Lee, J.David Cohen, Hyun-Chul Jin, and John R. Abelson. Optical spectra of crystalline silicon particles embedded in an amorphous silicon matrix. *Journal of Non-Crystalline Solids*, 227:1040 – 1044, 1998.

[15] G. van Elzakker, V. Nádaždy, F.D. Tichelaar, J.W. Metselaar, and M. Zeman. Analysis of structure and defects in thin silicon films deposited from hydrogen diluted silane. *Thin Solid Films*, 511:252 – 257, 2006. EMSR 2005 - Proceedings of Symposium F on Thin Film and Nanostructured Materials for Photovoltaics.

[16] B. Monemar and H. G. Grimmeiss. Optical characterization of deep energy levels in semiconductors. *Progress in Crystal Growth and Characterization*, 5(1–2):47–88, 1982.

[17] GD Cody, CR Wronski, B Abeles, RB Stephens, and Br Brooks. Optical characterization of amorphous silicon hydride films. *Solar cells*, 2(3):227–243, 1980.

[18] Ing-Shin Chen, Lihong Jiao, Robert W. Collins, and Christopher R. Wronski. A novel approach to the analysis of sub-bandgap absorption in a-si:h based materials. *Journal of Non-Crystalline Solids*, 198:391 – 394, 1996. Proceedings of the Sixteenth International Conference on Amorphous Semiconductors - Science and Technology.

[19] Daxing Han and H Fritzsche. Study of light-induced creation of defects in a-si:h by means of single and dual-beam photoconductivity. *Journal of Non-Crystalline Solids*, 59:397 – 400, 1983. Proceedings of the Tenth International Conference on Amorphous and Liquid Semiconductors.

[20] Warren B. Jackson, Nabi1 M. Amer, A. C. Boccara, and D. Fournier. Photothermal deflection spectroscopy and detection. *Applied optics*, 20(8):1333–1344, 1981.

[21] M. Vanecek, J. Kocka, A. Poruba, and A. Fejfar. Direct measurement of the deep defect density in thin amorphous silicon films with the "'absolute'"constant photocurrent method. *Journal of applied physics*, 78(10):6203–6210, 1995.

[22] Petr Sladek, Pavel Stahel, Pere Roca I. Cabarrocas, and Philippe Morin. Defect states in the intrinsic layer of amorphous silicon solar cells studied by the

constant-photocurrent method. *Philosophical Magazine Part B*, 77(4):1049–1061, Apr 1998.

[23] Manabu Sasaki, Shingo Okamoto, Yoshihiro Hishikawa, Shinya Tsuda, and Shoichi Nakano. Characterization of the defect density and band tail of an a-si:h i-layer for solar cells by improved {CPM} measurements. *Solar Energy Materials and Solar Cells*, 34(1–4):541 – 547, 1994.

[24] M. Vanecek and A. Poruba. Fourier-transform photocurrent spectroscopy of microcrystalline silicon for solar cells. *Applied Physics Letters*, 80(5):719–721, 2002.

[25] Jakub Holovsky. Fourier transform photocurrent spectroscopy on non-crystalline semiconductors. *Fourier Transforms-New Anal. Approaches FTIR Strateg., ed. Goran Nikolic, InTech Publishing*, page 257–282, 2011.

[26] J. W. Tomm, A. Jaeger, A. Bärwolff, T. Elsaesser, A. Gerhardt, and J. Donecker. Aging properties of high power laser diode arrays analyzed by fourier-transform photocurrent measurements. *Applied physics letters*, 71(16):2233–2235, 1997.

[27] Jakub Holovsky, Umit Dagkaldiran, Zdenek Remes, Adam Purkrt, Tibor Izak, Ales Poruba, and Milan Vanecek. Fourier transform photocurrent measurement of thin silicon films on rough, conductive and opaque substrates. *physica status solidi (a)*, 207(3):578–581, Mar 2010.

[28] Poruba A.and Vaněček, Rosa J., Feitknecht, Wyrsch N.and Meier J, and Shah A. Fourier transform photocurrent spectroscopy in thin film silicon solar cells. Proceeding of 17th European Photovoltaic Solar Energy Conference, 2001.

[29] R. Kravets, V. Ogorodniks, A. Poruba, P. Moravec, M. Nesladek, J. Rosa, and M. Vanecek. Fourier-transform photocurrent spectroscopy of defects in cvd diamond layers. *physica status solidi (a)*, 193(3):502–507, 2002.

[30] J. Melskens, G. van Elzakker, Y. Li, and M. Zeman. Analysis of hydrogenated amorphous silicon thin films and solar cells by means of fourier transform photocurrent spectroscopy. *Thin Solid Films*, 516:6877–6881, 2008.

[31] Xinwei Niu. *Nature and evolution of light induced defects in hydrogenated amorphous silicon*. ProQuest, 2006.

[32] Arno HM Smets, Chris R Wronski, Miro Zeman, and M Van de Sanden. The staebler-wronski effect: New physical approaches and insights as a route to reveal its origin. In *MRS Proceedings*, volume 1245, pages 1245–A14. Cambridge Univ Press, 2010.

[33] Shuai Lu and Sergei Pereverzyev. Numerical differentiation from a viewpoint of regularization theory. 75:1853–1870, 10 2006.

[34] Markus Grasmair, Markus Haltmeier, and Otmar Scherzer. *Sparsity in Inverse Geophysical Problems*, pages 763–784. Springer Berlin Heidelberg, Berlin, Heidelberg, 2010.

[35] Peter R. Griffiths and James A. De Haseth. *Fourier transform infrared spectrometry*. Chemical analysis. Wiley-Interscience, 2nd ed edition, 2007.

[36] D.A. Skoog, F.J. Holler, and S.R. Crouch. *Principles of Instrumental Analysis*. International student edition. Thomson Brooks/Cole, 2007.

[37] A. Rose. *Concepts in photoconductivity and allied problems*. Interscience tracts on physics and astronomy. Interscience Publishers, 1963.

[38] D. Ritter and K. Weiser. Suppression of interference fringes in absorption measurements on thin films. *Optics Communications*, 57(5):336–338, 1986.

[39] Bailat J. *Growth, microstructure and electrical performances of thin film microcrystalline silicon solar cells*. PhD thesis, Universite de Neuchatel, 2004.

[40] Sculati-Meillaud. *Microcrystalline silicon solar cells: theory, diagnosis and stability*. PhD thesis, Universite de Neuchatel, 2006.

[41] Python M. *Microcrystalline silicon solar cells: growth and defects*. PhD thesis, Universite de Neuchatel, 2009.

[42] Ales Poruba, Jiri Springer, Lenka Mullerova, Milan Vanecek, Tobias Repmann, Bernd Rech, Jamil Kuendig, Nicolas Wyrsch, and Arvind Shah. *Fast and sensitive defect characterization and spectral response measurement of thin film silicon solar structures*, volume 2, page 1631–1634. IEEE, 2003.

[43] M. Vanecek, R. Kravets, A. Poruba, J. Rosa, M. Nesladek, and S. Koizumi. Fourier transform photocurrent spectroscopy of dopants and defects in cvd diamond. *Diamond and Related Materials*, 12(3–7):521–525, Mar 2003.

[44] A. Poruba, J. Holovsky, A. Purkrt, and M. Vanecek. Advanced optical characterization of disordered semiconductors by fourier transform photocurrent spectroscopy. *Journal of Non-Crystalline Solids*, 354(19–25):2421–2425, May 2008.

[45] R Swanepoel. Determination of the thickness and optical constants of amorphous silicon. *Journal of Physics E: Scientific Instruments*, 16(12):1214, 1983.

[46] Corning Glass Catalogue.

[47] Jürgen Metzdorf, T. Wittchen, and K. Heidler. *The results of the PEP '87 round robin calibration of reference solar cells and modules: final reαt*. PTB-Bericht PTB-Opt-31. Wirtschaftsverl. NW, Verl. für neue Wiss, 1990.

[48] M. Python, D. Domine, T. Soderstrom, F. Meillaud, and C. Ballif. Microcrystalline silicon solar cells: effect of substrate temperature on cracks and their role in post-oxidation. *Progress in Photovoltaics: Research and Applications*, 18(7):491–499, Apr 2010.

[49] A. Bailat Vanecek M. Holovsky, J. Poruba. Separation of signals from amorphous and microcrystalline part of a tandem thin film silicon solar cell in fourier transform photocurrent spectroscopy. Proceedings of 22nd EU-PVSEC, 2007.

[50] Documentation of c-Si solar cell RQN6355.

[51] A. Poruba, A. Fejfar, Z. Remeš, J. Špringer, M. Vaněček, J. Kočka, J. Meier, P. Torres, and Arvind Shah. Optical absorption and light scattering in microcrystalline silicon thin films and solar cells. *Journal of Applied Physics*, 88(1):148–160, 2000.

[52] Michael Bass. *Handbook of optics*. McGraw-Hill, 2nd ed edition, 1995.

[53] P. Beckmann and A. Spizzichino. *The Scattering of Electromagnetic Waves from Rough Surfaces*. Radar Library. Artech House, 1987.

[54] R.H. Bartels, J.C. Beatty, and B.A. Barsky. *An Introduction to Splines for Use in Computer Graphics and Geometric Modeling*. Morgan Kaufmann Series in Comp. Morgan Kaufmann, 1995.

[55] F. Carreno, Juan Carlos Martinez-Anton, and E. Bernabeu. Optical interference method to obtain thickness and refractive indices of a uniaxial medium. *Review of scientific instruments*, 65(8):2489–2493, 1994.

[56] M. J. Powell and S. C. Deane. Improved defect-pool model for charged defects in amorphous silicon. *Physical Review B*, 48(15):10815, 1993.

[57] Sanjaykumar J. Patel, Ashish K. Panchal, and Vipul Kheraj. Extraction of solar cell parameters from a single current–voltage characteristic using teaching learning based optimization algorithm. *Applied Energy*, 119:384–393, Apr 2014.

[58] The DeOSt software developed at the GeePs allows to simulate different techniques of characterization of semiconductor materials.

[59] NF Mott and EA Davis. Conduction in non-crystalline systems. part v. *Phil. Mg*, 22:903, 1970.

[60] D. L. Wood and J. Tauc. Weak absorption tails in amorphous semiconductors. *Phys. Rev. B*, 5:3144–3151, Apr 1972.

[61] Enrico Fermi and A. Zannoni. On the quantization of the monoatomic ideal gas. *arXiv preprint condmat/9912229*, 1999.

[62] R. A. Street, J. Kakalios, C. C. Tsai, and T. M. Hayes. Thermal-equilibrium processes in amorphous silicon. *Phys. Rev. B*, 35:1316–1333, Jan 1987.

[63] R. A. Street, M. Hack, and W. B. Jackson. Mechanisms of thermal equilibration in doped amorphous silicon. *Phys. Rev. B*, 37:4209–4224, Mar 1988.

[64] R. A. Street and K. Winer. Defect equilibria in undoped a-si:h. *Phys. Rev. B*, 40:6236–6249, Sep 1989.

[65] M. Stutzmann, D. K. Biegelsen, and R. A. Street. Detailed investigation of doping in hydrogenated amorphous silicon and germanium. *Phys. Rev. B*, 35:5666–5701, Apr 1987.

[66] G. Müller. On the generation and annealing of dangling bond defects in hydrogenated amorphous silicon. *Applied Physics A*, 45(1):41–51, 1988.

[67] K Winer, I Hirabayashi, and L Ley. Distribution of occupied near-surface band-gap states in a-si: H. *Physical Review B*, 38(11):7680, 1988.

[68] K. Winer. Chemical-equilibrium description of the gap-state distribution in a-si:h. *Phys. Rev. Lett.*, 63:1487–1490, Oct 1989.

[69] Z E. Smith and S. Wagner. *Implications of the 'Defect Pool' concept for 'metastable' and 'stable' defects in amorphous silicon*, pages 409–460. WORLD SCIENTIFIC, 2013.

[70] Y. Bar-Yam, D. Adler, and J. D. Joannopoulos. Bar-yam, adler, and joannopoulos respond. *Phys. Rev. Lett.*, 58:2505–2505, Jun 1987.

[71] Howard M. Branz and Marvin Silver. Potential fluctuations due to inhomogeneity in hydrogenated amorphous silicon and the resulting charged dangling-bond defects. *Phys. Rev. B*, 42:7420–7428, Oct 1990.

[72] K. Winer. Defect formation in a-si:h. *Phys. Rev. B*, 41:12150–12161, Jun 1990.

[73] G.Schumm and G.H. Bauer. Thermodynamical equilibrium gap-state distribution in undoped a-si: H. *Philosophical Magazine Part B*, 64(4):515–527, 1991.

[74] G. Schumm and G.H. Bauer. Equilibrium and non-equilibrium gap state distribution in a-si:h. *Journal of Non-Crystalline Solids*, 137:315 – 318, 1991.

[75] C. Kittel and H. Kroemer. *Thermal Physics*. W. H. Freeman, 1980.

[76] Z E. Smith and S. Wagner. Band tails, entropy, and equilibrium defects in hydrogenated amorphous silicon. *Phys. Rev. Lett.*, 59:688–691, Aug 1987.

[77] M. Stutzmann, W. B. Jackson, and C. C. Tsai. Light-induced metastable defects in hydrogenated amorphous silicon: A systematic study. *Phys. Rev. B*, 32:23–47, Jul 1985.

[78] J.-K. Lee and E. A. Schiff. Modulated electron-spin-resonance measurements and defect correlation energies in amorphous silicon. *Phys. Rev. Lett.*, 68:2972–2975, May 1992.

[79] G. Schumm, E. Lotter, and G. H. Bauer. Charged dangling bonds in undoped amorphous silicon. *Applied Physics Letters*, 60(26):3262–3264, 1992.

[80] Heinz Werner Engl, Martin Hanke, and Andreas Neubauer. *Regularization of inverse problems*, volume 375. Springer Science & Business Media, 1996.

[81] Shuai Lu and Sergei Pereverzev. Numerical differentiation from a viewpoint of regularization theory. *Mathematics of computation*, 75(256):1853–1870, 2006.

[82] J. Melskens, M. Schouten, R. Santbergen, M. Fischer, R. Vasudevan, D.J. van der Vlies, R.J.V. Quax, S.G.M. Heirman, K. Jäger, V. Demontis, and et al. In situ manipulation of the sub gap states in hydrogenated amorphous silicon monitored by advanced application of fourier transform photocurrent spectroscopy. *Solar Energy Materials and Solar Cells*, 129:70–81, Oct 2014.

[83] R Gottschalg, M Rommel, D G Infield, and M J Kearney. The influence of the measurement environment on the accuracy of the extraction of the physical parameters of solar cells. *Measurement Science and Technology*, 10(9):796, 1999.

[84] Kashif Ishaque and Zainal Salam. An improved modeling method to determine the model parameters of photovoltaic (pv) modules using differential evolution (de). *Solar Energy*, 85(9):2349 – 2359, 2011.

[85] Kashif Ishaque, Zainal Salam, Hamed Taheri, and Amir Shamsudin. A critical evaluation of {EA} computational methods for photovoltaic cell parameter extraction based on two diode model. *Solar Energy*, 85(9):1768 – 1779, 2011.

[86] Joseph A Jervase, Hadj Bourdoucen, and Ali Al-Lawati. Solar cell parameter extraction using genetic algorithms. *Measurement Science and Technology*, 12(11):1922, 2001.

[87] M. Zagrouba, A. Sellami, M. Bouaïcha, and M. Ksouri. Identification of {PV} solar cells and modules parameters using the genetic algorithms: Application to maximum power extraction. *Solar Energy*, 84(5):860 – 866, 2010.

[88] Erees Queen B. Macabebe, Charles J. Sheppard, and E. Ernest van Dyk. Parameter extraction from i–v characteristics of {PV} devices. *Solar Energy*, 85(1):12 – 18, 2011.

[89] Meiying Ye, Xiaodong Wang, and Yousheng Xu. Parameter extraction of solar cells using particle swarm optimization. *Journal of Applied Physics*, 105(9):094502, 2009.

[90] R.V. Rao, V.J. Savsani, and D.P. Vakharia. Teaching–learning-based optimization: A novel method for constrained mechanical design optimization problems. *Computer-Aided Design*, 43(3):303 – 315, 2011.

[91] Ouafa Saadane. *Etude du silicium polymorphe hydrogéné en couches minces pour applications photovoltaïques*. PhD thesis, Université de Paris Sud, 2003.

[92] Andrea Saltelli, Karen Chan, E. Marian Scott, et al. *Sensitivity analysis*, volume 1. Wiley New York, 2000.

[93] *Sensitivity analysis in practice: a guide to assessing scientific models*. Wiley, 2004.

[94] Ted G. Eschenbach. Spiderplots versus tornado diagrams for sensitivity analysis. *Interfaces*, 22(6):40–46, 1992.

[95] Ted G. Eschenbach. Technical note: Constructing tornado diagrams with spreadsheets. *The Engineering Economist*, 51(2):195–204, 2006.

[96] Pere Roca i Cabarrocas and Huc J. Lloret A. Parey J. Y. Schmitt J. P. M. Chevrier, J. B. A fully automated hot-wall multiplasma-monochamber reactor for thin film deposition. *Journal of Vacuum Science and Technology A: Vacuum, Surfaces, and Films*, 9(4):2331–2341, 1991.

[97] P. Drude. Zur elektronentheorie der metalle. *Annalen der Physik*, 306(3):566–613, 1900.

[98] P. Drude. Zur elektronentheorie der metalle; ii. teil. galvanomagnetische und thermomagnetische effecte. *Annalen der Physik*, 308(11):369–402, 1900.

[99] A. Poruba, Z. Remes, J. Fric, M. Vanecek, J. Meier, P. Torres, N. Beck, N. Wyrsch, and A. Shah. Microcrystalline Silicon Thin Film Cells: Differences in the Cell and Material Properties. In *14th EC Photovoltaic Solar Energy Conference*, pages 2105–2108, 1997. IMT-NE Number: 252.